J. Mas Soldevilla

DYNAMIC ANALYSIS AND STABILITY STUDY OF THE ELECTROMAGNETIC SUSPENSION LEVITATION SYSTEM OF THE HYPERLOOP

Hyperloop case

TU Delft

Dynamic analysis and stability study of the electromagnetic suspension levitation system of the Hyperloop

Hyperloop case

By

J. Mas Soldevilla

in partial fulfilment of the requirements for the degree of

Master of Science
in Civil Engineering

at the Delft University of Technology,
to be defended publicly on Monday April 28th, 2022 at 10:00 AM.

Student number:	4947096	
Project duration:	March 15th, 2021 – April 28th, 2022	
Thesis committee:	Dr. ir. K. N. Van Dalen,	TU Delft, supervising chair
	Prof. dr. ir. A. V. Metrikine,	TU Delft, supervisor
	Dr. ir. J. M. de Oliveira Barbosa,	TU Delft, weekly supervisor
	ir. A. Faragau,	TU Delft, bi-weekly supervisor
	ir. A. Bougioukos,	Witteveen+Bos N. V., weekly supervisor

An electronic version of this thesis is available at http://repository.tudelft.nl/.

Delft University of Technology

Preface

After having a very interesting experience at TU Delft during a one year exchange program at the Civil Engineering Faculty, I felt very attracted to the course offer presented by the university in the field of structural engineering and structural dynamics and I decided to take on the challenge of moving to the Netherlands and take part in such a hurdle MSc programme. Throughout these years, I have learned much more new crafts and technologies than I would have ever imagined, and I have met many extraordinary people along the way. It has not been a straight path, but more like a roller coaster. Now, taking a look back, I feel very proud of all the academic, professional and personal achievements reached over the last two and a half years. I feel very blessed to have been part of such an incredible academic institution as TU Delft and to have had the chance of working along side many experts.

As an engineer, I am striving to develop engineering projects and concepts to cope with the current transportation, social, and environmental challenges by means of innovative, sustainable, and digitalized technologies and tools, always aiming at improving human welfare. This is what made me decide on taking the structural engineering MSc path, so as to be able to shape the cities and infrastructures of the future, trying to make a positive impact in society. This brought me to follow the annotation in structural dynamics, since it is a craft that is not that much develop in my country of origin. For these reasons, when Karel van Dalen proposed me to take part in the Hyperloop project, I did not hesitate to accept. I think this technology is going to be a game changer in the transportation sector as we currently know it and will provide cleaner, more efficient, more accessible, faster and better integrated transportation between relevant demographic node and goods distribution hubs.

I feel very grateful by the unique opportunity that Apostolos Bougioukos and Witteveen+Bos gave me to conduct this thesis with them. It has been an unbelievable opportunity to grow my professional career, improve my technical skills and my team working aptitude and to learn more about the Dutch culture.

I could not have completed this research without the help and support of all the members of my committee and I want to express my sincere thanks to all of them. My company supervisor Apostolos Bougioukos, and my daily supervisors Andrei Faragau and Joao de Oliveira have been the backbone of this project, working alongside me in every step of the way and making me give my best version. I am also very grateful to Karel van Dalen, who I first know as my first professor in the university and trusted me all the way until the date, providing me my first professional opportunity in my internship with Witteveen+Bos and, afterwards, giving me the opportunity to take part in this project and offering himself to be the chair of my committee. I feel very fortunate of having had the chance to be your a student and having worked alongside you all this time. I also want to thank professor Andrei Metrikine for his valuable input in every committee meeting, always bringing an alternative point view, inviting to critically think about any assumption and conclusion, and through which I gained very valuable knowledge.

Finally, I want to thank my family and friends for their unbelievable support, in such a hard time marked by a pandemic. A special thanks goes to my partner and my parents, for always keeping my back, helping me and cheering me in the very lows, and making me maintain my feet on the ground in the very highs. I am grateful for all the sacrifices and all the hours you devoted to me, so that I could reach this moment one day.

J. Mas Soldevilla
Delft, April 2022

Abstract

The Hyperloop is a high-speed means of transport, consisting of a bullet-shape vehicle travelling in a quasi-vacuum tube, electrically powered and moving through an electromagnetic levitating system. This allows the reduction of air resistance and wheel-rail contact friction, which translates in higher speeds for smaller power inputs. In the Netherlands, the Dutch company Hardt Hyperloop, has developed a new design concept of such technology, by means of electromagnetic suspension systems, unlike the most commonly applied levitating techniques.

The main aim of this project is to investigate the stability of the electromagnetic suspension levitation system, study the effect that the implementation of an error-based closed-loop control system has on the system dynamics and investigate the vehicle-structure interaction once a control system has been applied to the system.

Along these lines, the overall infrastructure-vehicle system is modelled through an equivalent two degrees of freedom system. In this manner, the inherent instability of the electromagnetic system is confirmed and the initial vehicle dynamics are highlighted. Afterwards, an error-based closed-loop PD-control system that applies to the system definition and reacts on the uncontrolled system dynamics is implemented and the effect of the control parameters on the dynamics and the stability of the system is studied. A certain stability region in the parametric space is derived, which ensures the stability of the system for significant perturbations of the vehicle from its equilibrium point. Besides, the existence of a subcritical bifurcation with respect to the parameter combination is demonstrated. The safety margin in the time delay of the controller response is studied, so as to define a slack time that accounts for not only processing and sampling delays, but also unforeseen events. Finally, the vehicle-infrastructure interaction is studied and its stability is ensured, by means of the previously defined control scheme.

List of Contents

LIST OF FIGURES

LIST OF TABLES

1
INTRODUCTION

1.1. BACKGROUND

With the current globalized society, the demand for more time-, power- and capacity-efficient modern transport is growing. Along these lines, the market share for high-speed transportation is increasing rapidly and, by 2050, it is predicted that around half of the total traffic in the world will be high-speed transportation [1]. In the last decades, a significant growth in the amount of high-speed rail lines has been experienced and, currently, fully connected high-speed rail networks have been constructed covering the whole Europe, Japan and China, which arise as the corner stone of this technological development. As observed over the last twenty years, the future of transport will meet technological advances in electric power, digitalisation and automation [2].

Whilst commercial aviation is still the cheapest and fastest means of transport for long-distance trips, its efficiency in terms of travel time (including commuting time to the service infrastructure, check-in, boarding, trip duration, landing, debarking and commuting time to the final destination), fuel consumption, pollution and frequency is more limiting. In spite of recent efforts of aircraft manufacturers to design more fuel efficient prototypes, commercial and freight aviation still represents one of the most polluting industries. In 2018, global aviation (i.e. commercial, freight and military aviation) represented a 2.5% of the total CO_2 emissions worldwide and, with respect to non-CO_2 climate impacts, it accounts for 3.5% of the global warming [3]. This becomes even more significant when one realizes the small amount of the worldwide population that has access to aviation. In this manner, the idea of a high-speed, sustainable, environmentally friendly, affordable and high-frequency traffic alternative was born, aiming at substituting such short-haul aviation routes.

The origin of such an alternative goes back to the 1799, when George Medhurst patented an atmospheric railway which could transport both cargo and people pneumatically through a pressurized cast iron tube. This initial design relied on steam power propulsion. This idea was later refined by Robert H. Goddard in 1904, presenting the so called vactrain, defined as a high-speed rail transportation moving through evacuated tubes in a reduced air environment with relatively little power. He wrote down his vision of it in *The High-speed Bet*, which was published in 1909 under the name *The Limit of Rapid Transit*. The main concept was then improved and further developed by several different engineering, always acknowledging that the biggest limitation for rail transportation to reach high-speed was the presence of air resistance.

Following the aforementioned ideas, in 2013, a new technology was proposed under the tag of Hyperloop, as an open-sourced technological concept to be developed in a participative manner for any company and research institutes in the world, with the goal to make all these ideas become real. The initial concept consisted of pressurized bullet-shaped capsules riding on air bearings driven by linear induction motors and axial compressors throughout reduced-pressure tubes [4]. This design was conceived to cope with friction, leading to faster seeds than conventional rail with significantly less power. Beside, the design was conceived to be electrically powered, avoiding the polluting emissions from aviation and road traffic. However, considering economic and engineering constraints, the initial idea has been modified leading to different designs which may vary significantly between companies and countries.

In this thesis, the focus is brought on the design proposed by Hardt Hyperloop, the company developing this technology in the Netherlands, which differentiates significantly from the rest of current designs by using an electromagnetic suspension system, a very innovative vehicle-infrastructure lay out and proposing a design compatible both for people and cargo transportation.

This chapter aims to introduce the problem statement, the objectives and the structure of the research addressed in this thesis project.

1.2. PROBLEM STATEMENT

Unlike other Hyperloop designs, Hardt Hyperloop's proposal is based on an electromagnetic suspension system, i.e. it uses electromagnets that attract a magnetically conductive track to maintain the vehicle at a constant spacing hanging from the rails. This poses an important challenge since, in general, the electromagnetic suspension is dynamically unstable unless properly controlled [5]. Besides, at the moment, there are no references on the study of electromagnetic suspension levitation systems applied to Hyperloop technologies. Consequently, this thesis tries to extend the theory in electromagnetic suspensions system developed up to the date for Maglev technologies to the Hyperloop design concept.

Hence, this thesis focuses on two things. Firstly, on addressing the challenge of stabilizing this vertical levitation system, such that the vehicle maintains a specific air gap with the rails at all times, by means of an error-based closed-loop PID-controlling scheme type. Secondly, on investigating the effect that this controller can have of the levitation system dynamic, understanding how the control parameters govern the vehicle dynamics (Fig. 1.1).

The sketch below illustrates the problem addressed in this report, representing a longitudinal cut of the vehicle and the track infrastructure of the Hardt Hyperloop design.

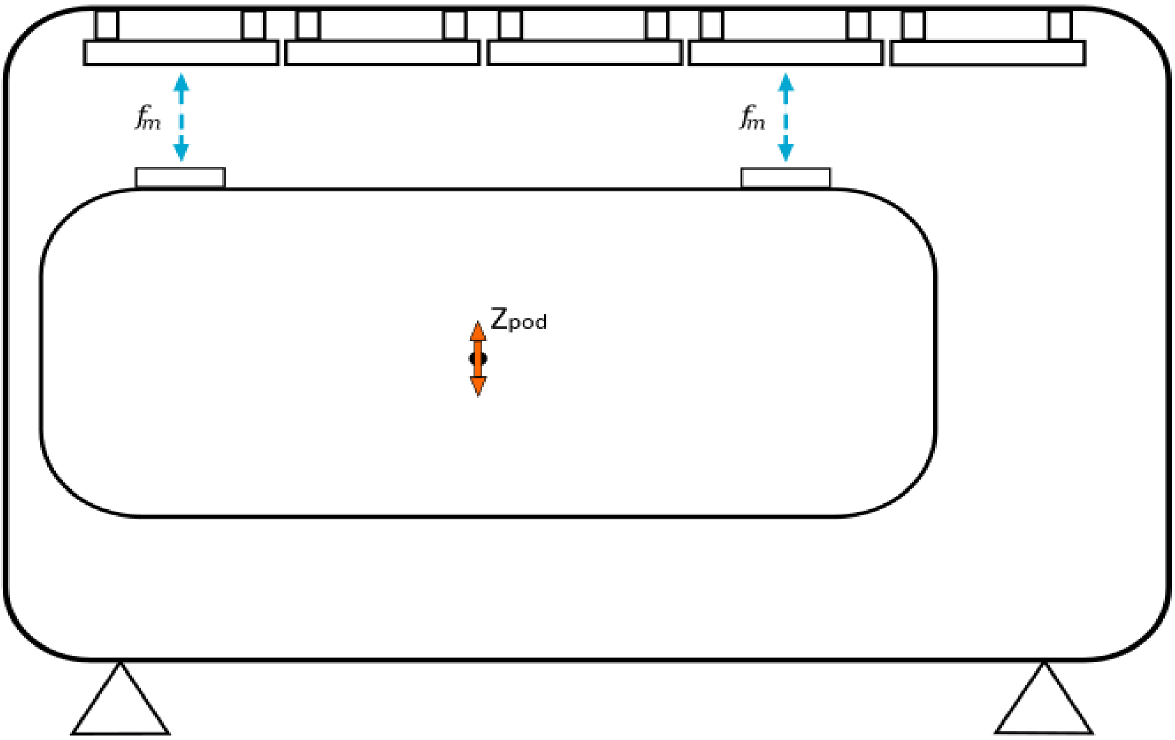

Figure 1.1 Longitudinal cut hyperloop system lay out featuring the levitation system and the vertical motion DOF

Along these lines, this project is built around: i) the understanding of the stability of the electromagnetic suspension levitation system, ii) the parametric study of several magnitudes of interest that take part in this system, iii) the investigation of the application of an error-based closed-loop control on the system that ensures the target air gap between rail and vehicle proposed by the company, iv) the analysis of the dynamic interaction between the rail and the vehicle, considering a flexible guideway modelling.

The design and implementation of electromagnetic suspension systems in Hyperloop entail interdisciplinary concepts such as electronics, electromagnetism, mechanical engineering, structural dynamics, control engineering and measurements.

1.3. RESEARCH OBJECTIVES

The stability of Electro-Dynamic Suspension (EDS) applied to Hyperloop technology and the stability of Electro-Magnetic Suspension (EMS) applied to Maglev technologies have been studied in several papers [6-18]. However, there are no references on the study of EMS applied to Hyperloop technologies. Consequently, the first objective addressed in this thesis should be described as follows:

1. Extrapolate EMS system definition for the Hardt Hyperloop design.

    1.a) Define the formulation and the critical parameters involved.

    1.b) Confirm that the system is inherently unstable and explain the reason for such an event.

Once the EMS system stability is better to understood, one can then propose a control strategy to ensure that the vehicle can be kept stable around an equilibrium target air gap. Along these lines, the extensive research produced up to date in error-based proportional – (P), derivative- (D), integral- (I), PD, PI and PID closed-loop controls can be applied for this specific application. As a consequence, the second objective of this project is described as:

2. Design an error-based closed-loop control following a fundamental approach that can stabilize the system.

    2. a) Define the control variables, the control function and the system plant function. Generate a clear understanding of the controlling scheme principles.

    2. b) Analyse the behaviour of the control concerning its control gains and clearly define a stability region of the system using a study of the linearized system.

    2. c) Provide a simple tuning basics of the control gains for further research steps.

After a clear study of the stability of the EMS system and the tracking of the position of the vehicle, the research is extended by considering the vibrations of the infrastructure (i.e. beam-rail and tube). Thus, the third objective of this thesis can be stressed as follows:

3. Study of the vehicle-infrastructure system at the design cross-section, only in the vertical direction.

1.4. REPORT OUTLINE

This report consists of five main sections: a literature review, a chapter presenting the model constructed and the derivation of the equation of motions and assumptions, a third chapter presenting the stability study from the open-loop most simplified system to the model with stabilizing closed-loop feedback control, another chapter presenting the delay of the linearized system and the dead time safety margin, and the last chapter featuring the dynamic analysis of the infrastructure-vehicle system. This is all concluded by a chapter listing the conclusions obtained from this research and the proposition of further research recommendations.

Chapter 2 serves to present the current state of the art of levitation technologies, their current applications and the control schemes developed for its stabilization. This section is useful to locate this project within the current developments and researches on this technology. Besides, its ultimate purpose is to provide the reader with all the basic engineering concepts that will later face in the presentation of our research, such that he/she can follow all the developments described.

Chapter 3 presents the modelling of the problem addressed in this report and all the modelling assumptions taken for the derivation of the equations of motion.

Chapter 4 serves to confirm the inherent instability of the EMS levitation system modelled for this problem and feature the vehicle dynamics without the implementation of any control technology (i.e. open-loop systems).

Chapter 5 features the modelling and results of the first closed-loop model with the simplest control scheme existent and how this affects the system response.

Chapter 6 presents the modelling of the closed-loop system applying a PD-control. This section serves to understand, first of all hoe this control system works and how it affects the vehicle dynamics, and secondly, to showcase that the stabilization of the system is possible. The sensibility of the system response with respect to the control parameters is explained and how this gives rise to certain bifurcations.

Chapter 7 serves to correct the model derived in the previous section by adding an on/off switch on the electromagnetic force, that avoids misleading electrical current outputs and increases the stabilization region with respect to the magnitude of the perturbation applied to the system.

Chapter 8 features the stability study of the vehicle-track coupled system and how applying the error-based PD-control system together with the on/off switch on the electromagnetic force the system is stable. The sensibility of the system response with respect to the control parameters is explained and how this gives rise to certain bifurcations.

Chapter 9 presents a study of the effect of time delay on the control system response and hoe critical it is to keep the system stable.

Chapter 10 summarizes the conclusions obtained from this project and proposes several recommendations for future researches on the topic.

2

LITERATURE REVIEW AND THEORETICAL FRAME

Aiming at clarifying concepts that might be used later when modelling the levitation system and studying the error based closed-loop control implementation, this section will serve to clarify both electrodynamic suspension systems (EDS) and electromagnetic suspension systems (EMS) conceptual levitating suspension systems, elaborate on the stability patterns resulting from the study of the eigenvalues of the system, review relevant theory on the dynamic behaviour of structures, and shed light on the principles of the control engineering and define several design alternatives.

2.1. MAGNETIC LEVITATION TECHNIQUES

Aiming at increasing the railway's traffic efficiency, the engineers have identified the friction at the contact interface between the wheels and the rail as a relevant source of energy loss. In this manner, over the last century, several engineers have focused on the research of levitating rail infrastructure design which eliminates this friction and allows the vehicles to reach higher speeds and provides a larger lifetime of the infrastructure. Along these lines, namely two main levitation technology designs have been developed: electromagnetic suspension (EMS) and electrodynamic suspension (EDS). The latter has led to two different design concepts for which one uses superconducting electromagnets and the other uses an array of permanent magnets. The last is better known as Inductrack. Each of these levitation techniques is schematically represented in the figure below (Fig. 2.1).

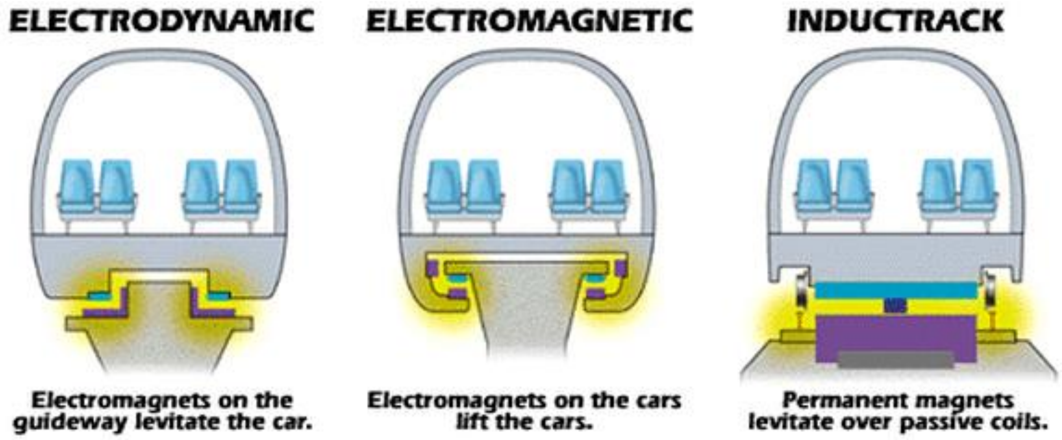

Figure 2.1 Representation of the different magnetic levitation systems [18]

2.1.1. Electromagnetic suspension (EMS)

The EMS system uses the attractive magnetic force of electromagnets placed in the vehicle's support frame (e.g. boogie) that draws the vehicle to a magnetically conductive track, maintaining it at a target spacing from the rails. The electromagnets use feedback control systems to actively monitor the air gap and maintain the train at a constant distance from a track [19].

There is little literature available on the Hyperloop, especially on the EMS system due to its reduced application to date. Moreover, the Hyperloop technology itself is at a proof of concept stage. However, wider research has been devoted to its application in Maglev trains applications, which can be extrapolated to our design. The electromagnetic levitation system of Maglev trains, has attracted much attention in recent years, due to its low noise, non-contact operation, and strong climbing ability [7].

For Maglev trains applications the EMS system can lift a train using attractive forces by the magnets beneath a guide-rail [15]. The onboard suspension electromagnet (or permanent magnet plus excitation control coils) that is placed under the track is energized to generate the electromagnetic field through the mutual attraction between the electromagnet and the rail. This is captured in the figure below (Fig. 2.2.). The vehicle is suspended on the rail. The suspension gap between electromagnet and electromagnetic rail is about 8–10 mm [20].

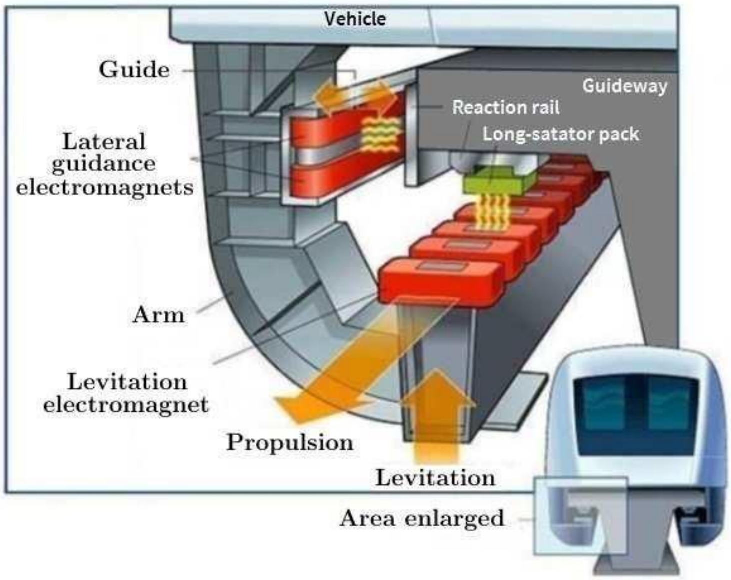

Figure 2.2 EMS system used in the Transrapid [18]

This levitation system has only been implemented in one Hyperloop design project, the Hardt Hyperloop. Nevertheless, this mechanism changes slightly its layout when it comes to Hardt Hyperloop's Design. In this case, the rail is placed on the ceiling of the hyperloop tube and consists of a magnetically conductive track, and the hybrid permanent magnets are placed fixed to the boogie frames which move below the rail, as shown in the figure below (Fig. 2.3.).

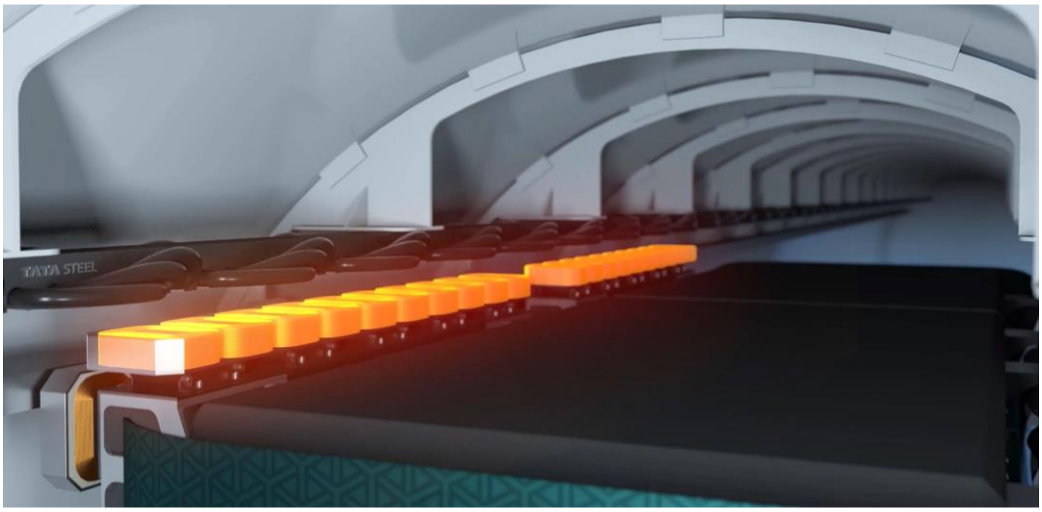

Figure 2.3 Initial EMS system concept projection Hardt Hyperloop [21]

2.1.2. Electrodynamic suspension (EDS)

In the EDS system both the rail and the train exert a magnetic field, and the train is levitated by the repulsive force between these magnetic fields. The magnetic field in the train can be produced by either superconducting electromagnets (e.g. JR-Maglev) or by an array of permanent magnets (e.g. Inductrack).

The repulsive force in the track is created by an induced magnetic field in wires or other conducting strips in the track [19]. However, the EDS train is suspended only when it reaches a certain speed. When the train is running, the moving magnetic field of the onboard magnet will excite the induced current in suspension coils (always low-temperature superconducting coils or permanent magnets) installed in the line. The moving field interacts with the induced current and produces an upward force to draw the car upon the road surface by a certain height around 10–15 cm generally [20].

Along these lines, at slow speeds, the current induced in these coils and the resultant magnetic flux is not large enough to support the weight of the train. For this reason, the train must have wheels or some other form of landing gear to support the train until it reaches a speed that can sustain levitation [19]. A slight increase in distance greatly reduces the repulsive force and returns the vehicle to the right separation again [20], meaning that the gravity is no longer a destabilizing action as in EMS, but a stabilizing one

This levitation technique is the most widely used on the globe for Hyperloop applications. Especially significant is its use by the two leading companies in Hyperloop development: Hyperloop Transportation Technologies (HTT) and Virgin Hyperloop.

The technology has been licensed to HTT from Lawrence Livermore National Labs (LLNL), which developed it as part of the Inductrack system. This method is thought to be cheaper and safer than traditional maglev systems. With this method, magnets are placed on the underside of the capsules in a Halbach array. This focuses the magnetic force of the magnets on one side of the array while almost entirely cancelling out the field on the other side. These magnetic fields cause the pods to float as they pass over electromagnetic coils embedded in the track. Thrust from linear motors propels the pods forward [22].

HTT’s main rival, Hyperloop One from Virgin Hyperloop is also using a passive magnetic levitation system where pod-side permanent magnets repel a passive track, with the only input energy coming from the speed of the pod [22]. The design layout of the Hyperloop One is presented below (Fig. 2.4.)

Figure 2.4 Pod design XP-2 Test Vehicle Virgin Hyperloop [23]

2.1.3. Comparison of different magnetic levitation technologies

Each of the aforementioned systems has advantages and disadvantages. A good understanding of these limitations and positive aspects will allow us to define attention points and drawbacks to address in the implementation of the EMS in the Hyperloop concept.

The main advantage of EMS systems is that they can work at all speeds and avoid the disadvantage of EDS which only work at a minimum speed of about 30 km/h, which can eliminate the requirement for a separate low-speed suspension system and can simplify the track layout as a result [20]. Its application in recently developed Maglev trains has proven to be a commercially available technology that can attain very high speeds of up to 500 km/h [19].

In contrast, the main disadvantage of the EMS technology is the dynamic unstable nature of electromagnetic attraction, explained in detail in the next section, which requires the constant monitoring of the levitation air gap which is controlled and corrected by computer systems integrated either on the rail or the vehicle [19]. These control systems can be centralized or decentralized.

On the other hand, the main advantage of EDS systems is that they are naturally stable. A minor narrowing in distance between the track and the magnets creates the strong forces to repel the magnets back to their original position. No feedback control is needed. Moreover, powerful onboard superconducting magnets and a large margin between rail and train enable the highest recorded train speeds of up to 581 km/h and heavy load capacity [19].

Whereas the main disadvantages are the fact that at the slow speed, the resultant magnetic flux and the current which is induced in these coils is not large enough to support the weight of the Maglev train. For this reason, the train must have wheels or some other form of landing gear to support the train until it reaches a speed that can sustain the levitation. Since a train may stop at any location, due to equipment problems, for instance, the entire track must be able to support both low-speed and high-speed operations, which increases significantly the costs [20]. Another disadvantage is that the EDS system naturally can produce a field in the track in front and to the rear of lift magnets, which can act against the magnets and produce the drag force [24]. Besides, such strong magnetic fields onboard the train might make the train inaccessible to passengers with pacemakers or magnetic data storage media such as hard drives and credit cards [19].

2.1.4. Stability of magnetic levitation technologies

Static magnetic bearings using only electromagnets and permanent magnets are unstable, as explained by Earnshaw's theorem. Samuel Earnshaw showed that it is not possible to place a collection of bodies, subject only to electrostatic forces, in such a way that they remain in a stable equilibrium configuration [5]. This theorem applies to magnetic forces as well. In fact, it is true for any force that varies with the inverse square of the distance, or any combination of such forces [25].

In this manner, EMS systems rely on active electronic stabilization. Such systems constantly measure the bearing distance and adjust the electromagnet current accordingly [19]. Many different control schemes can be applied for such purpose. Extensive coverage of this concept is provided in section 2.5.

Since all EDS systems are generate the electromagnetic force based on electrodynamic forces, Earnshaw's theorem does not apply to them. This is an important advantage of this type of magnetic levitation technique.

2.1.5. Research and major achievements in the field

Electromagnetic levitation is not a new thing, but has been studied for long. However, in recent years, its study in applications such as Maglev trains and high speed trains has increased significantly. Lately, several papers have brought the spotlight on the study of the levitation stability, the stabilization of the system using different control schemes and the stability of the vehicle-track coupled system for flexible guideways.

The study of the stability of EMS Maglev trains running through a flexible guideway has been widely studied [6 - 18]. In general, all of them present the same design principles for the EMS levitation system definition, with slight changes in the magnet shape, and the vehicle-infrastructure fitting and interaction. The most significant differences are come with the type of control system applied or the guideway modelling.

Following the literature review, the most commonly applied control scheme are error-based close-loop PD-control on the electrical current or the voltage across the electromagnet [6-14, 15-18]. These are generally formulated by monitoring levitation air gaps, vertical accelerations of the vehicle or/and electrical current in the circuit. Others implement also the integral components, leading to error-based close-loop PID-control [26] or PI-control [15]. Others proposed multiple level feedback control schemes, controlling electrical current, magnetic air gap flux density and air gap, with complementary frequency filters [27]. Others use more complex scheme to derive a robust controller, such as Linear Quadratic Gaussian (LQR) regulator or Sliding Mode Control (SMC) based on Karman filters [28].

The most common modelling of the flexible guideway is by simplifying the track beam to a single-span simply supported Euler-Bernoulli beam [6 – 12, 14 - 18]. In these cases, a modal analysis is then conducted for the model of the beam int the system. Then, as more extensively explained in chapter 3, the vibration frequency corresponding to the maximum amplitude of track beam with maglev train running on its upper part is distributed within a range, wherein the first-order frequency of the track beam has the greatest impact [11]. Therefore, only the influence of the first order bending mode of the track beam is taken into account in most of the papers [6 - 18]. Others model the track beam as a double span continuous beam [13].

Junxiong Hu et al. [9] analysed the mechanical characteristics of single electromagnet system and elastic track beam of EMS maglev train and established a five-dimensional dynamics model of single electromagnet-track beam coupled system with classical PD control strategy adopted for its levitation system. In this paper, based on the Hurwitz algebraic criterion and the high-dimensional Hopf bifurcation theory, the stability of the coupled system is analysed, proving the existence of a subcritical Hopf bifurcation governed by the K_p value [9].

The investigation time delay in the control system has also been addresses for the EMS Maglev levitation system of on a flexible guideway, like in the paper written by Junqi Xu et al. [14], where the study of a the Hopf bifurcation with double time-delay feedback of maglev train running on the flexible guideway is presented considering time-delayed position feedback signal τ_1 and velocity feedback signal τ_2. A novel method is presented to develop the double-parametric Hopf bifurcation diagram in relation to τ_1 and τ_2 [14].

R. P. Talukdar et al. [13] outline an approach for the modelling and simulation of Maglev vehicle–guideway in a block diagram environment, optimizing the suspension parameters for increased ride comfort. They modelled the guideway as a two span continuous beam and four EMS suspension frames connecting the total vehicle length with the beam. In this paper, the guideway surface roughness is defined by power spectral density function. They proved that the vehicle operating speed is the primary criteria that govern the magnitude of response of both the guideway and the vehicle. They concluded that the two-span continuous guideway performs better than a single-span guideway because of the redistribution of sagging moment to the interior support. It is showed that the guideway irregularity has a greater impact on the car-body response than on the guideway response [13].

Considering the literature review, the main gap covered by this thesis is the application of an EMS levitation system in a Hyperloop technology, since to date no papers have been published on the application of this levitation technique for such a technology concept. In this sense, this thesis aims at understanding the dynamics of this levitation system, investigating the implementation of an error-based close-loop PD control on the voltage across the electromagnet coil only monitoring the levitation air gap. In this manner, this report provides a study of the effect of the control parameters in the system dynamics, of the appearance of bifurcations or other (in)stability patterns, of the definition of the needed set up to stabilize the system and of the effect on the system stability of possible time-delay in the control response.

Aiming at meeting these research benchmarks, several different concepts and engineering methods learned form the aforementioned literature review will be applied in different section, such as the Hurwitz algebraic criterion, the definition of classical error-based closed-loop PD-controls, the study of time delayed control responses, etc.

2.2. ELECTROMAGNETICS FUNDAMENTALS

The author of this report has written a theoretical summary of the most important fundamental concepts of electromagnetism, that later are used to develop the equations of motion of the system in chapter 3, based on the H. -S. Han et al. book [29]. This can be found in Annex A.

The phenomenon of magnetic levitation is developed through magnetic fields between magnetic objects. Such magnetic fields are generated by the movement of electric charges and are generally represented by field lines with no beginning or end, forming closed loops. The field lines come from the North pole (N) and enter the South pole (S), they are continuous and do not meet each other.

In this manner, an attractive force is generated between two magnetized objects when the field lines go from one to another. Whereas if the same poles are facing each other, the field lines are pressured, resulting in a repulsive force between them.

A flux ϕ is a series of field lines. The value of the flux corresponds to the number of field lines, as a measure of the magnetic field's strength. Such that, the more lines, the stronger the magnetic field and the larger the flux. Then, the flux density B is defined as the flux per unit area normal to a magnetic field.

If electrons with negative charges flow through a conductor, a magnetic field is produced around it. This field is called an electromagnetic field. Magnetic permeability μ represents the relative ease of establishing a magnetic field in a given material. Whereas, reluctance $\Re$ is a magnetic resistance in materials, which is the counterpart of electrical resistance.

An electromagnet is defined as a type of magnet in which the magnetic field is produced by an electric current. Generally, it consists of a large number of closely spaced turns of wire that create the magnetic field. Along these lines, the magnetomotive force F_m is the cause of the magnetic flux in a magnetic circuit. Therefore, it can be defined as the effective current flow applied to the core $F_m = NI\ [A \cdot\ N^o\, turns]$, where I is the electrical current and N is the number of coil turns around the core. The degree to which a magnetic field by a current can magnetize a material is called magnetizing force H, and it is defined as the magnetomotive force F_m per unit length of material. The magnetic flux B induced in the material depends upon the nature of the material, such that $B = \mu H$.

In electromagnetism and electronics, inductance is the property of a conductor by which a change in current flowing through it induces a voltage or electromotive force in both the conductor itself (i.e. self-inductance) and any nearby conductors (i.e. mutual inductance). A changing electric current through a circuit that contains inductance induces a proportional voltage that opposes the change in current. The relationship among the parameters for a coil with inductance L is defined as

$$V = IR - L\frac{dI}{dt} \tag{2.1}$$

where $L = \dfrac{N^2 \mu A}{l}$.

Considering the aforementioned definitions of electromagnets, it is important to introduce the concept of Kirchhoff's law of voltage and current which state that "the total voltage around a loop is equal to the sum of all the voltage drops within the same loop" and "the total current or charge entering a junction or node is equal to the charge leaving the node, cause the charge has no other place to go except to leave as no charge is lost within the node", respectively. As aforementioned, this later will allow us to relate the magnetic and electric variables all in one equation such that the full behaviour of the electromagnet will be captured through the expression.

$$V = IR - L\frac{dI}{dt} - K\frac{d\delta}{dt} \tag{2.2}$$

Where δ describes the levitation air gap. In this manner, eq. 2.11 defines the total voltage of the system, from its ohmic term input subtracting the associated losses due to variation rates of electrical current and levitation air gap.

Then, throughout the combination of the magnetomotive force, the magnetizing force, reluctance and inductance, an electromagnetic force definition can be derived, governing the electromagnetic suspension levitation system.

2.3. STRUCTURAL DYNAMICS REVIEW

Aiming at modelling the electromagnetic suspension system in Hyperloop, one has to first address the layout of the mechanism as a simple single degree of freedom mass-spring-dashpot system considering only the vehicle motion and assuming an infinitely stiff beam. Once the beam flexibility is accounted for, the problem transforms into a double mass and single spring-dashpot system.

The vibration of the guideway play an important role in the dynamics of Maglev vehicles. This is significantly important, considering the fact that the elevated guideway supported by piers deforms and vibrates when the Maglev vehicle travels over it [8]. Thereby, this yields a vehicle-structure coupled vibration system. If the parameters of the vehicle system do not match the track beam system, coupled self-excited vibrations may occur between the electromagnet and the track beam, affecting the stable levitation of the vehicle [6]. The flexibility of the track beam, which has a significant impact on the levitation stability ([16], [30]), is the main cause of the self-excited vibration of the electromagnet-track beam coupling, especially during stationary or low-speed operation ([10], [17]).

The author of this report has written a theoretical summary of the most important fundamental concepts of structural dynamics on the fields of single degree of freedom (SDOF) spring-dashpot system dynamics, multiple degrees of freedom (MDOF) system, Euler-Bernoulli simply supported beam equation, and Laplace transform, that later are used to develop the equations of motion of the system in chapter 3, based on the H. -S. Han et al. book [29], A. Metrikine structural dynamics lecture notes book [31] and E. M. J. Vicca MSc thesis [32]. This can be found in Annex B.

Following this summary, the derivation of the equations of motion governing the SDOF spring-dashpot, both for free and forced vibrations, is presented and system response becomes clear for different damping values. Besides, from this explanation the influence of the damping ratio on the system stability becomes obvious. This is then directly applied in the derivation of the equations of motion of our model, since the definition of SDOF oscillators and a spring-dashpot system play an important role.

From the explanation presented on Annex B, one can see which parameters play a role when describing the equation of motion of the track beam that is implemented in the model in a later section. Especial emphasis is required for the definition of the beam stiffness, structural damping and mass.

Last, but not least, the summary introduces the concept of the Laplace transform. It is defined as an integral transform which serves to transform signals and functions from the time domain to the frequency domain. In this project, this tool is particularly useful, so as to solve linear ordinary differential equations, since in the frequency domain, these become simply algebraic equations. The Laplace transform of a function $G(t)$ is defined as

$$\Im_t[G(t)] = g(s) = \int_0^{+\infty} G(t)\exp(-st)dt \tag{2.3}$$

where $G(t)$ is a function of the real variable t and s is the complex variable, i.e. $s = \sigma + i\omega$. $G(t)$ is called the original function and $g(s)$ is called the image function [31].

This method will prove to be very useful to compute the poles of our linearized system around the fixed points, given that the equations of motion are all linear ordinary differential equations. Besides, it makes the implementation of a control within the system easier to analyse and formulate in the frequency domain in case a study of the transfer functions, the frequency bandwidth of stabilization or a phase delay analysis wants to be performed.

2.4. STABILITY

Considering that the main core of this report focuses on the stability study of the EMS levitation system, it is important to review some basic concepts about stability and sumarize some of the stability patterns that can be found in the models developed.

There are two main types of dynamical systems: differential equations and iterated maps [33]. This project only features differential equations, such that the evolution of the system in continuous time is defined, and its behaviour and stability will feature 1D and 2D flows, limit cycles and bifurcations.

2.4.1. One dimensional flow

The one-dimensional flow can be represented by a dynamic system described as follows

$$\dot{x} = f(x) \tag{2.4}$$

Where $x(t)$ is a real-valued function of time t and $f(x)$ is a smooth real-valued function of x. The dependence on t is no explicit, defining an autonomous system as the one derived for this project. If f would depend explicitly on time, the system would be nonautonomous and, consequently, two-dimensional.

Then, if one draws the graph of $f(x)$ and uses it to sketch the vector field on the real line represented by the x-axis (Fig. 2.5). One can imagine as if a fluid is flowing along the real line with a local velocity $f(x)$. This imaginary fluid is called the phase fluid and the real line is the phase space. The flow is to the right where $f(x) > 0$ and to the left where $f(x) < 0$. In this manner, to find a solution to eq. 2.54 starting from an arbitrary initial condition x_0, an imaginary particle called phase point is placed at x_0 and one can then observe how it is carried along by the flow. As time goes on, the phase point moves along the x-axis according to some function $x(t)$. This function is called trajectory based at x_0, and it represents the solution of the differential equation starting from the initial condition x_0. The representation of one or different trajectories of the system is called a phase portrait (Fig. 2.5) [33].

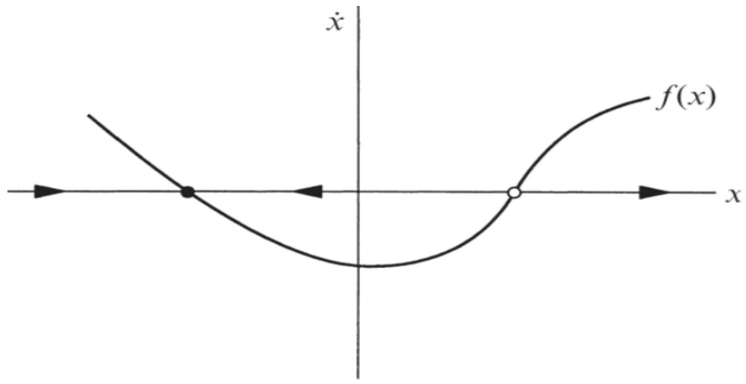

Figure 2.5 Phase portrait of the system [33]

The appearance of the phase portrait is controlled by the fixed points x^*, defined by $f(x^*)=0$ and they correspond to stagnation points of the flow. In the example resented in Fig. 2.5, the solid black dot is stable fixed point , since the flow is toward it in both sides, and the open dot is an unstable fixed point, since flow is way from it [33].

In terms of the original differential equation, fixed points represent equilibrium solutions, which are sometimes called steady, constant or rest solutions, since if $x = x^*$ initially, then $x(t) = x^*$ for all time. An equilibrium is defined to be stable if all sufficiently small disturbances away from it damp out in time. Thus stable equilibria are represented geometrically by stable fixed points. Conversely, unstable equilibrium, is which disturbances grow in time, are represented by unstable fixed points [33].

Note that the definition of stable equilibrium is based on small disturbances and certain large disturbances may fail to decay. In such a case, the fixed point in question is defined to be locally stable, but not globally stable. For it to be globally stable, it has to be approached from all initial conditions [33].

Nevertheless, so far, only graphical methods have been discussed to determine in a qualitative way the stability of fixed points. For a quantitative assessment, an eigenvalue problem needs to be conducted. However, nonlinear dynamic systems, like the one formulated for this project, do not have eigenvalues. Consequently, as a first step, the system needs to be linearized around the fixed point.

Let x^* be a fixed point and let $\eta(t) = x(t) - x^*$ be a small perturbation away from x^*. To see whether the perturbation grows or decays, a differential equation for η needs to be derived [33].

$$\dot{\eta} = \frac{d}{dt}(x - x^*) = \dot{x} = f(x) = f(x^* + \eta) \tag{2.5}$$

Afterwards, Taylor's expansion can be applied in eq. 2.5.

$$f(x^* + \eta) = f(x^*) + \eta f'(x^*) + O(\eta^2) \tag{2.6}$$

Where $O(\eta^2)$ denotes quadratically small terms in η. Note that $f(x^*)=0$ since x^* is a fixed point.

$$\dot{\eta}=\eta f'(x^*)+O(\eta^2) \tag{2.7}$$

Now, if $f'(x^*)\neq 0$, the $O(\eta^2)$ terms are so small compared to it that can be neglected. This of course has some effect on the system solution. If the focus of the stability study is local, the nonlinear and the linearized system are almost equal. But, if the spotlight is moved far from the fixed point, the linearized solution can differ significantly from the nonlinear one. The linearized approximation about x^* is then expressed as [33]

$$\dot{\eta}\approx\eta f'(x^*) \tag{2.8}$$

This shows that the perturbation $\eta(t)$ grows exponentially if $f'(x^*)>0$ and decays if $f'(x^*)<0$. If $f'(x^*)=0$, the $O(\eta^2)$ terms are not negligible and a nonlinear analysis is needed to determine stability [33].

The upshot is that the slope $f'(x^*)$ at the fixed point determines its stability. If one looks back at the earlier examples, it can be seen that the slope was always negative at a stable fixed point. The importance of the sign of $f'(x^*)$ was clear from our graphical approach; the new feature is that now, one has a measure of how stable a fixed point is. This is determined by the magnitude of $f'(x^*)$. This magnitude plays the role of an exponential growth or decay rate. Its reciprocal $1/f'(x^*)$ is a characteristic time scale; it determines the time required for $x(t)$ to vary significantly in the neighbourhood of x^* [33].

Besides, there exist a theorem that proves the existence and uniqueness of the solution to the initial value problem. Consider the initial value problem consisting on eq. 2.4 and initial condition $x(0)=x_0$. Suppose that $f(x)$ and $f'(x)$ are continuous on an open interval R of the x-axis and suppose that x_0 is a point in R. Then the initial value problem has a solution $x(t)$ on some time interval $(-\tau,\tau)$ about $t=0$ and the solution is unique. This theorem says that if $f(x)$ is smooth enough, then solutions exist and are unique. Even so, there is no guarantee that solutions exist forever, due to the existence of blow-up phenomena, proper from models of combustion and other runaway processes [33].

Fixed points dominate the dynamics of first-order systems. The only things that can happen for a vector field on the real line is that all trajectories either approached a fixed point, or diverged to $\pm\infty$. The reason is that trajectories are forced to increase or decrease monotonically, or remain constant. To put it more geometrically, the phase point never reverses direction [33].

Thus, if a fixed point is regarded as an equilibrium solution, the approach to equilibrium is always monotonic, overshoot and damped oscillations can never occur in a first-order system. For the same reason, undamped oscillations are impossible. Hence there are no periodic solutions to eq. 2.4. These general results are fundamentally topological in origin. They reflect the fact that eq. 2.4 corresponds to flow on a line. If you flow monotonically on a line, you will never come back to your starting place, that is why periodic solutions are impossible [33].

The qualitative structure of the flow can change as parameters are varied. In particular, fixed points can be created or destroyed, or their stability can change. These qualitative changes in the dynamics are called bifurcations and the parameter values at which they occur are called bifurcation points. Bifurcations are important scientifically since they provide models of transitions and instabilities as some control parameter is varied [33]. The most representative one-dimensional flow bifurcations are the saddle node bifurcation, the transcritical bifurcation and the supercritical pitchfork bifurcation. Each of this patterns are described in detail in the summary presented in Annex C, based on the S. H. Strogatz book [33].

But, there are other one-dimensional flows not governed by 2.4, but rather

$$\dot{\theta} = f(\theta) \tag{2.9}$$

Which corresponds to a vector field on the circle, such that θ is a point on a circle and $\dot{\theta}$ is the velocity vector at that point. However, this one-dimensional flow differs significantly from the previous ones for one property: by flowing in one direction, a particle can eventually return to its starting position (Fig. 2.6). Consequently, periodic solutions become possible, providing the most basic model of systems that can oscillate. The rest of properties are similar to flows on the line [33].

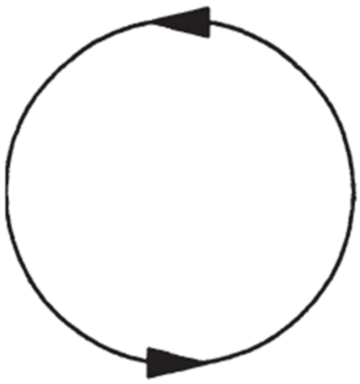

Figure 2.6 Circle flow [33]

A vector field on the circle is a rule that assigns a unique velocity vector to each point on the circle. In practice, such vector fields arise when one has a first-order system as eq. 2.9, where $f(\theta)$ is a real-valued 2π - periodic function, i.e. $f(\theta + 2\pi) = f(\theta)$ for all θ, and assume that $f(\theta)$ is smooth enough to guarantee existence and uniqueness of solutions [33].

2.4.2. Two-dimensional flows

In higher-dimensional phase-spaces, trajectories have much more room to manoeuvre and so, a wider range of dynamical behaviour becomes possible.

As explained for the one-dimensional flow, the nonlinear system does not have eigenvalues. Hence, either a linear system is considered as

$$\begin{cases} \dot{x} = ax + by \\ \dot{y} = cx + dy \end{cases} \tag{2.10}$$

or a nonlinear system is considered and then the linearized approximation as described in section 2.4.1 needs to be applied.

Once the linearized system is defined in the time domain, the eigenvalue problem can be solved aiming at studying the stability of the system around the fixed point. This stability is governed by the trajectories described by the system on the phase portrait. For the sake of generality, one seeks trajectories of the form

$$\mathbf{x}(t) = \exp(\lambda t)\,\mathbf{v} \tag{2.11}$$

Where $\mathbf{v} \neq 0$ is some fixed vector to be determined and λ is the growth rate, also to be determined. If such solutions exist, they correspond to exponential motion along the line spanned by the vector $\mathbf{v}$. To fins the conditions on $\mathbf{v}$ and λ, the expression $\mathbf{x}(t) = \exp(\lambda t)\,\mathbf{v}$ is substituted in the linearized system $\dot{\mathbf{x}} = \mathbf{A}\mathbf{x}$ and obtain $\lambda \exp(\lambda t)\mathbf{v} = \exp(\lambda t)\mathbf{A}\mathbf{v}$. Then, cancelling the non-zero scalar factor $\exp(\lambda t)$ yields [33].

$$\mathbf{A}\mathbf{v} = \lambda \mathbf{v} \tag{2.12}$$

Which says that the desired straight line solutions exist if $\mathbf{v}$ is an eigenvector of $\mathbf{A}$ with corresponding eigenvalue λ. This may be called eigensolution. The eigenvalues of a matrix $\mathbf{A}$ are given by the characteristic equation $\det(\mathbf{A} - \lambda \mathbf{I}) = 0$, where $\mathbf{I}$ is the identity matrix. For a simple 2×2 matrix, as in this study case [33],

$$\mathbf{A} = \begin{bmatrix} a & b \\ c & d \end{bmatrix} \tag{2.13}$$

the characteristic equation becomes

$$\det\begin{bmatrix} a - \lambda & b \\ c & d - \lambda \end{bmatrix} = 0 \tag{2.14}$$

Expanding the determinant yields

$$\lambda^2 - \tau\lambda + \Delta = 0 \tag{2.15}$$

Where $\tau = trace(\mathbf{A}) = a + b$ and $\Delta = \det(\mathbf{A}) = ad - bc$.Then, the solution of the quadratic equation are:

$$\lambda_{1,2} = \frac{\tau \pm \sqrt{\tau^2 - 4\Delta}}{2} \tag{2.16}$$

The typical situation is for the eigenvalues to be different $\lambda_1 \neq \lambda_2$. In this case, a theorem of linear algebra states that the corresponding eigenvectors $\mathbf{v}_1$ and $\mathbf{v}_2$ are linearly independent, and hence span the entire plane. In particular, any initial condition $\mathbf{x}_0$ can be written as a linear combination of eigenvectors as $\mathbf{x}_0 = c_1\mathbf{v}_1 + c_2\mathbf{v}_2$ [33].

For real valued eigenvalues, exponential trajectories are drawn in the phase portrait decaying up to a straight-line trajectory passing through the fixed point. Either such trajectories are straight along their entire domain or they are straight around the fixed point. In the most common situation, for the eigenvalues to be different $\lambda_1 \neq \lambda_2$ (i.e. zero-multiplicity), one can see both eigensolutions decay exponentially leading to two different trajectories with different direction passing through the fixed point, as shown in the example phase portrait presented below (Fig. 2.8).

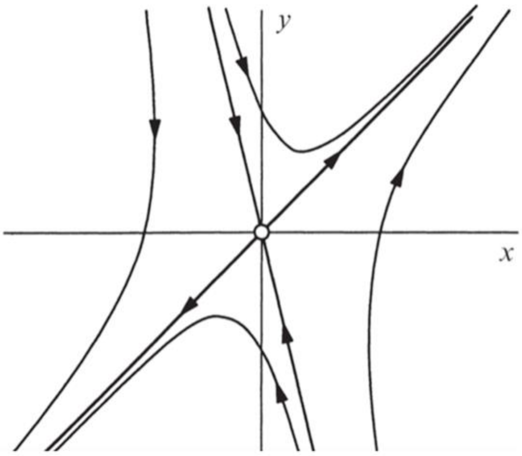

Figure 2.7 Example phase portrait trajectories for system with $\lambda_1 \neq \lambda_2$ for $\lambda_2 < \lambda_1 < 0$ [33]

Along these lines, trajectories typically approach the fixed point tangent to the slow eigendirection, defined as the direction spanned by the eigenvector with the smaller $|\lambda|$. Whereas, in backwards time $(t \to -\infty)$, the trajectories become parallel to the fast eigendirection, as shown in the example phase portrait presented below (Fig. 2.9) [33].

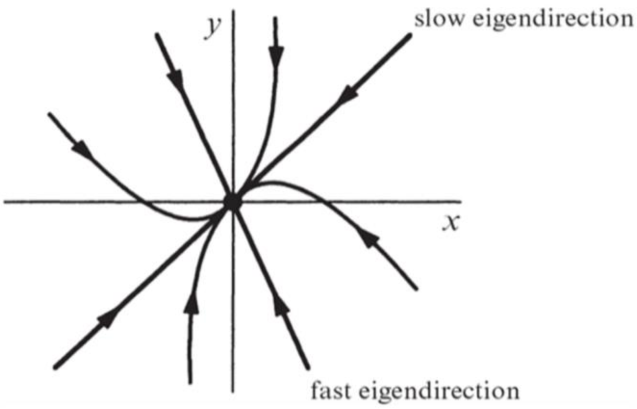

Figure 2.8 Example trajectories behaviour tending to the fixed point and tending to t→ -∞ [33]

On the contrary, if the eigen values are complex numbers, the fixed point is a center or a spiral, which are illustrated in the phase portrait example presented below (Fig. 2.10. a). If the real part of the complex conjugate pair of eigenvalues is zero, a center is drawn. Whereas if it is non-zero a spiral is defined (Fig. 2.10. b) [33].

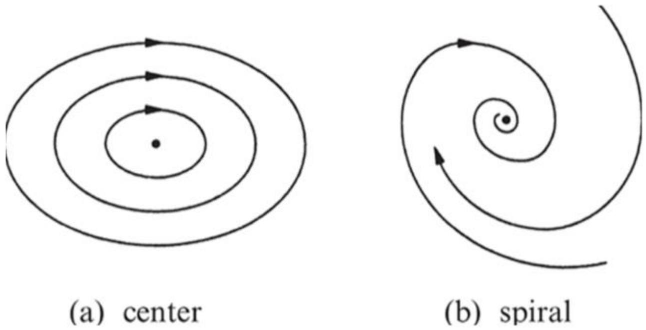

Figure 2.9 Example phase portrait for a) center and b) spiral [33]

Note that centers are neutrally stable, since nearby trajectories are neither attracted to nor repelled from the fixed point. A spiral would occur if the harmonic oscillator was slightly damped. Then the trajectories would fail to close, because the oscillator loses a bit of energy on each cycle, since it is a non-conservative system [33].

The aforementioned statements can be proven considering the eigenvalues definition provided in eq. 2.16, for which complex eigenvalues are obtained when $\tau^2 - 4\Delta < 0$. Hence, these eigenvalues can be written as $\lambda_{1,2} = \alpha \pm i\omega$ where

$$\begin{cases} \alpha = \dfrac{\tau}{2} = \mathrm{Re}(\lambda) \\ \omega = \dfrac{1}{2}\sqrt{4\Delta - \tau^2} = \mathrm{Im}(\lambda) \end{cases} \tag{2.17}$$

In this manner, assuming $\omega \neq 0$ provides different eigenvalues (i.e. zero-multiplicity). Then, the general solution still hold the same shape, but now $c_{1,2} \in \mathbb{C}$ and $\mathbf{v} \in \mathbb{C}$. Thus, in order to define $\mathbf{x}(t)$, linear combinations of $\exp[(\alpha \pm i\omega)t]$ need to be considered, which can be reformulated using the Euler's formula as $\exp(i\omega t) = \cos(\omega t) + i\sin(\omega t)$. Thereby, $\mathbf{x}(t)$ can be defined as a combination of $\exp(\alpha t)\cos(\omega t)$ and $\exp(\alpha t)\sin(\omega t)$, such that if $\alpha > 0$ growing oscillations are developed, i.e. unstable spiral, and if $\alpha < 0$ decaying oscillations are developed, i.e. stable spiral. Besides, if $\alpha = 0$ the eigenvalues are purely imaginary and all the solutions are periodic $T = 2\pi / \omega$. Since the oscillations have a fixed amplitude, the fixed point is a center [33].

In case the eigenvalues are equal $\lambda_1 = \lambda_2 = \lambda$ (i.e. multiplicity 1) two possible eigenvector setups are defined: either there is a unique eigenvector or there are two independent eigenvectors. When there are two independent eigenvectors, they span the plane and so every vector is an eigenvector with this same eigenvalue λ. This can be seen by writing an arbitrary vector $\mathbf{x}_0$ as a linear combination of both eigenvectors $\mathbf{x}_0 = c_1\mathbf{v}_1 + c_2\mathbf{v}_2 \rightarrow \mathbf{A}\mathbf{x}_0 = \mathbf{A}(c_1\mathbf{v}_1 + c_2\mathbf{v}_2) = c_1\lambda\mathbf{v}_1 + c_2\lambda\mathbf{v}_2 = = \lambda\mathbf{x}_0$ which proves that $\mathbf{x}_0$ is also an eigenvector with eigenvalue λ. Since multiplication by $\mathbf{A}$ simply stretches every vector by a factor of λ, the matrix must be a multiple of the identity: If $\lambda \neq 0$ all trajectories are straight lines through the fixed point $\mathbf{x}(t) = \exp(\lambda t)\mathbf{x}_0$ leading to a star node (Fig. 2.11) ; If $\lambda = 0$ the whole plane is filled with fixed points.

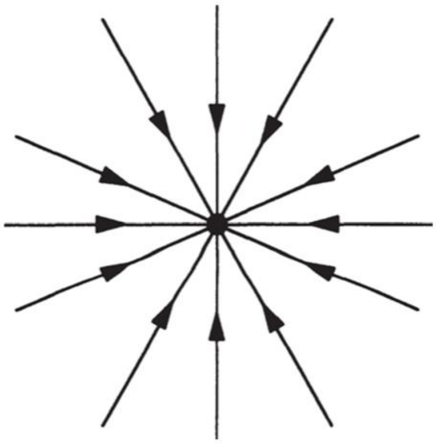

Figure 2.10 Example star node for eigenvalues $\lambda_1 = \lambda_2 = \lambda \neq 0$ [33]

Alternatively, when there is only one eigenvector (i.e. the eigenspace corresponding to λ in 1D), the fixed point is a degenerated node, as shown in the phase portrait example below (Fig. 2.12), where as $t \to +\infty$ and as $t \to -\infty$ all trajectories become parallel to the only available eigendirection [33].

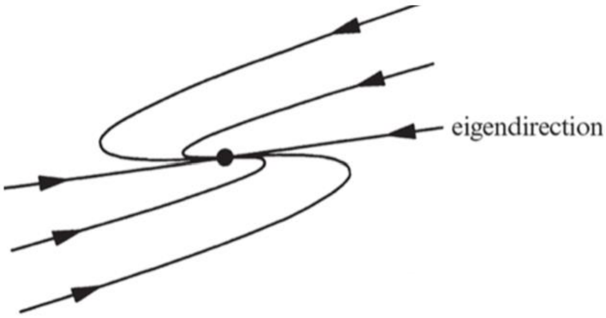

Figure 2.11 Example degenerated node for eigenvalues $\lambda_1 = \lambda_2 = \lambda = 0$ [33]

Note that a degenerated node is on the edge between a spiral and a node. The trajectories are trying to wind around in a spiral, but they do not quite make it. Unlike a degenerated node, an ordinary node has two independent eigendirections. All trajectories are parallel to the slow eigendirection close to the fixed point, and to the fast eigendirection as $t \to +\infty$ (Fig. 2.13) [33].

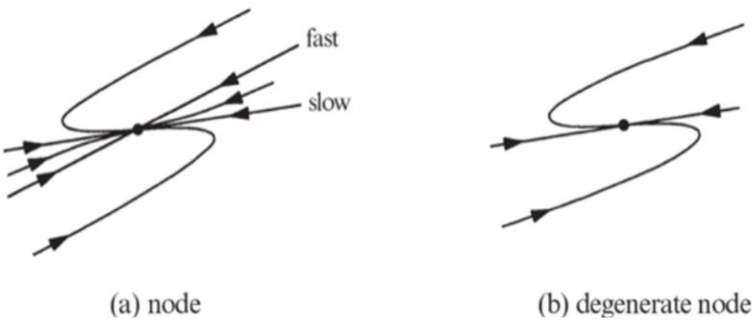

Figure 2.12 Representation in phase portrait of a) an ordinary node and b) a degenerated node [33]

Considering the variability and complexity of nodes that can be obtain in our stability studies, a classification of fixed points is proposed below. Such a classification can be conducted namely using the trace $\tau = \lambda_1 + \lambda_2$ and the determinant $\Delta = \lambda_1 \lambda_2$ of the matrix $\mathbf{A}$, which can then be plotted in a diagram as shown below (Fig. 2.14) [33].

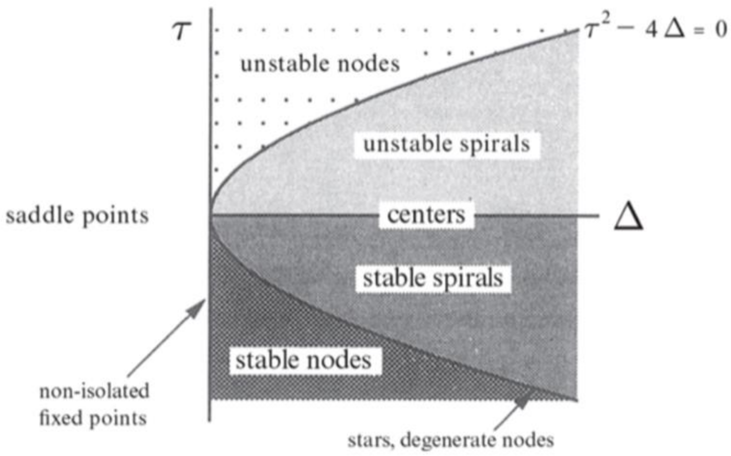

Figure 2.13 Diagram representing the classification of fixed points [33]

- If $\Delta < 0 \Leftrightarrow \lambda_{1,2} \in \mathbb{R} \wedge \{(\lambda_1 < 0, \lambda_2 > 0) \vee (\lambda_1 > 0, \lambda_2 < 0)\}$ → Saddle point
- If $\Delta > 0 \Leftrightarrow \lambda_{1,2} \in \mathbb{R} \wedge \{(\lambda_{1,2} < 0) \vee (\lambda_{1,2} > 0)\} \wedge \tau^2 - 4\Delta > 0$ → Node
- If $\Delta > 0 \Leftrightarrow \{\lambda_{1,2} \in \mathbb{C} \wedge \{(\lambda_1 = \bar{\lambda}_2) \vee (\lambda_2 = \bar{\lambda}_1)\}\}$ →
  - If $\tau^2 - 4\Delta < 0$ → Spiral
    - If $\tau > 0$ → Unstable spiral
    - If $\tau < 0$ → Stable spiral
  - If $\tau = 0$ → Centre
- If $\Delta = 0 \Leftrightarrow \{(\lambda_1 = 0) \vee (\lambda_2 = 0)\}$ → Whole line of fixed points
- If $\Delta = 0 \Leftrightarrow \{(\lambda_{1,2} = 0)\}$ → Plane of fixed points

Where the parabola $\tau^2 - 4\Delta = 0$ is the borderline between nodes and spirals. Star nodes and degenerate nodes lie on this parabola. One can see that centres, stars, degenerate nodes and non-isolated fixed points are borderline cases that occur along curves on the (Δ, τ) plane, as shown above (Fig. 2.14) [33].

The stability of nodes and spirals is determined by τ:

- For $\tau < 0 \Leftrightarrow Re(\lambda_1) = Re(\lambda_2) < 0$ → Stable fixed points
- For $\tau > 0 \Leftrightarrow Re(\lambda_1) = Re(\lambda_2) > 0$ → Unstable fixed points
- For $\tau = 0 \Leftrightarrow Re(\lambda_{1,2}) = 0 \mid \lambda_{1,2} = \pm i\omega$ → Neutrally stable centres

One can say that x^* is attracting if there is a $\delta > 0$ such that $\lim_{x \to \infty} \mathbf{x}(t) = x^*$ whenever $\|\mathbf{x}(0) - x^*\| < \delta$, i.e. any trajectory that starts within a distance δ of x^* is guaranteed to converge to x^* eventually (Fig. 2. 15) [33].

Whereas Liapunov stability requires that nearby trajectories remain close for all time as x^* is Liapunov stable if for each $\varepsilon > 0$, there is a $\delta > 0$ such that $\|\mathbf{x}(0) - x^*\| < \varepsilon$ whenever $\|\mathbf{x}(0) - x^*\| < \delta$. Thus, trajectories that start within δ of x^* remain within ε of x^* for all positive time (Fig. 2. 15) [33].

Consequently, x^* is asymptotically stable if it is both attracting and Liapunov stable.

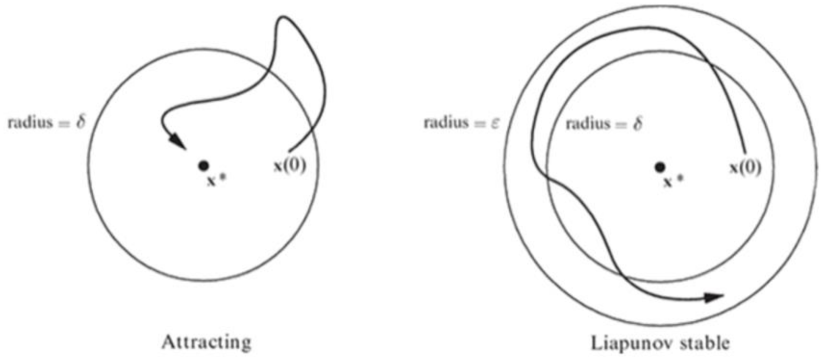

Figure 2.14 Representation of attracting point and Liapunov stability [33]

A limit cycle is an isolated closed trajectory, i.e. the neighbouring trajectories are not closed, but they spiral either towards or away from the limit cycle (Fig. 2.16). If all neighbouring trajectories approach the limit cycle, the limit cycle is stable or attracting. Otherwise, the limit cycle is unstable, or in some cases, half-stable [33].

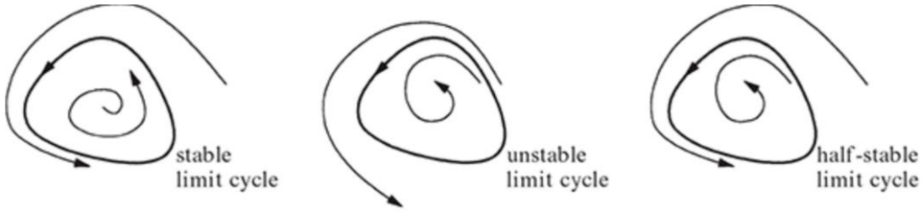

Figure 2.15 Limit cycle classification [33]

Stable limit cycles are very important scientifically, since they model systems exhibit self-sustained oscillations. In this manner, there is a standard oscillation of some preferred period, waveform, and amplitude. If the system is perturbed slightly, it always returns to the standard cycle [33].

Limit cycles are inherently nonlinear phenomena; they can't occur in linear systems. Of course, a linear system can have closed orbits, but they won't be isolated; if $\mathbf{x}(t)$ is a periodic solution, then so is $c\mathbf{x}(t)$ for any constant $c \neq 0$. Hence $\mathbf{x}(t)$ is surrounded by a one-parameter family of closed orbits (Fig. 2.17). Consequently, the amplitude of a linear oscillation is set entirely by its initial conditions; any slight disturbance to the amplitude will persist forever. In contrast, limit cycle oscillations are determined by the structure of the system itself [33].

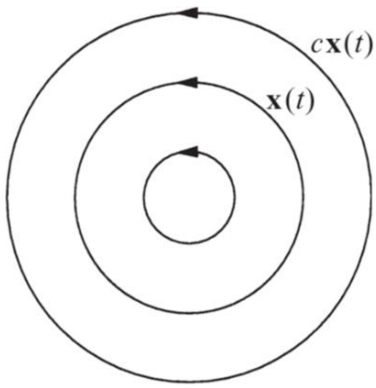

Figure 2.16 Parameter family of closed orbits

The same bifurcation patterns described in section 2.4.1 apply to this case using the same normal form definitions presented in Annex C for the x equation and adding as the second system equation $\dot{y} = -y$ for all cases. For all these cases the bifurcation occurs when $\Delta = 0$, or equivalently, when one of the eigenvalues is zero, called zero-eigenvalue bifurcations. Such bifurcations always involve the collision of two or more fixed points. Nevertheless, for the two-dimensional flow, a new type of bifurcation exists which provides a way for a fixed point to lose stability without colliding with any other fixed point. These are called Hopf bifurcations. This happens when a pair of complex conjugate eigenvalues simultaneously crosses the imaginary axis into the right half complex plane. There are two types of Hopf bifurcation: subcritical and supercritical [33].

Suppose we have a physical system that settles down to equilibrium through exponentially damped oscillations (Fig. 2.18. a). Now suppose that the decay rate depends on a control parameter μ. If the decay becomes slower and slower and finally changes to growth at a critical value μ_c, the equilibrium state will lose stability. In many cases the resulting motion is a small-amplitude, sinusoidal, limit cycle oscillation about the former steady state (Fig. 2.18. b). Then we say that the system has undergone a supercritical Hopf bifurcation [33].

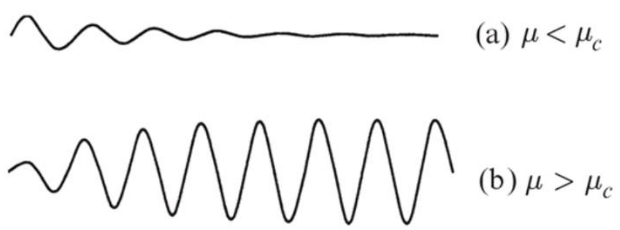

Figure 2.17 Equilibrium decay and supercritical bifurcation growth depending on the control parameter [33]

In terms of the flow in phase space, a supercritical Hopf bifurcation occurs when a stable spiral changes into an unstable spiral surrounded by a small, nearly elliptical limit cycle. Hopf bifurcations can occur in phase spaces of any dimension n ≥ 2. The size of the limit cycle grows continuously from zero, and increases proportional to $\sqrt{\mu - \mu_c}$, for μ close to μ_c. The frequency of the limit cycle is given approximately by $\omega = \mathrm{Im}(\lambda)$, evaluated at $\mu = \mu_c$. This formula is exact at the birth of the limit cycle, and correct within $O(\mu - \mu_c)$ for μ close to μ_c. The period is therefore $T = [2\pi / \mathrm{Im}(\lambda)] + O(\mu - \mu_c)$ [33].

The subcritical case is always much more dramatic, and potentially dangerous in engineering applications. After the bifurcation, the trajectories must jump to a distant attractor, which may be a fixed point, another limit cycle, infinity or, in three and higher dimensions, a chaotic attractor (Fig. 2.19) [33].

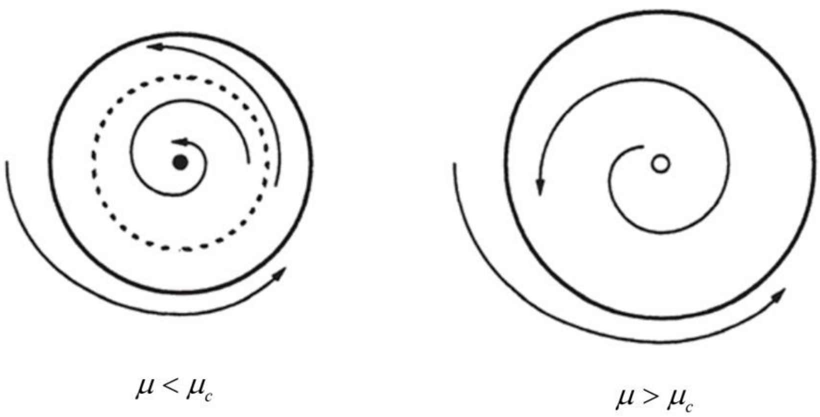

Figure 2.18 Behaviour subcritical Hopf bifurcation before and after it happens

This sort of bifurcation will be observed in the model showcased in sections 6 and 8 of this report.

2.5. CONTROL

Aiming at understanding the control engineering that will be needed for the stabilization of the EMS levitation system, this chapter serves to feature the basic concepts of the process control and to set the basis for the design of the control later applied in this project.

Process controls are necessary for designing safe and productive plants. A variety of process controls are used to manipulate processes, however the most simple and often most effective is the PID controller. The controller attempts to correct the error between a measured process variable and desired setpoint by calculating the difference and then performing a corrective action to adjust the process accordingly. A PID controller controls a process through three parameters: Proportional (P), Integral (I), and Derivative (D). These parameters can be weighted, or tuned, to adjust their effect on the process [34].

This thesis focuses on a fundamental approach to the control design, shaping it as a closed-loop feedback control. The main structure of a general closed-loop feedback control is described as follows (Fig. 2. 20).

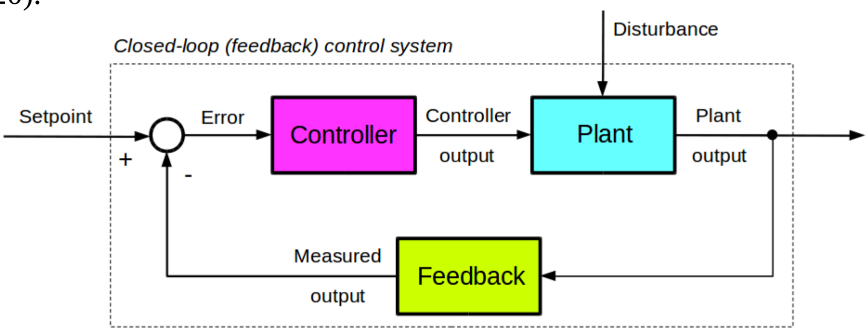

Figure 2.19 Closed-loop feedback control general structure [35]

Where one has to define the reference setpoint $r(t)$, the error $e(t)$ defined as the difference between the measured value and the reference setpoint, which activates the controller, the controller transfer function $G_c(t)$ which depends on the control type and controller coefficients, the controller output that is the input of the system $u(t)$, the plant transfer function $G_p(t)$ which corresponds to the model formulation, the plant output $y(t)$ and, in some cases, the sensor transfer function $h(t)$. The symbolic notation for each component described in this paragraph is presented in Fig. 2.21.

This type of process control is known as error-based control because the actuating signal is determined from the error between the actual and desired setting. The different types of error-based controls vary in the mathematical way they translate the error into an actuating signal, the most common of which are the PID-controllers. Additionally, it is critical to understand feed-forward and feed-back control before exploring P, I, and D controls [34].

The system over which the control is applied is the so called plant. The main idea of this engineering concept is the definition of a control variable that is altered and then is inputted in the system. The output of this system is then the new state/correction of the system. Then a monitored variable is defined which is measured for each loop and is then compared to a reference value in the defined error. The system can be defined either with a transfer function, in the frequency domain, or the state space modelling, in time domain. The most common representation is the transfer function which effectively defines the system as a relation between the output and the input to the system.

$$G_p(s) = \frac{output(s)}{input(s)} \tag{2.18}$$

Such a transfer function can be directly related to the stability of the system through root locus. The poles are the values of the system complex variable s that make the transfer function to tend to ∞, i.e. the roots of the denominator. The poles are the eigenvalues of the system represented in the complex plane, which illustrates the stability of the system. The zeros are the values of the system complex variable s that make the transfer function zero, i.e. the roots of the numerator.

Focusing on the controller definition itself, since the PID is often the most effective, it is the one that is desired to be implemented in this project. The PID controller consists of three components which can be represented as branches in the control scheme, as shown below (Fig. 2. 21). Along these lines, it is important to first understand what is the definition of each of these branches and how do they effect the system

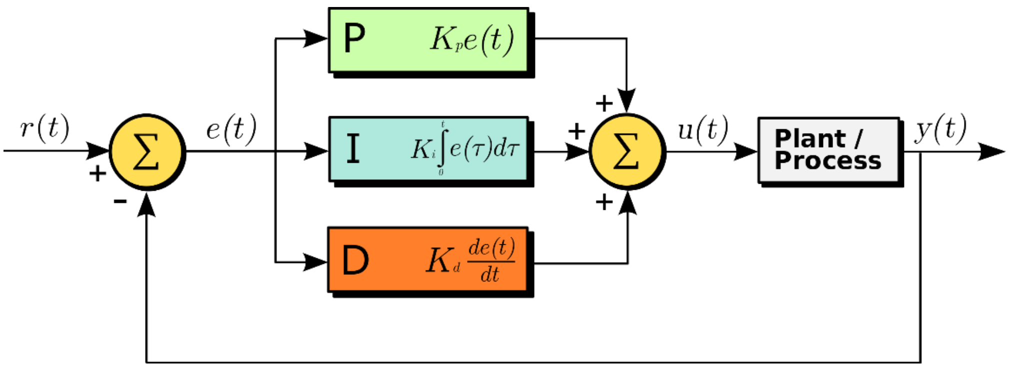

Figure 2.20 PID Controller closed-loop feedback scheme [36]

The proportional control is a form of feedback control. It is the simplest form of continuous control that can be used in a closed-looped system. P-only control minimizes the fluctuation in the process variable, but it does not always bring the system to the desired set point. It provides a faster response than most other controllers, initially allowing the P-only controller to respond a few seconds faster. However, as the system becomes more complex (i.e. more complex algorithm) the response time difference could accumulate, allowing the P-controller to possibly respond even a few seconds faster. Although the P-only controller does offer the advantage of faster response time, it produces deviation from the set point. This deviation is known as the offset, and it is usually not desired in a process. The existence of an offset implies that the system could not be maintained at the desired set point at steady state. It is analogous to the systematic error in a calibration curve, where there is always a set, constant error that prevents the line from crossing the origin. The offset can be minimized by combining P-only control with another form of control, such as I- or D- control. It is important to note, however, that it is impossible to completely eliminate the offset, which is implicitly included within each equation. P-control linearly correlates the controller output (actuating signal) to the error (difference between measured signal and set point) [34]

$$u_p(t) = K_p e(t) + b \tag{2.19}$$

Where $u_P(t)$ is the controller output, K_P is the controller gain, $e(t)$ is the error and b is the bias. The bias and controller gain are constants specific to each controller. The bias is simply the controller output when the error is zero [34] and the control gain corresponds to the control activity related to the given error.

The integral control is a second form of feedback control. It is often used because it is able to remove any deviations that may exist. Thus, the system returns to both steady state and its original setting. A negative error will cause the signal to the system to decrease, while a positive error will cause the signal to increase. However, I-only controllers are much slower in their response time than P-only controllers because they are dependent on more parameters. If it is essential to have no offset in the system, then an I-only controller should be used, but it will require a slower response time. This slower response time can be reduced by combining I-only control with another form, such as P or PD control. I-only controls are often used when measured variables need to remain within a very narrow range and require fine-tuning control. I controls affect the system by responding to accumulated past error. The philosophy behind the integral control is that deviations will be affected in proportion to the cumulative sum of their magnitude. The key advantage of adding a I-control is that it will eliminate the offset. The disadvantages are that it can destabilize the controller, and there is an integrator windup, which increases the time it takes for the controller to make changes [34].

I-control correlates the controller output to the integral of the error. The integral of the error is taken with respect to time. It is the total error associated over a specified amount of time.

$$u_I(t) = \frac{1}{T_i}\int e(t)dt + u(t_0) \tag{2.20}$$

Where $u_I(t)$ is the controller output, T_i is the integral time, $e(t)$ is the error and $u(t_0)$ is the controller output before integration. The integral time is the amount of time that it takes for the controller to change its output by a value equal to the error. The controller output before integration is equal to either the initial output at time $t = 0$, or the controller output at the time one step before the measurement [34].

Unlike P-only and I-only controls, D-control is a form of feed forward control. D-control anticipates the process conditions by analyzing the change in error. It functions to minimize the change of error, thus keeping the system at a consistent setting. The primary benefit of D controllers is to resist change in the system, the most important of these being oscillations. The control output is calculated based on the rate of change of the error with time. The larger the rate of the change in error, the more pronounced the controller response will be [34].

Unlike proportional and integral controllers, derivative controllers do not guide the system to a steady state. Because of this property, D controllers must be coupled with P, I or PI controllers to properly control the system. D-control correlates the controller output to the derivative of the error. The derivative of the error is taken with respect to time. It is the change in error associated with change in time [34].

$$u_D(t) = T_d \frac{de(t)}{dt} \tag{2.21}$$

Where $u_D(t)$ is the controller output, T_d is the derivative time constant, $de(t)$ is the differential change in error and dt is the differential change in time. Mathematically, derivative control is the opposite of integral control. Although I-only controls exist, D-only controls do not exist. D-controls measure only the change in error. D-controls do not know where the setpoint is, so it is usually used in conjunction with another method of control, such as P-only or a PI combination control. D-control is usually used for processes with rapidly changing process outputs [34].

PD-control is combination of feedforward and feedback control, because it operates on both the current process conditions and predicted process conditions. In PD-control, the control output is a linear combination of the error signal and its derivative. PD-control contains the proportional control's damping of the fluctuation and the derivative control's prediction of process error. As mentioned, PD-control correlates the controller output to the error and the derivative of the error [34].

$$u_{PD}(t) = K_p(e(t) + T_d \frac{de(t)}{dt}) + U \tag{2.22}$$

Where $u_{PD}(t)$ is the controller output, K_p is the controller gain, T_d is the derivative time constant, $e(t)$ is the error and U is the initial value of the controller. The equation indicates that the PD-controller operates like a simplified PID-controller with a zero integral term. Alternatively, the PD-controller can also be seen as a combination of the P-only and D-only control equations. In this control, the purpose of the D-only control is to predict the error in order to increase stability of the closed loop system [34].

Proportional-integral-derivative control is a combination of all three types of control methods. PID-control is most commonly used because it combines the advantages of each type of control. This includes a quicker response time because of the P-only control, along with the decreased/zero offset from the combined derivative and integral controllers. This offset was removed by additionally using the I-control. The addition of D-control greatly increases the controller's response when used in combination because it predicts disturbances to the system by measuring the change in error [34].

PID-control correlates the controller output to the error, integral of the error, and derivative of the error. Hence, the PID control function in time domain is defined as

$$\begin{aligned} &u_{PID}(t) = K_p e(t) + K_i \int_0^t (e(\tau)d\tau) + K_d \frac{de(t)}{dt} \xrightarrow{K_i = \frac{K_p}{T_i} \wedge K_d = K_p T_d} \\ &u_{PID}(t) = K_p(e(t) + \frac{1}{T_i}\int_0^t (e(\tau)d\tau) + T_d \frac{de(t)}{dt}) \end{aligned} \tag{2.23}$$

Where T_i is the integration time, T_d is the derivative time, K_p is the proportional gain, K_i is the integral gain, K_d is the derivative gain, $e(t)$ is the error of the system, $u_{PID}(t)$ is the controller output and t is the time. The gains of the controller have a direct effect on the stability of the system. For certain values of such coefficients an unstable system can be stabilized.

The proportional term is the only one that affects the equilibrium position of the system. The derivative term relates to the type of stability of the equilibrium point and the integration term relates to the smoothness of the solution and the minimization of the error oscillation.

3

MODELLING OF THE VEHICLE EMS LEVITATION SYSTEM

This section serves as the presentation of the model of EMS suspension developed in this thesis that constitutes the basis of all analytical study cases. Such a model have been developed following the design proposed by Hardt Hyperloop. The chapter features the modelling of the rail infrastructure, the modelling of the vehicle, the modeling of the electromagnets and the derivation of the main equations of motion.

3.1. RAIL INFRASTRUCTURE MODEL

There are several differences between high speed Maglev applications and Hyperloop, but one that becomes immediately evident is the type of rail infrastructure. Whilst Maglev's rails are fully open sky defined and, even with all power and magnetic equipment, barely consist in a couple of continuous beams elevated which are generally simply supported by piers. Hyperloop's infrastructure is radically opposite, aiming at providing a safe quasi-vacuum environment for the pods to run. In this manner, the entire Hyperloop track is sheltered within a compartmented tube, which is generally elevated and supported periodically by columns as shown in the sketches below (Fig. 3.1-3.3), and there are two rails fixed to the ceiling of the tube.

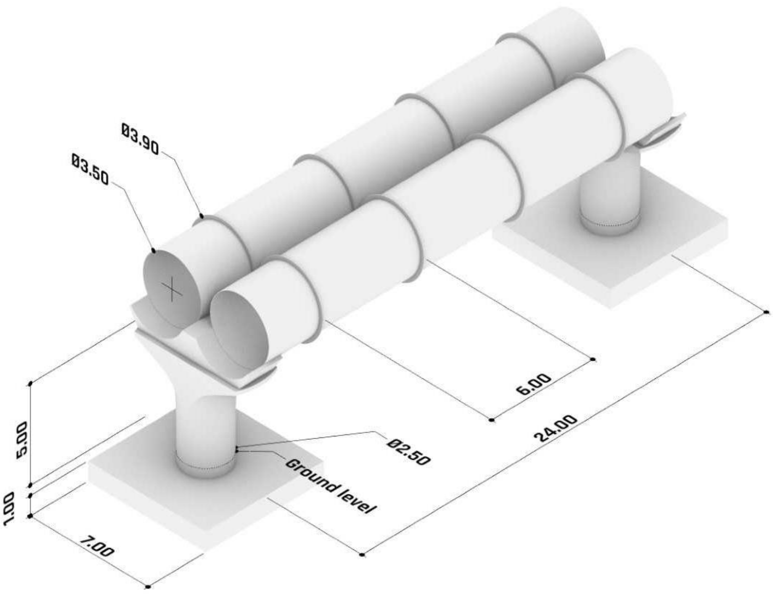

Figure 3.1 Hardt Hyperloop infrastructure layout sketch

Figure 3.2 Hardt Hyperloop infrastructure tender European Test Centre [7]

Figure 3.3 Hardt Hyperloop vehicle run along tube simulation [7]

The tube is steel based and thin walled. The actual Hyperloop track is build by 1 m rectangular section steel beams, placed one after the other and connected to the ceiling by hanging metallic connections. Considering these specifications, the track beam itself has been modeled as a continuous solid rectangular section beam, considering the little spacing between the segments and that the connecting stiffness between the rail segments and the tube is not governing.

After an analysis of the current state of the art and the information provided of the design, it was concluded that the bending stiffness of the tube itself was governing over other stiffness, such as the shear stiffness of the tube itself or the bending stiffness of the track beam. In this manner the track model developed for this thesis is an equivalent Euler-Bernoulli beam with an equivalent mass, second moment of inertia, stiffness and damping resulting from the combination of both the tube and the track beam.

While conducting studies on the coupled vibration of the EMS maglev train, Shi et al. found that the high-order vibration mode can only occur with exceptionally high energy excitation [12]. According to the vibration theory of continuous beam, it can be found that the vibration of higher modes can occur only when the energy of the excitation is very high [37], [14]. The problem from the latest test results from Li and others on the Changsha maglev line, it can be seen that for a definite track beam structure, the vibration frequency corresponding to the maximum amplitude of track beam with maglev train running on its upper part is distributed within a range, wherein the first-order frequency of the track beam has the greatest impact [11]. Therefore, only the influence of the first order bending mode of the track beam is taken into account in the analysis of this paper. Since the length of the electromagnet is much smaller than the span of the track beam, the electromagnetic force f_m can be considered as a concentrated load acting at position x_0 on the track beam when seeking the limit through the generalized force expression.

In this case, without loss of generality, the following assumptions have been adopted so as to derive the dynamic equations of motion used in the coming chapters:

1) We are interested in reducing the full system to a two degree of freedom system in order to focus on the control dynamics. Considering that the cross section height, i.e. diameter, is much smaller than the length of the tube, the tube is modelled as an Euler Bernoulli beam, and the parameters governing the stiffness and damping of its equivalent spring-dashpot system representation in the two degrees of freedom system have been derived according to this beam theory, assuming that the 1st vibration mode is governing in this system.

2) For the sake of simplicity, although the whole track rail is by definition a continuous beam, in this project, a simple span between piers is modelled as a simply supported beam.

3) The length of the electromagnet is very small compared to the length of one span of tube. Consequently, the magnet is considered as a point mass.

Along these lines, one span of track is modeled as a simply supported with equal cross-section Euler-Bernoulli beam defined following the explanation provided in section 2.3.2 as presented below (Fig. 3.4). Where z represents the position of the vehicle, w is the beam deflection, x_0 is the position of the magnet over the length of the beam, f_m is the electromagnetic force, M is the mass of the magnet/vehicle, R is the electrical resistance, i is the electrical current and u is the voltage.

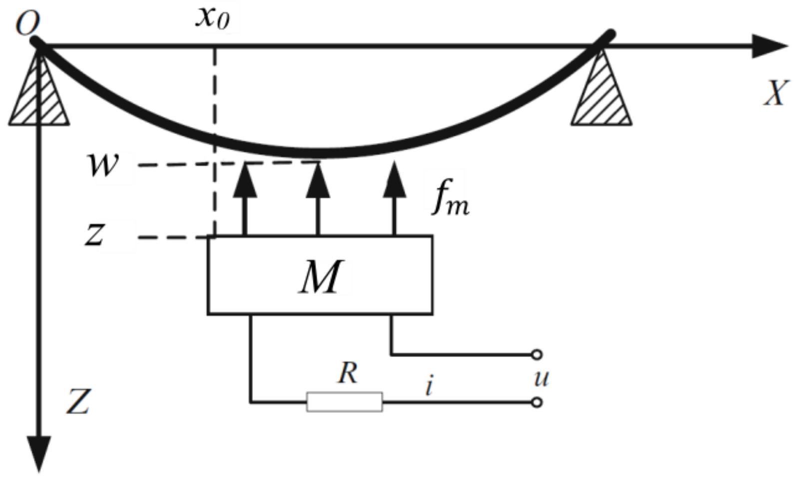

Figure 3.4 Equivalent Euler-Bernoulli, represented under the influence of the electromagnet

The overall model lay-out developed based on Hardt Hyperloop's design is presented below (Fig. 3.5). This sketch provides cross-sectional view of the design concept, giving a good representation of the fit of the vehicle on the tube, the main degrees of freedom and the representation of the levitation system (vertical), although it is not at scale.

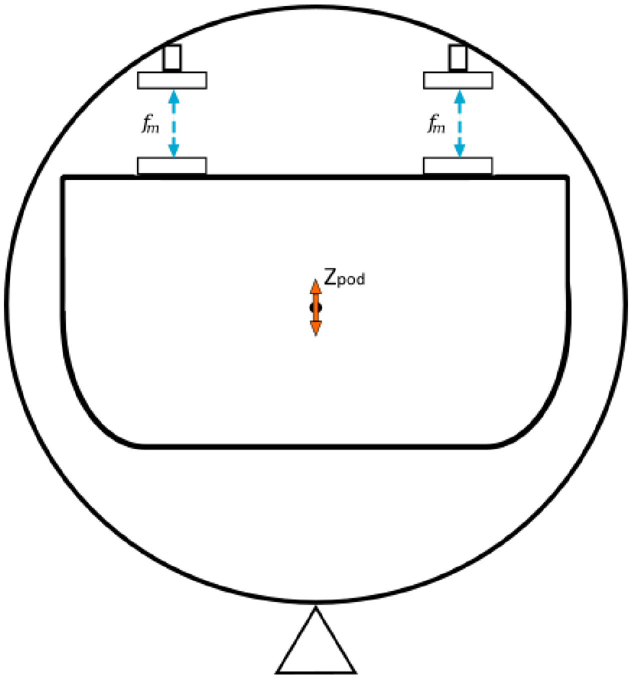

Figure 3.5 Overall cross-section model of the Hyperloop vehicle, levitation system and track infrastructure

Below the sketch and dimensions of the tube and the continuous rail are presented (Fig. 3.6). Where $t = 0.018\,m$, $r = 1.75\,m$, $L = 30\,m$, $b = 0.25\,m$ and $h = 0.1\,m$. As indicated in the drawings, all elements are assumed to be made of S355 steel, consequently the density is taken as $\rho_{S355} = 7800\ \ kg/m^3$ and the Young's modulus as $E = 210 \cdot\ 10^9\ N/m^2$.

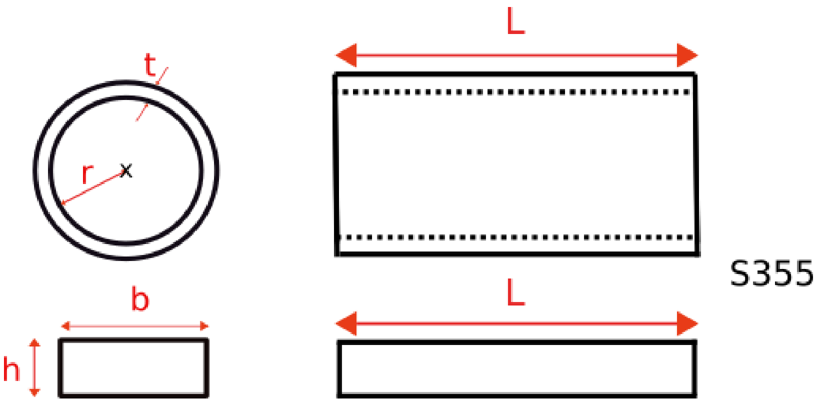

Figure 3.6 Drawings of the hollow tube and the rectangular prismatic beam

Thus, the equivalent mass of the beam per $l = 1m$ length is obtained as

$$M_{eq} = 2M_{beam} + M_{tube} = 2bhl\rho_{S355} + \pi((r+t)^2 - r^2)l\rho S355 = 1941.7\,kg \tag{3.1}$$

The equivalent second moment of inertia is defined as

$$I_{eq} = 2(I_{beam} + A_{beam}d^2) + I_{tube} = 2(\frac{1}{12}bh^3 + A_{beam}d^2) + \frac{1}{4}\pi((r+t)^4 - r^4) = 0.35\ m^4 \tag{3.2}$$

We consider the most adverse set up with the smallest stiffness, that happens when the simply supported beam is subject to a point load located at the mid-span, considering that the first vibration mode is governing as aforementioned in this section pg. 52. Then, the beam is transformed into an equivalent single degree of freedom oscillator, such that it has no beam and length attributions but only its stiffness and damping parameters (Fig. 3.7).

In this manner, the equivalent static stiffness of the simply supported beam to a point located at the centre is

$$k_{eq} = \frac{48EI_{eq}}{L^3} = 1.2892 \cdot\ 10^8\ N/m \tag{3.3}$$

The damping ratio of the rectangular prismatic track beams has been assumed to be of 0.5%. Consequently, the damping coefficient of the beam can be defined as

$$\begin{aligned} \xi_{beam} &= 0.005 = \frac{c_{beam}}{2\sqrt{k_{beam}M_{beam}L}} \rightarrow c_{beam} = \\ &= 2 \cdot\ 0.005\sqrt{7.7778 \cdot\ 10^3 \cdot\ 195 \cdot\ 30} = 32.2492\,N \cdot\ s/M \end{aligned} \tag{3.4}$$

The determination of the damping coefficient of the tube requires a first assessment of the viscous damping associated with an evenly elastic and viscous tube. According to F. Orban an approximation of the material damping coefficient of any structural member can be calculated as [38]

$$c = D_{am} V \alpha_k \alpha_h = c_{tube} \tag{3.5}$$

where D_{am} is the damping belonging to the maximum stress amplitude, V is the volume of the structure, α_k is the cross-section factor and α_h length factor of the member. In this case, for large diameter continuous steel piping structure $D_{am} \approx 0.03$, the volume of the tube is $V = \pi((r+t)^2 - r^2)L = 5.9681 m^3$, the cross-section factor for a tube is $\alpha_k = 1.27(1-(t/r)) = 1.2569$ and the length factor for a simply supported beam is $\alpha_h = 1$. Then, the damping coefficient and the damping ratio of the equivalent Euler-Bernoulli beam can be computed as

$$c_{eq} = 2c_{beam} + c_{tube} = 2\cdot\ 32.2492 + 0.2250 = 64.7234\, N\cdot\ s/m \tag{3.6}$$

$$\xi_{eq} = 2\cdot\ 0.005 + \frac{c_{tube}}{2\sqrt{k_{tube} M_{tube} L}} = 2\cdot\ 0.005 + \frac{D_{am} V \alpha_k \alpha_h}{2\sqrt{k_{tube} M_{tube} L}} = 0.01 \tag{3.7}$$

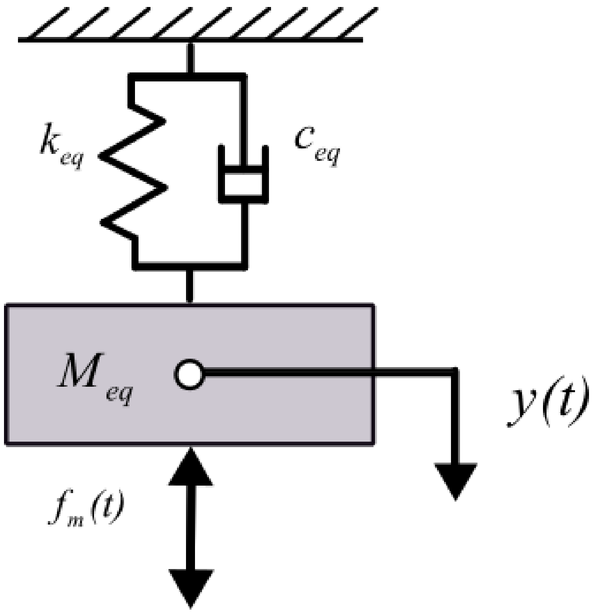

Figure 3.7 Beam SDOF oscillator equivalent model

3.2. EMS AND VEHICLE MODEL

If one zooms in on the levitation system within Fig. 3.5, the model build for such system is represented as shown below (Fig. 3.8).

This model has been constructed following the model assumptions presented in the previous section 3.1 for the beam definition on the cross-sectional EMS system by an equivalent single degree of freedom oscillator system.

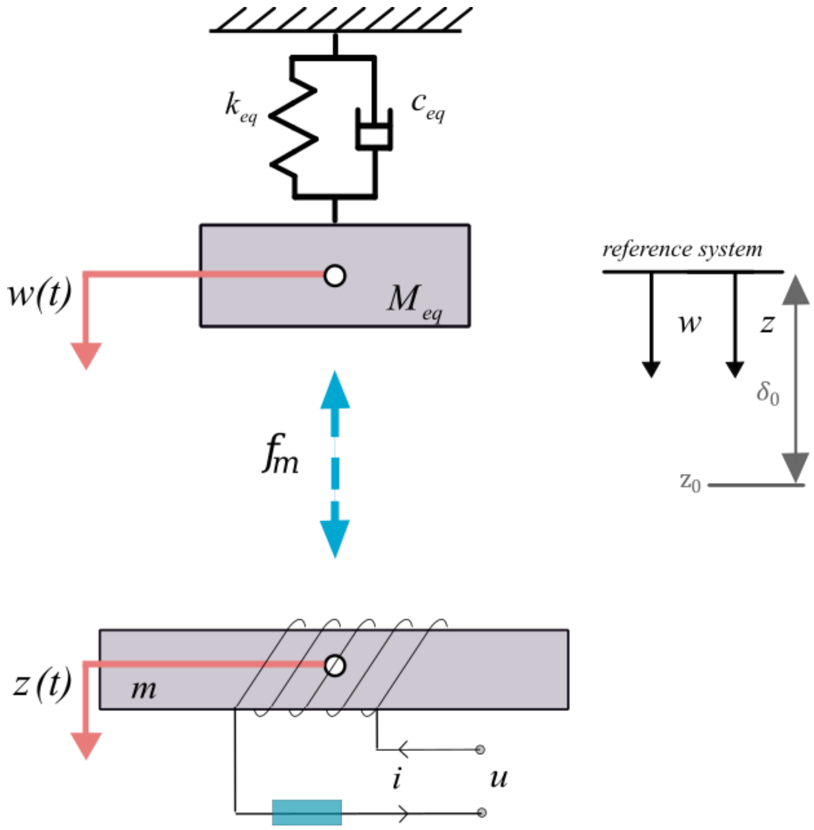

Figure 3.8 Model of the EMS levitation system cross-section with reference system definition

Following the model sketch above, the track beam can be seen as to a single-degree-of-freedom vibrating body with mass M, which refers to the equivalent mass computed in eq. 3.1, support stiffness k_{eq} and damping c_{eq} and the electromagnet-vehicle system of mass m is levitated below the track beam. The choice of the reference system has been made for a more intuitive understanding and a better representation of the results.

The dynamics of the oscillator versus the track beam can also be compared to those of a pendulum hanging from a beam, for which one can find two equilibrium positions: one for the oscillator hanging under the rail; and the other for the oscillator mounted on top of the rail. However, the equilibrium position on top of the rail is physically meaningless since the oscillator is constraint to move below the rail.

The coupling system has two mechanical degrees of freedom, namely the vertical displacement of the electromagnet z $[m]$ and the deflection of the rail at the levitation position w $[m]$. The electromagnetic force between the electromagnet and the track beam f_m $[N]$ is a function of the electromagnet coil current i $[A]$ and the levitation gap δ $[m]$. The coil current i is driven by a voltage u $[V]$ acting across the coil, which has a total resistance of R $[Ohm]$.

The levitation gap δ is defined as the relative displacement between the deflection of the beam and the position of the oscillator.

$$\delta = z - w \tag{3.8}$$

Optionally, irregularities present on the track bottom phase embracing the magnetized area can be added to the levitation gap δ model as a time and longitudinal coordinate dependent function $p(x,t)$.

The electromagnetic force between the electromagnet and the track beam f_m can be defined as shown below. Where the relation between electromagnetic constant parameters has been derived following the theoretical derivation presented in chapter 2.2 and the nonlinear dependency of the electromagnetic force on the levitation air gap δ and the electrical current i is taken from previous literature [6 - 17].

$$f_m = \mathrm{sgn}(\delta)\frac{\mu_0 N^2 A_m}{4}\frac{i^2}{\delta^2} \tag{3.9}$$

where μ_0 $[T \cdot m / A]$ is the permeability in vacuum, N is the number of turns of the coil, A_m is the area of the magnetic pole of the electromagnet and $\mathrm{sgn}(\delta)$ refers to the sign of the actual air gap. The latter, has been added to ensure that the electromagnetic suspension is always working in attraction, so that in the unrealistic case that the oscillator can move above the rail, the electromagnetic force is always pointing towards the rail. For the sake of simplicity all constant parameters are grouped in a generic constant $C = \frac{\mu_0 N^2 A_m}{4}$.

Then the electrical parameters can be related by means of the Kirchhoff's law of total voltage following the explanation provided in chapter 2.2. Thus, the control voltage can be related to the coil current variation and the air gap variation as follows [6 - 15]:

$$u = iR + L_0\dot{i} + k_L\dot{\delta} = iR + 2C\frac{1}{\delta}\dot{i} + 2C\frac{i}{\delta^2}\dot{\delta} \tag{3.10}$$

where L_0 and k_L are defined as follows:

$$\begin{aligned} L_0 &= \frac{\mu_0 N^2 A_m}{2}\frac{1}{\delta} \\ k_L &= \frac{\mu_0 N^2 A_m}{2}\frac{i}{\delta^2} \end{aligned} \tag{3.11}$$

Considering the fact that this is an open loop system, we lack a feedback term for the control of the voltage through the coil. Therefore, for such a model, the voltage is considered to be a constant parameter, whereas the electrical current i and the actual air gap δ are variables.

For its inclusion into the equations of motion, eq 3.16 is rewritten in such a way that the left hand-side term of the equality contains the derivative of the variable of interest, in this case the electrical current i, for a better fit in the construction of a system of Ordinary Differential Equations (ODEs). This equation reads

$$\dot{i} = \frac{\delta}{2C}(u - iR - 2C\frac{i}{\delta^2}\dot{\delta}) \rightarrow \dot{i} = \frac{z-w}{2C}[u - iR - 2C\frac{i}{(z-w)^2}(\dot{z} - \dot{w})] \tag{3.12}$$

The translational degrees of freedom of interest can then be defined by means of the equilibrium of forces in their respective bodies based on Newton's second Law and the derivation of the SDOF equations of motion presented in chapter 2.3. In this manner, two coupled equations of motion are obtained, written in the same form as eq. 3.18. The first equation governs the vehicle motion and the second equation governs the track beam motion.

$$\begin{cases} \ddot{z} = g - \mathrm{sgn}(\delta)\dfrac{C}{m}\dfrac{i^2}{\delta^2} \\ \ddot{w} = g + \mathrm{sgn}(\delta)\dfrac{C}{M}\dfrac{i^2}{\delta^2} - 2\xi_{eq}\omega_n\dot{w} - \omega_n{}^2 w \end{cases} \tag{3.13}$$

where $\omega_n = \sqrt{k_{eq}/M}$ is the natural frequency of the track beam, $\xi_{eq} = c_{eq}/2\sqrt{k_{eq}M}$ is the damping ratio of the track beam, and the zero points of z and w are located in the static equilibrium position.

Then, combining all the aforementioned expressions eq. 3.18 and eq. 3.19, an ODE system of equations can be build formulating all equations of motion governing the system described by our model (Fig. 3.7). The equations can be converted into an alternative form, by transforming $\{x_1 \quad x_2 \quad x_3 \quad x_4 \quad x_5\} = \{z \quad \dot{z} \quad w \quad \dot{w} \quad i\}$ and expanding δ the system equations is defined as:

$$\begin{cases} \dot{x}_1 = x_2 \\ \dot{x}_2 = g - \mathrm{sgn}(x_1 - x_3)\dfrac{C}{m}\dfrac{x_5{}^2}{(x_1 - x_3)^2} \\ \dot{x}_3 = x_4 \\ \dot{x}_4 = g + \mathrm{sgn}(x_1 - x_3)\dfrac{C}{M}\dfrac{x_5{}^2}{(x_1 - x_3)^2} - 2\xi_{eq}\omega_n x_4 - \omega_n{}^2 x_3 \\ \dot{x}_5 = \dfrac{x_1 - x_3}{2C}[u - x_5 R - 2C\dfrac{x_5}{(x_1 - x_3)^2}(x_2 - x_4)] \end{cases} \tag{3.14}$$

The system is defined to have two translational degrees of freedom (x_1 for the vehicle and x_3 for the beam) and one electronic degree of freedom (x_5 for the electrical current on the electromagnet). x_2 and x_4 are only state variables of x_1 and x_3, respectively, namely their first derivative.

It is assumed that the system at $t = 0$ is defined at its static equilibrium, i.e. the resultant of the forces on the vehicle vanishes $f_m - mg = 0$. In order to account for this set up, two parameters need to be defined accordingly at $t = 0$. Namely, that the initial air gap is set to be the target air gap and the initial voltage input to the system is such that the generated electromagnetic force is exactly the same as the weight.

$$\begin{cases} \delta\,|_{t=0} = \delta_0 \\ u\,|_{t=0} = u_0 = \{u \mid f_m - mg = 0\} \end{cases} \tag{3.15}$$

Such a voltage input value can be computed as follows

$$C\frac{i^2}{\delta^2} = mg \xrightarrow{i|_{t=0}=\frac{u_0}{R} \wedge \delta|_{t=0}=\delta_0} \frac{{u_0}^2}{R^2{\delta_0}^2} = \frac{mg}{C} \rightarrow u_0 = \delta_0 R\sqrt{\frac{mg}{C}} \tag{3.16}$$

Following this definition and the requirements for the system to be in such equilibrium position, the system set up at $t = 0$ is expressed as

$$\begin{cases} z_0 = w_0 + \delta\,|_{t=0} \rightarrow x_{1_s} = x_{3_s} - \delta_0 \\ \dot{z}_0 = 0 \rightarrow x_{2_s} = 0 \\ w_0 = \dfrac{mg}{k_{eq}} \rightarrow x_{3_s} = \dfrac{mg}{k_{eq}} \\ \dot{w}_0 = 0 \rightarrow x_{4_s} = 0 \\ i_0 = \dfrac{u_0}{R} = \delta_0\sqrt{\dfrac{mg}{C}} \rightarrow x_{5_s} = \delta_0\sqrt{\dfrac{mg}{C}} \end{cases} \tag{3.17}$$

After a quick look on the system of equations of motion eq. 3.20 and the electromagnetic force definition eq. 3.15, one can easily see that the EMS hyperloop levitation system is nonlinear, which entails some challenges when it comes to solving it. Consequently, in this report, the focus will be brought on the local stability of the coupled system around the equilibrium point. A constant in this project is the linearization of the nonlinear systems around the fixed points, which will provide as with nonlinear solutions and linearized solutions of the system. Given the fact that the nonlinear system does not have eigenvalues, the linearized system will result very useful to perform any eigenvalue problem.

Throughout the project, the different problems have been studied both by deriving simplified analytical models, analytical linearized solutions, and numerical nonlinear simulations through MATLAB. All the parameters defining the model described above have been accurately defined numerical. All input numerical values are collected in the table below (Tab. 3.1).

Table 3.1 Input numerical value of model parameters

PARMETER	VALUE	UNTS
Total mass of vehicle	30000	$[kg]$
Mass of one Magnet	150	$[kg]$
Lumped Mass Oscillator	15300	$[kg]$
Gravity	9.81	$[m/s^2]$
Resistance	9.71	$[Ohm]$
Nº of coil turns	800	[-]
Permeability of air	$4\pi \cdot 10^{-7}$	$[T \cdot m/A]$
Magnetized Area	0.25	$[m^2]$
Equilibrium voltage	251.7479	$[V]$
Target Air Gap	0.015	$[m]$

4

STABILITY STUDY OF THE OPEN-LOOP EMS LEVITATION SYSTEM

In this section the stability of the initially proposed model for the EMS levitation system of the vehicle presented in chapter 3.2 will be studied in depth. As explained in chapter 2, following Earnshaw's theorem, all EMS systems are unstable. Therefore, the first objective of this section is to confirm that the derived system is unstable, and second, understand the resulting stability pattern and how does this translate in the behaviour of the vehicle run.

4.1. VEHICLE DYNAMICS FOR THE OPEN-LOOP EMS LEVITATION SYSTEM

The voltage across the coil represents the input of energy to the system. If no feedback control over the voltage is applied, this translates in the fact that the power provided to the system is constant along time and does not change when the vehicle deviates from its target position. Along these lines, one can conclude that for an open-loop design the influence of the electronic parameters on the motion of the vehicle is limited. Consequently, aiming at understanding the vehicle dynamic behaviour, we focus only on studying the first two equations of the ODE system eq. 3.14, considering a constant electrical current and an infinitely stiff beam.

Since the two equations of motion governing the motion of the vehicle and the beam are coupled, if one wants to focus on studying only the vehicle motion, this can be done by assuming an infinitely stiff track beam, which yields

$$x_3 = x_4 = 0 \tag{4.1}$$

The influence of the electrical parameters on the vehicle dynamics is tried to be reduced to the minimum. This translates in

$$\dot{x}_5 = 0 \wedge x_5 = x_{5_s} = \frac{u_0}{R} \tag{4.2}$$

This assumptions directly affect the definition of the air gap and the electromagnetic force which become

$$\begin{cases} \delta = x_1 \\ f_m = \mathrm{sgn}(\delta)\, C\, \dfrac{{x_{5_s}}^2}{\delta^2} \end{cases} \tag{4.3}$$

Considering all the equations presented above, the equations of motion reduce to eq. 4.4, which has been written based on the standard form used to define the ODE system in eq. 3.14. In this case, the system state variables are $\{x_1 \quad x_2\} = \{z \quad \dot{z}\}$.

$$\begin{cases} \dot{x}_1 = x_2 \\ \dot{x}_2 = g - \mathrm{sgn}(x_1)\dfrac{C}{m}\dfrac{{x_{5_s}}^2}{{x_1}^2} \end{cases} \tag{4.4}$$

As aforementioned in chapter 3.2, the focus is put on the local stability of the coupled system around the equilibrium point. Firstly, we determine the system's equilibrium points, also called fixed points, are determined.

Following the theoretical explanation in chapter 2.4, the equilibrium points $\mathbf{x}^*$ are the points at which the derivative of the state variables is zero ($\{\dot{x}\} = \{\dot{x}_1 \quad \dot{x}_2\} = f\ \mathbf{x}^* = 0$). From the nonlinear system eq. 4.4, the equilibrium points of the system can be defined as $({x_1}^*, {x_2}^*) = \{(x_1, x_2) \,|\, \dot{x}_1 = 0;\ \dot{x}_2 = 0\}$ which yields four possible solutions, which need to be sorted out, considering that for this system, all parameters, namely $\mu_0, A_m, N, m, g, u_0, R$, are all strictly positive.

$$\begin{cases} \dot{x}_1 = 0 \rightarrow x_2 = 0 \\ \dot{x}_2 = 0 \rightarrow x_1 = \dfrac{\sqrt{\mathrm{sgn}(x_1)\, gmC}}{gm} x_{5_s} \xrightarrow{2 \ possible \ solutions} \\ \begin{cases} x_1^1 = \dfrac{\sqrt{gmC}}{gm} x_{5_s} \Rightarrow \{\exists x_1^1 \xleftrightarrow{physically \ possible} x^* \in \mathbb{R}\} \\ x_1^2 = \dfrac{\sqrt{-gmC}}{gm} x_{5_s} \Rightarrow \{\nexists x_1^2 \xleftrightarrow{physically \ not \ possible} x^* \notin \mathbb{R}\} \end{cases} \end{cases} \tag{4.5}$$

Keep in mind that any equilibrium point must be real-valued by definition. For this reason, only one fixed point is feasible, as shown in eq. 4.5.

$$(x_1^*, x_2^*) = (\frac{\sqrt{gmC}}{gm} x_{5_s} \,, \, 0) \tag{4.6}$$

Then, if one inputs the numerical value of the system parameters presented in Tab. 3.1, one can see that the fixed point represents exactly the initial equilibrium position of the system, described by the initial conditions. It is noted that, for such a set up, the oscillator is positioned exactly at the target air gap and the vertical variation of the oscillator position is 0, i.e. $(x_1^*, x_2^*) = (0.015, 0)$.

Once the fixed point is defined, the system can be linearized around the fixed point. As a starting point, a generic two ODE nonlinear system is considered as presented below.

$$\begin{cases} \dot{x}_1 = f(x_1, x_2) \\ \dot{x}_2 = g(x_1, x_2) \end{cases} \tag{4.7}$$

Let (x_1^*, x_2^*) be a fixed point. Then, defining two generic variable u, v such that

$$u = x_1 - x_1^* ; \ v = x_2 - x_2^* \tag{4.8}$$

Which denote the components of a small disturbance from the fixed point. In order to see whether the disturbance grows or decays, the differential equations for u and v need to be derived, which for example for u reads

$$\begin{gathered} \dot{u} = \dot{x} \xrightarrow{by \ substitution} \dot{u} = f(x_1^* + u, x_2^* + v) \xrightarrow{Taylor \ series} \dot{u} = f(x_1^*, x_2^*) + u \frac{\partial f}{\partial x_1}|_{(x_1^*, x_2^*)} + \\ + v \frac{\partial f}{\partial x_2}|_{(x_1^*, x_2^*)} + O(u^2, v^2, uv) \xrightarrow{\mathrm{since} \ f(x_1^*, x_2^*) = 0} \dot{u} = u \frac{\partial f}{\partial x_1}|_{(x_1^*, x_2^*)} + v \frac{\partial f}{\partial x_2}|_{(x_1^*, x_2^*)} + O(u^2, v^2, uv) \end{gathered} \tag{4.9}$$

Where $O(u^2, v^2, uv)$ denotes the quadratic terms in u and v of the Taylor series expansion. The same procedure can be derived for $\dot{v}$ yielding

$$\dot{v} = u \frac{\partial g}{\partial x_1}|_{(x_1^*, x_2^*)} + v \frac{\partial g}{\partial x_2}|_{(x_1^*, x_2^*)} + O(u^2, v^2, uv) \tag{4.10}$$

Hence, the entire disturbance (u, v) evolves according to

$$\begin{bmatrix} \dot{u} \\ \dot{v} \end{bmatrix} = \begin{bmatrix} \dfrac{\partial f}{\partial x_1} & \dfrac{\partial f}{\partial x_2} \\ \dfrac{\partial g}{\partial x_1} & \dfrac{\partial g}{\partial x_2} \end{bmatrix}_{(x_1^*, x_2^*)} \begin{bmatrix} u \\ v \end{bmatrix} + \underbrace{O(u^2, v^2, uv) + \dots}_{\text{Higher order terms}} \tag{4.11}$$

Where the first matrix is defined as the Jacobian of the system evaluated at the fixed point (x_1^*, x_2^*), which is the multivariable analog of the derivative $f\,'(x_1^*)$.

$$\mathbf{J} = \begin{bmatrix} \dfrac{\partial f}{\partial x_1} & \dfrac{\partial f}{\partial x_2} \\ \dfrac{\partial g}{\partial x_1} & \dfrac{\partial g}{\partial x_2} \end{bmatrix}_{(x_1^*, x_2^*)} \tag{4.12}$$

The same procedure can be analogously applied to the system being studied eq. 4.4. However, since the effect of the higher order terms is generally very small compered to the first order term and it has been assumed that they can be neglected, leading to the linearized system presented below. This has consequences that need to be considered. Whilst, locally around the fixed point the linearized solution will be very close to the real solution, for further regions this solution will lose accuracy and might not be reliable anymore. The focus is put on the local stability analysis around the fixed point. This is especially useful considering the little range of tolerance of relative movement of the vehicle with respect to the beam.

$$\dot{\mathbf{x}} = \mathbf{J}\mathbf{x} + f(\mathbf{x}) \tag{4.13}$$

Where $f(\mathbf{x})$ is the right hand-side vector of external forces, which in our case is assumed to be 0.

Once the system has been linearized, the Jacobian matrix of the system can be written as in eq. 4.14 and we can evaluate it at the fixed point presented in eq. 4.6.

$$\mathbf{J} = \begin{bmatrix} 0 & 1 \\ \dfrac{2C\,x_{5_s}^{\;2}}{m\,x_1^3} & 0 \end{bmatrix} \Rightarrow \mathbf{J}\,|_{(x_1^*, x_2^*)} = \begin{bmatrix} 0 & 1 \\ \dfrac{2mg^2}{x_{5_s}\sqrt{gmC}} & 0 \end{bmatrix} \tag{4.14}$$

Hence, the linearized system around the fixed point reads

$$\begin{Bmatrix} \dot{x}_1 \\ \dot{x}_2 \end{Bmatrix} = \begin{bmatrix} 0 & 1 \\ \dfrac{2mg^2}{x_{5_s}\sqrt{gmC}} & 0 \end{bmatrix} \begin{Bmatrix} x_1 \\ x_2 \end{Bmatrix} \tag{4.15}$$

Eq. 4.15 can be equivalently written in a single equation with variable x_1 and coefficients corresponding to the Jacobian terms, which are all strictly positive defined.

$$\ddot{x}_1 - J_{21}x_1 = 0 \ where \ J_{21} > 0 \tag{4.16}$$

In this manner, one can see that the system is governed by a negative stiffness, which implies that the system is unstable. This can be proven in a clearer way, by transforming the system from the time domain to the Laplace domain, as defined in chapter 2.3.4, assuming trivial initial condition and analysing the response of the system to a unit pulse input forcing term.

$$\ddot{x}_1 - J_{21}x_1 = \delta(t) \xrightarrow{Laplace\ trans.} s^2\hat{x}_1 - J_{21}\hat{x}_1 = 1 \tag{4.17}$$

Then, following the theory presented in chapter 2.4, one can compute the poles of the system, i.e. the eigenvalues, by deriving the transfer function of $\hat{x}_1$ and finding the roots of its denominator.

$$\hat{x}_1 = \frac{1}{s^2 - J_{21}} \xrightarrow{Poles} s^2 - J_{21} = 0 \rightarrow s_{1,2} = \pm\sqrt{J_{21}} = \pm 36.1663 \tag{4.18}$$

This result can be represented in the complex plane as a root locus mapping as follows (Fig. 4.1)

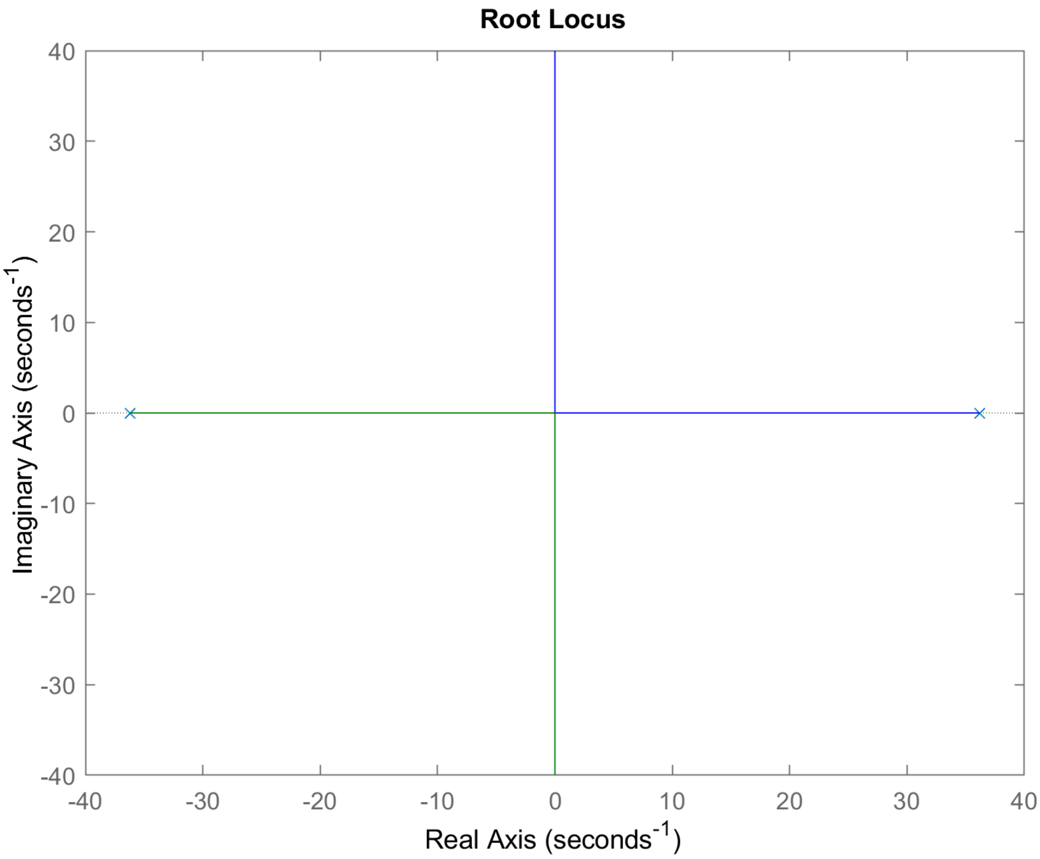

Figure 4.1 Root Locus mapping of the SDOF system in the complex plane

From fig. 4.1, it becomes obvious that the system is unstable, since one of the two eigenvalues has a negative real part. The poles are represented by a cross. This plot and the numerical value of the eigenvalues have been obtained by applying the numerical value proposed for the system parameters in Tab. 3.1.

This serves as a confirmation that the system is unstable, which is a conclusion that meets Earnshaw's theorem. After eq. 4.18, one can see that both eigenvalues are different from each other, both are real-valued, they are equal in absolute value but one is positive and the other one is negative. Following the theory presented in chapter 2.4, this fixed point can be classified as a saddle point.

Besides, for a fixed point to be stable, both main directions, i.e. eigenvectors, point toward the node. This is not the case for a saddle point as shown in the plot of the phase portrait of the system presented below (Fig. 4.2 and 4.3), where one eigen direction points towards the fixed point and the other moves away.

Considering the system definition eq. 4.4, the eigenvalues of the system have been found to be $s_{1,2} = \pm 36.1663$ and the eigenvectors $\mathbf{v}_1 = [-1 \quad -36.1663]^T$ and $\mathbf{v}_2 = [-1 \quad 36.1663]^T$, respectively. This allows to draw a phase portrait based on the position of the vehicle and its vertical position variation $x_1 - x_2$ around fixed point eq. 4.13 of the system as presented below (Fig. 4.2 and 4.3).

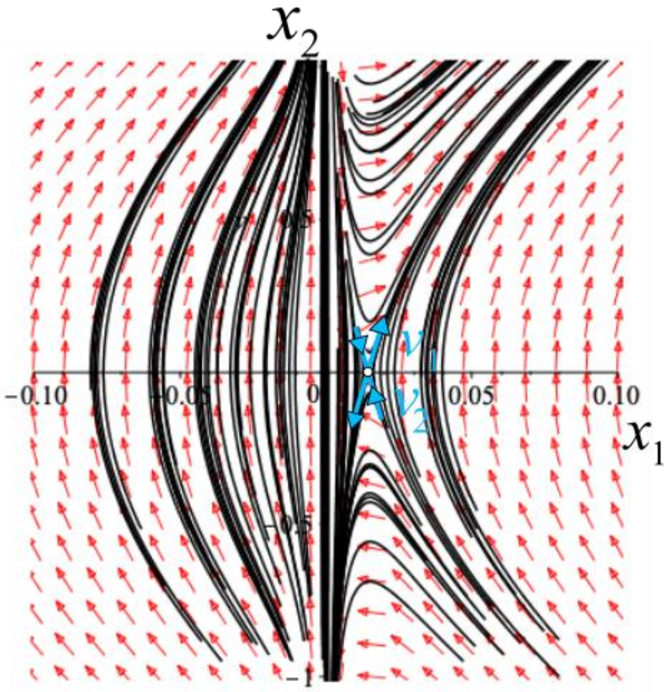

Figure 4.2 Phase Portrait SDOF vehicle for EMS open-loop levitation system

Figure 4.2 presents the phase portrait for several random trajectories each for a different randomly chosen initial condition. The most interesting information that one can derive from such a phase portrait is a clear picture of the vehicle dynamics behaviour, which can be classified in 4 different behaviour classes, corresponding to different regions of this phase portrait. For this reason, a second mapping of the results has been produced, aiming at providing a deeper understanding (Fig. 4.3).

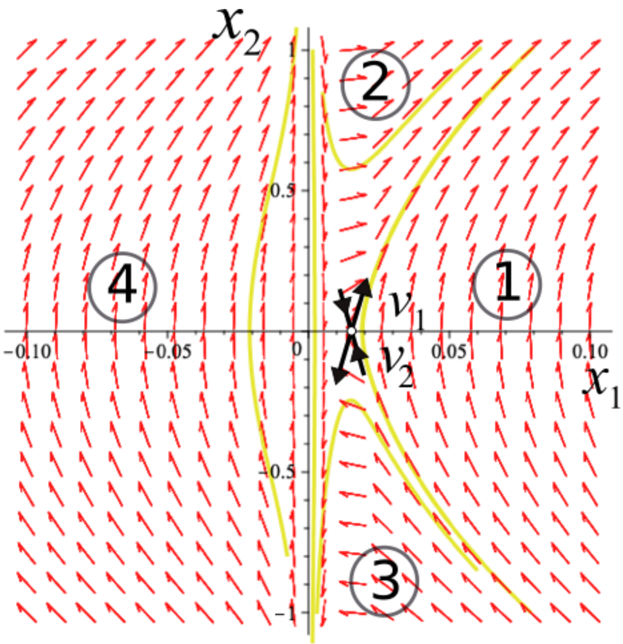

Figure 4.3 Phase Portrait with dynamic behaviour classes SDOF vehicle

The best way to analyse this plot is to think of the vertical axis ($x_1 = 0$) as the hyperloop track and the fixed point represents the equilibrium position of the vehicle at Hardt Hyperloop's target air gap, below the rail. In this sense, one can look at this figure in a more natural way by rotating it 90^o to the right.

Region $N^o 1$ is governed by vehicle self-weight taking over the electromagnetic force at some point, which impedes that for any case with initial conditions within this region the vehicle never reaches to be attracted within the target air gap range. From the moment that the self-weight force takes over, the vehicle ends up falling down and moving away progressively from the track. Normally, this behaviour is characteristic for initial condition combinations quite far below the track, with both upwards (negative) and downwards (positive) velocities, that are not sufficiently high to lead the vehicle towards this target air gap band. This phenomena is easy to understand given the fact that the electromagnetic force as defined in eq. 4.3, has the air gap as its denominator squared. Along these lines, the farther away the vehicle is located, the bigger this denominator and the lower the electromagnetic force.

Region $N^o 2$ is governed by the electromagnetic force being unable to compensate the downward forces of the vehicle, lead by high initial downwards velocities. This region is characterized by vehicles starting located very close to the track, within the target airgap electromagnetic influence band, but its positive (downwards) velocity combined with the self-weight load prove to be too much for the electromagnetic force and the vehicle ends up falling down and moving away progressively from the track. This phenomena follows form the electromagnetic force definition in the same way that is described for region $N^o 1$.

Region $N^o 3$ can be seen as quite the opposite from region $N^o 2$. It is governed by the electromagnetic force which combined with high upwards vertical velocities lead to a force build up that pushes the vehicle upwards until it crashes against the rail and gets stuck to it. In this case, self-weight forces are unable to counteract the attraction force combined with negative position rates and,, the vehicle cannot be maintained at a position around the target air gap. This behaviour can be explained by reflecting on the electromagnetic force mathematical definition, for which the closer the vehicle moves to the rail, the shorter the levitation air gap and the larger the electromagnetic force.

Region $N^o 4$ is then characterized by system set ups for which, generally, the vehicle both starts and ends up colliding with the rail. This region comprises not only a very small region below the rale very close to the track beam, for which the air gap is so short, that for any downward velocity and self/weight the large electromagnetic force cannot be compensated. But also, all unrealistic set ups for which the vehicle initial conditions are defines such that it is located above the rail. In this case all loads acting on the vehicle have down ward component (self-weight as always and electromagnetic force since it is attractive). Thus, even for large negative velocity inputs, the vehicle ends up falling on the rail. However, this case is not representative for this project, since our the design does only consider the vehicle levitating below the rail.

In fact, this plot shows the system behaviour around the unstable equilibrium point, at the target air gap that we aim to, given any possible initial conditions, confirming all the results presented above.

It can be concluded that this section confirms that the EMS levitation system without control is inherently unstable due to the electromagnetic force definition. As illustrated with the explanation of the different mechanical behaviour classes, the squared of a distance magnitude variable in the denominator is governing these patterns, corroborating that Earnshaw's law applies on our system.

4.2. VEHICLE DYNAMICS FOR THE OPEN-LOOP EMS LEVITATION SYSTEM CONSIDERING THE VARIABILITY OF THE ELECTRICAL CURRENT

This section aims at understanding the role that the electric variables and the Kirchhoff's law of total voltage can have in the vehicle stability, when no feedback loop is defined to update the power input on the system if required. The assumption of having an infinitely stiff track beam eq. 4.1 still holds for this study case.

However, unlike the previous study case, now, the electrical current x_5 is no longer assumed to be constant. However, since the system being studied is open-loop, the input voltage across the electromagnetic coil is assumed constant and no iterative correction is available. Along these lines, the voltage is assumed to the constant initial value associated with the target air gap position, likewise in the previous case.

In this manner, the equations of motion eq. 3.14 are adapted here for the aforementioned assumptions. The main difference with eq. 4.3 is that the electrical current is now represented by the time dependent variable i.

$$\begin{cases} \delta = x_1 \\ f_m = \operatorname{sgn}(\delta) C \dfrac{i^2}{\delta^2} \end{cases} \tag{4.19}$$

Considering all the equations presented above, the equations of motion reduce to eq. 4.22, which has been written based on the standard form used to define the ODE system in eq. 3.15. Where the equation based on Kirchhoff's total voltage law derived in chapter 2.2 has been added. In this case, the system state variables are $\{x_1 \quad x_2 \quad x_5\} = \{z \quad \dot{z} \quad i\}$.

$$\begin{cases} \dot{x}_1 = x_2 \\ \dot{x}_2 = g - \operatorname{sgn}(x_1) \dfrac{C}{m} \dfrac{x_5^2}{x_1^2} \\ \dot{x}_5 = \dfrac{x_1}{2C}(u_0 - x_5 R - 2C \dfrac{x_5}{x_1^2} x_2) \end{cases} \tag{4.20}$$

The first thing to be addressed is to define the equilibrium points. Considering the shape of the system, four fixed points are expected, but in this case with 3 components each, defining the system in a 3D space, although the system is still effectively a single degree of freedom system with a complementary variable accounting for the electronics of the system. Thereby, this can be referred to as a one and a half degree of freedom system.

The equilibrium points of the system can be defined as $(x_1^*, x_2^*, x_5^*) = \{(x_1, x_2, x_5) \mid \dot{x}_1 = 0;\ \dot{x}_2 = 0;\ \dot{x}_5 = 0\}$ which yields four possible solutions, which need to be sorted out, considering that for this system, all parameters, namely $\mu_0, A_m, N, m, g, u_0, R$, are all strictly positive.

$$\begin{cases} \dot{x}_1 = 0 \rightarrow x_2 = 0 \\ \dot{x}_2 = 0 \rightarrow x_1 = \dfrac{\sqrt{\operatorname{sgn}(x_1)\, gmC}}{gm} x_{5_s} \xrightarrow{2 \ possible \ solutions} \\ \quad \begin{cases} x_1^1 = \dfrac{\sqrt{gmC}}{gm} x_{5_s} \Rightarrow \{\exists x_1^1 \xleftrightarrow{physically \ possible} x^* \in \mathbb{R}\} \\ x_1^2 = \dfrac{\sqrt{-gmC}}{gm} x_{5_s} \Rightarrow \{\nexists x_1^2 \xleftrightarrow{physically \ not \ possible} x^* \notin \mathbb{R}\} \end{cases} \\ \dot{x}_5 = 0 \rightarrow \dfrac{x_1}{2C}(u_0 - x_5 R - 2C \dfrac{x_5}{x_1^2} x_2) = 0 \rightarrow x_5 = \dfrac{u_0}{R} \end{cases} \tag{4.21}$$

As explained in eq. 4.23, only one fixed point is find to be feasible

$$(x_1^*, x_2^*, x_5^*) = (\frac{\sqrt{gmC}}{gm} \frac{u_0}{R},\ 0,\ \frac{u_0}{R}) \tag{4.22}$$

As expected, the same fixed point as before has been obtained, corresponding to the initial equilibrium position at the target air gap, with an equilibrium electrical current equal to the initial equilibrium value, which evaluated using the numerical value of the system parameters presented in Tab. 3.1 yields $(x_1^*, x_2^*, x_5^*) = (0.015, 0,\ 25.92)$.

The Jacobian matrix of the system can be written as in eq. 4.23 and we can evaluate it at the fixed point presented in eq. 4.22.

$$\mathbf{J} = \begin{bmatrix} 0 & 1 & 0 \\ \frac{2C}{m}\frac{x_5^2}{x_1^3} & 0 & -\frac{2C}{m}\frac{x_5}{x_1^2} \\ \frac{1}{2C}(-x_5 R - 2C\frac{x_2 x_5}{x_1^2}) + 2\frac{x_2 x_5}{x_1^2} & -\frac{x_5}{x_1} & \frac{x_1}{2C}(-R - 2C\frac{x_2}{x_1^2}) \end{bmatrix} \Rightarrow \mathbf{J}\big|_{(x_1^*, x_2^*, x_5^*)} = \begin{vmatrix} 0 & 1 & 0 \\ \frac{2mg^2}{x_{5_s}\sqrt{gmC}} & 0 & -\frac{2g}{x_{5_s}} \\ 0 & -\frac{gm}{\sqrt{gmC}} & -\frac{\sqrt{gmC}\, u_0}{2gmC} \end{vmatrix} \tag{4.23}$$

Hence, the linearized system around the fixed point reads

$$\begin{Bmatrix} \dot{x}_1 \\ \dot{x}_2 \\ \dot{x}_5 \end{Bmatrix} = \begin{vmatrix} 0 & 1 & 0 \\ \frac{2mg^2}{x_{5_s}\sqrt{gmC}} & 0 & -\frac{2g}{x_{5_s}} \\ 0 & -\frac{gm}{\sqrt{gmC}} & -\frac{\sqrt{gmC}\, u_0}{2gmC} \end{vmatrix} \begin{Bmatrix} x_1 \\ x_2 \\ x_5 \end{Bmatrix} \tag{4.24}$$

Then, the same method used in the previous chapter can be used to reduce the two first rows of the matrix system to an equivalently single equation with variable x_1 and x_5, and coefficients corresponding to the Jacobian terms, which are all strictly positive defined, and a second equation corresponding to the last row with variables x_1 and x_5.

$$\begin{cases} \ddot{x}_1 - J_{21}x_1 + J_{23}x_5 = 0 \\ \dot{x}_5 + J_{32}\dot{x}_1 + J_{33}x_5 = 0 \end{cases} \tag{4.25}$$

In this manner, one can see that the one term in the equations of motion system has a negative stiffness in the first equation, which implies that the system is unstable. Then, following the definition in chapter 2.3.4, the system can be transformed into the Laplace domain, assuming trivial initial condition and analysing the response of the system to a unit pulse input forcing term as follows.

$$\begin{cases} \ddot{x}_1 - J_{21}x_1 + J_{23}x_5 = 0 \\ \dot{x}_5 + J_{32}\dot{x}_1 + J_{33}x_5 = \delta(t) \end{cases} \xrightarrow{\textit{Laplace trans.}} \begin{cases} s^2\hat{x}_1 - J_{21}\hat{x}_1 + J_{23}\hat{x}_5 = 0 \\ s\hat{x}_5 + J_{32}s\hat{x}_1 + J_{33}\hat{x}_5 = 1 \end{cases} \tag{4.26}$$

Then, following the theory presented in chapter 2.4, one can compute the poles of the system, i.e. the eigenvalues, by deriving the transfer function of $\hat{x}_1$ and finding the roots of its denominator.

$$\hat{x}_5 = \frac{1 - J_{32} s \hat{x}_1}{s + J_{33}} \Rightarrow s^2 \hat{x}_1 - J_{21}\hat{x}_1 + J_{23}\left(\frac{1 - J_{32} s \hat{x}_1}{s + J_{33}}\right) = 0 \rightarrow$$

$$\hat{x}_1 = \frac{-\frac{J_{23}}{s + J_{33}}}{s^2 - J_{21} - \frac{J_{23}J_{32}s}{s + J_{33}}} = -\frac{1}{\frac{1}{J_{23}}[s^3 + J_{33}s^2 - (J_{23}J_{32} + J_{21})s - J_{21}J_{33}]} \xrightarrow{Poles} \tag{4.27}$$

$$\frac{1}{J_{23}}[s^3 + J_{33}s^2 - (J_{23}J_{32} + J_{21})s - J_{21}J_{33}] = 0 \rightarrow s_1 = -51.5155;\ s_2 = -0.7243;\ s_3 = 50.7910$$

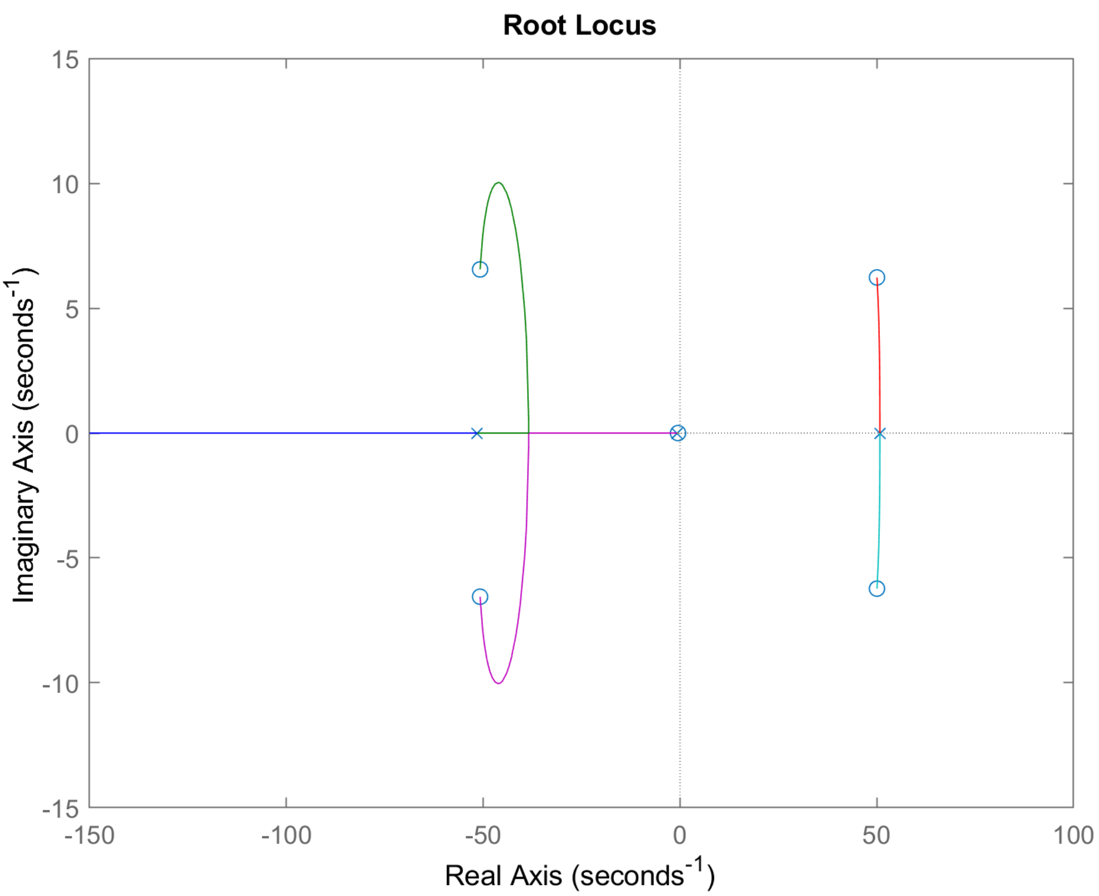

Figure 4.4 Root Locus mapping for1.5DOF open loop system

The root locus is presented in Fig. 4.4, where it becomes obvious that the system is unstable, since one of the three eigenvalues has a positive real part, i.e. it is represented in the RHS complex plane. The system is defined by three real-valued eigenvalues two with negative real part and one with positive real part. These poles correspond to the crosses in the map, whereas the circles represent the zeros of the system. This plot has been obtained by applying the numerical value proposed for the system parameters in Tab. 3.1.

This serves as a verification that the system is unstable, even after the inclusion of a third equation governed by Kirchhoff's law to the system. Now, it is important to understand which type of 3D stability pattern governs the dynamic behaviour of the system.

Following the theory presented in chapter 2.4, one can see that around the only fixed point a saddle point of index 1 is defined since all 3 eigenvalues are strictly real, one of them has a positive real part and the other two have a negative real part. Note that the index indicates the dimensions of the unstable manifold, 1 dimensional in this case.

In this case, the construction of a 3D phase portrait of the system does not bring any new information compared to the one presented for the previous study case (Fig. 4.2). Since the system drown presents very similar eigen directions as the previous one, with an extra eigenvector associated to the inclusion of Kirchhoff's law equation which is close to vertical, the projection of the phase portrait on the phase plane $x_1 - x_2$ draws the same behaviour as presented in Fig. 4.2 and 4.3. For this reason, it has not been included to this report, avoiding trivial information.

It can be concluded that this section shows that, even after including the electric variables in the system, the system is inherently unstable due to the electromagnetic force definition. As illustrated with the explanation of the different mechanical behaviour classes, the squared of a distance magnitude variable in the denominator is governing these instability patterns, corroborating that Earnshaw's law applies on our system.

5

STABILITY STUDY OF THE CLOSED-LOOP EMS SYSTEM WITH P-CONTROL

In the previous section, the modelled EMS levitating systems have been proven to be unstable. Hence, a feedback control system is required to make the system stable. The idea behind this concept is the definition of a tool that monitors continuously the levitation air gap throughout time and adjusts the voltage input to the EMS system to ensure the stability of the system. In this manner, the electrical current present in the numerator of the electromagnetic force, redefines the magnitude of electromagnetic attractive force to compensate such position of the vehicle.

The use of a PID-control seems convenient due to its simplicity, ease of implementation and robustness. The PID-control is a combination of the PI- (proportional-integral) and PD- (proportional-derivative) controls. The PID-control is used when the system performance requires improvement in both the transient and steady-state performance.

One of the main goals of this thesis, as presented in chapter 1.3, is the design of a feedback control following a pragmatic approach, so as to stabilize the system, analyse the effect of such a tool on the vehicle-track stability and understand the effect that each components has. The objective is to build a similar scheme to a PID-control. However, for a better understanding, the overall design concept has been broken down into simpler components, studying its effect on the system stability.

The reference PID-control scheme can be described as follows (Fig. 5.1). The system will monitor uniquely the levitation air gap δ. Then, the target air gap δ_0 is taken as reference, so that the definition of the error is $e = \delta - \delta_0$. The control function is applied on the voltage u, which becomes the input to the system plant. Finally, the outcome of the system is the entire state variable vector $\mathbf{x} = \{x_1 \quad x_2 \quad x_3 \quad x_4 \quad x_5\}$, through which a new δ is defined referring to the new air gap that resulted form the new voltage compensation input to the system activated by an error different than 0.

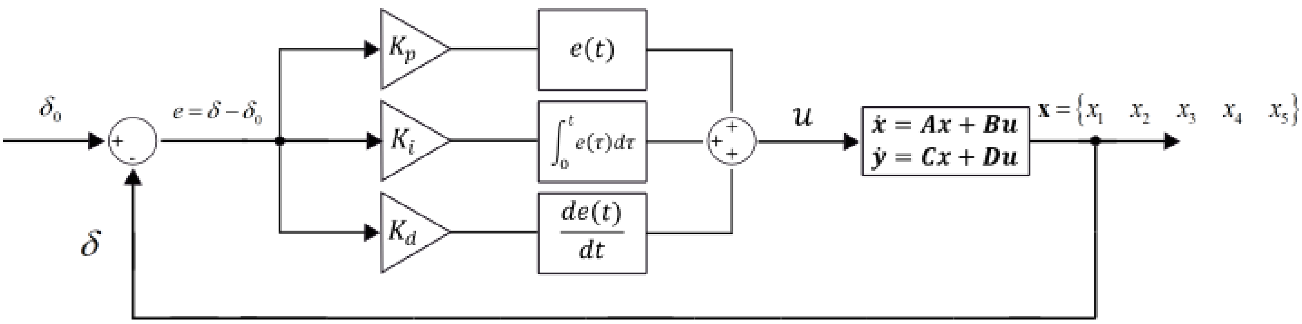

Figure 5.1 Definition PID-Control scheme for the EMS levitation system stabilization Each of the branches of control correspond to a component of the PID-control: the proportional P-component, the integral I-component and the derivative D-control.

This chapter serves to feature the design of the simplest possible control scheme for this system. A P-control monitoring the levitation air gap and controlling the voltage across the electromagnetic coil is described. Following the theory presented in chapter 2.5, a P-control scheme is a form of feedback control that minimizes the fluctuation in the process variable and provides the faster response among controllers. P-control linearly correlates the controller output (actuating signal) to the error (difference between measured signal and set point).

In the same way as the model developed in chapter 4, this study case aims at analysing only the vehicle dynamics. For this reason, the assumption of having an infinitely stiff track beam eq. 4.1 still holds for this study case.

In this manner, the error defined for this analysis is expressed as $e = x_1 - \delta_0$ and the system outputs $\{x_1 \quad x_2 \quad x_5\} = \{z \quad \dot{z} \quad i\}$. The monitored variable is the air gap δ and the controlled variable is the voltage u. The controlled is defined in time domain as part of the equations of motion. The control loop can be described as

$$u = K_p(x_1 - \delta_0) + u_0 \tag{5.1}$$

where K_p is the proportional control gain to be tuned and u_0 is the reference value of the control value. In this case it is defined as the voltage input that initially defines the system at the target air gap equilibrium position.

Hence, the system of equations of motion can be defined as

$$\begin{cases} \dot{x}_1 = x_2 \\ \dot{x}_2 = g - \operatorname{sgn}(x_1)\dfrac{C}{m}\dfrac{x_5{}^2}{x_1{}^2} \\ \dot{x}_5 = \dfrac{x_1}{2C}(K_p(x_1-\delta_0)+u_0-x_5R-2C\dfrac{x_5}{x_1{}^2}x_2) \end{cases} \tag{5.2}$$

For this reason, the same procedure described in chapter 4.1 and 4.2 will be applied for this case study. Thus, the first thing to be addressed is to define the equilibrium points. The equilibrium points of the system can be defined as $(x_1{}^*, x_2{}^*, x_5{}^*) = \quad = \{(x_1, x_2, x_5) \,|\, \dot{x}_1 = 0;\ \dot{x}_2 = 0;\ \dot{x}_5 = 0\}$ which yields four possible solutions, which need to be sorted out. However, in this case study, not all parameters are all strictly positive. The majority are, namely $\mu_0, A_m, N, m, g, u_0, R$, are all strictly positive. But, the proportional control gain K_p can be both positively and negatively defined. Consequently, the identification of the feasible fixed points, is not that straight forward and further assessment will be required.

From the computation of the equilibrium points, several solutions are obtained, from which only two are feasible, considering the fact that any equilibrium point must be real-valued by definition. These are described as

$$\begin{aligned} (x_1^{1*}, x_2^{1*}, x_5^{1*}) &= (\frac{(CK_p-\sqrt{gmC})(K_p\delta_0-u_0)}{-R^2gm+CK_p{}^2},\ 0,\ \frac{K_p[\dfrac{(CK_p-\sqrt{gmC})}{-R^2gm+CK_p{}^2}](K_p\delta_0-u_0)-K_p\delta_0+u_0}{R}) \\ (x_1^{2*}, x_2^{2*}, x_5^{2*}) &= (\frac{(CK_p+\sqrt{gmC})(K_p\delta_0-u_0)}{-R^2gm+CK_p{}^2},\ 0,\ \frac{K_p[\dfrac{(CK_p+\sqrt{gmC})}{-R^2gm+CK_p{}^2}](K_p\delta_0-u_0)-K_p\delta_0+u_0}{R}) \end{aligned} \tag{5.3}$$

In order to determine which fixed point is feasible, first, the voltage and the electrical current for the system to have a fixed point at the target air gap δ_0 for both equilibrium points

$$\begin{aligned} u_0^1 &= \frac{(Rgm-K_p\sqrt{gmC})R\delta_0}{CK_p-R\sqrt{gmC}};\ x_{5_s}^1 = \frac{(Rgm-K_p\sqrt{gmC})\delta_0}{CK_p-R\sqrt{gmC}} \\ u_0^2 &= \frac{(Rgm+K_p\sqrt{gmC})R\delta_0}{CK_p-R\sqrt{gmC}};\ x_{5_s}^2 = \frac{(Rgm+K_p\sqrt{gmC})\delta_0}{CK_p-R\sqrt{gmC}} \end{aligned} \tag{5.4}$$

Afterwards, if one considers the results obtained for the open loop case featured in chapter 4, only one fixed point was feasible corresponding to the target air gap position. Along this lines, it is reflected that the feasibility of both points can be assessed by imposing them to be at $x_1 = \delta_0$. This has been done in two steps, first taking the 1st fixed point solution to be at δ_0 and the 2nd is defined accordingly to this set up, which yields the following results (Fig. 5.2 - 5.4). In these plots, the solution (z/cu/u0) _star 11 holds for the 1st fixed point and the (z/cu/u0) _star 21 for the 2nd fixed point. In these plots the two fixed points are represented with respect to K_p for the case of imposing $x_1 = \delta_0$ in fixed point 1.

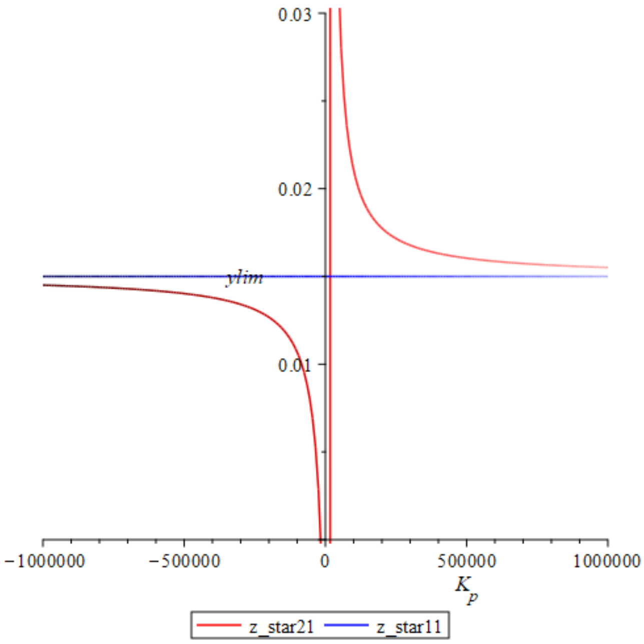

Figure 5.2 Vehicle position imposing fixed point 1 at δ_0

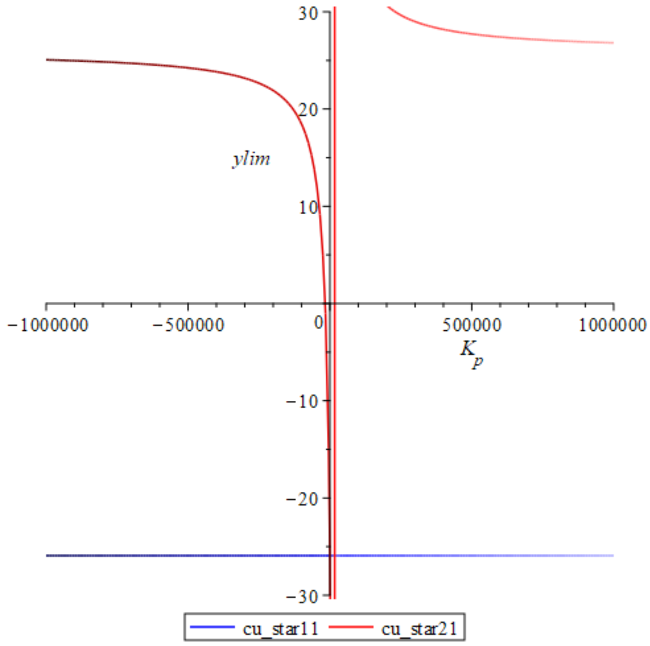

Figure 5.3 Electrical current imposing fixed point 1 at δ_0

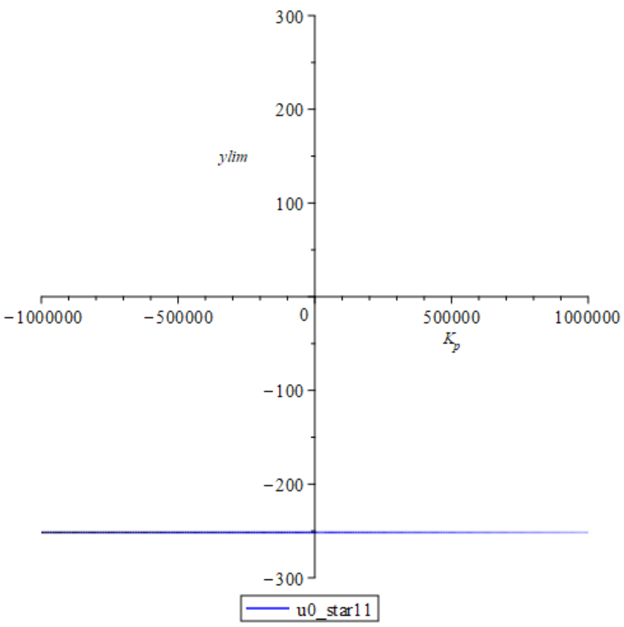

Figure 5.4 Voltage for target air gap equilibrium position for fixed point 1 at δ_0

Whereas, if the 2nd fixed point is imposed to be at δ_0 and the 1st is defined accordingly to this set up, yields the following results (Fig. 5.5 - 5.7). In this plots, the solutions (z/cu/u0) _star 12 holds for the 1st fixed point and the (z/cu/u0) _star 22 for the 2nd fixed point. In these plots the two fixed points are represented with respect to K_p for the case of imposing $x_1 = \delta_0$ in fixed point 2.

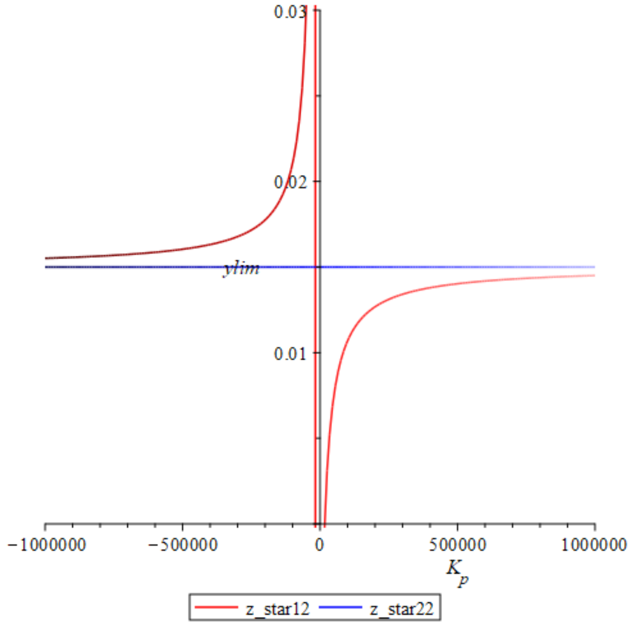

Figure 5.5 Vehicle position imposing fixed point 2 at δ_0

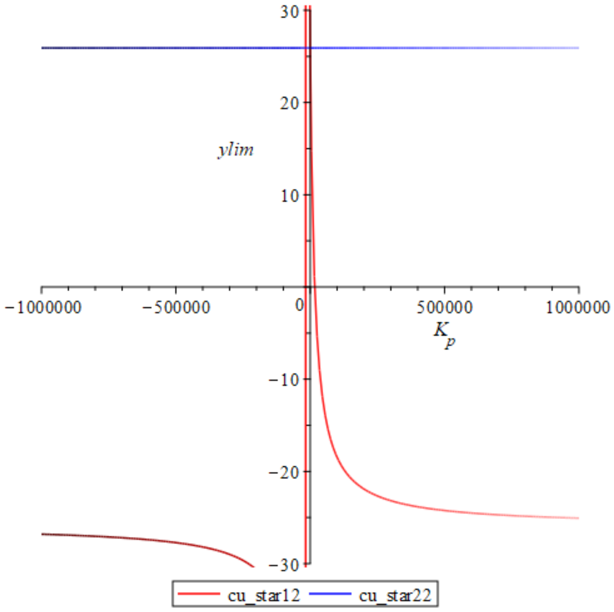

Figure 5.6 Electrical current imposing fixed point 1 at δ_0

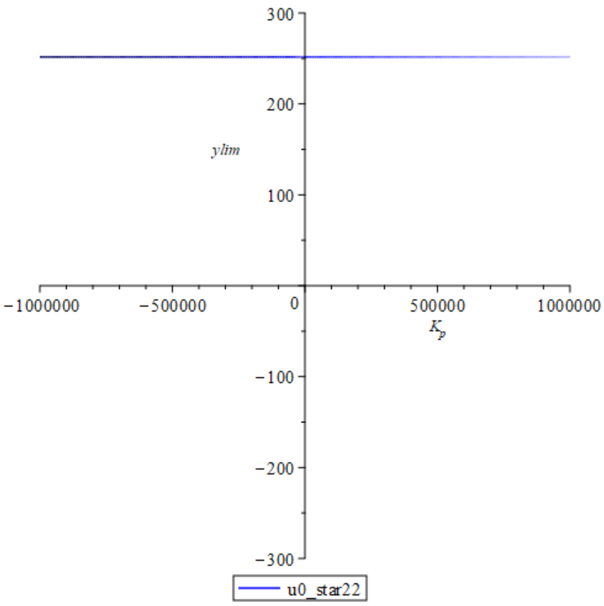

Figure 5.7 Voltage for target air gap equilibrium position for fixed point 2 at δ_0

From the figures presented above, one can see that there are two admissible fixed points, One can freely choose the value of u_0 such that one of the of the two fixed points lies at $x_1 = \delta_0$. If the 1st fixed point is chosen to be at $x_1 = \delta_0$, then both the electrical current and the voltage at this fixed point will be mostly negative. Whilst, if the 2nd fixed point is chosen to be at $x_1 = \delta_0$, then both the electrical current and the voltage at this fixed point will be mostly positive. This means that irrespective of our choice of u_0, there are two fixed points on the positive and negative half-spaces (i.e. in the 3D parameter space) of the electrical current x_5.

Since, by definition of our system, we work with positive values of u and i, the second fixed point is chosen to represented the feasible fixed point. This can be reasoned due to the attractive EMS system definition. In this manner, focusing on the physical meaning of the system and it components, a negative electrical current x_5, would translate on a change of polarization of the electromagnet which would be understood to be working on repulsion instead of in attraction, which makes completely o sense for such application. Focusing on the voltage u_0 similarly, a negative value would implement a change on the direction of the electrical flow on the circuit. Along these lines, the 2nd fixed point is defined to be the physically feasible one at $x_1 = \delta_0$.

Following the fixed point analysis, the eigenvalue problem is also conducted as a function of K_p, since it is the control gain, which is the tunable value that is assumed to make the system stable. Therefore, one expects to be able to define different regions of stability depending on the value of this parameter.

The Jacobian matrix of the system can be written as in eq. 5.5 and we can evaluate it at the fixed point presented in eq. 5.4.

$$
\mathbf{J} = \begin{bmatrix} 0 & 1 & 0 \\ \frac{2C}{m}\frac{x_5^2}{x_1^3} & 0 & -\frac{2C}{m}\frac{x_5}{x_1^2} \\ \frac{1}{2C}[u_0 + K_p(x_1-\delta_0) - x_5 R - 2C\frac{x_2 x_5}{x_1^2} + x_1(K_p + 4C\frac{x_2 x_5}{x_1^3})] & -\frac{x_5}{x_1} & \frac{x_1}{2C}(-R - 2C\frac{x_2}{x_1^2}) \end{bmatrix} \Rightarrow
$$

$$
\mathbf{J}|_{(x_1^*, x_2^*, x_5^*)} = \begin{bmatrix} 0 & 1 & 0 \\ \frac{2C(Rgm + K_p\sqrt{gmC})^2(-R^2 gm + CK_p^2)}{m(K_p\delta_0 - u_0)(CK_p + R\sqrt{gmC})^3} & 0 & -\frac{2C(Rgm + K_p\sqrt{gmC})(-R^2 gm + CK_p^2)}{m(K_p\delta_0 - u_0)(CK_p + R\sqrt{gmC})^2} \\ \frac{(K_p\delta_0 - u_0)(CK_p + R\sqrt{gmC})K_p}{2C(-R^2 gm + CK_p^2)} & \frac{-Rgm - K_p\sqrt{gmC}}{CK_p + R\sqrt{gmC}} & -\frac{(K_p\delta_0 - u_0)(CK_p + R\sqrt{gmC})R}{2C(-R^2 gm + CK_p^2)} \end{bmatrix} \tag{5.5}
$$

Hence, the linearized system around the fixed point reads

$$\begin{Bmatrix} \dot{x}_1 \\ \dot{x}_2 \\ \dot{x}_5 \end{Bmatrix} = \begin{bmatrix} 0 & 1 & 0 \\ \dfrac{2C(Rgm+K_p\sqrt{gmC})^2(-R^2gm+CK_p{}^2)}{m(K_p\delta_0-u_0)(CK_p+R\sqrt{gmC})^3} & 0 & -\dfrac{2C(Rgm+K_p\sqrt{gmC})(-R^2gm+CK_p{}^2)}{m(K_p\delta_0-u_0)(CK_p+R\sqrt{gmC})^2} \\ \dfrac{(K_p\delta_0-u_0)(CK_p+R\sqrt{gmC})K_p}{2C(-R^2gm+CK_p{}^2)} & \dfrac{-Rgm-K_p\sqrt{gmC}}{CK_p+R\sqrt{gmC}} & -\dfrac{(K_p\delta_0-u_0)(CK_p+R\sqrt{gmC})R}{2C(-R^2gm+CK_p{}^2)} \end{bmatrix} \begin{Bmatrix} x_1 \\ x_2 \\ x_5 \end{Bmatrix} \tag{5.6}$$

Then, the same method used in the previous chapter can be used to reduce the two first rows of the matrix system to an equivalently single equation with variable x_1 and x_5, and coefficients corresponding to the Jacobian terms and a second equation corresponding to the last row with variables x_1 and x_5.

$$\begin{cases} \ddot{x}_1 - J_{21}x_1 + J_{23}x_5 = 0 \\ \dot{x}_5 - J_{31}x_1 - J_{32}\dot{x}_1 + J_{33}x_5 = 0 \end{cases} \tag{5.7}$$

In this case, no conclusions can be drawn about stability of the system solely from the sign of the coefficients/stiffness od the system, the Jacobian terms cannot be guaranteed to be strictly positive due to the presence of K_p. The sign of the real part of the eigenvalues needs to be investigated. Along these lines, following the same method previously applied in chapter 4, the system in eq. 5.7 in the Laplace domain reads

$$\begin{cases} \ddot{x}_1 - J_{21}x_1 + J_{23}x_5 = 0 \\ \dot{x}_5 - J_{31}x_1 - J_{32}\dot{x}_1 + J_{33}x_5 = \delta(t) \end{cases} \xrightarrow{\text{Laplace trans.}} \begin{cases} s^2\hat{x}_1 - J_{21}\hat{x}_1 + J_{23}\hat{x}_5 = 0 \\ s\hat{x}_5 - J_{31}\hat{x}_1 - J_{32}s\hat{x}_1 + J_{33}\hat{x}_5 = 1 \end{cases} \tag{5.8}$$

Then, following the theory presented in chapter 2.4, one can compute the poles of the system, i.e. the eigenvalues, by deriving the transfer function of $\hat{x}_1$ and finding the roots of its denominator.

$$\begin{gathered} \hat{x}_5 = \frac{1 + J_{31}\hat{x}_1 + J_{32}s\hat{x}_1}{s + J_{33}} \Rightarrow s^2\hat{x}_1 - J_{21}\hat{x}_1 + J_{23}\left(\frac{1 + J_{31}\hat{x}_1 + J_{32}s\hat{x}_1}{s + J_{33}}\right) = 0 \rightarrow \\ \hat{x}_1 = \frac{-\dfrac{J_{23}}{s + J_{33}}}{s^2 - J_{21} + \dfrac{J_{23}(J_{31} + J_{32}s)}{s + J_{33}}} = -\frac{1}{\dfrac{1}{J_{23}}[s^3 + J_{33}s^2 + (J_{23}J_{32} - J_{21})s - J_{21}J_{33} + J_{23}J_{31}]} \\ \xrightarrow{\text{Poles}} \frac{1}{J_{23}}[s^3 + J_{33}s^2 + (J_{23}J_{32} - J_{21})s - J_{21}J_{33} + J_{23}J_{31}] = 0 \end{gathered} \tag{5.9}$$

The poles of the expression in eq. 5.11 have then been evaluated with respect to K_p, which yield to the following patterns (Fig. 5.8 and 5.9). These are presented in two plots, the first one featuring the real part of the eigenvalues $\mathrm{Re}\{s_{1,2,3}\}$ and the second one featuring the imaginary part $\mathrm{Im}\{s_{1,2,3}\}$.

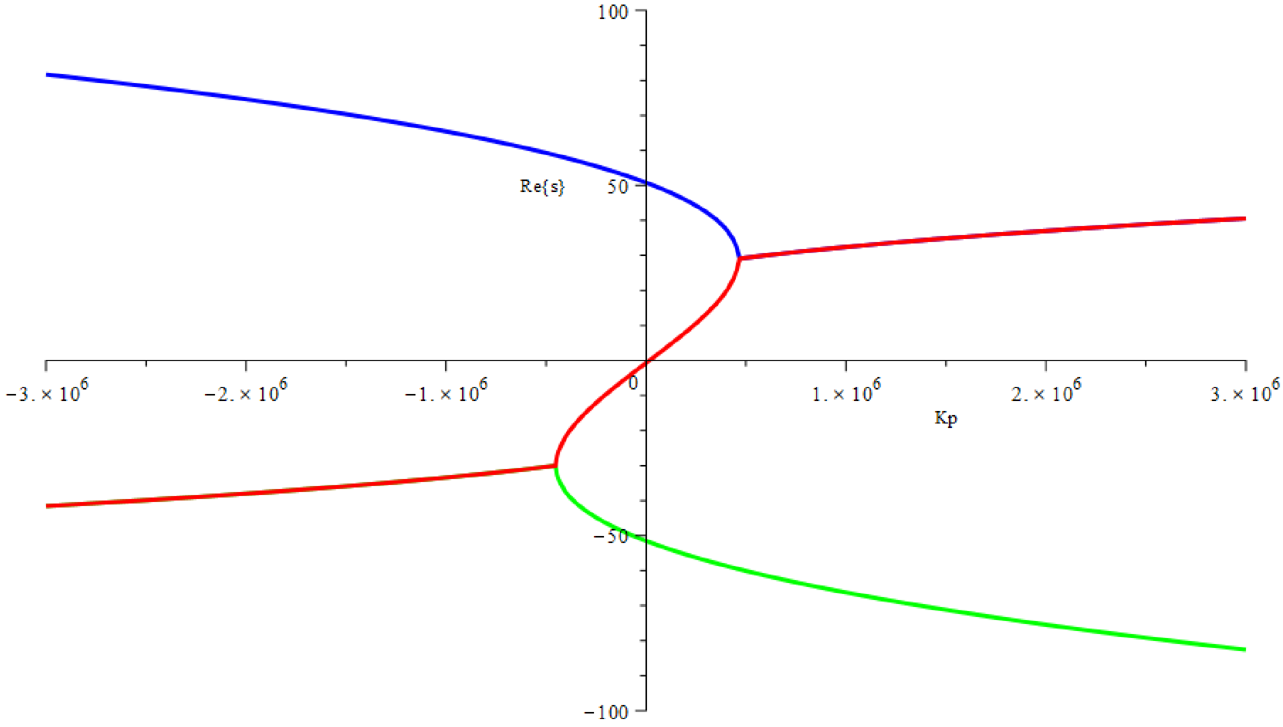

Figure 5.8 Real part of the eigenvalues with respect to the proportional control gain

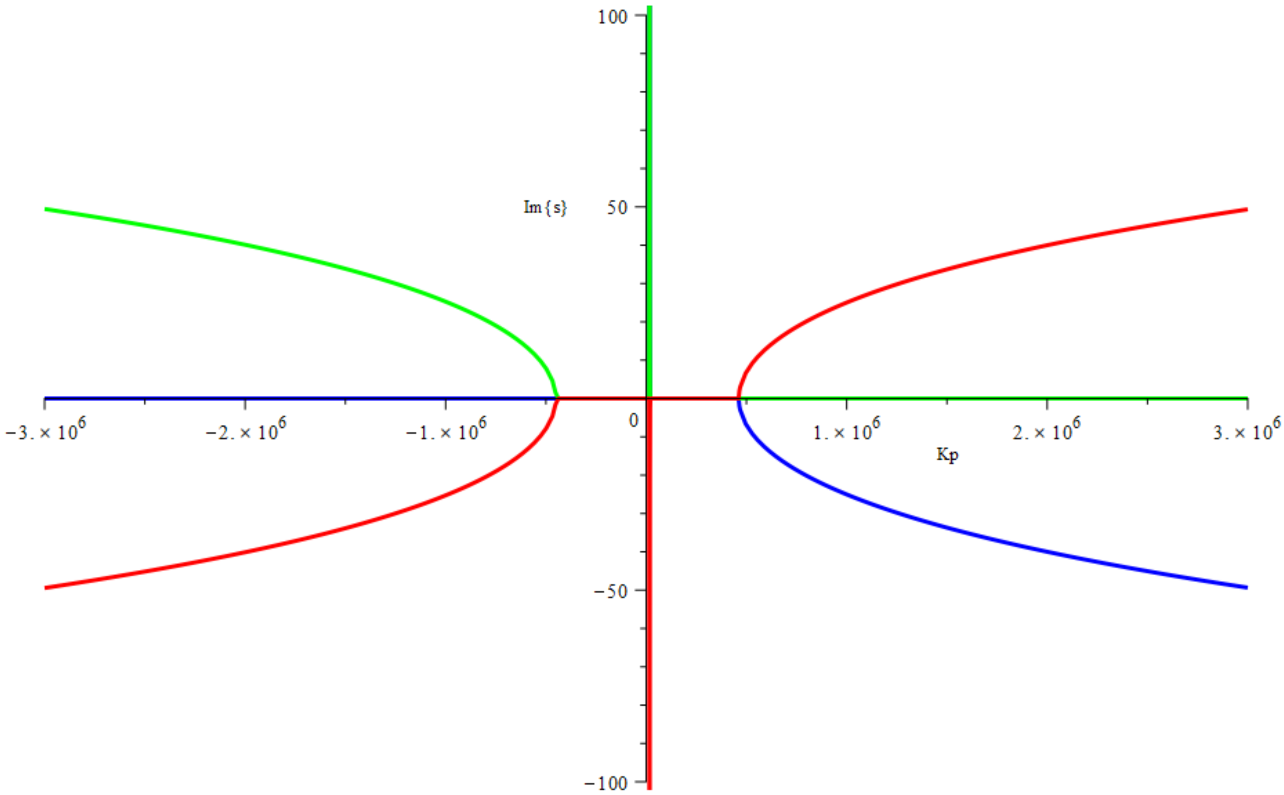

Figure 5.9 Imaginary part of the eigenvalues with respect to the proportional control gain

From the figures above, one can see namely three regions. On the one hand, there are two semi-finite regions of the K_p for which two of the eigenvalues are complex conjugates: in the LHS plane poles green and red, and in the RHS plane poles blue and red; and one of the eigenvalues strictly real: in the LHS plane the blue eigenvalue, and in the RHS plane the green one. It is important to realize that when the real part of the complex poles is negative, the real part of the real eigenvalue is positive, and vice versa. The distribution of those depends on the sign of the proportional gain. As a consequence, one can conclude that for K_p values within this regions, the system is unstable.

On the other hand, there is a third region between the two aforementioned for which the three eigenvalues are strictly real. Similarly to the previous cases, when two of the poles are positive (blue and red), the other one is negative (green), and when two of the eigenvalues are negative (green and red), the other one is positive (blue). Consequently, one can conclude that for K_p values within this regions, the system is unstable.

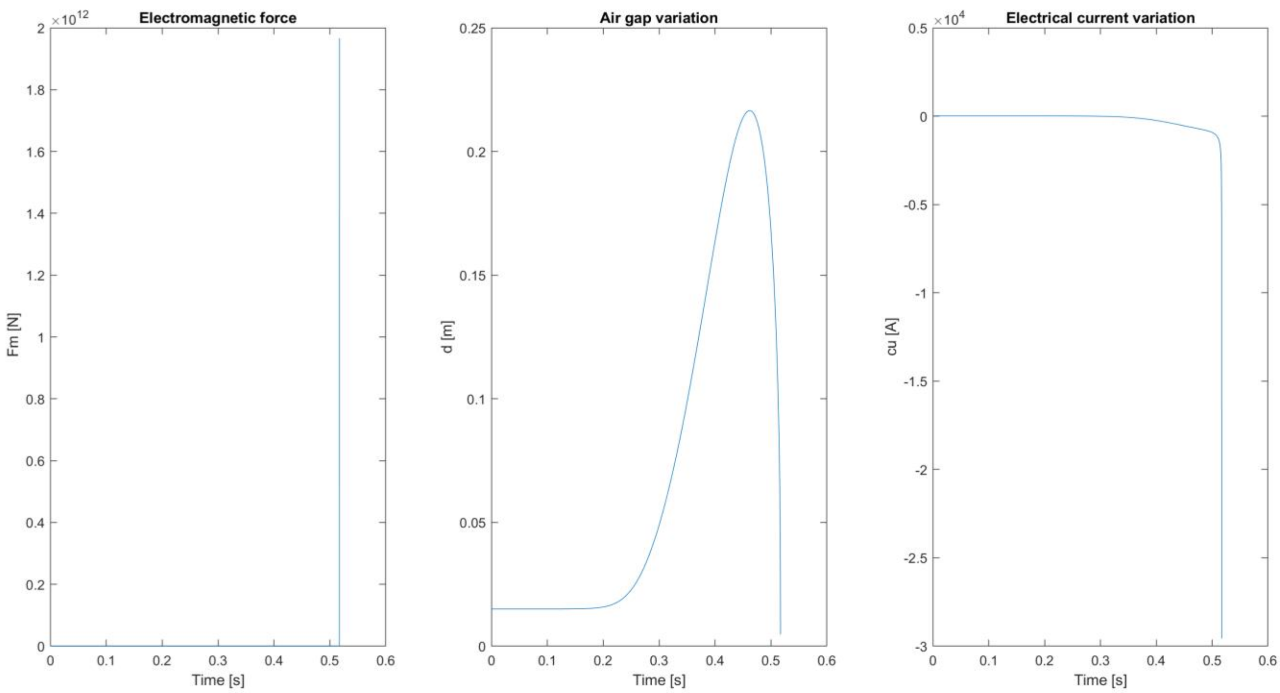

Figure 5.10 Nonlinear solution of the system with P-control against time

This becomes clear when plotting the position of the vehicle and the electromagnetic force against time using the nonlinear simulation. From this figures, it becomes obvious that the control takes over and, unlike in the previous section for which the vehicle moves progressively away, in this case the motion of the vehicle is reversed, the electromagnetic forced is increase and the vehicle is pushed upwards until it clashes with the track. Along these lines, two conclusions can be drown: first, the control has an effect on the vehicle motion; second, as proven with the eigenvalue problem, the system is still unstable, but as shown in this case, it either falls down or crashes with the track.

In this manner, it is proven that for such a proportional control the system is still unstable and there is no possible value of K_p for which it can be stabilized. Hence, a higher level of complexity need to be applied to the control scheme definition.

6

STABILITY STUDY OF THE CLOSED-LOOP EMS SYSTEM WITH PD-CONTROL

Despite of the implementation of an initial feedback control system in the one and a half dof system closed loop system, the stabilization of the system has not been reached. Aiming at designing a control system like the one described in in chapter 5 and presented in Fig. 5.1, in this section, a D-control component is added to the previously derived P-control scheme, increasing the control system by adding another control gain and another control variable.

Following the theory presented in chapter 2.5, the derivative control (D-control) is a feed forward control that anticipates the process conditions by analysing and minimizing the change in error. D-control correlates the controller output to the derivative of the error. The derivative of the error is taken with respect to time.

In the same way as the model developed in chapter 4 and 5, this study case focuses only on the vehicle dynamics. For this reason, the assumption of having an infinitely stiff track beam eq. 4.1 still holds for this study case.

Following the design trend of the error-based closed-loop control presented in chapter 5, for this control the error defined for this analysis is expressed as $e = x_1 - \delta_0$ and the system outputs $\{x_1 \quad x_2 \quad x_5\} = \{z \quad \dot{z} \quad i\}$. The monitored variable is the air gap δ and the controlled variable is the voltage u. The controlled is defined in time domain as part of the equations of motion. Then, the control loop can be described as

$$u = K_p(x_1 - \delta_0) + K_d \frac{\partial(x_1 - \delta_0)}{\partial t} + u_0 = K_p(x_1 - \delta_0) + K_d x_2 + u_0 \tag{6.1}$$

Where K_p is the proportional control gain and K_d is the derivative control gain, both to be tuned, and u_0 is called the bias, which namely is the reference value of the control value. In this case it is defined as the voltage input that initially defines the system at the target air gap equilibrium position.

Hence, the system of equations of motion can be defined as

$$\begin{cases} \dot{x}_1 = x_2 \\ \dot{x}_2 = g - \mathrm{sgn}(x_1)\dfrac{C}{m}\dfrac{x_5^{\,2}}{x_1^{\,2}} \\ \dot{x}_5 = \dfrac{x_1}{2C}\left(K_p(x_1 - \delta_0) + K_d x_2 + u_0 - x_5 R - 2C\dfrac{x_5}{x_1^{\,2}} x_2\right) \end{cases} \tag{6.2}$$

As aforementioned in chapter 3.2, the focus is put on the local stability of the coupled system around the equilibrium point. Then, the equilibrium points of the system can be defined as $(x_1^*, x_2^*, x_5^*) = \ = \{(x_1, x_2, x_5) \,|\, \dot{x}_1 = 0;\ \dot{x}_2 = 0;\ \dot{x}_5 = 0\}$ which yields four possible solutions, which need to be sorted out. However, in this case study, not all parameters are all strictly positive. The majority are, namely $\mu_0, A_m, N, m, g, u_0, R$, are all strictly positive. But, the proportional control gain K_p and the derivative control gain K_d can be both positively and negatively defined. Consequently, now, the identification of the feasible fixed points, is not that straight forward and further assessment will be required.

From the computation of the equilibrium points, several solutions are obtained, from which only two are feasible, considering the fact that any equilibrium point must be real-valued by definition. These are described as

$$\begin{aligned} (x_1^{1*}, x_2^{1*}, x_5^{1*}) &= \left(\frac{(CK_p - \sqrt{gmC})(K_p\delta_0 - u_0)}{-R^2 gm + CK_p^{\,2}},\ 0,\ \frac{K_p\left[\dfrac{(CK_p - \sqrt{gmC})}{-R^2 gm + CK_p^{\,2}}\right](K_p\delta_0 - u_0) - K_p\delta_0 + u_0}{R}\right) \\ (x_1^{2*}, x_2^{2*}, x_5^{2*}) &= \left(\frac{(CK_p + \sqrt{gmC})(K_p\delta_0 - u_0)}{-R^2 gm + CK_p^{\,2}},\ 0,\ \frac{K_p\left[\dfrac{(CK_p + \sqrt{gmC})}{-R^2 gm + CK_p^{\,2}}\right](K_p\delta_0 - u_0) - K_p\delta_0 + u_0}{R}\right) \end{aligned} \tag{6.3}$$

If one compares the components of the feasible fixed points obtained in this case with the ones previously derived, they are identical. This can be explained by the fact that K_p is the only control parameter which conditions the location of the fixed points of the system. Whereas K_d relates to the stability nature of the fixed points.

Considering that the two feasible fixed points are the same as in chapter 5, the same exact procedure of analysing the feasibility of both alternatives is applied here, which yields the same result. The only admissible fixed point is the second one. The reasoning is the same, the definition of a negative electrical current and voltage is not correct in this design.

Now, the eigenvalue problem is not only conducted as a function of K_p, but also as a function of K_d since both are control gains, which are the tunable value that is assumed to make the system stable. Therefore, one expects to be able to define different regions of stability depending on the value of these parameters, but now in a 3D space, representing the eigenvalues as surfaces.

Once the fixed point has been calculated, following eq. 4.9 and 4.11, the next step is to define the Jacobian matrix of the system and evaluate it at the fixed point. However, since the expressions get more and more involved as the complexity of the system increase, several terms have been defined as complementary parameters in order to shorten the expressions. These are $\psi = (CK_p + R\sqrt{gmC})$, $\gamma = (-R^2 gm + CK_p{}^2)$, $\varpi = (-RK_d K_p \delta_0 - R^2 gm + CK_p{}^2 + RK_d u_o)$ $\chi = (K_p \delta_0 - u_0)$, $\varepsilon = (Rgm + K_p \sqrt{gmC})$, $\eta = (-2CRgm - CK_d u_0)$.

$$\mathbf{J} = \begin{bmatrix} 0 & 1 & 0 \\ \frac{2C}{m}\frac{x_5{}^2}{x_1{}^3} & 0 & -\frac{2C}{m}\frac{x_5}{x_1{}^2} \\ \frac{1}{2C}[u_0 + K_p(x_1 - \delta_0) + K_d x_2 - x_5 R - 2C\frac{x_2 x_5}{x_1{}^2} + x_1(K_p + 4C\frac{x_2 x_5}{x_1{}^3})] & \frac{1}{2C}(K_d x_1 - \frac{2Cx_5}{x_1}) & \frac{x_1}{2C}(-R - 2C\frac{x_2}{x_1{}^2}) \end{bmatrix} \Rightarrow$$

$$\mathbf{J}\big|_{(x_1{}^*, x_2{}^*, x_5{}^*)} = \begin{bmatrix} 0 & 1 & 0 \\ \frac{2C\varepsilon^2\gamma}{m\chi\psi^3} & 0 & -\frac{2C\varepsilon\gamma}{m\chi\psi^2} \\ \frac{\chi\varepsilon K_p}{2C\gamma} & \frac{-2K_p\sqrt{gmC}\varpi + CK_d K_p{}^3\delta_0 + \eta K_p{}^2 + K_d K_p R^2 gm\delta_0 + 2R^3 g^2 m^2 - K_d R^2 gmu_0}{2\psi\gamma} & -\frac{\varepsilon\psi R}{2C\gamma} \end{bmatrix} \tag{6.4}$$

Hence, the linearized system around the fixed point reads

$$\begin{Bmatrix} \dot{x}_1 \\ \dot{x}_2 \\ \dot{x}_5 \end{Bmatrix} = \begin{bmatrix} 0 & 1 & 0 \\ \dfrac{2C\varepsilon^2\gamma}{m\chi\psi^3} & 0 & -\dfrac{2C\varepsilon\gamma}{m\chi\psi^2} \\ \dfrac{\chi\varepsilon K_p}{2C\gamma} & \dfrac{-2K_p\sqrt{gmC}\varpi + CK_dK_p{}^3\delta_0 + \eta K_p{}^2 + K_dK_pR^2gm\delta_0 + 2R^3g^2m^2 - K_dR^2gmu_0}{2\psi\gamma} & -\dfrac{\varepsilon\psi R}{2C\gamma} \end{bmatrix} \begin{Bmatrix} x_1 \\ x_2 \\ x_5 \end{Bmatrix} \tag{6.5}$$

Then, the same trick used in the previous chapter can be used to reduce the two first rows of the matrix system to an equivalently single equation with variable x_1 and x_5, and coefficients corresponding to the Jacobian terms and a second equation corresponding to the last row with variables x_1 and x_5.

$$\begin{cases} \ddot{x}_1 - J_{21}x_1 + J_{23}x_5 = 0 \\ \dot{x}_5 - J_{31}x_1 - J_{32}\dot{x}_1 + J_{33}x_5 = 0 \end{cases} \tag{6.6}$$

In the same manner as chapter 5, no conclusions can be drawn about stability of the system solely from the sign of the coefficients/stiffness od the system, the Jacobian terms cannot be guaranteed to be strictly positive due to the presence of K_p and K_d. The sign of the real part of the eigenvalues needs to be investigated. Along these lines, following the same method previously applied in chapter 4 and 5, the system in eq. 6.6 in the Laplace domain reads

$$\begin{cases} \ddot{x}_1 - J_{21}x_1 + J_{23}x_5 = 0 \\ \dot{x}_5 - J_{31}x_1 - J_{32}\dot{x}_1 + J_{33}x_5 = \delta(t) \end{cases} \xrightarrow{\text{Laplace trans.}} \begin{cases} s^2\hat{x}_1 - J_{21}\hat{x}_1 + J_{23}\hat{x}_5 = 0 \\ s\hat{x}_5 - J_{31}\hat{x}_1 - J_{32}s\hat{x}_1 + J_{33}\hat{x}_5 = 1 \end{cases} \tag{6.7}$$

Then, following the theory presented in chapter 2.4, one can compute the poles of the system, i.e. the eigenvalues, by deriving the transfer function of $\hat{x}_1$ and finding the roots of its denominator.

$$\begin{gathered} \hat{x}_5 = \frac{1 + J_{31}\hat{x}_1 + J_{32}s\hat{x}_1}{s + J_{33}} \Rightarrow s^2\hat{x}_1 - J_{21}\hat{x}_1 + J_{23}\left(\frac{1 + J_{31}\hat{x}_1 + J_{32}s\hat{x}_1}{s + J_{33}}\right) = 0 \rightarrow \\ \hat{x}_1 = \frac{-\dfrac{J_{23}}{s + J_{33}}}{s^2 - J_{21} + \dfrac{J_{23}(J_{31} + J_{32}s)}{s + J_{33}}} = -\frac{1}{\dfrac{1}{J_{23}}[s^3 + J_{33}s^2 + (J_{23}J_{32} - J_{21})s - J_{21}J_{33} + J_{23}J_{31}]} \\ \xrightarrow{\text{Poles}} \frac{1}{J_{23}}[s^3 + J_{33}s^2 + (J_{23}J_{32} - J_{21})s - J_{21}J_{33} + J_{23}J_{31}] = 0 \end{gathered} \tag{6.8}$$

The poles of the expression in eq. 6.11 have then been evaluated with respect to K_p and K_d, which yield to the following patterns (Fig. 6.1 – 6.4). These are presented in four plots. The first one features the negative real half-space with respect to K_p and K_d with the three eigenvalues $\mathrm{Re}\{s_{1,2,3}\}$ (Fig. 6.1). The reason for this follows from stability theory as explained in chapter 2.4, for which the stability of any system is, in general terms, ensured by the unique and sufficient condition that all eigenvalues have negative real part.

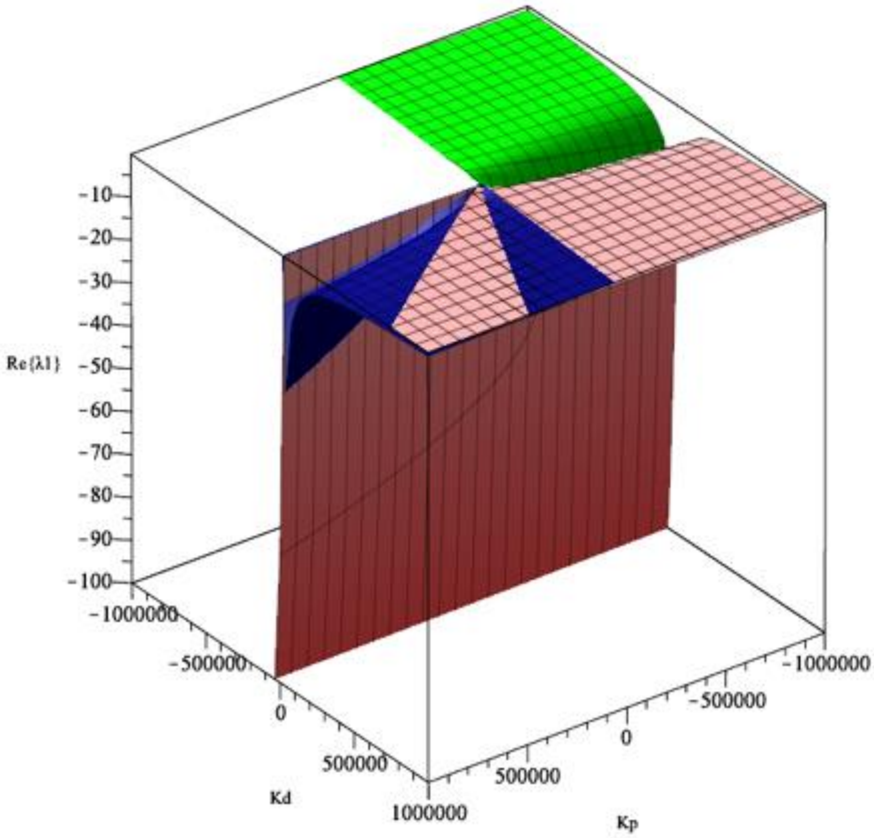

Figure 6.1 Eigenvalues at the negative real half-space with respect to K_p and K_d

From this plot, it can be seen that there is actually one region for which, namely the positive quarte in the K_p and K_d plane, where the three eigenvalues coincide, taking a negative real part. This can be seen as a stable region in the parametric space, for which combinations of gain values when tuning the control, provide a stabilization of the system. With the objective of analysing this region, the next three plots feature the stability region of negative real part eigenvalues within the parametric plane $K_p - K_d$ for each of the three eigenvalues (Fig. 6.2 – 6.4).

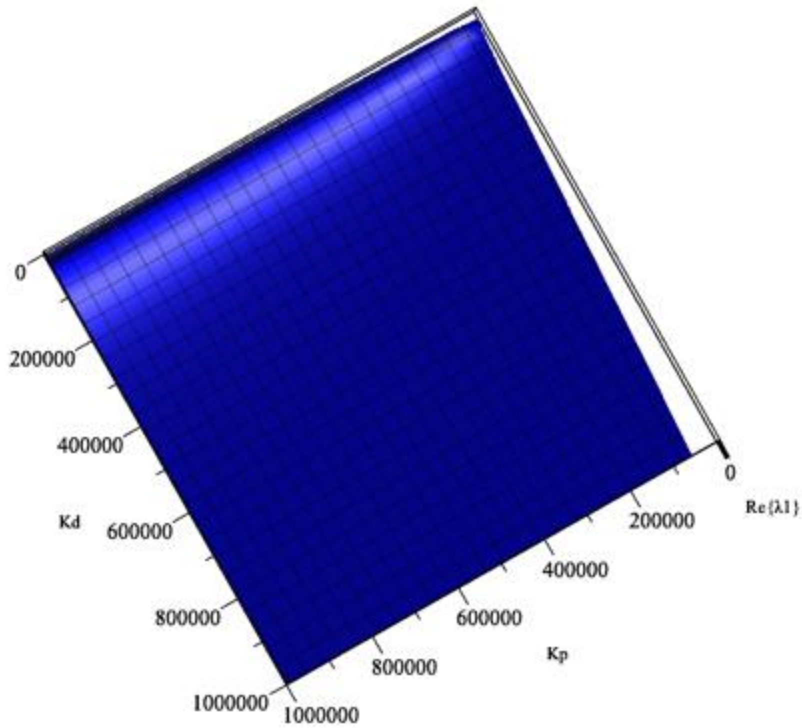

Figure 6.2 1st eigenvalue stability region of negative real part within the parametric plane $K_p - K_d$

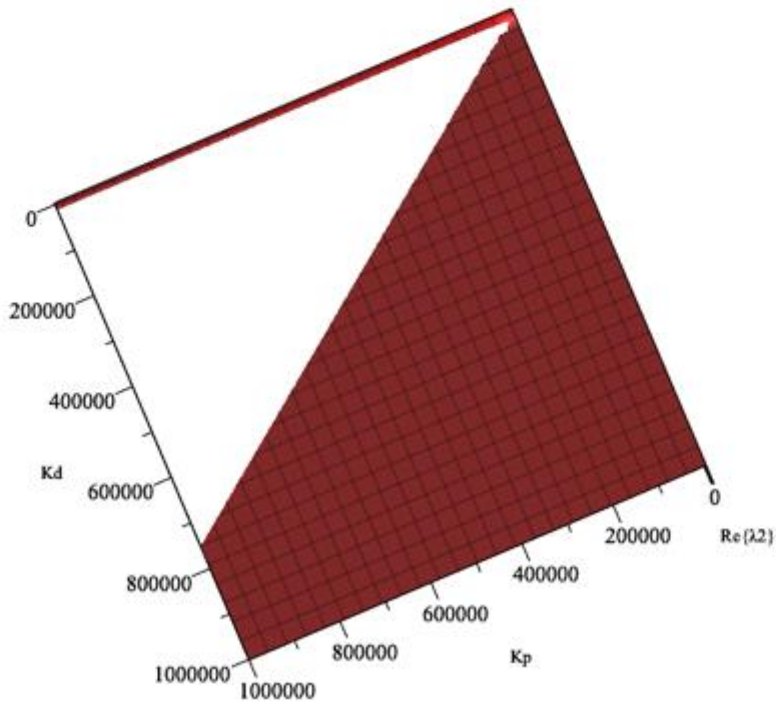

Figure 6.3 2nd eigenvalue stability region of negative real part within the parametric plane $K_p - K_d$

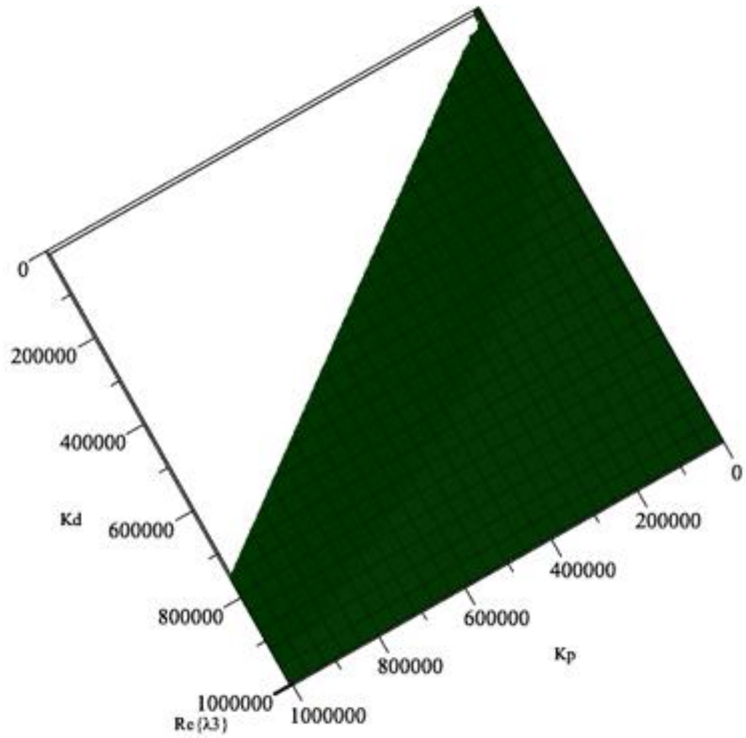

Figure 6.4 3[rd] eigenvalue stability region of negative real part within the parametric plane $K_p - K_d$

From the plots above, it becomes obvious that there is a region in the parametric space for which the system can be stabilized. An important check for correctness is that the combination of the three surfaces confirms that no stabilization is possible with only a P-control (i.e. $K_d = 0 \wedge K_p \neq 0$), neither for only a D-control (i.e. $K_p = 0 \wedge K_d \neq 0$), nor for an open loop system without control (i.e. $K_p = 0 \wedge K_d = 0$).

The boundaries stability region within the parametric space can be defined by illustrating the intersection of the three surfaces with the 0 plane (Fig. 6.5).

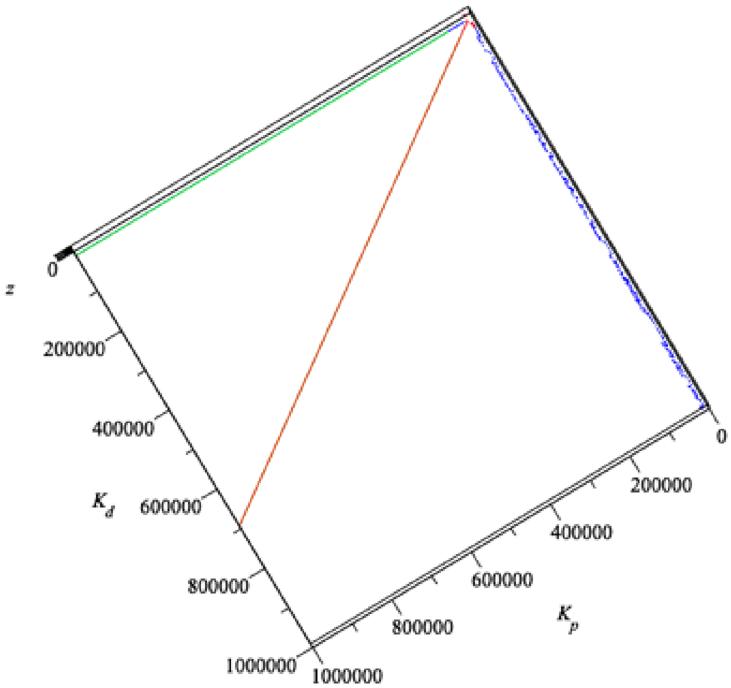

Figure 6.5 Intersection pole surfaces with 0-plane. Limits of stability region

From this map, the stability region and stability thresholds can be defined as shown below (Fig. 6.6). These stability limits can be defined by the inequality expression below. This directly corresponds to the intersection of the real part of the eigenvalues with the zero-plane.

$$11867.65 \le K_p \le 1.4496236 K_d - 16785.332 \tag{6.9}$$

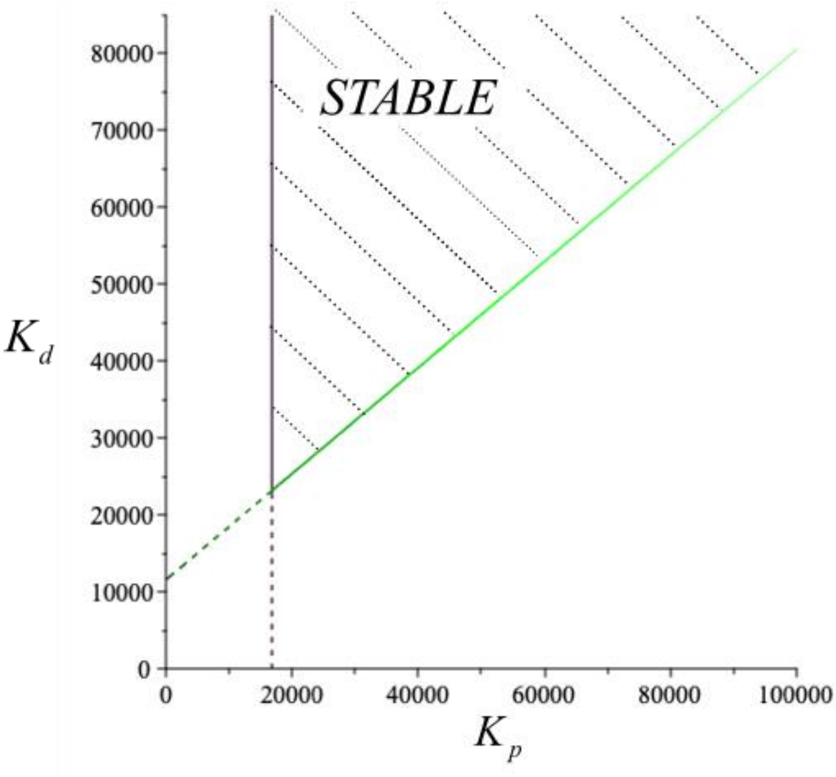

Figure 6.6 Definition of the stability region

Moreover, the equilibrium point obtained for the PD-control nonlinear system is exactly the same as the one found for P-control. This validates the conceptual frame mentioned in chapter 2.4, for which the fixed point location is only dependent on the P-component. Whereas, the D-component and the I-component define the type of fixed point.

Once a stability region has been identified, two analysis of this case study can be produced. First, one can study the dynamic behaviour of the vehicle depending on the input control gain values both within the phase portrait and for the evolution of the main variables of the system against time. Second, one can draw the most general phase portrait of the system by running a set of simulations with different initial conditions and perturbations, trying to picture out the tolerance in the variable space for which the system is able to stay stable.

Along these lines, coming next several study cases are presented varying the control gain parameters and the initial conditions.

6.1. SYSTEM RESPONSE STUDY BASED ON CONTROL PARAMETERS

For this project, the control gain parameters have been defined to be constant in time. In this manner, the control system is kept on a fundamental definition, avoiding more complex time dependent tuning techniques or parametric space dependent tuning techniques, such as gain scheduling.

Considering the first analysis type, the most simplified strategy is the definition of a fixed K_d value, defining a horizontal line through out the stability region plane presented in Fig. 6.6, and present the results evolution for different K_p values along this horizontal line. In this manner, the effect K_p and K_d on the vehicle motion becomes more clear. The several case studies addressed in this section are presented in Tab. 6.1.

Table 6.1 Summary of the study cases presented in this section

Gain parameters study cases based on $K_d = 28000$

Case Nº	Location Stable Region	K_p value
Case 1	Close to Left Boundary In Stable Region	17000
Case 2	In the Middle of the Stable Region	20000
Case 3	Close to Right Boundary In Stable Region	23700
Case 4	Close to Left Boundary Outside Stable Region	16600
Case 5	In the Right Boundary In Stable Region	23804
Case 6	Close to Right Boundary Outside Stable Region	24200

Below, the behaviour of the system state-variables $\{z \quad \dot{z} \quad i\}$ is presented against time (Fig. 6.7, 6.9 and 6.11), proving that stabilization around a designed point occurs for all variables of interest of the system and that the effect of the controller gain parameters on those variables is globally very similar.

These plots feature not only the nonlinear simulation solution of the system state variables $\{x_1 \quad x_2 \quad x_5\} = \{z \quad \dot{z} \quad i\}$ (in black), but also the linearized solution derived analytically from the linearization of the system around the fixed point (in blue) and the design equilibrium value (in red).

Using the strategy defined above, the case 1 featured results correspond the case for which K_p is significantly smaller than K_d, located close to the left stability boundary $K_p = 16783.35$ (Fig. 6.7). In this case, the input combination of gain parameters is $K_p = 17000$ and $K_d = 28000$, whilst the initial perturbation to the vehicles position is $1 \cdot 10^{-4}\, m$ from the target air gap of the system.

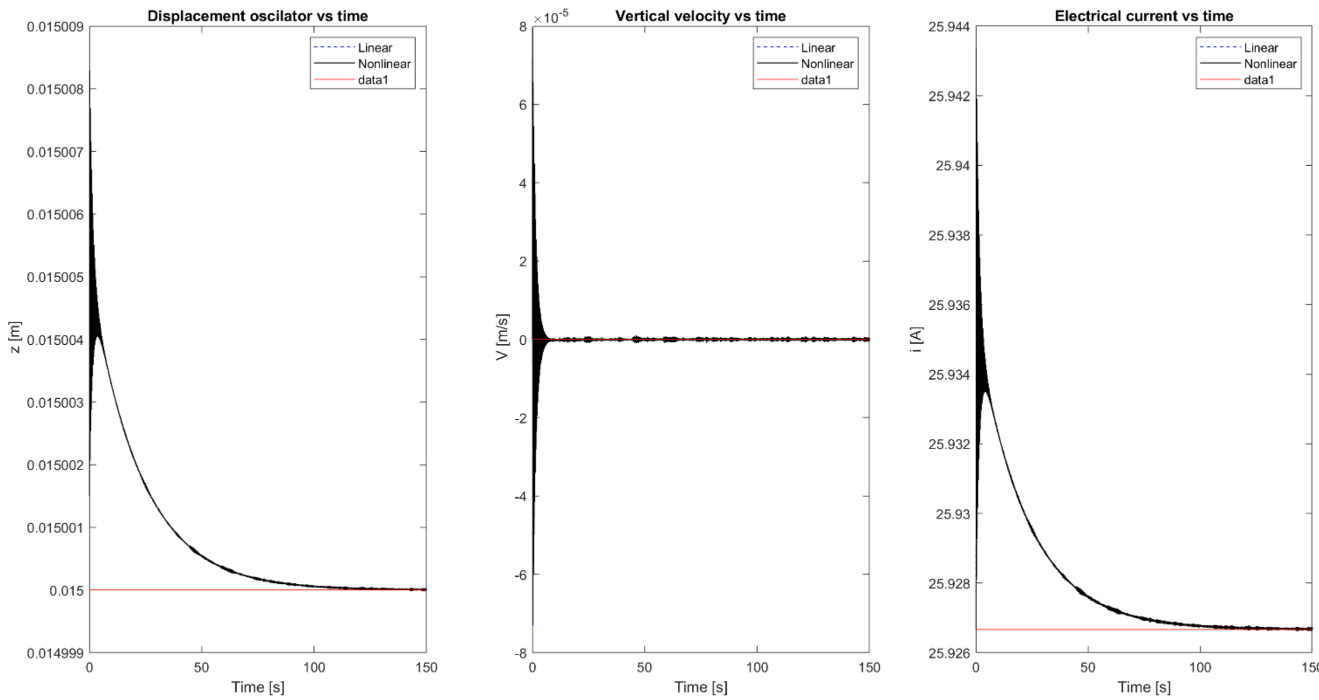

Figure 6.7 Nonlinear and linearized solutions of the system against time for a K_p value close to the left boundary of the stability region

From Fig. 6.7, it becomes obvious that the system is stable around the equilibrium point represented by the red line and the behaviour along time presented by all represented magnitudes is very similar. An important conclusion drawn from this figure is that for cases where K_d parameter gain governs K_p, i.e. is significantly larger than K_p, the convergence rate is quite slow. This translates in a longer time for the solution of variables, such as the vehicle position z and the electrical current i, to reach values around the designed equilibrium value. This can be explained, due to the fact that K_p is one to one related with how fast the system approaches the equilibrium solution by definition. Whereas the K_d governs the error change amplitude. In this manner, a high value of K_d yield a very small amplitude of oscillation of the actual solution around the equilibrium point, whilst it takes some time far all the variables to reach a band of values around the fixed point.

Besides, from these results, the relation between the vehicle vertical velocity and the vehicle position becomes apparent. When the vehicle position oscillates with significant amplitude around the system response value, the vertical velocity also oscillates around the equilibrium value as a result of the relatively large position variations. Whereas, when the vehicle position oscillation amplitude around a solution value is reduced to a small band and its response move closer to the equilibrium value in a smooth trajectory, the velocity reduces its amplitude oscitation around the design value drastically.

In this case, the nonlinear and the linearized solution are almost equal and no significant offset can be observed, since the initial conditions are given close to the equilibrium point. The observations described above also apply for the phase portrait representation of the system (Fig. 6.8). In this map it becomes obvious the slow convergence rate. Nevertheless, the amplitude of the trajectory oscillation around the fixed point is significantly small. In this plot, the initial condition is marked with a circle and the direction is represented by an arrow.

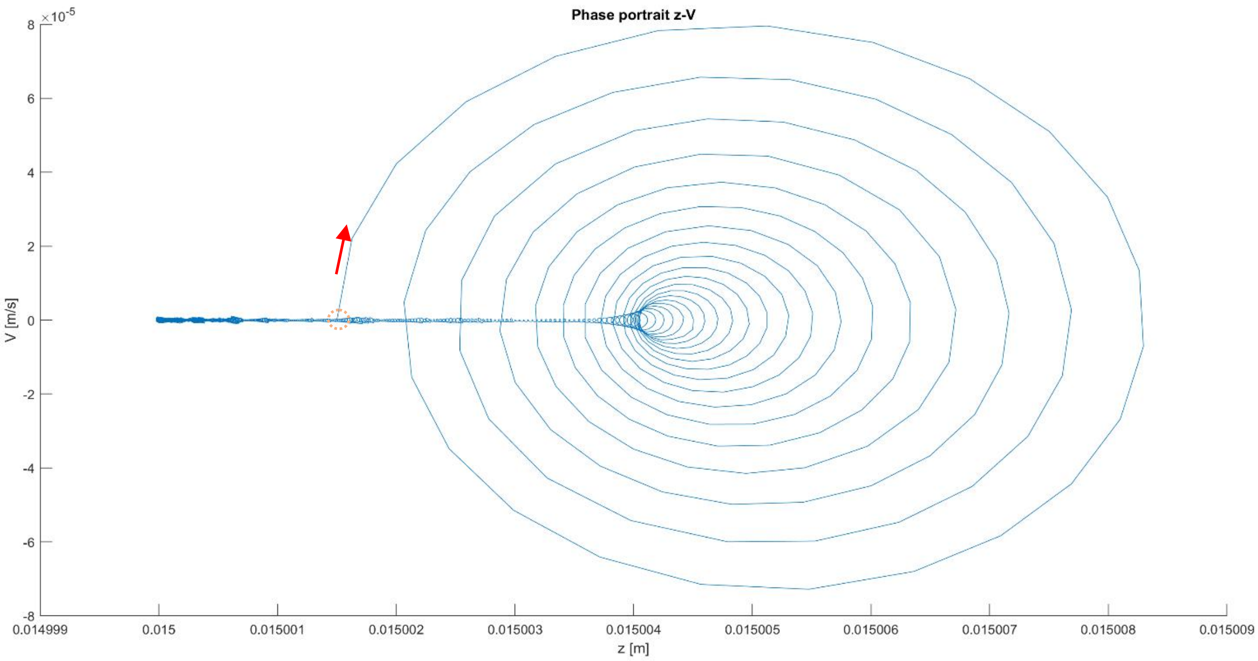

Figure 6.8 Phase portrait of the system for a K_p value close to the left boundary of the stability region

The second featured results correspond the case for which K_p is about in the middle of the stable region within both the right and the left boundaries defined in eq. 6.12. (Fig. 6.9). In this case, the input combination of gain parameters is $K_p = 20000$ and $K_d = 28000$, whilst the initial perturbation to the vehicles position is $1 \cdot 10^{-4}\, m$ from the target air gap of the system.

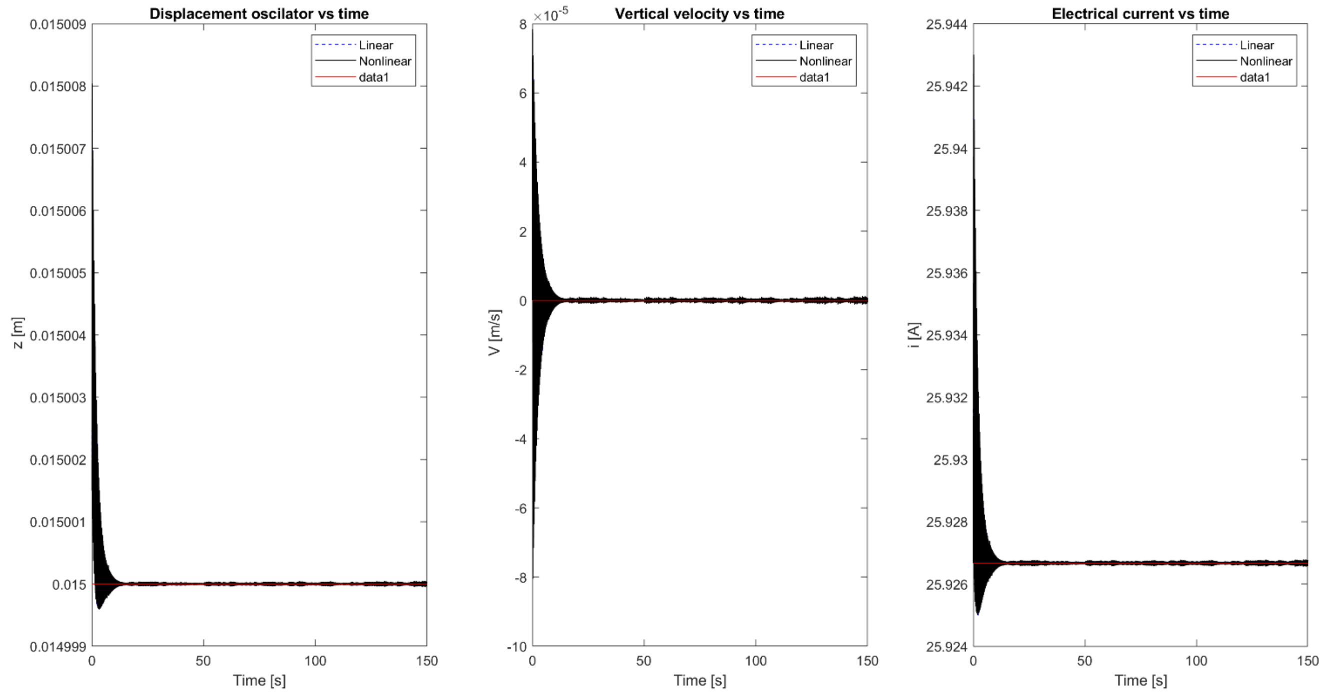

Figure 6.9 Nonlinear and linearized solutions of the system against time for a K_p value centered within the stability region

From this figure, it becomes obvious the effect that the shift of K_p causes on the behaviour of the solutions versus time, leading to a much faster convergence. This results from the fact that the difference between K_p and K_d has been reduced and K_d is no longer significantly larger than the value of K_p. As aforementioned, this follows directly from the fact that K_p is one to one related with how fast the system approaches the equilibrium solution by definition. Besides, the same relation observed previously between the vertical velocity of the vehicle and the vehicle position is observed in this case.

A good point about the results showcased above (Fig. 6.9) is that the shift on K_p has not been sufficiently large for the amplitude of oscillation of the actual solution around the equilibrium point to change significantly, leading to a quite optimal behaviour of the derived solution, featuring a fast convergence and a small error amplitude. Likewise the previous case, the nonlinear and the linearized solution are almost equal and no significant offset can be observed.

The observations described above also apply for the phase portrait representation of the system (Fig. 6.10). In this map it becomes obvious that the convergence is much faster than in the previous case, drawing a progressive approach in form of a conical spiral, and the trajectory to the stable equilibrium point is reached with a small amplitude of error oscillation about the point.

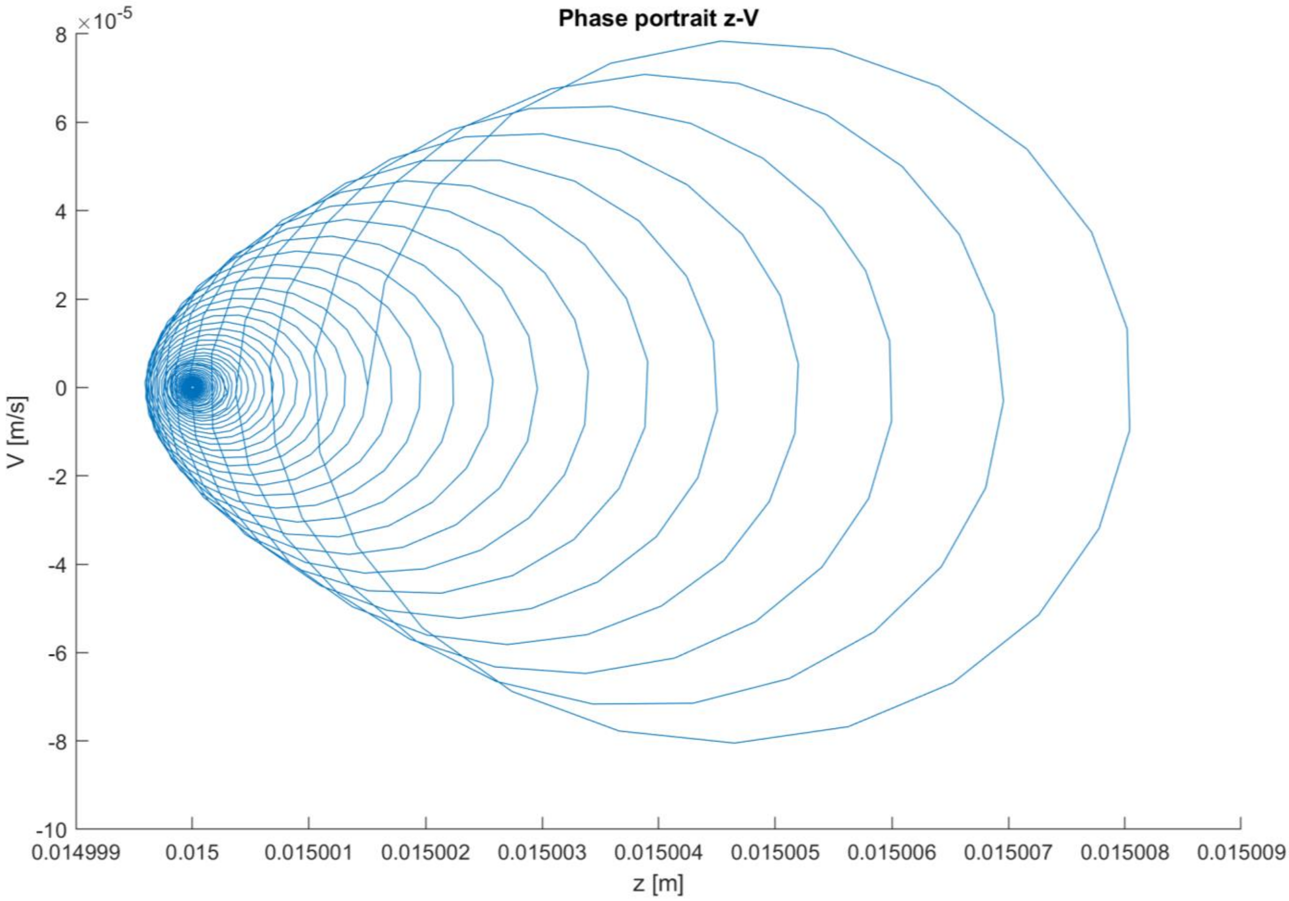

Figure 6.10 Phase portrait of the system for a K_p value centered within the stability region

The third featured results correspond the case for which K_p is close to the right boundary $K_p = 1.4496236 K_d - 16785.332$ (Fig. 6.11). In this case, the input combination of gain parameters is $K_p = 23700$ and $K_d = 28000$, whilst the initial perturbation to the vehicles position is $1 \cdot 10^{-4}\, m$ from the target air gap of the system.

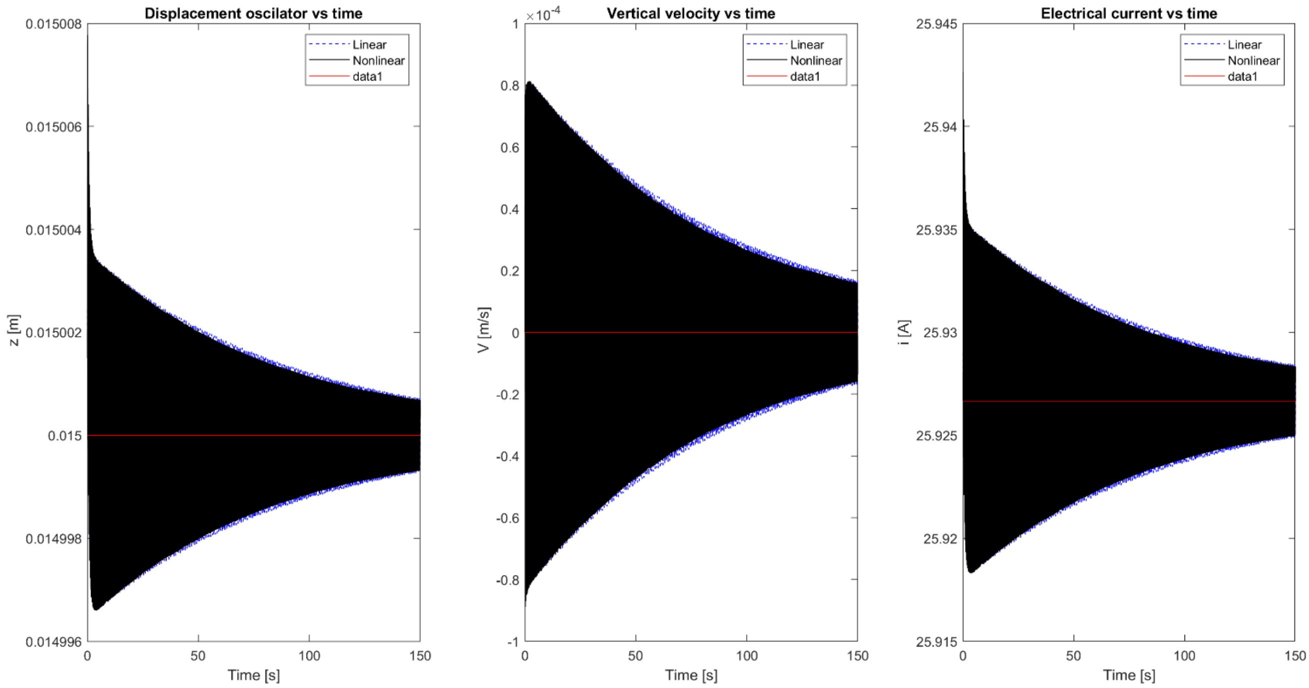

Figure 6.11 Nonlinear and linearized solutions of the system against time for a K_p value close to the right boundary of the stability region

From these plots, an apparent change in behaviour with respect to time is observed. The trend for all the magnitudes represented, i.e. system state variables, control variable and electromagnetic force, is more similar for all variables. For all of them the convergence rate is very fast, in such a way that the first step already overshoots and crosses the equilibrium point line. This means that since the beginning of the solution simulation the variables are varying around the design point. This results from the shift on K_p coming closer to the value of K_d. However, within the trade between the effect of each of the gains to the overall system response, the fast convergence comes to a price, since now the amplitude of the oscillation of the system response around the fixed point is much larger and will keep on increasing as K_p increases until the stability threshold is met.

The explanation for such a trade of can be derived not only through the natural definition of each of the control components as previously done, but also through the system eigenvalues. In this sense, within the stability region, at any point of this sub-space, the system is defined by one purely real eigenvalue and two complex conjugate eigenvalues. Further proof of this is provided below, for the explanation of the existence of a Hopf bifurcation in the system, as defined in chapter 2.4.2. Nevertheless, for each combination of parameters within this sub-space the magnitude of both real and negative parts changes.

Using the strategy defined above of fixing a K_d value and defining a horizontal line across the stability region, one can evaluate the change of the system eigenvalues along this horizontal line. In this manner, it is observed that the main change on the eigenvalues' nature between the left boundary and the right boundary is translated in the magnitude of the real part of the complex conjugate pair of eigenvalues. Along these lines, the magnitude of such real part is at its maximum when the parameter combination is taken at the left boundary and it progressively reduces tending to zero when moving to the right.

If one takes the parameter combination just at the right boundary, the real part of the complex conjugate pair of eigenvalues is exactly zero. This is the so called bifurcation, the point in which stability is lost and a change on the stability pattern of the system is defined. Now, if one approached the limit of the real value of the complex conjugate poles through its negative value, one can see that the stability pattern for a pair of complex conjugates with real part negative tending to 0 and non-zero imaginary part corresponds to a stable centre. Relating this to the effect of the control gain parameters tuning on the system response, this can be seen as the point at which K_p takes over in the aforementioned trade of and the amplitude on the error change around the equilibrium starts growing exponentially, it is in this bifurcation point, when the fixed point will lose its stability and the amplitude of this oscillations around the equilibrium will grow as a spiral trajectory on the phase portrait plane move away from the fixed point will be observed.

Considering this explanation, one can understand that the phase portrait for the third set of results presented below (Fig. 6.12) starts shaping up to a limit cycle.

In this case, since the amplitude of the oscillation of the system response around the fixed point is much larger, the velocity solution cannot close in to the design value as in the previous case. Moreover, in this case, some offset between the linearized and the nonlinear solutions starts to appear (Fig. 6.11), which will accentuate when approaching the bifurcation point and will completely differ right after it as showcased below.

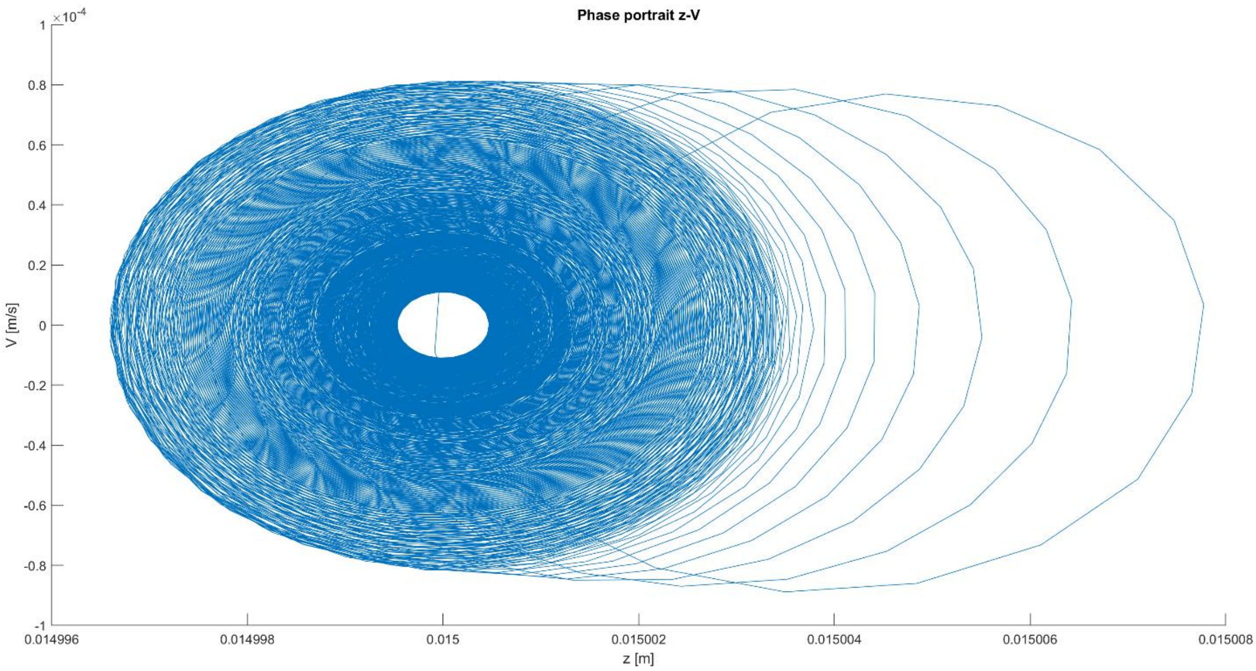

Figure 6.12 Phase portrait of the system for a K_p value close to the right boundary of the stability region

As aforementioned in this very same section 6 and in chapter 2.4, the existence of a Hopf bifurcation is directly a consequence of finding a complex conjugate pair of eigenvalues with zero real part. Therefore, an eigenvalue study is necessary. In this case, it is quite simple, since the system is defined by three eigenvalues, which as performed before, can be plotted in a 3D space. A way of showcasing the existence of this bifurcation, following the approach defined above on fixing K_d and varying K_p, is to plot the analytical expression of the eigenvalues with respect to K_p (Fig. 6.13). In this case, the plot is produced fixing $K_d = 28000$.

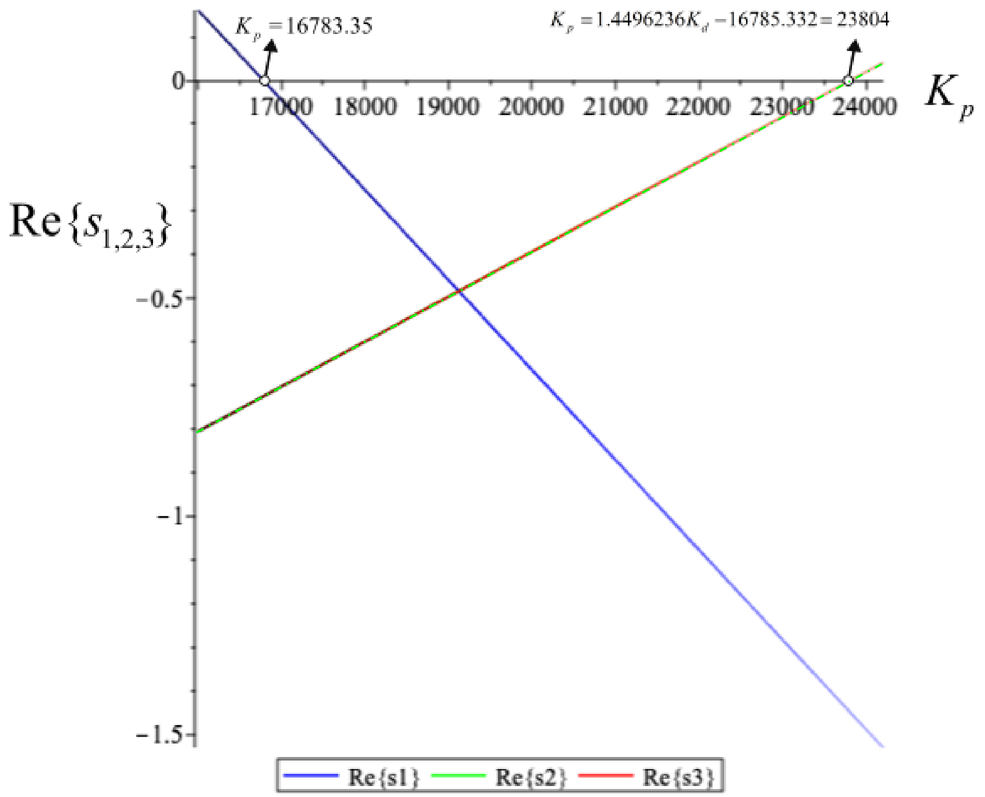

Figure 6.13 Plot of the real part of the three eigenvalues of the linearized system with respect to K_p

From the figure, the definition of the stability thresholds becomes evident and, consequently, at the location where the pair of complex conjugates intersect the horizontal axis $\mathrm{Re}\{s_{1,2,3}\} = 0$ and the bifurcation is created. The red line overlaps with the green one, since the real part of the complex conjugate pair of eigenvalues s_2 and s_3 is equal. Besides, one can conclude that no Hopf bifurcation is expected around the left stability threshold, since in that case, the real part of the complex conjugate pair of poles is not zero, but the purely real eigenvalue s_1 becomes zero.

The behaviour of the system response around both boundaries for a fixed $K_d = 28000$ is presented below (Fig. 6.14 – 6.18). At the left boundary, the behaviour of the system for a K_p value a little bit lower than the boundary ($K_p = 16600$) is unstable. From the behaviour of the system state variables and the control variable versus time (Fig. 6.14), it becomes obvious that the low value of K_p leads to a control that is not able to maintain the vehicle attracted at the target air gap level and it falls downs, moving away from the design value. Given the correct definition of the system, it tries to over compensate this by inputting more voltage to the system and raising the electrical current, without success.

As a side note, from this figure (Fig. 6.14), it becomes obvious that the farther away from the equilibrium point around which the system was linearized, the larger the divergence between the linearized solution in blue and the nonlinear one in black.

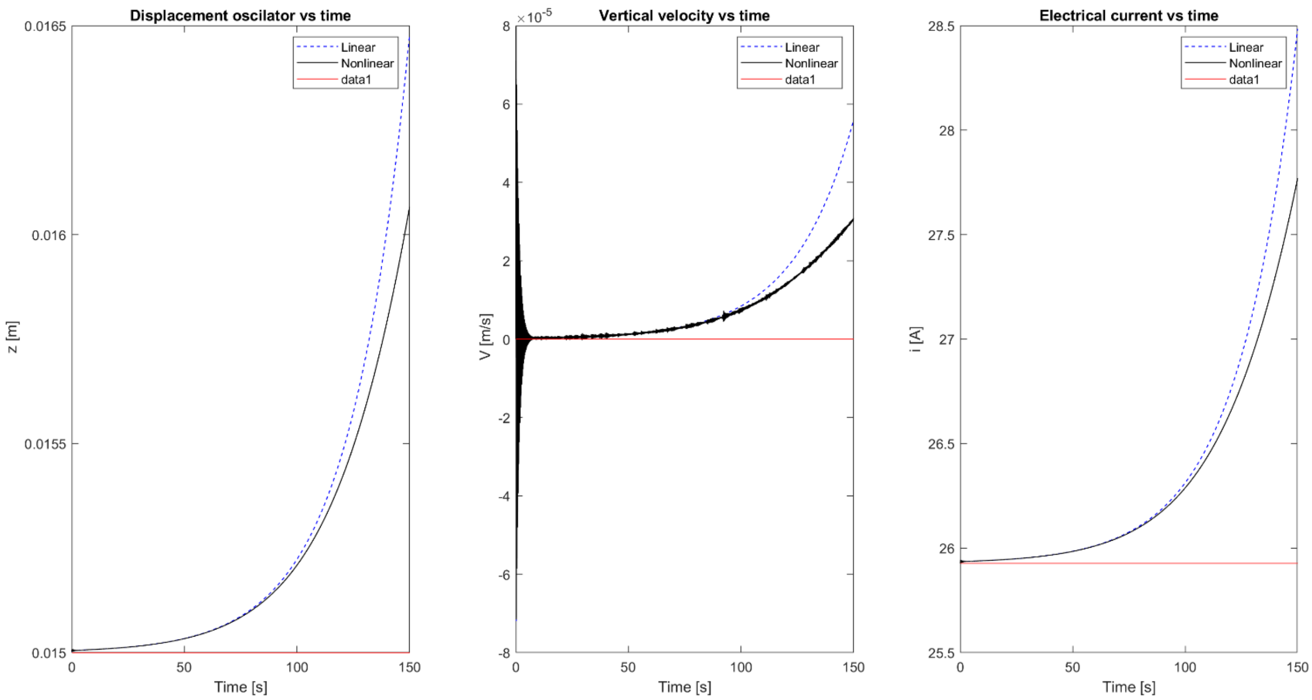

Figure 6.14 Nonlinear and linearized solutions of the system against time for a K_p value smaller than the left boundary of the stability region

In this case, the phase portrait also shows an unstable response (Fig. 6.15). From the plot, one can see that the system tries to oscillate around the fixed point in the initial stages, but it cannot hold for long and starts deviating and moving away.

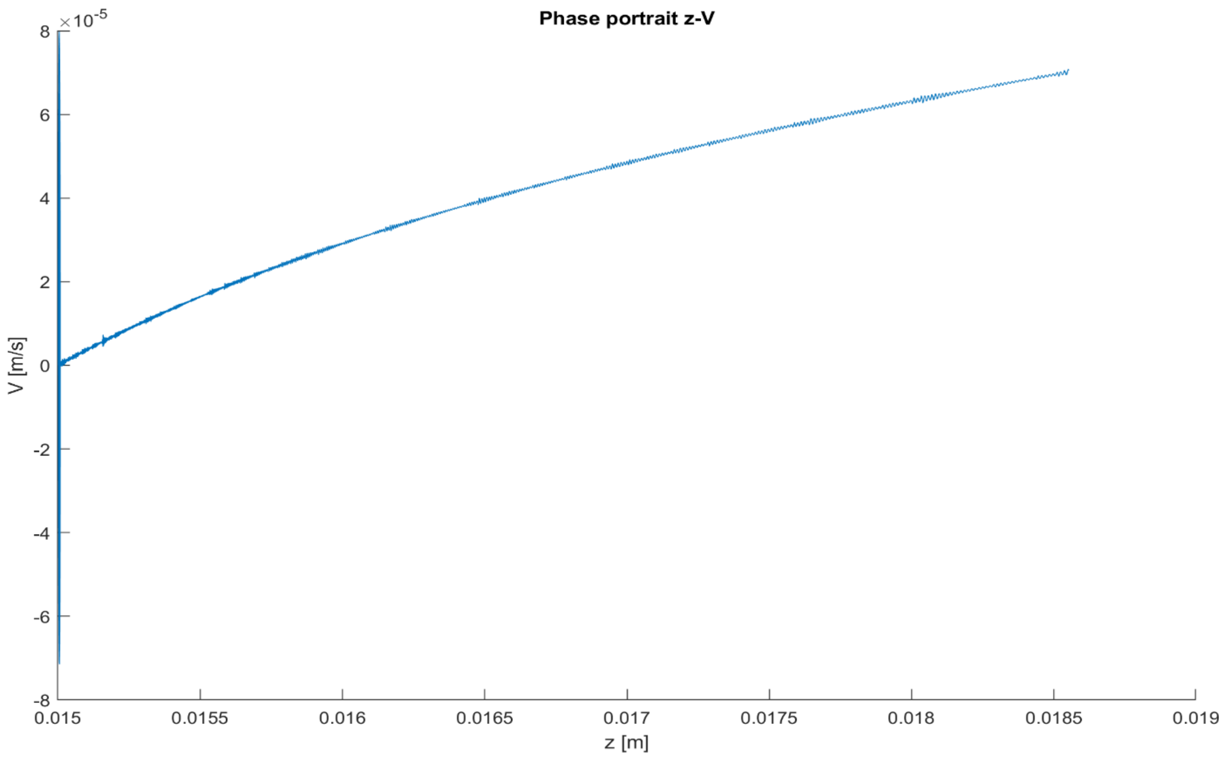

Figure 6.15 Phase portrait of the system for a K_p *value smaller than the left boundary of the stability region*

Oppositely, if one focuses on the system response for a K_p value exactly at the right stability threshold ($K_p = 23804$) represented in Fig. 6.16 and 6.17, and a little larger than the right stability boundary ($K_p = 24200$) represented in Fig. 6.18 and Fig. 6.19.

In this way, the creation of the Hopf bifurcation is captured in the system response. As explained in chapter 2.4, the idea behind a Hopf bifurcation, is the change of stability pattern of the system. In this case, fixing the K_d parameter and varying the value of the K_p, a critical value K_{p_0} is found, for which the stability of the system is changed from a point stability to a limit cycle. This is captured by the nonlinear simulation. Nevertheless, the linearized system cannot capture this new stability level and it translates into an unstable system response. Along these lines, for the nonlinear solution, the fixed point becomes unstable and a spiral trajectory is drawn, moving away from the point to a new stable level in the shape of an orbit. In this manner, the fact that the fixed point derived in eqs. 6.4 – 6.6 loses its stability makes by definition the linearized system around this point unstable. This becomes very obvious in the representation of the nonlinear and the linearized solution for each state variable in Fig. 6.18, where while the nonlinear solutions in black stabilize at a certain orbit the linearized solutions in blue grow exponentially to $\pm\infty$.

Keep in mind, that this new stability level is not captured in the currently defined eigenvalue problem, meaning that after K_p values cross the stability boundary not all eigenvalues have a negative real part. In this case, the pair of complex conjugate eigenvalues have positive real part. This is explained by the fact that these eigenvalues are computed for the linearized system around the fixed point, since, as aforementioned, the nonlinear system does not have eigenvalues. For this reason, once the fixed point becomes unstable the eigenvalues also capture instability.

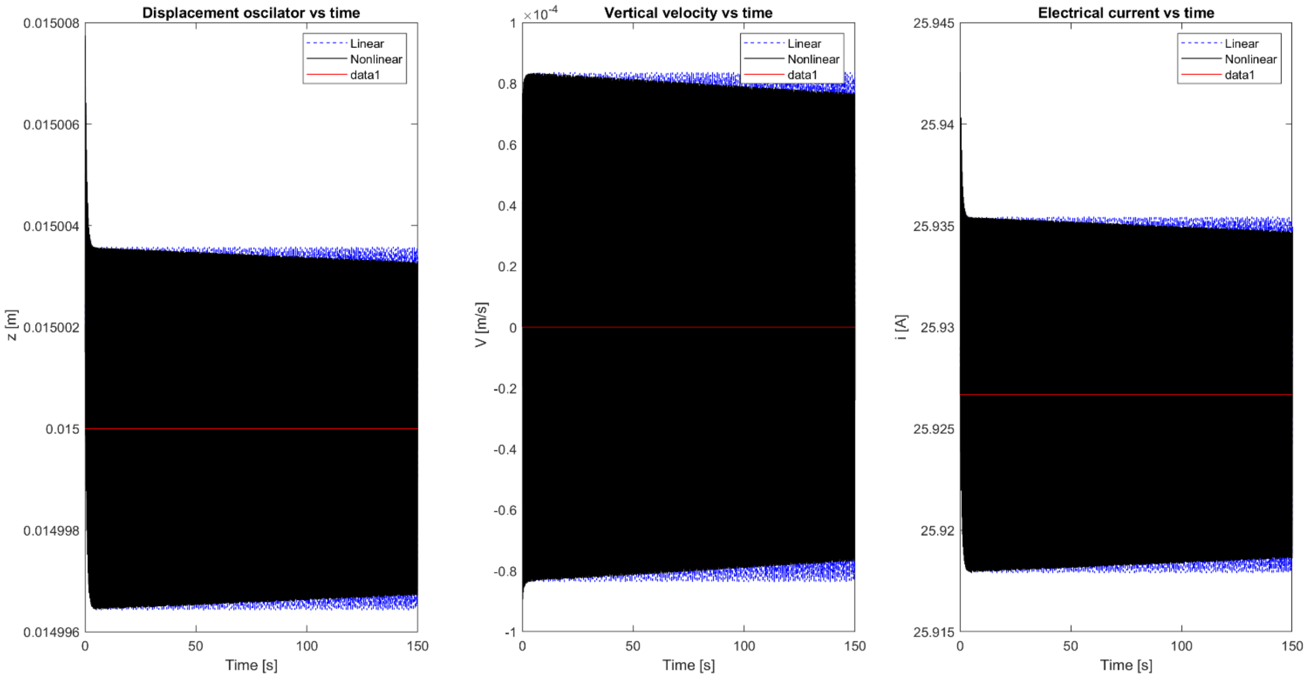

Figure 6.16 Nonlinear and linearized solutions of the system against time for a K_p value exactly at the right boundary of the stability region

From this figure, it can be seen that the system is marginally stable, present a limit cycle around the design equilibrium point with a certain amplitude. The linearized solution describes a center stability pattern around the fixed point at a fixed amplitude, following the real parts of the complex conjugate pair of eigenvalues tending through negative values to zero derived from the linearized system. Such a limit cycle can be then presented in the phase portrait plane (Fig. 6.17).

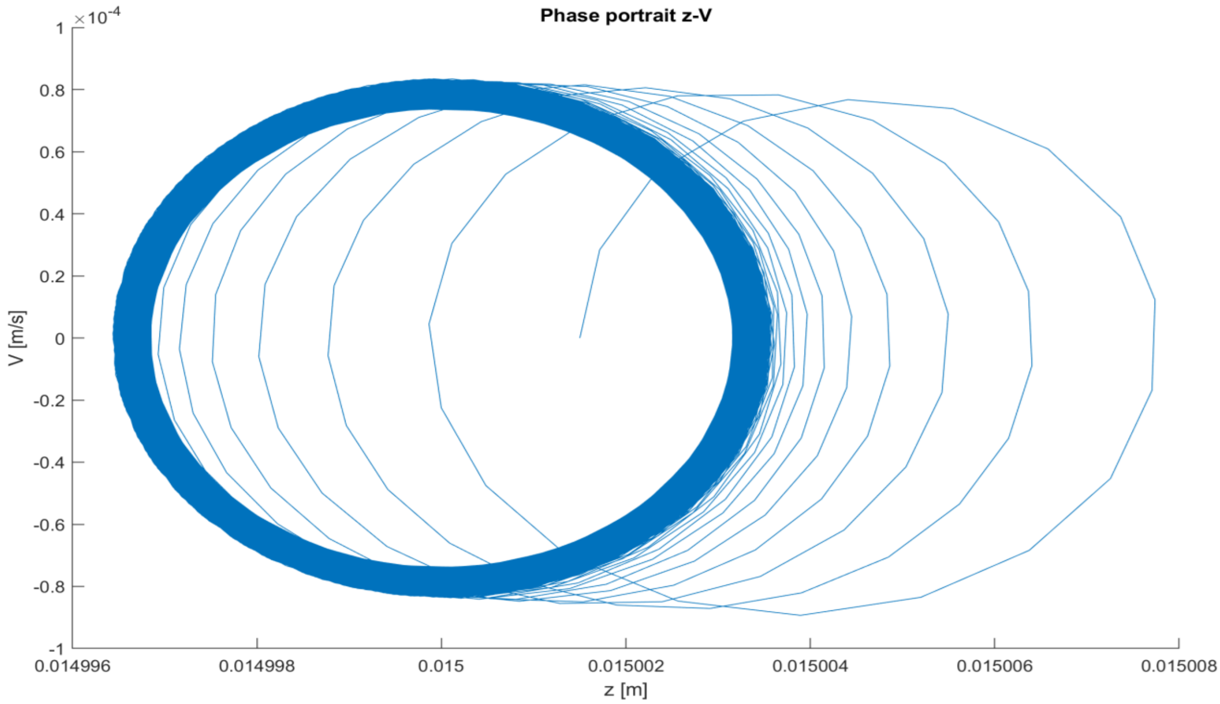

Figure 6.17 Phase portrait of the system for a K_p value exactly at the right boundary of the stability region

Once the input combination of gain parameters is defined crossing the right stability boundary, the fixed point becomes unstable, the linearized solution for each of the state variables is no longer stable, whilst the nonlinear system solution stabilizes at a new stability level, shaping an orbit around the unstable fixed point (Fig. 6.18 and 6.19).

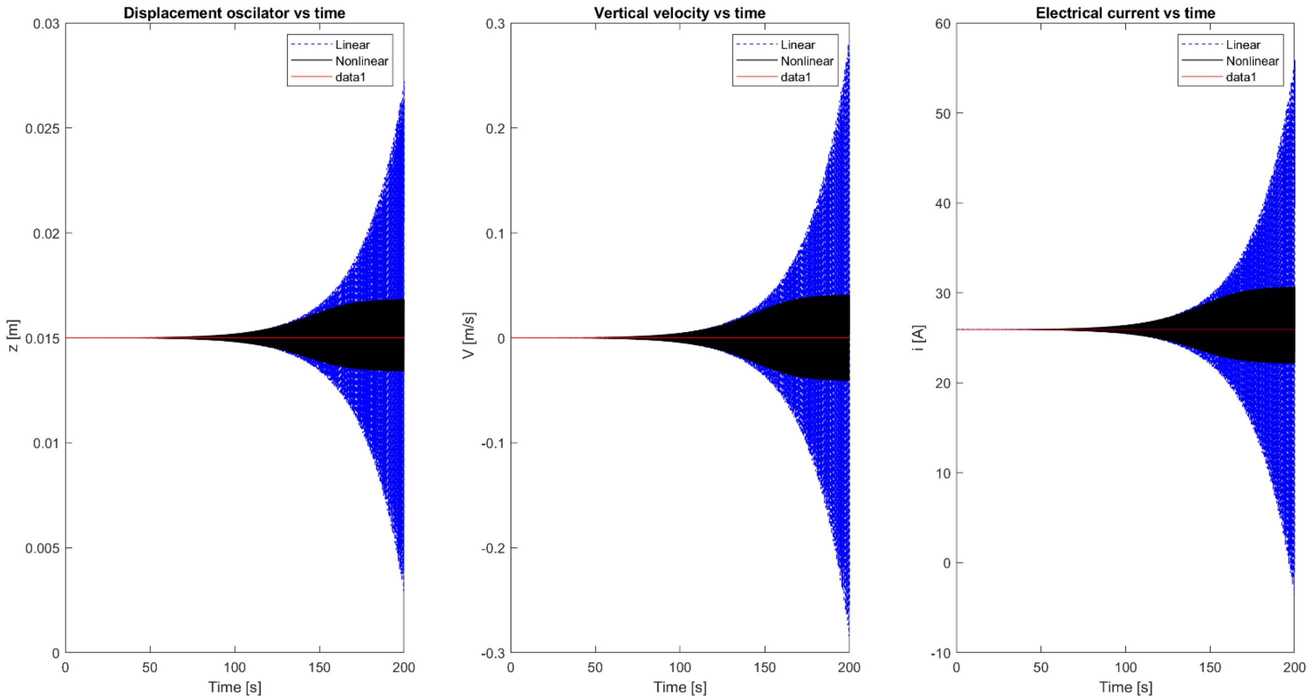

Figure 6.18 Nonlinear and linearized solutions of the system against time for a K_p value after the right boundary of the stability region

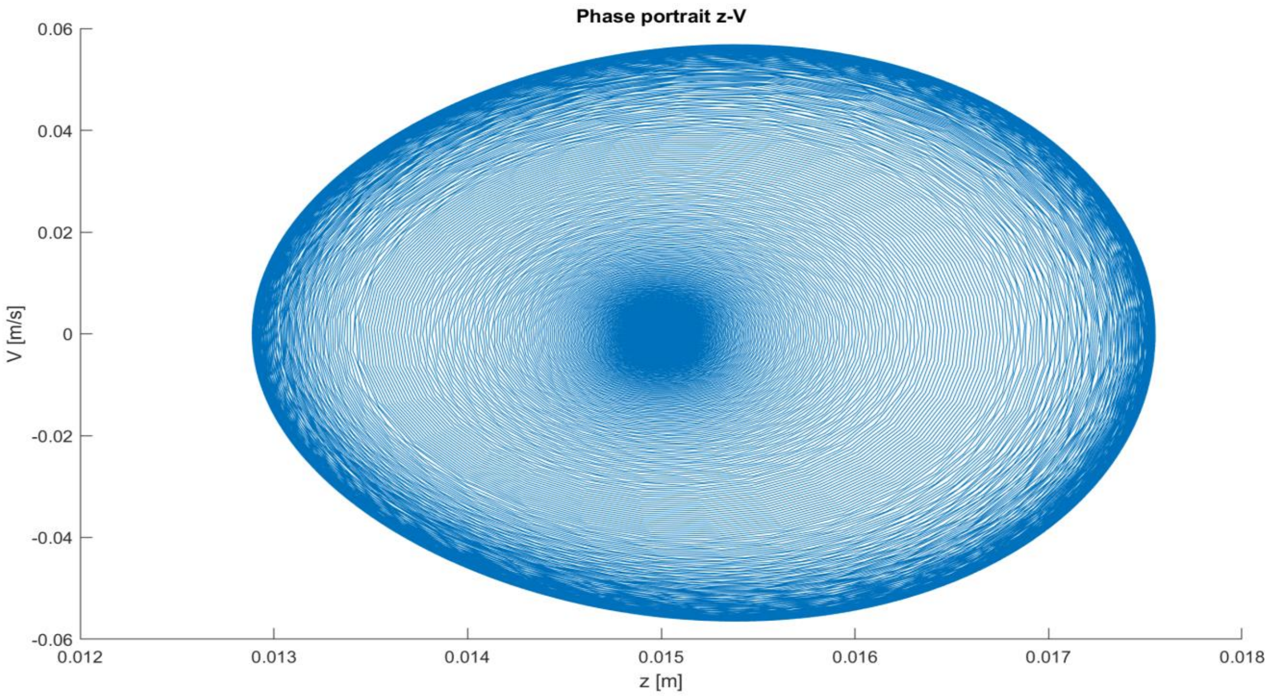

Figure 6.19 Phase portrait of the system for a K_p value after the right boundary of the stability region

6.2. SYSTEM RESPONSE STUDY BASED ON INITIAL CONDITIONS

Considering the second analysis type, the idea is to produce a significant amount of nonlinear simulations with various initial conditions combinations, such that a variety of trajectories can be plotted on the system phase portrait $z-\dot{z}$, providing a representation of the extend up to which the system can stabilize the levitation system. With these results, one can prove that the system is stable for the variable tolerances defined for the real design case with a fixed control gain parameter combination.

For the sake of understanding, a significantly meaningful study case can consist on studying the system response in time for four initial conditions combinations, one for each of the four behavioural regions presented in Fig. 4.3, which were derived without any type of control. In this manner, four cases are described in Tab. 6.2. All cases share the same electrical current, defined as the design equilibrium point value x_{5_s}. Whereas the initial vehicle position and velocity is different for each case, following Fig. 4.3.

Table 6.2 Summary of the study cases presented in this section

Initial conditions study cases

Case Nº	Region Nº in Fig. 4.3	x_1	x_2
Case 1	Region 1	$2\delta_0$	0
Case 2	Region 2	$\delta_0(1+1e-2)$	0.03
Case 3	Region 3	$\delta_0(1+1e-2)$	-0.03
Case 4	Region 4	$\delta_0(1-2e-2)$	0

These results are presented below (Fig. 6.20 – 6.26). For this analysis, the control gain parameters have been fixed to $K_p=20000$ and $K_d=28000$. As shown for the first type of analysis, they are defined to be constant in time.

The first results feature the case of having an initial perturbation of the vehicle position of an entire target air gap spacing $0.015m$ from the equilibrium position (Fig. 6.20 and 6.21), corresponding to region 1 of vehicle dynamics behaviour in Fig. 4.3.

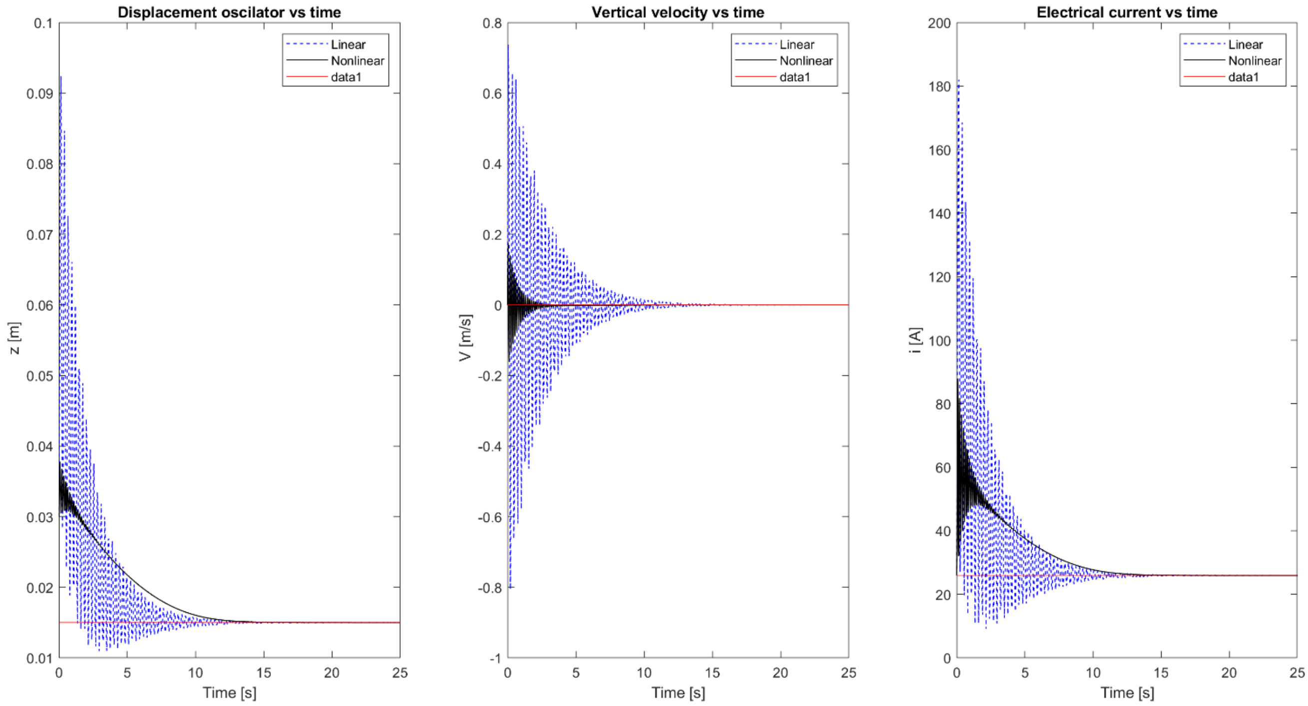

Figure 6.20 Nonlinear and linearized solutions for study case within vehicle dynamics region 1

From this figure, the divergence between the linearized and the nonlinear solution for locations far from the equilibrium point becomes obvious, although it is not very relevant in magnitude and the quality of the stable outcome, it might be used to understand the difference in behaviour between the two.

The behaviour of the three system state variables, the control variable and the electromagnetic force show a stabilization of the system. Going somewhat more in depth, it is very interesting to see how the system tries to react to a rather large perturbation of the vehicles levitation air gap by increasing the electrical current. This is directly related with the definition of the electromagnetic force leading to a trade off between air gap and electrical current to define an electromagnet force that tends to move to a constant equilibrium value. This ultimately translates on an increase on the input voltage required for the system to bring back the vehicle to the desired design air gap.

The representation of the stabilization of the system from a distant initial point to the fixed point, describing a stable spiral trajectory is captured in the phase portrait plane below (Fig. 6.21).

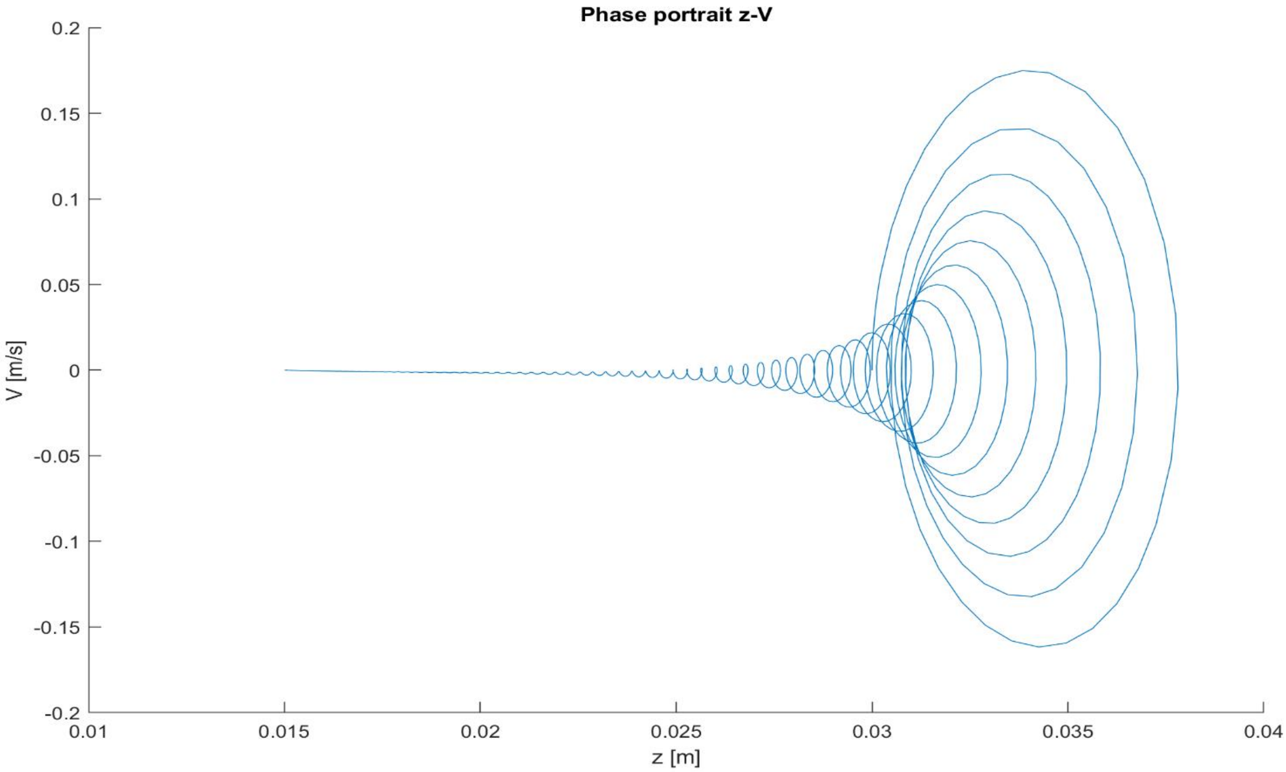

Figure 6.21 Phase portrait of the system for study case within vehicle dynamics region 1

The second results feature the case of having an initial perturbation of the vehicle position of $1\cdot 10^{-2}\,m$ of the equilibrium position and an initial velocity of $0.03\,m/s$ (Fig. 6.22 and 6.23), corresponding to region 2 of vehicle dynamics behaviour in Fig. 4.3.

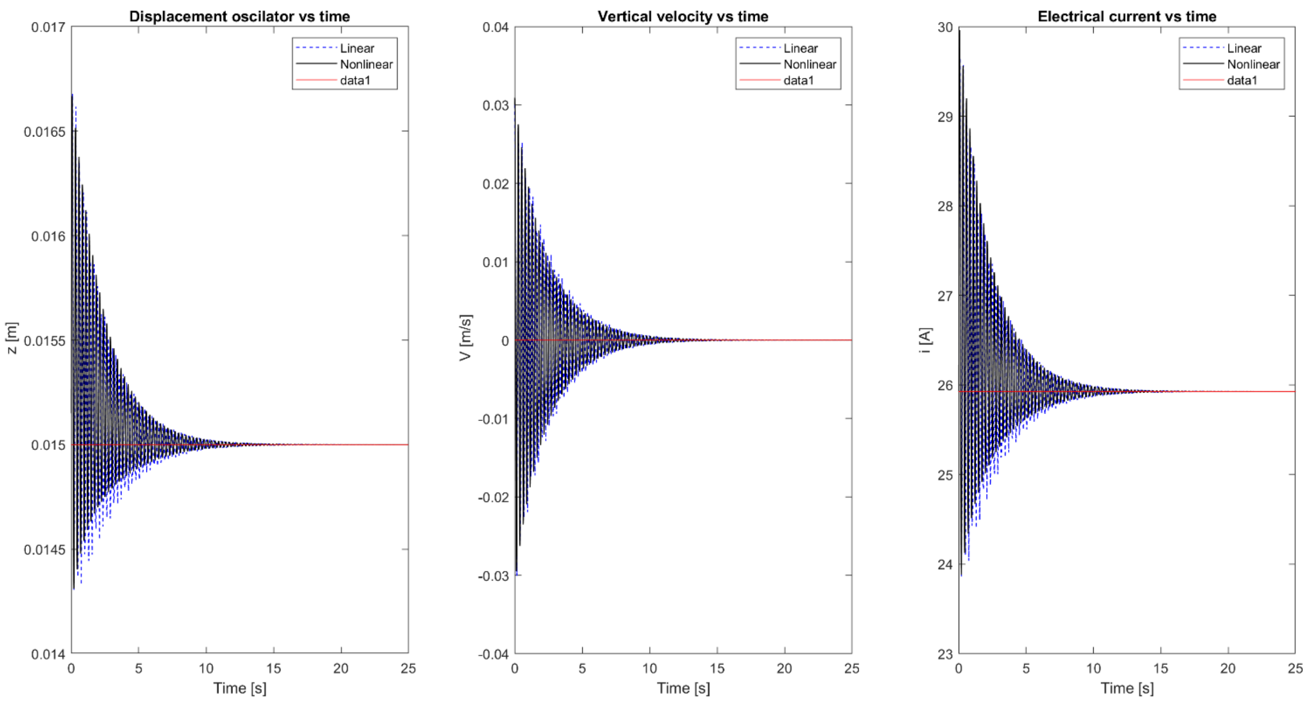

Figure 6.22 Nonlinear and linearized solutions for study case within vehicle dynamics region 2 and 3

In this case, the divergence between the nonlinear and the linearized solution is much smaller since the initial position of the vehicle is much closer to the fixed points. From the plot of the behaviour of the three system state variables, the control variable and the electromagnetic force against time, it becomes clear that the stabilization of the system is much faster in this case than in the previous. The behaviour of each of the represented magnitudes is very similar, implying that the trade off between the variables, aforementioned for study case 1, is less relevant in this case to compensate deviations from the equilibrium set up.

The representation of the stabilization of the system from case 2 initial conditions to the fixed point, describing a stable spiral trajectory is captured in the phase portrait plane below (Fig. 6.23).

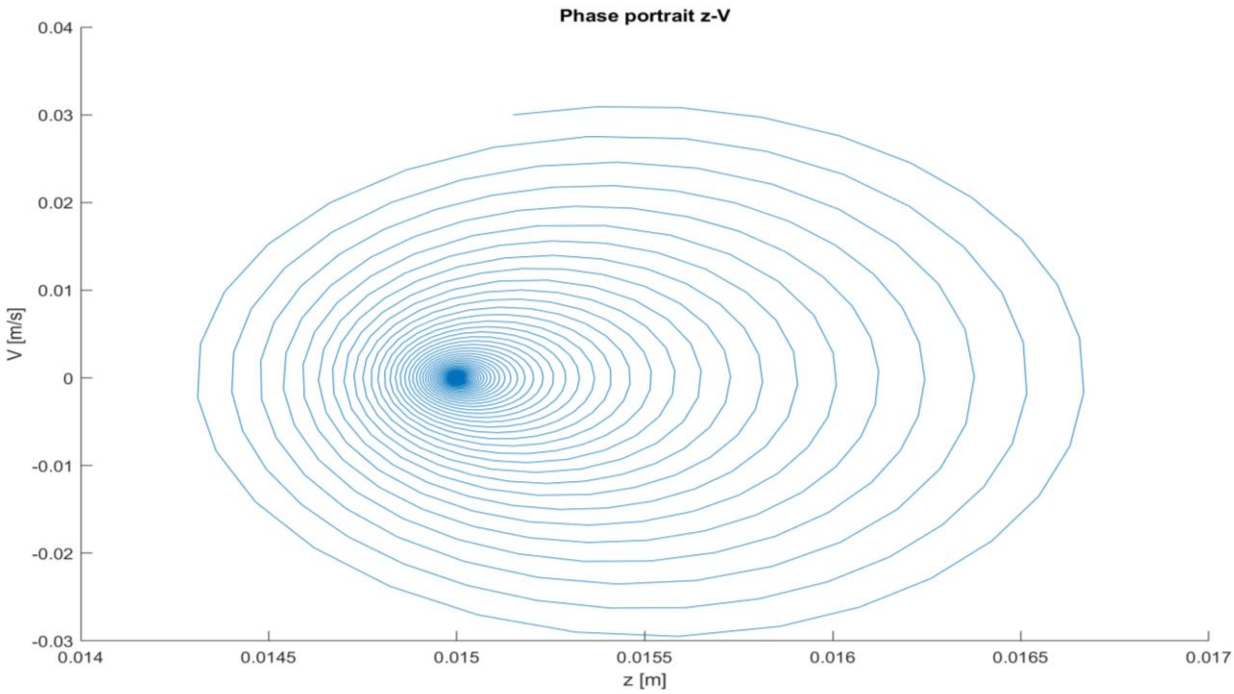

Figure 6.23 Phase portrait of the system for study case within vehicle dynamics region 2

Oppositely to the second set, the third results feature the case of having an initial perturbation of the vehicle position of $1 \cdot 10^{-2}\, m$ of the equilibrium position and an initial velocity of $-0.03 m/s$ (Fig. 6.22 and 6.24), corresponding to region 3 of vehicle dynamics behaviour in Fig. 4.3.

In this case, the plot of the behaviour of the three system state variables, the control variable and the electromagnetic force against time is very similar to the one for presented for the second set. Therefore, the system can be already represented through Fig. 6.22 with respect to time. Then, the representation of the stabilization of the system from case 3 initial conditions to the fixed point, describing a stable spiral trajectory is captured in the phase portrait plane below (Fig. 6.24).

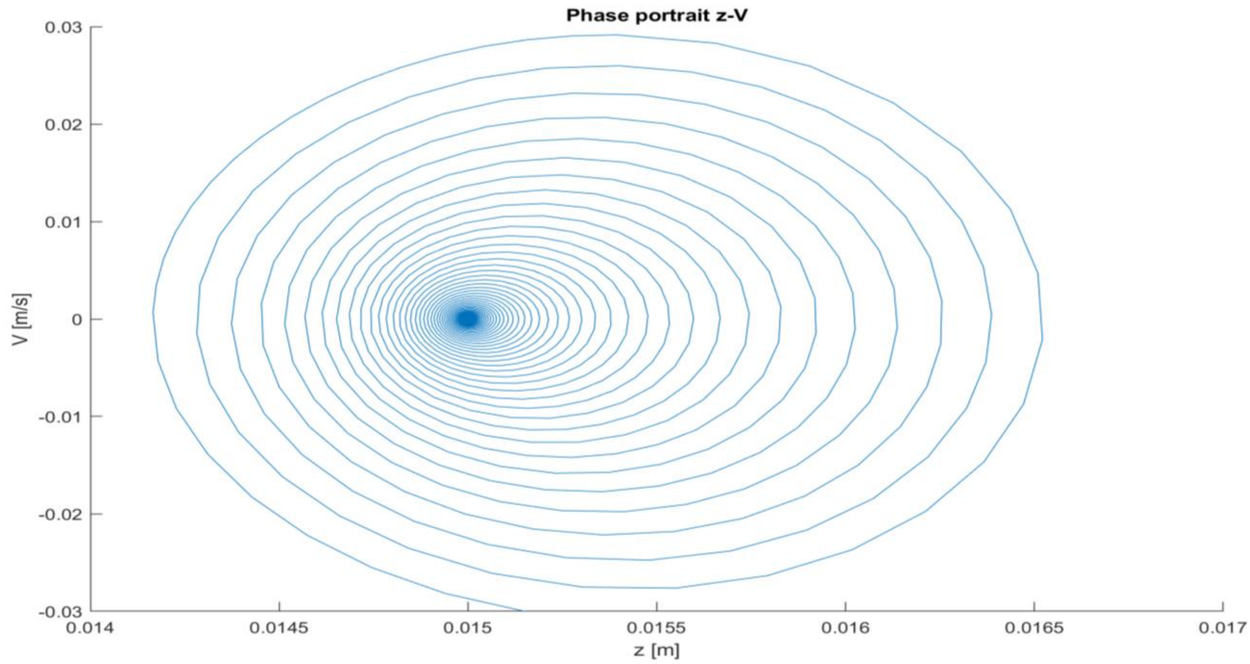

Figure 6.24 Phase portrait of the system for study case within vehicle dynamics region 3

The fourth results feature the case of having an initial perturbation of the vehicle position of $-2\cdot 10^{-2}\,m$ from the equilibrium position (Fig. 6.25 and 6.26), corresponding to region 4 of vehicle dynamics behaviour in Fig. 4.3.

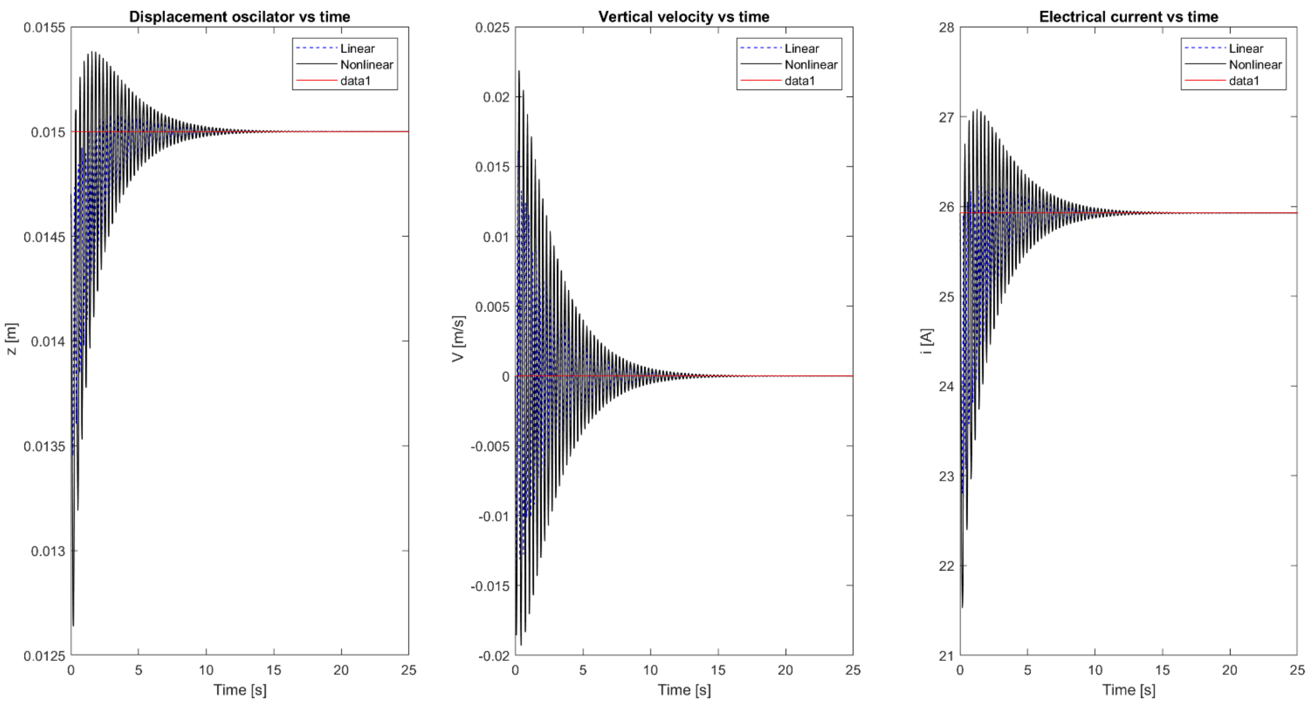

Figure 6.25 Nonlinear and linearized solutions for study case within vehicle dynamics region 4

The behaviour of the three system state variables, the control variable and the electromagnetic force show a stabilization of the system. It is interesting to see how the system tries to react to a negative perturbation of the vehicle levitation air gap, placing it closer to the rail, by decreasing the electrical current, reducing the attractive action on the vehicle and making self wight dominant on the force balance. This is directly related with the definition of the electromagnetic force leading to a trade off between air gap and electrical current to define an electromagnet force that tends to move to a constant equilibrium value.

The representation of the stabilization of the system from case 4 initial conditions to the fixed point, describing a stable spiral trajectory is captured in the phase portrait plane below (Fig. 6.26).

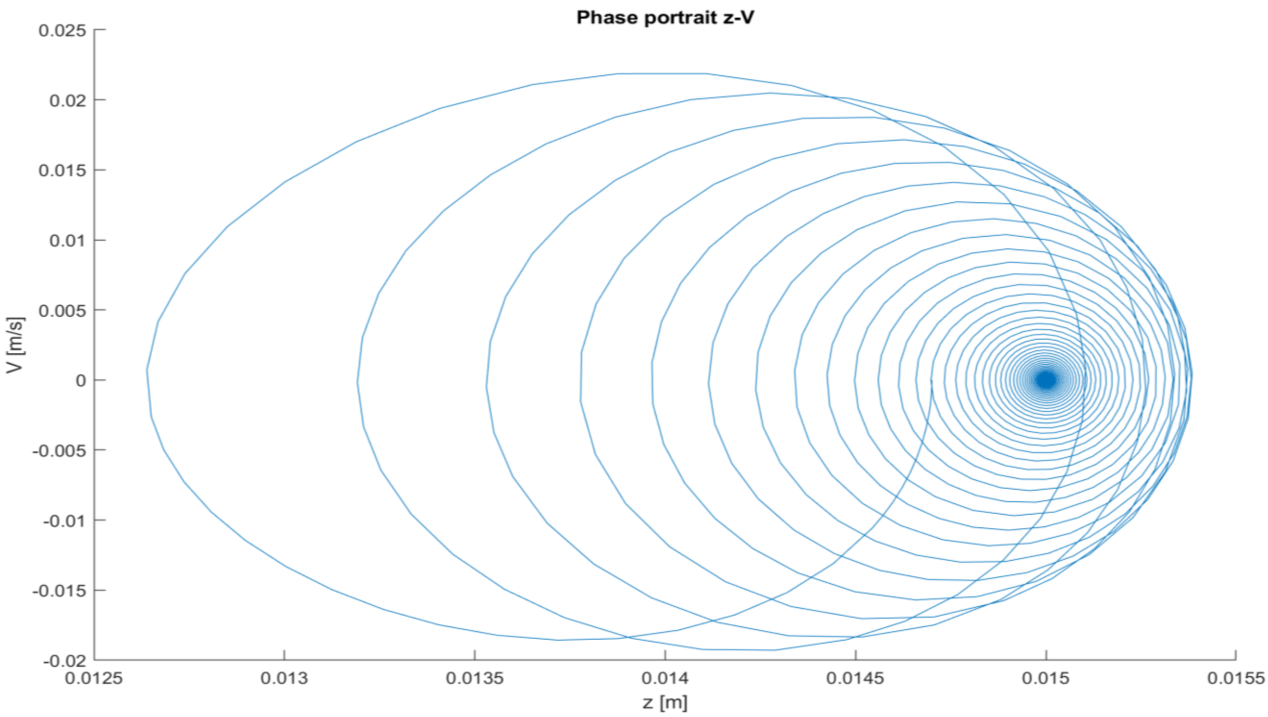

Figure 6.26 Phase portrait of the system for study case within vehicle dynamics region 4

From these results, one can conclude that the system has been stabilized for each of the vehicle dynamics behavioural region studied previously for an open-loop system without control. Nevertheless, further study is needed to understand the extend of these stabilization and prove that the system guaranties a stabilization that covers the main state variables tolerances. A representative way of showcasing such results is the plotting of the phase portrait of the system for different initial conditions leading to different trajectories (Fig. 6.27 and 6.28).

Throughout the representation in the phase portrait plane $z-\dot{z}$ of such a kind of studies, it is found the existence of two stability patterns. Not only the systems presents a local point stability at the previously derived fixed point, but also an outer unstable limit cycle exists (Fig. 6.27 and 6.28). This outer unstable limit cycle is obtained by finding the limit initial conditions in the phase plane space for which the system response does no longer converge to the fixed point. Consequently, a stabilization region on the phase portrait plane is defined, meaning that the system is stable for any initial conditions combination of $(z_0, \dot{z}_0)$ within the space surrounded by the outer unstable orbit and an initial electrical current fixed to the design equilibrium value i_0.

Moreover, the dimensions and the shape of the outer unstable orbit are dependent on the control gain parameters choice (K_p, K_d). The parameter combinations must be defined within the $K_p - K_d$ stable space are used. As a general rule of thumb, the larger the values of K_p and K_d, the larger the stability space. In this report, two simple examples (Fig. 6.27 and 6.28) are presented for at a local scale and for K_p and K_d values at close range to the ones used in other case studies.

The first example is produced for $K_p = 20000$ and $K_d = 28000$ (Fig. 6.27). A total of six trajectories are represented in the plot, five of them stable, from which there is one trajectory for each vehicle dynamics behavioural class from Fig. 4.3 and one starting at the equilibrium point, and one of them unstable that allows to figure out how the unstable behaviour is drawn. The plot is only represented partly, focusing on a local range around the fixed point, but it is more extensive as z increases. The unstable outer limit cycle is represented by a red line. In this case, since it was obtained as a function, the whole cycle was not possible to be represented in one line, but two lines were defined. One represents the top half and the other one the bottom half of the cycle. All the initial conditions are listed in the legend and represented by a orange circle in Fig. 6.27 and 6.28.

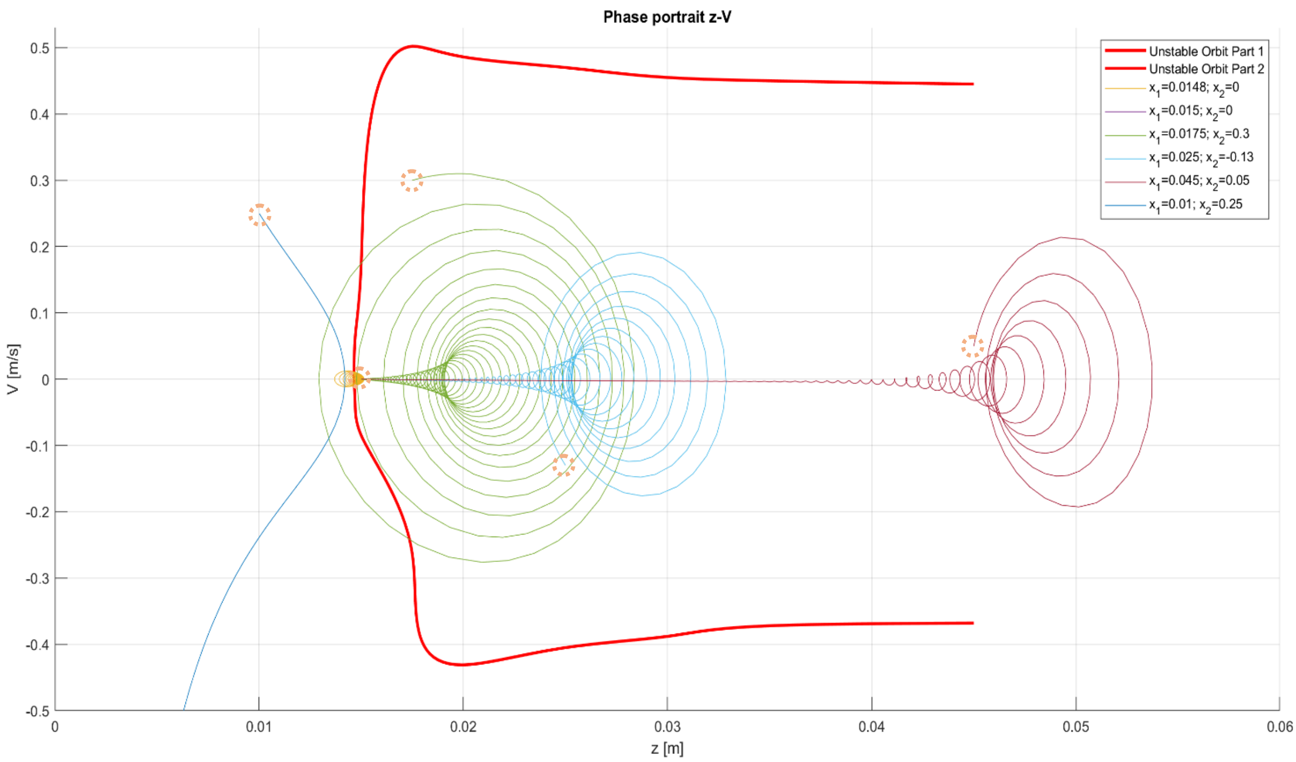

Figure 6.27 Phase portrait of the system for $K_p = 20000$ *and* $K_d = 28000$ *with all the initial conditions listed in the legend and represented by a orange circle*

From this figure, One can see that all trajectories starting inside the outer red unstable orbit converge to the fixed point, i.e. the system is stable. Whilst, the trajectory for initial conditions given outside it do not succeed to converge around the equilibrium point and ends up diverging and moving towards the track outside the range presented in the graph. In this case, the stability region in the phase plane is very small to the left of the equilibrium point. Whereas the range of the vehicle vertical position rate is quite large.

To prove the effect that the tunning of K_p and K_d values on the shape of this orbit, a second example is presented with larger control gain values that increases the stability for vehicle positions closer to the track, but, as a trade off, the range of the vehicle vertical position rate is reduced. This case study is produced for $K_p = 60000$ and $K_d = 100000$ (Fig. 6.28). As before, a total of six trajectories are represented in the plot, five of them stable, from which there is one trajectory for each vehicle dynamics behavioural class from Fig. 4.3 and one starting at the equilibrium point, and one of them unstable that allows to figure out how the unstable behaviour is drown.

From Fig. 6.28, it becomes obvious that this second $K_p - K_d$ combination results in a wider stability region. This is specially useful to the left of the equilibrium point, since the stability space, now, is much larger. This translates in the fact that, for such a control parameter combination, the system is stable for a larger amounts of scenarios in which the levitation air gap is smaller than the target value. Considering that the stability region in the parametric space (Fig. 6.6) has no upper limit, it seems clear that larger gain parameter values with a similar ratio between each other provide a larger limit cycle.

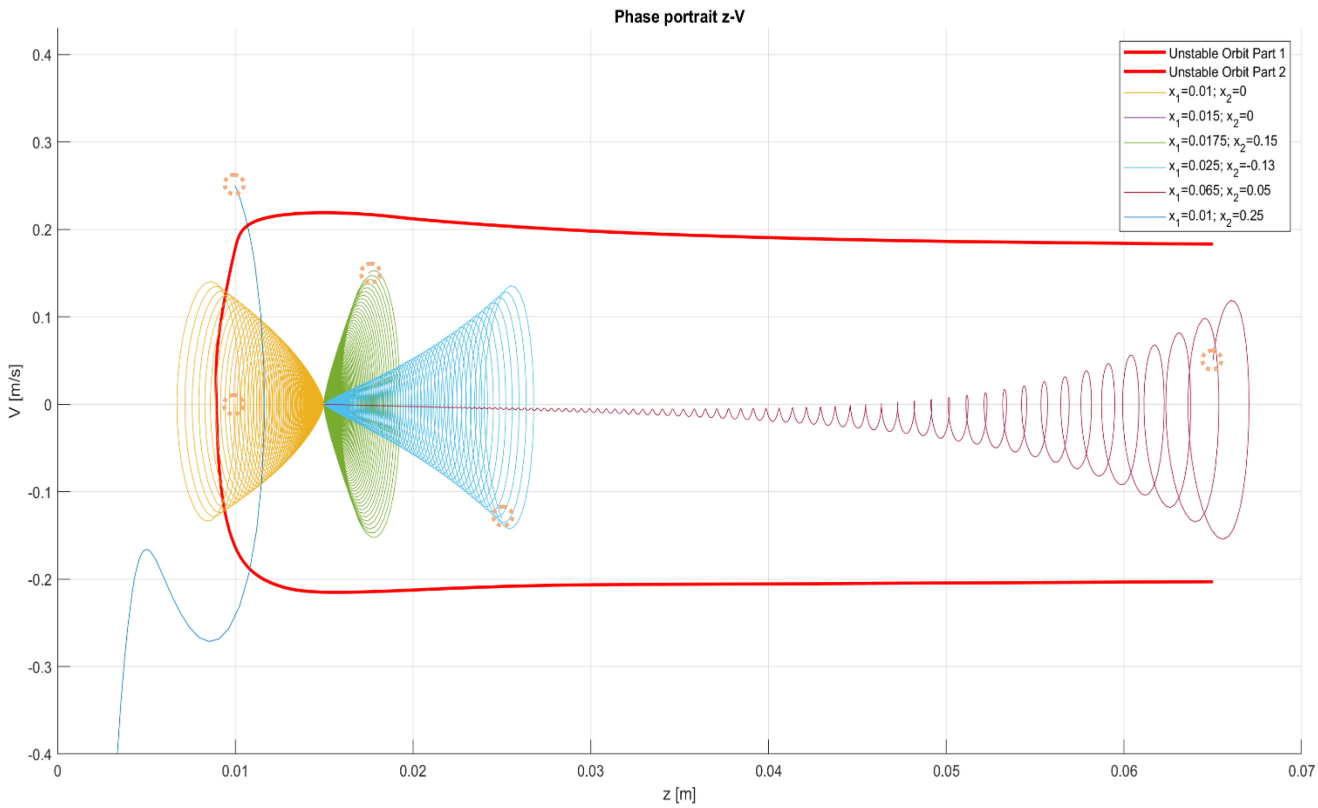

Figure 6.28 Phase portrait of the system for $K_p = 60000$ *and* $K_d = 100000$ *with all the initial conditions listed in the legend and represented by a orange circle*

To sum up, this section shows that the stabilization of the system using a PD-control on the voltage is possible and a large stable region is obtained on the parametric space $K_p - K_d$, allowing the definition of several different behaviours of the system for a large range of control gain parameters combinations.

Besides, the trade off in the effect that K_p and K_d generate in the system has been shown, aiming at understanding better which is the suitable tunning of the control gains depending on the system demands and constraint. Along these lines, the existence of a Hopf bifurcation in the system linked to the choice of control parameters has been investigated. Finally, the region of stabilization generated by the control has been explained and contrasted for different gains.

6.3. STUDY APPEARANCE OF A POSSIBLE NUMERICAL ARTIFACT

To conclude this section of the report, a phenomenon about the stability of the system around the fixed point around is addressed. Throughout the study of the EMS closed-loop model with a PD-control, it has been shown that the nature of the stability of the equilibrium point derived by means of the linearized system eigenvalue problem indicates that a point stability is expected at the design equilibrium point. Nevertheless, the nonlinear solution differs a little at a very local scale around the fixed points.

If one zooms in within the phase portrait plane around the fixed point, the appearance of a small stable orbit around the equilibrium point becomes evident (Fig. 6.29). The order of magnitude of the this orbit with respect to z is about $r_z = 10^{-8}$ and with respect to $\dot{z}$ is about $r_V = 10^{-7}$, which is quite insignificant for the model outcome and it has no relevant effect on the system response. Since this only appears in the nonlinear simulations and the radius of the orbit is sensitive to the ODE solver used in the programming language, one may argue that this is solely due to numerical errors.

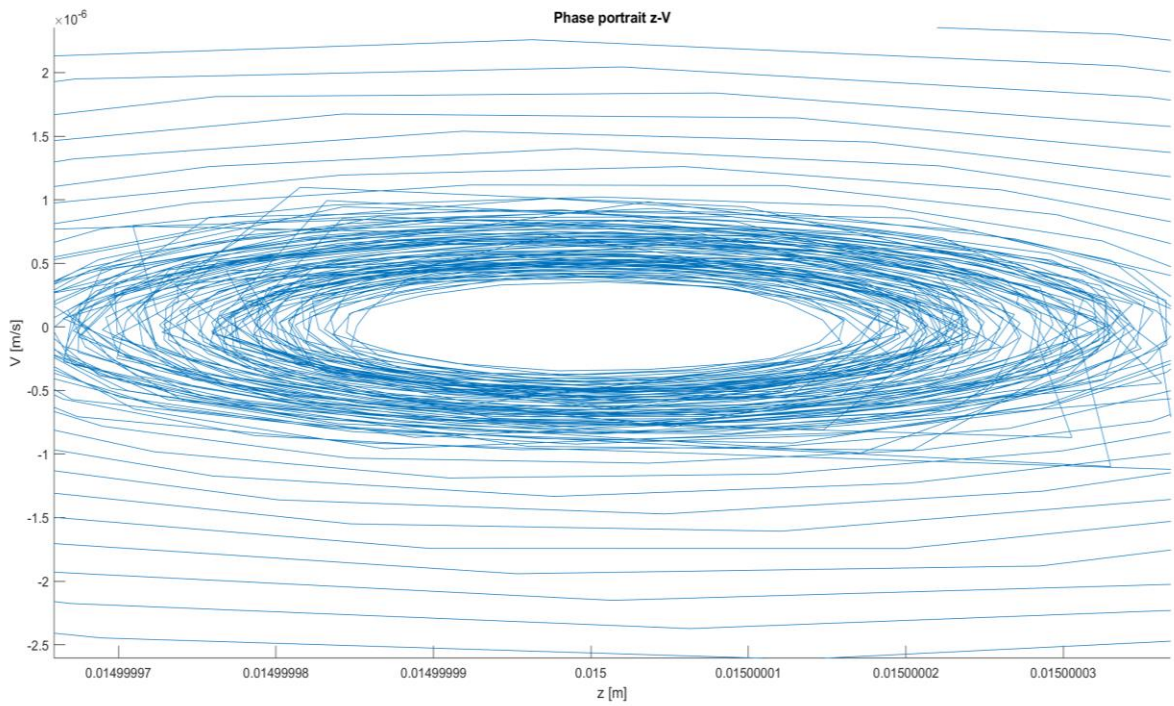

Figure 6.29 Small stable orbit around the fixed point in the phase portrait od the system

It is important to note that the system does not consider any type of damping on the interface between the track, i.e. the support point, and the vehicle through the levitation electromagnetic field. This is unrealistic, so a certain amount of artificial damping can be added to the system and, in case this yields a significant reduction of this orbit or directly vanishes, it proves that the nature of such an orbit is associated with numerical errors.

Following this approach, one can see a progressive regression of the radius of the orbit already for the application of a 0.5%. For values of artificial damping around the 10%, the radius is already moving to an order of magnitude of $r_z = 10^{-9}$. However, it does not vanish for realistic damping values. This investigation is inconclusive on whether the small limit cycles are of numerical or physical origin. In case they are physically admissible, more advanced control definitions can be applied, like linearized feedback techniques, time dependent control gain definitions or even gain scheduling for any variable of interest.

As a side node, it is important to point out that since a successful stabilization of the system has been reached already with a PD-control scheme, no I-component will be added for this problem description avoiding adding more complexity to the system. This decision is taken considering the fact that the integral component does not change the stability of the system but just smoothens the system response [34].

7

ADDITION OF A FORCE ON/OFF SWITCH IN THE EMS SYSTEM WITH PD-CONTROL

The previous section has proven a satisfactory stabilization of the system around the equilibrium point and has featured the effect of the controller and the tunning of the contrail gains on the system response. However, the implementation of such a control scheme has led to a side effect that needs to be addressed and calibrated for a correct definition of the overall EMS levitation system.

Throughout several different study cases presented above, it has been observed that for unstable system set ups, or even close to unstable but still within the stabile region, the system tends to shift the electrical current state variable solution to negative values. As explained in chapter 5, for the choice of feasible fixed points of the systems, in this project, negative electrical current variables are associated with a change of the polarization of the electromagnets in an attempt of the system to stabilize the system and compensate the perturbations on the vehicle positions through the generation of repulsive electromagnetic forces.

This is incompatible with the system definition provided in chapter 3, since this technological scheme is thought to work only in attraction. In this manner, the definition of the electromagnetic force defined for this project does not consider the possibility of becoming repulsive. This has been guaranteed by the definition of the electromagnetic force as a relation between the squared electrical current over the squared levitation air gap as shown in eq. 3.10. Consequently, the shift of electrical current to negative values does not translate to the generation of repulsive electromagnetic forces, but contributes to a build up of the electromagnetic force which grows in the opposite sense, i.e. attractive, contributing to the contrary effect as the one the system intends.

This behaviour imposed by the control strategy is undesired, because in the response of the system for rather small air gaps, lower than the design target one, the appearance of negative electrical current trying to induce a change on the direction of the electromagnetic force ends up leading to larger attractive electromagnetic force that pulls the system towards the track, making it unstable. Hence, the representations of the stabilized region provided in chapter 6 (Fig, 6.27 and 6.28) can be improved by applying a complementary control strategy.

This problem can be solved in several different ways. One, that entails a significant addition of complexity to the system, is the definition of time dependent control gain parameters and the formulation of an optimization tuning scheme, which allows to define for each time step an optimal combination of K_p and K_d that ensures stability of the system and always positive electrical current values. Nevertheless, due to time constraints and following the aforementioned goal of keeping the definition of the control fundamental, generic and simple, this option is not applied.

In this case, the solution that is applied is simpler. The main idea is that every time a negative value of electrical current is computed a change of electromagnetic force is intended to be induced. Thereby, it has been thought that the application of an on/off switch on the electromagnetic force depending on the values of the electrical current could be applied. In this way the main condition of operating the system only using attractive electromagnetic forces is met and, at the same time, the appearance of unfeasible negative electrical current values is mitigated.

An on/off switch on the electromagnetic force can be implemented by defining an alternative variable, the electrical current prediction i_p which monitor the electrical current and predicts the next step electrical current value. In this manner, the actual electrical current x_5 can be defined as

$$x_5 = i_p \cdot \; H(i_p) \tag{7.1}$$

where $H(i_p)$ is the Heaviside function on the predicted electrical current.

This allows to differentiate two system responses, as for $x_5 \leq 0$ the electrical current is defined to be zero $x_5 = 0$, whereas for $x_5 > 0$ both variables are equal $x_5 = i_p$. Hence, for the first case, the electromagnetic force is switch off and stops playing a role in the force balance of the vehicle, allowing the self wight to take over and be the unique non-zero force acting on it. This is then maintained until the moment in which the predicted electrical current crosses the zero axis again and the electromagnetic force is switched on again.

In this manner, the vector of system state variables is defined as $\{x_1 \quad x_2 \quad x_{5_p}\} = \{z \quad \dot{z} \quad i_p\}$ and the system can be defined as follows

$$\begin{cases} \dot{x}_1 = x_2 \\ \begin{cases} \dot{x}_2 = g - \text{sgn}(x_1)\dfrac{C}{m}\dfrac{x_{5_p}^{\ 2}}{x_1^{\ 2}} & , if \ x_{5_p} > 0 \\ \dot{x}_2 = g & , if \ x_{5_p} \leq 0 \end{cases} \\ \dot{x}_{5_p} = \dfrac{x_1}{2C}[K_p(x_1 - \delta_0) + K_d x_2 + u_0 - x_{5_p} R - 2C\dfrac{x_{5_p}}{x_1^{\ 2}} x_2] \end{cases} \tag{7.2}$$

The implementation of this control alternative does not change the system nature, meaning that the fixed point and the eigenvalue problem are the same as the ones previously derive in chapter 6 for the PD-control.

The effect of this measure is represented below, initially featuring the system response without the electromagnetic force switch control (Fig. 7.1) and, later, showcasing the system response for the same system set up with the electromagnetic force switch control (Fig. 7.2). These results are produced for a combination of $K_p = 20000$ and $K_d = 28000$, and initial conditions $x_{1_s} = 0.0175\,m$ and $x_{2_s} = -0.43\,m/s$. Such an upwards initial vertical vehicle position rate is the reason of negative electrical current values appearing in this case.

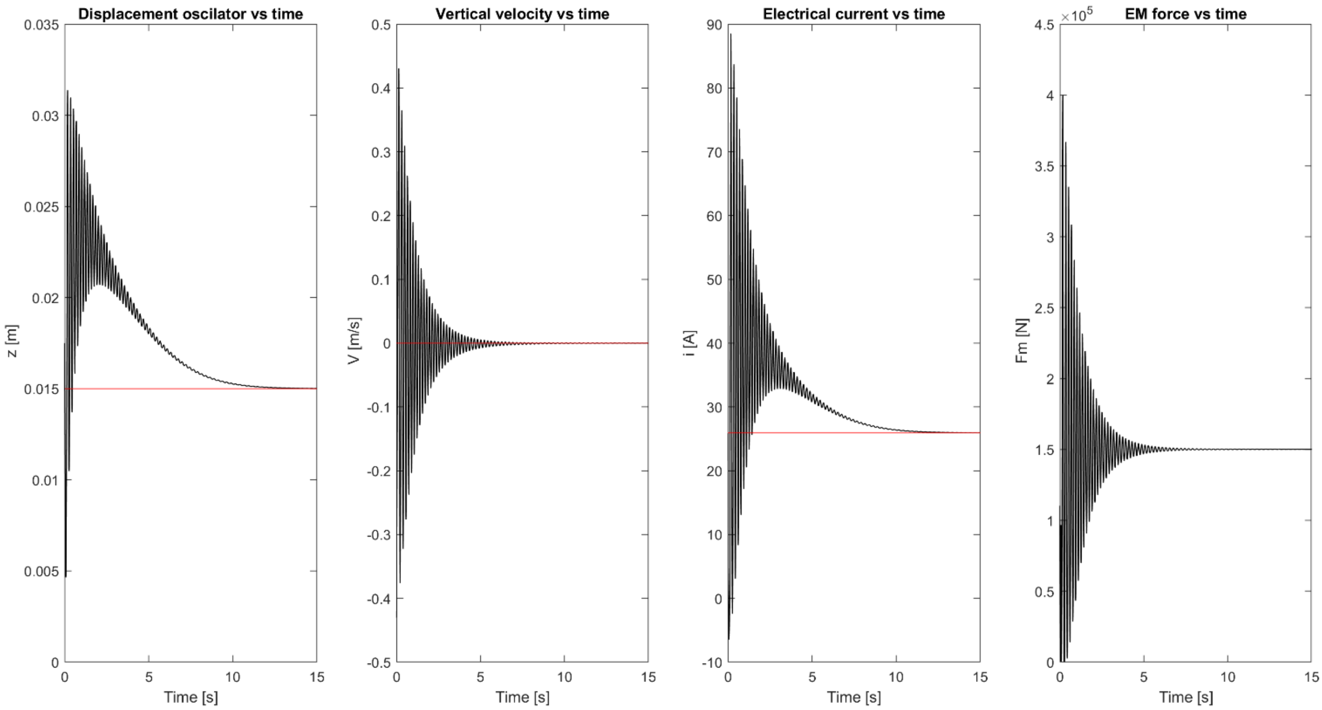

Figure 7.1 Nonlinear solution of the closed-loop EMS levitation system with PD-Control

From this plot it becomes obvious that the system tries to compensate a high upwards velocity by using negative electrical current values in the initial time steps up to $-10\,A$, whilst the electromagnetic force is strictly positive defined. This contrasts with the figure below (Fig. 7.2), for which the current becomes strictly positive defined, using the electromagnetic force on/off switch. The electromagnetic force defined in the exact same way as before and the rest of state variables present the same behaviour.

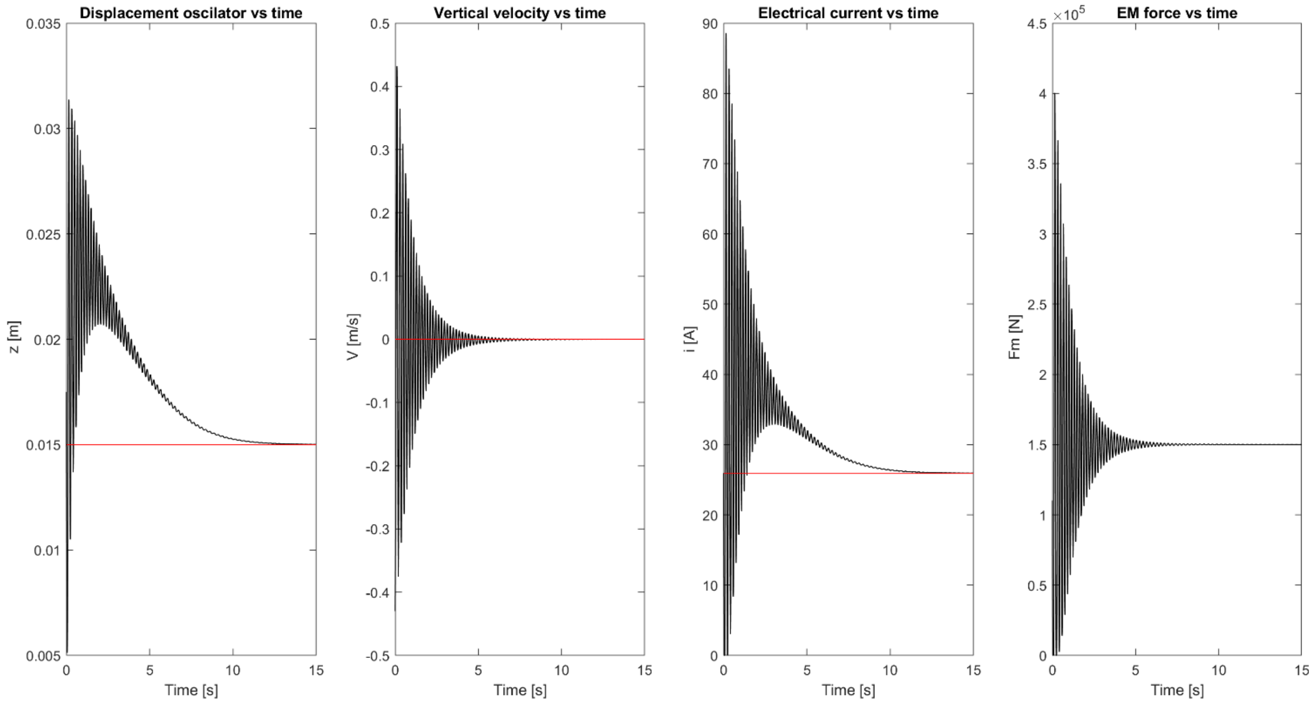

Figure 7.2 Nonlinear solution of the closed-loop EMS levitation system with PD-Control and force on/off switch

Following the explanations and results above, it becomes obvious that the representation of the stabilized regions previously derived (Fig. 6.27 and 6.28) need to be corrected by means of the implementation of the on/off switch in the electromagnetic force. Along these lines, a new representation of the stabilization region is produced using the same system set up as for Fig. 6.28, for $K_p = 60000$ and $K_d = 100000$ (Fig. 7.3).

As before, a total of six trajectories are represented in the plot, five of them stable, from which there is one trajectory for each vehicle dynamics behavioural class from Fig. 4.3 and one starting at the equilibrium point, and one of them unstable that allows to figure out how the unstable behaviour is drown. Likewise, the plot is only represented partly, focusing on a local range around the fixed point, but it is more extensive as z increases.

From Fig. 7.3, it becomes obvious that the system stabilization region size is increased significantly once the on/off switch on the electromagnetic force is applied, compensating for the correction of the electrical current. At this point, the stabilization region obtained through this double control scheme seems large enough to cover the main tolerances in levitation air gap and rate of variation of the air gap for projected in the real project. Therefore, one can conclude that the definition of such a control and the implementation of it in the EMS levitation system is satisfactory.

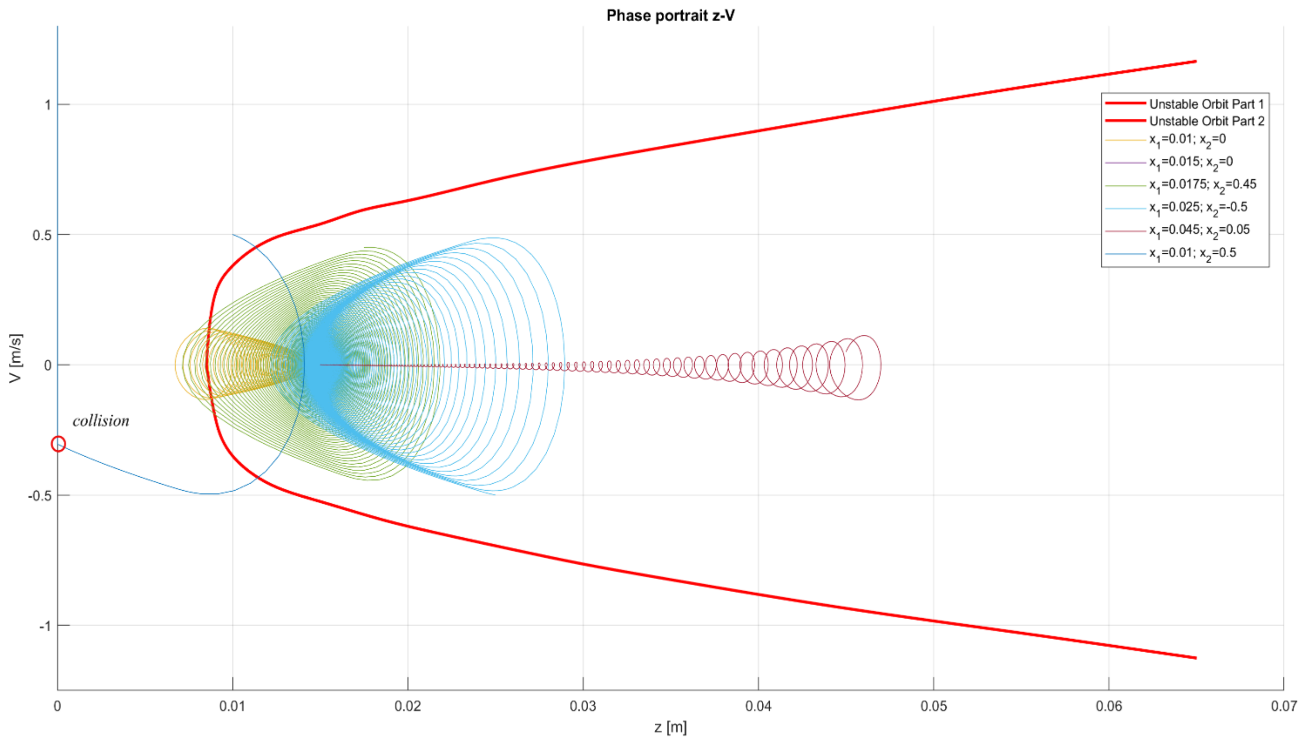

Figure 7.3 Phase portrait of the system for $K_p = 60000$ *and* $K_d = 100000$

8

STUDY OF THE VEHICLE – TRACK INTERACTION

The previous sections have served to define a control system based on a PD-control scheme alongside an on/off switch on the electromagnetic force that has proven to be successful for the stabilization of the inherently unstable EMS levitation system. Once the successful implementation has been confirmed, its performance in the overall system considering the deflection of the beam should be studied.

Thus, the main objective featured in this section is the study of the vehicle-track coupled system and of the performance of the previously described control system in such a set up. Along these lines, the assumption used in the derivation of the models presented in chapter 4, 5 and 6 on considering the track equivalent beam to be infinitely stiff (eq. 4.1, 5.1 and 6.1) does no longer apply to this system.

This study is based on the model presented in Fig. 3.7, which accounts for the modelling of the first mode of the equivalent beam…

Hence, the vector of the system state variables is written as $\left\{x_1 \quad x_2 \quad x_3 \quad x_4 \quad x_{5_p}\right\} = \left\{z \quad \dot{z} \quad w \quad \dot{w} \quad i_p\right\}$ and the system of equations of motion can be defined as

$$\begin{cases} \dot{x}_1 = x_2 \\ \begin{cases} \dot{x}_2 = g - \mathrm{sgn}(x_1 - x_3)\dfrac{C}{m}\dfrac{{x_{5_p}}^2}{(x_1 - x_3)^2}, & if \;\; x_{5_p} > 0 \\ \dot{x}_2 = g & , \; if \;\; x_{5_p} \le 0 \end{cases} \\ \dot{x}_3 = x_4 \\ \begin{cases} \dot{x}_4 = g + \mathrm{sgn}(x_1 - x_3)\dfrac{C}{M}\dfrac{{x_{5_p}}^2}{(x_1 - x_3)^2} - 2\xi_{eq}\omega_n x_4 - {\omega_n}^2 x_3 \;, & if \;\; x_{5_p} > 0 \\ \dot{x}_4 = g - 2\xi_{eq}\omega_n x_4 - {\omega_n}^2 x_3 & , \; if \;\; x_{5_p} \le 0 \end{cases} \\ \dot{x}_5 = \dfrac{x_1 - x_3}{2C}[K_p(x_1 - \delta_0) + K_d x_2 + u_0 - x_{5_p} R - 2C\dfrac{x_{5_p}}{(x_1 - x_3)^2}(x_2 - x_4)] \end{cases} \tag{8.1}$$

Where $\omega_n = \sqrt{k_{eq} / M}$ is the natural frequency of the track beam, $\xi_{eq} = c_{eq} / 2\sqrt{k_{eq} M}$ is the damping ratio of the track beam

In this case, the equilibrium points have 5 components each, defining the system in a 5D space, although the system is effectively a two degree of freedom system with a complementary variable accounting for the electronics of the system. Thereby, this can be commonly referred to as a one and a half degree of freedom system.

Nevertheless, one has to realize that the fact that five eigenvalues define the system, makes the eigenvalue problem more challenging than for the previous study cases, since the real part on the five eigenvalues can no longer be plotted as a 5D plot would be needed.

Thus, the equilibrium points of the system can be defined as $(x_1^*, x_2^*, x_3^*, x_4^*, {x_{5_p}}^*) = \{(x_1, x_2, x_3, x_4, x_5) \,|\, \dot{x}_1 = 0;\; \dot{x}_2 = 0;\; \dot{x}_3 = 0;\; \dot{x}_4 = 0;\; \dot{x}_5 = 0\}$ and, as in previous study cases, not all parameters in the system are positively defined.

In this case, the fixed points are exactly the same as the previously derived in chapter 5 and 6 with two extra components defining the beam deflection and the rate of deflection. Consequently, the same exact procedure of analysing the feasibility of both alternatives is applied here, which yields the same result. So the only admissible fixed point is the second one.

The inclusion of the lumped mass and the spring-dashpot system representing the beam only introduces two new components/dimensions to the fixed point and significant complexity on the symbolic description of components x_1^* and ${x_{5_p}}^*$. Despite of this, the fixed point still describes exactly the design equilibrium position at the target levitation air gap, accounting for the deflection of the track due to the vehicle hanging of it, with initial position rates zero for both masses (track and vehicle) and with an initial electrical current corresponding to the initial voltage input on the system to locate the vehicle at the design air gap.

$$(x_1^*, x_2^*, x_3^*, x_4^*, x_{5_p}^*) = (\delta_0 + \frac{(M+m)g}{K_{eq}}, 0, \frac{(M+m)g}{K_{eq}}, 0, \frac{u_0}{R}) = (0.0164, 0, 0.0014, 0, 25.9257) \tag{8.2}$$

Now, the eigenvalue problem is not only conducted as a function of K_p, but also as a function of K_d since both are control gains, which are the tunable value that is assumed to make the system stable. Therefore, one expects to be able to define different regions of stability depending on the value of these parameters. However, now in a 5D space, which will not be possible to represent. An alternative analysis will be proposed below.

Hence, the Jacobian matrix of the system and Jacobian evaluated at the fixed point are written below. However, since the expressions get more and more involved as the complexity of the system increase, several terms have been defined as complementary parameters in order to shorten the expressions. These are $\gamma = (-R^2 gm + CK_p{}^2)$, $\chi = (K_p\delta_0 - u_0)$, $\theta = \sqrt{CM^2R^2gm\omega^4\chi^2}$, $\eta = (-2CRgm - CK_d u_0)$, $\beta = (-K_d K_p R\delta_0 - R^2 gm + CK_p{}^2 + K_d R u_0)$, $\varphi = (C\delta_0 K_d K_p{}^3 + \eta K_p{}^2 + \delta_0 R^2 gm K_d K_p + 2R^3 g^2 m^2 - gm K_d u_0 R^2)$.

$$\mathbf{J} =$$

$$\begin{bmatrix} 0 & 1 & 0 & 0 & 0 \\ \frac{2Cx_{5_p}^2}{m(x_1-x_3)^3} & 0 & -\frac{2Cx_{5_p}^2}{m(x_1-x_3)^3} & 0 & \frac{2Cx_{5_p}}{m(x_1-x_3)^2} \\ 0 & 0 & 0 & 1 & 0 \\ -\frac{2Cx_{5_p}^2}{M(x_1-x_3)^3} & 0 & \frac{2Cx_{5_p}^2}{M(x_1-x_3)^3} - \omega_n{}^2 & -2\xi_{eq}\omega_n & \frac{2Cx_{5_p}}{M(x_1-x_3)^2} \\ \frac{u_0 + K_p(x_1-x_3-\delta_0) + K_d(x_2-x_4) - x_{5_p}R - \frac{2C(x_2-x_4)x_{5_p}}{(x_1-x_3)^2}}{2C} + \frac{(x_1-x_3)[K_p + \frac{4C(x_2-x_4)x_{5_p}}{(x_1-x_3)^3}]}{2C} & \frac{(x_1-x_3)[K_d - \frac{2Cx_{5_p}}{(x_1-x_3)^2}]}{2C} & -\frac{u_0 + K_p(x_1-x_3-\delta_0) + K_d(x_2-x_4) - x_{5_p}R - \frac{2C(x_2-x_4)x_{5_p}}{(x_1-x_3)^2}}{2C} + \frac{(x_1-x_3)[-K_p - \frac{4C(x_2-x_4)x_{5_p}}{(x_1-x_3)^3}]}{2C} & \frac{(x_1-x_3)[-K_d + \frac{2Cx_{5_p}}{(x_1-x_3)^2}]}{2C} & \frac{(x_1-x_3)[-R - \frac{2C(x_2-x_4)}{(x_1-x_3)^2}]}{2C} \end{bmatrix} \tag{8.3}$$

$$\left|\mathbf{J}\right|_{(x_1^*, x_2^*, x_5^*)} =$$

$$\begin{bmatrix} 0 & 1 & 0 & 0 & 0 \\ \frac{2M\omega_n{}^2C\gamma(K_p\theta + MR^2gm\omega_n{}^2\chi)^2}{mR^2(\theta + MCK_p\omega_n{}^2\chi)^3} & 0 & -\frac{2M\omega_n{}^2C\gamma(K_p\theta + MR^2gm\omega_n{}^2\chi)^2}{mR^2(\theta + MCK_p\omega_n{}^2\chi)^3} & 0 & -\frac{2M\omega_n{}^2C\gamma(K_p\theta + MR^2gm\omega_n{}^2\chi)}{mR(\theta + MCK_p\omega_n{}^2\chi)^2} \\ 0 & 0 & 0 & 1 & 0 \\ -\frac{2\omega_n{}^2C\gamma(K_p\theta + MR^2gm\omega_n{}^2\chi)^2}{R^2(\theta + MCK_p\omega_n{}^2\chi)^3} & 0 & -\frac{1}{(\theta + MCK_p\omega_n{}^2\chi)^3}\{MC\omega_n{}^4\chi[CM^2K_p\omega_n{}^4\chi^2(3R^2gm + CK_p{}^2) + M\chi(-2C^2gmK_p{}^4 + 3CK_p{}^2\theta + R^2\omega_n{}^2gm(2R^2g^2m^2 + \theta)) - 4K_pgm\theta\gamma]\} & -2\xi_{eq}\omega_n & \frac{2\omega_n{}^2C\gamma(K_p\theta + MR^2gm\omega_n{}^2\chi)}{R(\theta + MCK_p\omega_n{}^2\chi)^2} \\ \frac{K_p(\theta + MCK_p\omega_n{}^2\chi)}{2MC\omega_n{}^2\gamma} & \frac{-2K_p\theta\beta - RM\omega_n{}^2\chi\varphi}{2R\gamma(\theta + CMK_p\omega_n{}^2\chi)} & -\frac{K_p(\theta + MCK_p\omega_n{}^2\chi)}{2MC\omega_n{}^2\gamma} & \frac{2K_p\theta\beta + RM\omega_n{}^2\chi\varphi}{2R\gamma(\theta + CMK_p\omega_n{}^2\chi)} & -\frac{R(\theta + MCK_p\omega_n{}^2\chi)}{2MC\omega_n{}^2\gamma} \end{bmatrix} \tag{8.4}$$

From eq. 8.5, the characteristic equation of the system can be expressed as

$$f(\lambda) = \lambda^5 + a_1\lambda^4 + a_2\lambda^3 + a_3\lambda^2 + a_4\lambda + a_4 \tag{8.5}$$

Where each of the coefficients of this polynomials is derived from the Jacobian matrix evaluated in the system fixed points by calculating $\det\left|\mathbf{J}\,|_{(x_1^*, x_2^*, x_3^*, x_4^*, x_5^*)} - \lambda\mathbf{I}\right|$ and grouping the terms corresponding to each of the polynomial terms order.

As addressed in chapter 2.4, according to Lienard-Chipart criterion, the necessary and sufficient conditions for all eigenvalues of the characteristic equation eq. 8.6 to have a negative real part are that the characteristic equation coefficients are all greater than zero and half of the Harwitz determinant Δ_i is grater than zero [9]. This translate in the following expressions

$$
\begin{aligned}
& a_i > 0,\ \forall i = 1 \ldots 5 \\
& \Delta_2 = \begin{vmatrix} a_1 & 1 \\ a_3 & a_2 \end{vmatrix} = a_1 a_2 - a_3 > 0 \\
& \Delta_4 = \begin{vmatrix} a_1 & 1 & 0 & 0 \\ a_3 & a_2 & a_1 & 1 \\ a_5 & a_4 & a_3 & a_2 \\ 0 & 0 & a_5 & a_4 \end{vmatrix} = -a_1^2 a_4^2 - a_1 a_2^2 a_5 + a_1 a_2 a_3 a_4 + 2 a_1 a_4 a_5 + a_2 a_3 a_5 - a_3^2 a_4 - a_5^2 > 0
\end{aligned}
\tag{8.6}
$$

In this manner, the region of the parametric space $K_p - K_d$ for which the system is stable can be found (Fig. 8.1). This map has been produced by analysing the real part of the eigenvalues of the system and its intersection with the zero plane.

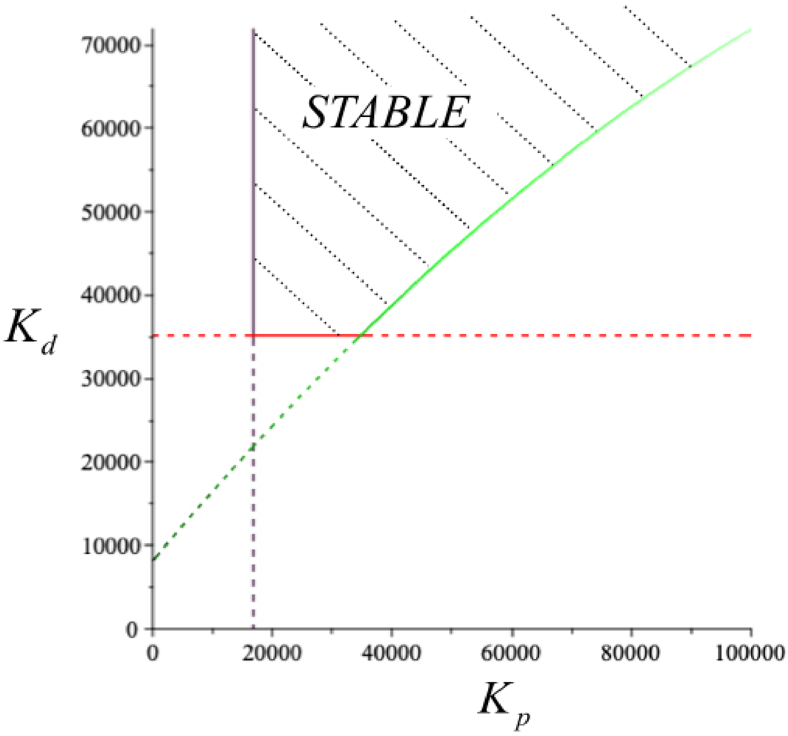

Figure 8.1 Definition of the stability region

Then, the existence of a Hopf bifurcation with respect to K_p , in the same way as the one presented in chapter 6, can be proven using an algebraic criterion. This can be done if the following theorems is met.

Theorem. The necessary and sufficient conditions for the characteristic equation eq. 8.6 to have a pair of pure imaginary eigenvalue and the remaining n-2 eigenvalues to have negative real parts are [9]

$$
a_i > 0 \ (\forall i = 1 \ldots 5) \ \wedge \ \Delta_i > 0 \ (\forall i = n-3, n-5, \ldots) \ \wedge \ \Delta_{n-1} = 0 \tag{8.7}
$$

Applying the aforementioned theory and following Fig. 8.1 map of the stability region, the following range of control parameters guaranties the stability of the region.

$$\begin{cases} 16783.35 \leq K_p \leq -8715.1169 + 1.0133 K_d + 6.257 \cdot 10^{-6} {K_d}^2 \\ K_d \geq 35177.95 \end{cases} \tag{8.8}$$

Once a stability region has been identified, one can study the dynamic behaviour of the vehicle depending on the input control gain values both within the phase portrait and for the evolution of the main variables of the system against time.

The same strategy used in chapter 6 is applied in this case, fixing $K_d = 56000$ and defining a horizontal line through out the stability region plane presented in Fig. 8.1. Similarly, also several different cases are defined depending on the value of K_p. This can be found in Tab. 8.1.

Table 8.1 Summary of the study cases presented in this section

Gain parameters study cases based on $K_d = 56000$

Case Nº	**Location Stable Region**	**K_p value**
Case 1	Close to Left Boundary In Stable Region	20000
Case 2	In the Middle of the Stable Region	40000
Case 3	Close to Right Boundary In Stable Region	67600

Below, the behaviour of the three main system state-variables $\{z \quad w \quad i_p\}$ and the levitation air gap δ are presented against time (Fig. 8.2, 8.3 and 8.4), proving that stabilization around a designed point occurs for all variables of interest of the system and that the effect of the controller gain parameters on those variables is globally very similar.

These plots feature only the nonlinear simulation solution of the system state variables $\{x_1 \quad x_3 \quad x_{5_p}\} = \{z \quad w \quad i_p\}$ and the levitation air gap δ (in black), and the design equilibrium value (in red).

Using the strategy defined above, the first featured results correspond the case for which $K_p << K_d$, located close to the left stability boundary $K_p = 16783.35$ (Fig. 8.1). In this case, the input combination of gain parameters is $K_p = 20000$ and $K_d = 56000$, whilst the initial perturbation to the vehicles position is $1 \cdot 10^{-4}\, m$ from the target air gap of the system.

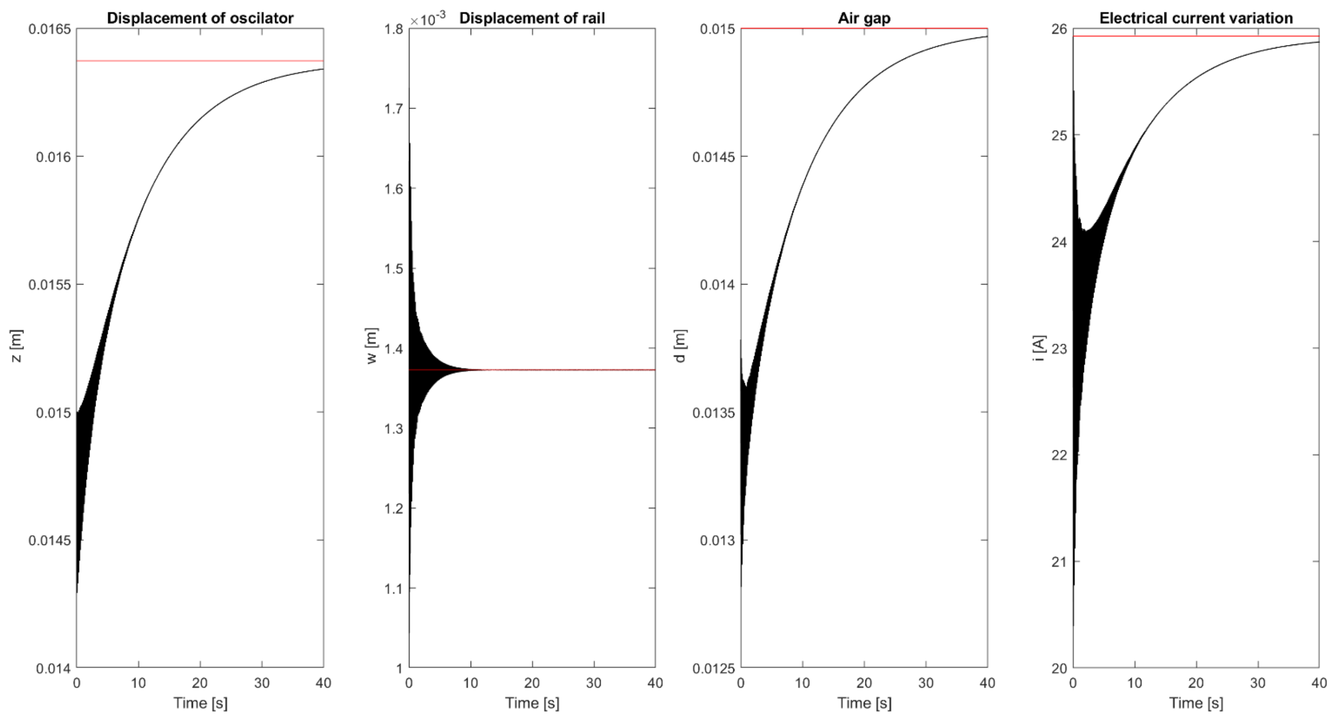

Figure 8.2 Nonlinear solution of the system against time for a K_p value close to the left boundary of the stability region

From this figure, the same conclusions drawn in chapter 6 for the case study 1 are extrapolated, amid the slow convergence rate with a very small amplitude of oscillation of the actual solution around the equilibrium point. From Fig. 8.2, it is interesting to see how the levitation air gap is defined as the relative difference between the track deflection and the vehicle displacement. Nevertheless, one can conclude that no significant changes in the system response are observable, due to the inclusion of the track motion.

The observations described above also apply for the phase portrait representation of the system (Fig. 8.3) for the levitation air gap $\delta - \dot{\delta}$. In this map it becomes obvious the slow convergence rate . Nevertheless, the amplitude of the trajectory oscillation around the fixed point is significantly small. It is important to note, that the phase portraits for such a case study, are not the complete picture to the actual system behaviour, due to the simple reason that one is trying to represent in a 2D plane the entire information of a 5D space. For this reason, unlike previous sections, this chapter will not feature the phase portraits of the system, but only the solutions with respect to time. Fig. 8.3 is the only exception on this rule, aiming at illustrate the aforementioned phenomena with the perturbations on the trajectory, which unlike in previous sections does not draw a perfect spiral around the design equilibrium point.

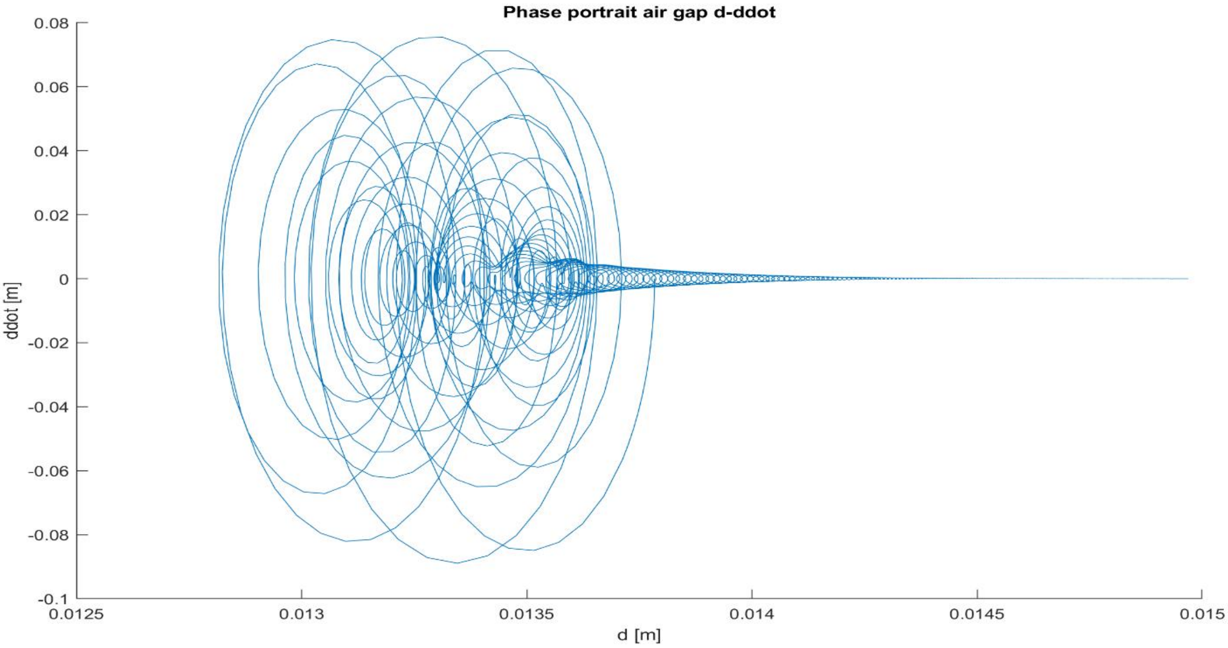

Figure 8.3 Phase portrait of the system $\delta - \dot{\delta}$ *for a* K_p *value close to the left boundary of the stability region*

The second featured results correspond the case for which K_p is about in the middle of the stable region within both the right and the left boundaries defined in eq. 8.9. (Fig. 8.4). In this case, the input combination of gain parameters is $K_p = 40000$ and $K_d = 56000$, whilst the initial perturbation to the vehicles position is $1 \cdot 10^{-4}\, m$ from the target air gap of the system.

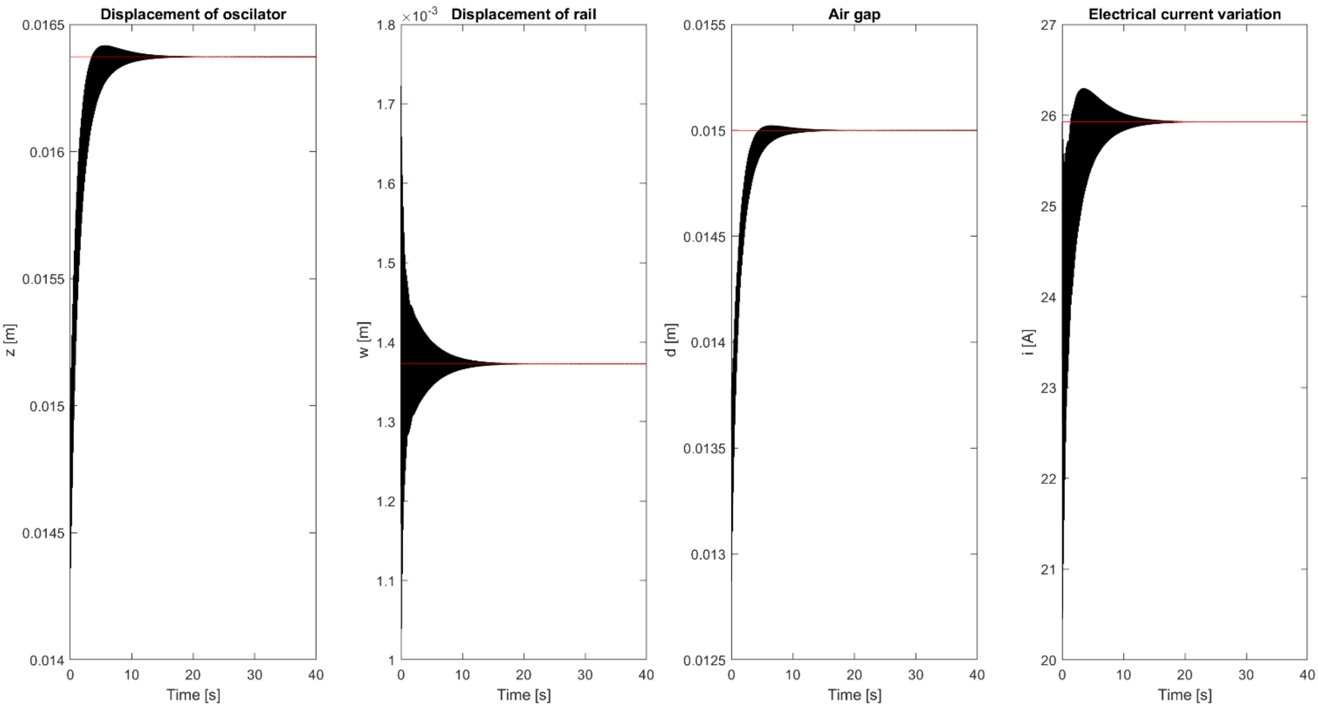

Figure 8.4 Nonlinear solution of the system against time for a K_p *value centered within the stability region*

From this figure, the same conclusions drawn in chapter 6 for the case study 2 are extrapolated, amid the faster convergence rate due to the shift of K_p with a little larger amplitude of oscillation of the actual solution around the equilibrium point, compared to the previous one. From Fig. 8.3, it is interesting to see how the levitation air gap is defined as the relative difference between the track deflection and the vehicle displacement. Nevertheless, one can conclude that no significant changes in the system response are observable, due to the inclusion of the track motion.

For this second case study, the interaction in motion between the rail track and the vehicle becomes clearer that before. It is important to see how, once the vehicle is converging around the design equilibrium point, the oscillation of the track deflection oscillation around the fixed becomes much smaller. This is explained due to the fact that the vehicles motion oscillation has also reduced and its influence on the variation of the deflection on the beam reduces drastically. Along these lines, once this stabilization pattern occurs, at the same time the voltage input in the system and the electromagnetic force also close in to the equilibrium value and damped out the oscillations around it.

The third featured results correspond the case for which K_p is close to the right boundary $K_p = -8715.1169 + 1.0133 K_d + 6.257 \cdot 10^{-6} K_d^{\,2}$ (Fig. 8.5). In this case, the input combination of gain parameters is $K_p = 67600$ and $K_d = 56000$, whilst the initial perturbation to the vehicles position is $1 \cdot 10^{-4}\, m$ from the target air gap of the system.

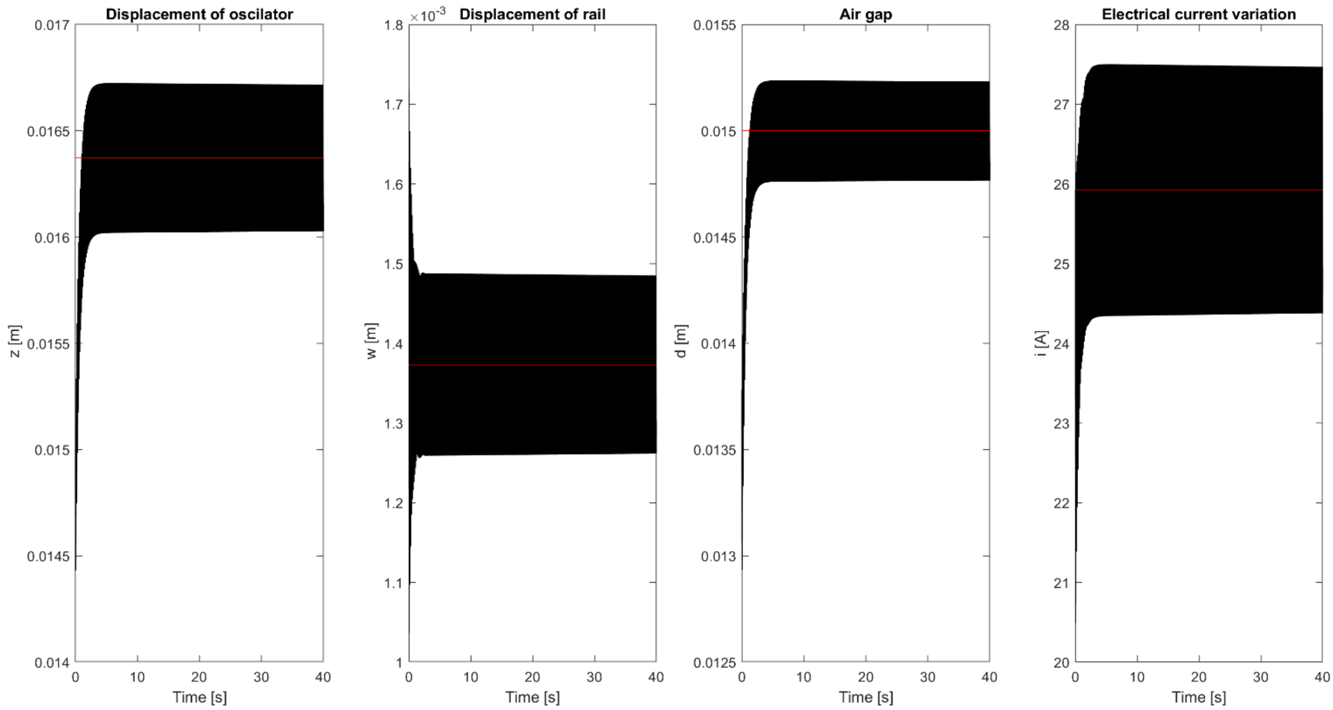

Figure 8.5 Nonlinear and linearized solutions of the system against time for a K_p value close to the right boundary of the stability region

From this figure, the same conclusions drawn in chapter 6 for the case study 3 are extrapolated, amid an immediate convergence rate due to the shift of K_p with a significantly larger amplitude of oscillation of the actual solution around the equilibrium point, compared to all previous cases. From Fig. 8.3, it is interesting to see how the levitation air gap is defined as the relative difference between the track deflection and the vehicle displacement. Nevertheless, one can conclude that no significant changes in the system response are observable, due to the inclusion of the track motion. From this plot, it becomes obvious the presence of a Hopf bifurcation close to the parametric combination chosen for this case study.

In this coupled vehicle-track model, there are five eigenvalues. In this case, there are two pairs of complex conjugates and one real valued eigenvalue. As previously explained, the system is stable if and only if the real part of both five is negative. This is indeed true within the stability region presented in Fig. 8.1, as proven with the plot of the real part of all five eigenvalues against K_p, fixing a certain value of K_d, which showcases the evolution of the eigenvalues within the stability region explaining the behaviours presented in Fig. 8.2-8.5 and confirms the presence of a Hopf bifurcation at the right boundary of such region (Fig. 8.6).

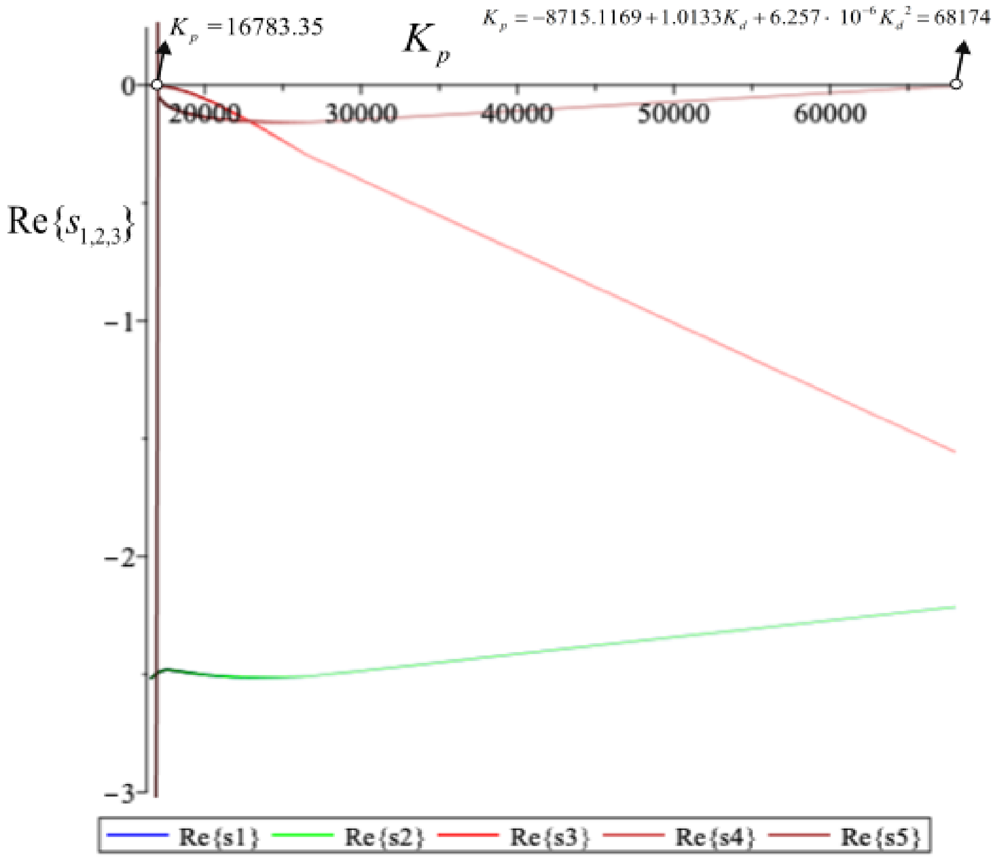

Figure 8.6 Plot of the real part of the three eigenvalues of the linearized system with respect to K_p

Using the strategy defined above of fixing a K_d value and defining a horizontal line across the stability region, one can evaluate the change of the system eigenvalues along this horizontal line. In this manner, it is observed that the main change on the eigenvalues' nature between the left boundary and the right boundary is translated in the magnitude of the real part of the complex conjugate pair of eigenvalues. Along these lines, the magnitude of such real part is at its maximum when the parameter combination is taken at the left boundary and it progressively reduces tending to zero when moving to the right. Then, once these cross the right boundary of the stability region, their real part becomes zero, implying the existence of a Hopf bifurcation.

Since the nature of the bifurcation is exactly the same as the one presented in chapter 6, no further discussion is addressed on its shape and its development. For any doubt, see pages 77-83. It is important to note, that the influence of the addition of the beam motion in the system, yield a larger amplitude secondary limit cycle, after the subcritical Hopf bifurcation, making it a little more critical than when only the vehicle is considered.

At the left boundary, the behaviour of the system for a K_p value a little bit lower than the boundary is unstable. From the behaviour of the system state variables and the control variable versus time, it becomes obvious that the low value of K_p leads to a control that is not able to maintain the vehicle attracted at the target air gap level and it falls downs, moving away from the design value. Given the correct definition of the system, it tries to over compensate this by inputting more voltage to the system and raising the electrical current, creating an overshooting reaction that crashes with the track.

In conclusion, likewise chapter 6, proving that the overall coupled vehicle-track system is stable using a PD-control on the voltage and an on/off switch on the electromagnetic force and a large stable region is defined on the parametric space $K_p - K_d$, allowing the definition of several different behaviours of the system for a large range of control gain parameters combinations.

Moreover, one can conclude that the inclusion of the beam motion yields a little more restrictive stable region with respect to K_d, considering that there is a new bottom threshold in the stability region at $K_d = 35177$, but is extended progressively with respect to K_p , the higher the value of K_d. This becomes visually obvious in Fig. 8.1.

Besides, the the inclusion of the beam motions yield a little more subcritical Hopf bifurcation. In this sense, the K_p and K_d trade off observed in chapter 6 is maintained in this system.

Finally, this chapter also serves to feature the interaction between the motion of the track modelled as a SDOF oscillator and the motion of the vehicle, and how its relative difference provides the resulting levitation air gap, which shows a mixed behaviour resulting of the combination between both motions.

9

CONTROL DELAY SAFETY MARGIN FOR STABILITY

This chapter serves to feature the definition of time delay in the control system and its effect on the stability of the EMS levitation system.

Most dynamical systems have an inherent amount of delay and, if one builds a controller for such a system, this must be taken into account. It is common to associate short delays with low disturbances that can sometimes even be ignored, and long delays lead to larger disturbances that may even trigger change in stability of the system. Along these lines, two main types of delay can be defined. On the one hand, there are distorting delays for which the signal is distorted when its original shape is altered in some way. This happens when time delay is different for various frequencies that make up the signal (Fig. 9.1).

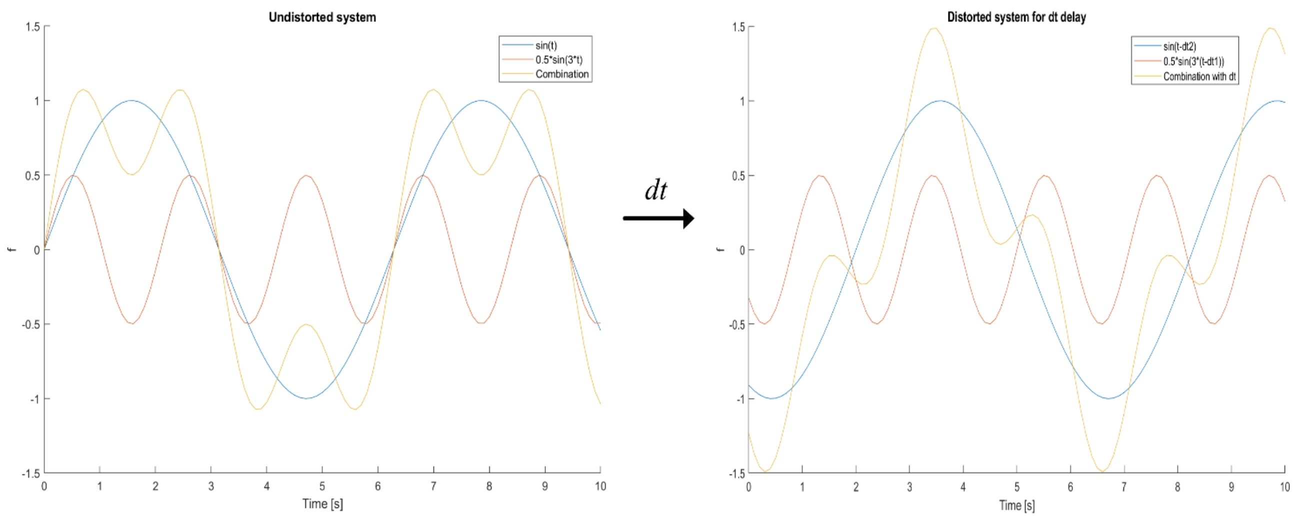

Figure 9.1 Example of distorting delay in time domain

Rather than thinking about these delays in the time domain, since each frequency is delayed differently, it is more helpful to think about it in the frequency domain. How much each frequency is delayed through a process can be represented in the phase portion of a bode plot, leading to the so called phase delay.

On the other hand, there are disturbing delays for which the delay affects the whole signal equally and results in a shift of the entire signal, which maintains the same shape but it is just postponed by a certain amount of delay (Fig. 9.2). Such a type of delays is most commonly know as transport delays.

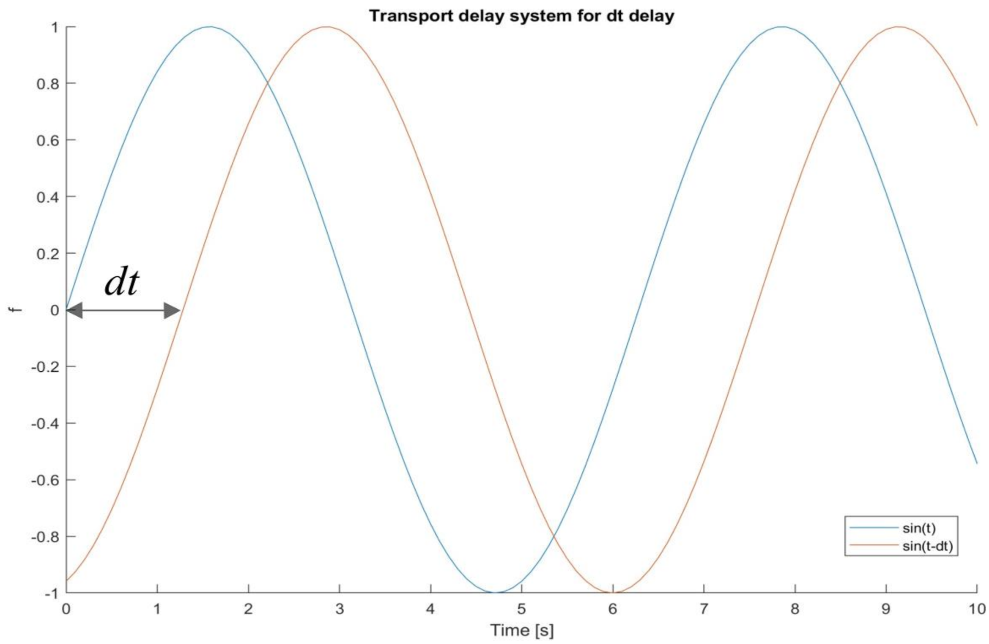

Figure 9.2 Example of a transport delay in time domain

Both of these types of delays exist in real physical systems and they both can cause problems in our controller design. This is because the controller has to use old information in order to determine the current controller output, or it has to predict into the future how its output will impact the system. Overall, this has the effect of effectively lowering the sample time of our system and, therefore, to counter it one has to lower the bandwidth or speed of the controller. If the bandwidth is not lowered, then the delay could cause stability issues. However, this slows down the system and makes it less responsive.

If one knows the source of the delay, one can trade the cost of trying to remove it versus just building around it. In order to know how to remove the delays, one needs to understand where they come from in the system.

There are unintentional delays, which are a by-product of the design and not something that was included on purpose. All real dynamic systems introduce phase delay or distort the system by delaying some frequencies more than others. This is true for either mechanical or electrical. In addition there are design components that might be added into the system for a necessary reason, but then, increase phase delay as a by-product. These are thinks like low-pass filters to remove noise, anti-aliasing filters prior to digitizing an analog signal, and building integrators into a controller.

This means that all sensors, actuators and processes create some amount of phase delay across the spectrum, and depending on the controller design it can also add phase delay. If this is the cause of the delays in our system, then, it might be necessary to look into faster sensors and actuators that do not have as much lag.

However, phase delay is not the whole story, but transport delay needs also to be considered. This one is associated to computation time, processing time, sampling time, slack time or even extra safety margin times to account for unforeseen events.

There are also intentional delays. These are pauses that are designed into the system on purpose, such as slack time, which can be added to the system accounting for the estimated processing time plus an extra safety margin accounting for any random variations. This might be preferable to occasionally having a process failed to complete within the deadline of a real-time system.

The combination of all of these delays create the so-called dead time. That’s the non-distorting transport delay part. If this dead-time is too long, one can find the system to become unstable. This is our focus in this chapter, with the objective to determine a safety margin before the system becomes unstable that could account for any processing, synchronization, sampling, unforeseen cause, etc. delays.

In this case, our nonlinear system can be well approximated by a linearized model. For the sake of simplicity, this chapter will be focused on the linearized system used in chapter 6, eq. 6.3, rewritten below. Therefore, the initial model assumption of considering the track to be infinitely stiff is applied. Therefore, the vector of state variables is defined as $\{x_1 \quad x_2 \quad x_5\} = \{z \quad \dot{z} \quad i\}$.

$$\begin{cases} \dot{x}_1 = x_2 \\ \dot{x}_2 = g - \mathrm{sgn}(x_1)\dfrac{C}{m}\dfrac{x_5{}^2}{x_1{}^2} \\ \dot{x}_5 = \dfrac{x_1}{2C}(u - x_5 R - 2C\dfrac{x_5}{x_1{}^2}x_2) \end{cases} \tag{9.1}$$

However, now, the definition of the controlled voltage across the electromagnet coil present in the 3rd equation is different. Aiming at accounting for a generic extra delay within the definition of the controller, a variation of time is added for those variables dependent implicitly on time within the error-based PD-control loop.

$$u(t-\Delta t) = K_p[x_1(t-\Delta t) - \delta_0] + K_d x_2(t-\Delta t) + u_0 \tag{9.2}$$

The implementation of the time delay presented in eq. 9.2 is chosen to be conducted in the linearized system for simplicity. The fixed point is defined in the same way as in chapter 5 and 6, as shown in eq. 9.3. Then the Jacobian of the eq. 9.1 system evaluated at the fixed point reads

$$(x_1^{2*}, x_2^{2*}, x_5^{2*}) = (\delta_0\,,\, 0\,,\, \frac{u_0}{R}) \tag{9.3}$$

$$\mathbf{J}|_{(x_1{}^*, x_2{}^*, x_5{}^*)} = \begin{bmatrix} 0 & 1 & 0 \\ \dfrac{2C\varepsilon^2\gamma}{m\chi\psi^3} & 0 & -\dfrac{2C\varepsilon\gamma}{m\chi\psi^2} \\ \dfrac{\chi\varepsilon K_p}{2C\gamma} & \dfrac{-2K_p\sqrt{gmC}\varpi + CK_dK_p{}^3\delta_0 + \eta K_p{}^2 + K_dK_pR^2gm\delta_0 + 2R^3g^2m^2 - K_dR^2gmu_0}{2\psi\gamma} & -\dfrac{\varepsilon\psi R}{2C\gamma} \end{bmatrix} \tag{9.4}$$

Where $\psi = (CK_p + R\sqrt{gmC})$, $\varepsilon = (Rgm + K_p\sqrt{gmC})$, $\gamma = (-R^2gm + CK_p{}^2)$, $\varpi = (-RK_dK_p\delta_0 - R^2gm + CK_p{}^2 + RK_du_o)$, $\chi = (K_p\delta_0 - u_0)$, $\eta = (-2CRgm - CK_du_0)$.

Then, the same method used in chapters 4, 5 and 6 can be used to reduce the two first rows of the matrix system to an equivalently single equation with variable x_1 and x_5, and coefficients corresponding to the Jacobian terms and a second equation corresponding to the last row with variables x_1 and x_5. In this step, the time delay is applied, only to the variables involved in the control.

$$\begin{cases} \ddot{x}_1(t) - J_{21}x_1(t) + J_{23}x_5(t) = 0 \\ \dot{x}_5(t) - J_{31}x_1(t-\Delta t) - J_{32}\dot{x}_1(t-\Delta t) + J_{33}x_5(t) = 0 \end{cases} \tag{9.5}$$

Similarly, no conclusions can be drawn about stability of the system due to the presence of K_p and K_d and the eigenvalue problem needs to be derived. This is done in the Laplace domain.

Note that the Laplace transform for a force with time delay is defined as $\Im[f(t-\Delta t)] = F(s)\exp(-s\Delta t)$.

$$\begin{cases} \ddot{x}_1(t) - J_{21}x_1(t) + J_{23}x_5(t) = 0 \\ \dot{x}_5(t) - J_{31}x_1(t-\Delta t) - J_{32}\dot{x}_1(t-\Delta t) + J_{33}x_5(t) = \delta(t) \end{cases} \xrightarrow{\text{Laplace trans.}} \begin{cases} s^2\hat{x}_1 - J_{21}\hat{x}_1 + J_{23}\hat{x}_5 = 0 \\ s\hat{x}_5 - J_{31}\hat{x}_1\exp(-s\Delta t) - J_{32}s\hat{x}_1\exp(-s\Delta t) + J_{33}\hat{x}_5 = 1 \end{cases} \tag{9.6}$$

Then, following the theory presented in chapter 2.4, one can compute the poles of the system, i.e. the eigenvalues, by deriving the transfer function of $\hat{x}_1$ and finding the roots of its denominator.

$$\hat{x}_5 = \frac{1 + J_{31}\hat{x}_1\exp(-s\Delta t) + J_{32}s\hat{x}_1\exp(-s\Delta t)}{s + J_{33}} \Rightarrow s^2\hat{x}_1 - J_{21}\hat{x}_1 + J_{23}\left(\frac{1 + J_{31}\hat{x}_1\exp(-s\Delta t) + J_{32}s\hat{x}_1\exp(-s\Delta t)}{s + J_{33}}\right) = 0 \rightarrow$$

$$\hat{x}_1 = \frac{-\dfrac{J_{23}}{s+J_{33}}}{s^2 - J_{21} + \dfrac{J_{23}(J_{31} + J_{32}s)\exp(-s\Delta t)}{s + J_{33}}} = -\frac{1}{\dfrac{1}{J_{23}}[s^3 + J_{33}s^2 + (J_{23}J_{32}\exp(-s\Delta t) - J_{21})s - J_{21}J_{33} + J_{23}J_{31}\exp(-s\Delta t)]} \tag{9.7}$$

$$\xrightarrow{\text{Poles}} \frac{1}{J_{23}}[s^3 + J_{33}s^2 + (J_{23}J_{32}\exp(-s\Delta t) - J_{21})s - J_{21}J_{33} + J_{23}J_{31}\exp(-s\Delta t)] = 0$$

The equation defining the poles is no longer polynomial due to the presence of exponential functions with the complex variable s in the argument. Therefore, to determine the poles of such an equation, it is chosen to approximate the exponential function through the first two terms in the Taylor's expansion $\exp(-s\Delta t) \approx 1 - s\Delta t + \underbrace{higher\ order(s)}_{\approx 0}$. Hence, the polynomial equation reads

$$\frac{1}{J_{23}}[s^3 + J_{33}s^2 + (J_{23}J_{32}(1 - s\Delta t) - J_{21})s - J_{21}J_{33} + J_{23}J_{31}(1 - s\Delta t)] = 0 \tag{9.8}$$

Hence, the eigenvalues can be plotted with respect to Δt, which allows to see for which values of Δt the system is stable and for which not. Considering the same strategy followed in previous chapters of fixing a value of K_d and varying the value of K_p within the stable region in the parametric space, three cases have been differentiated. The first one corresponds to the case for which K_p is close to the left boundary (Fig. 9.3).

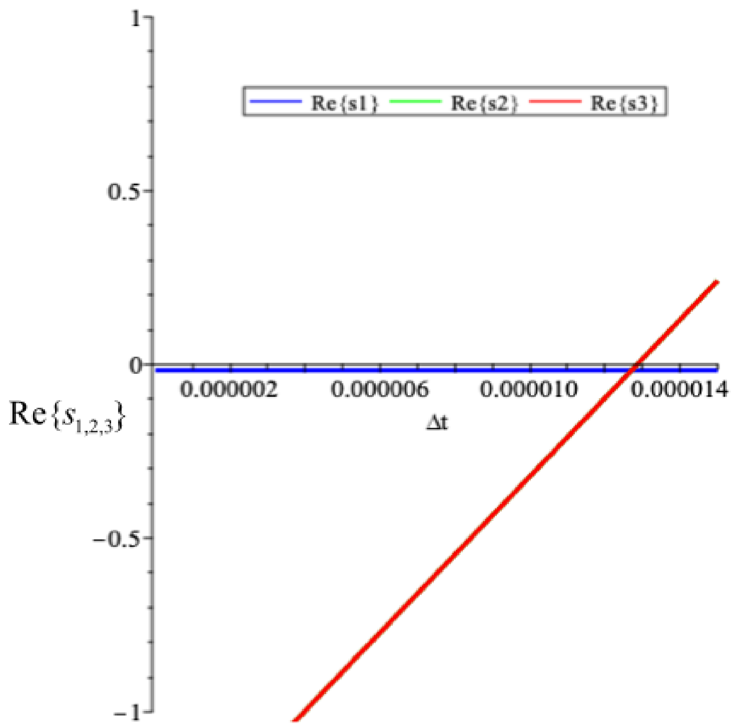

Figure 9.3 Eigenvalues plotted versus the time delay for K_p *value close to the left boundary of the stable region*

From Fig. 9.3, it becomes obvious that the system behaviour is exactly the same as described when plotting the eigenvalues against K_p for the PD-control Fig. 6.13. For such a value of K_p the real-valued eigenvalue is close to cross the real axis, which means that the system is close to the stability boundary. Whilst the pair of complex conjugate eigenvalues have a rather large negative real part. For $K_p - K_d$ combinations close to the left boundary of stability provide the largest time delay safety margin.

The second one corresponds to the case for which K_p is in the middle of the stability region defined in the parametric space (Fig. 9.4).

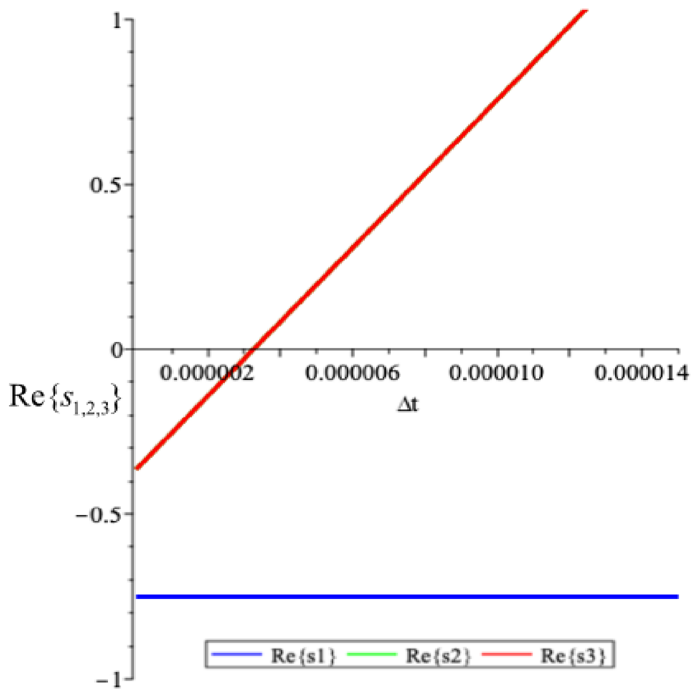

Figure 9.4 Eigenvalues plotted versus the time delay for K_p value in the middle of the stable region

As before, the system behaviour is confirmed as both eigenvalues start from the negative complex half-space with time delay zero. For such a $K_p - K_d$ combination the reduction of the safety margin is reduced significantly.

The third one corresponds to the case for which K_p is close to the right boundary of the stability region defined in the parametric space (Fig. 9.5).

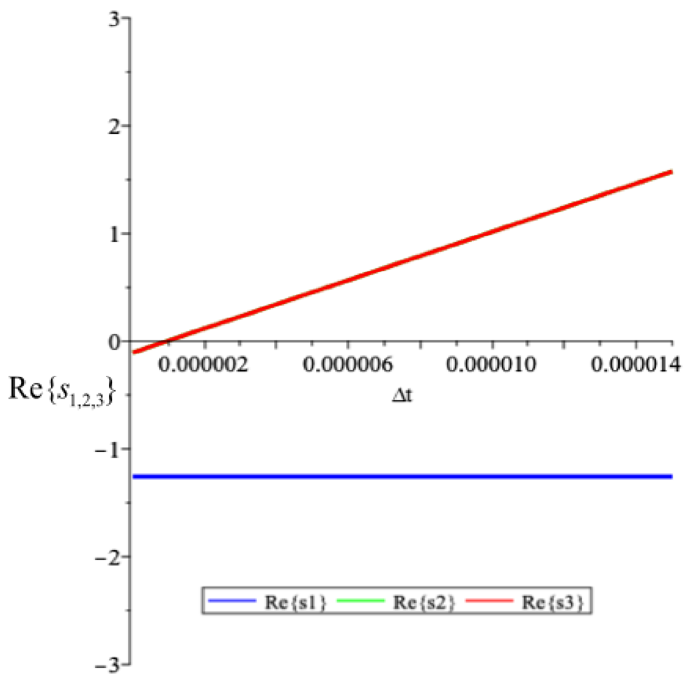

Figure 9.5 Eigenvalues plotted versus the time delay for K_p value close to the right boundary of the stable region

As before, the system behaviour is confirmed as both eigenvalues start from the negative complex half-space with time delay zero, but now the pair of complex conjugates real part is much closer to zero, i.e. to the bifurcation. For such a $K_p - K_d$ combination the reduction of the safety margin is to its minimum.

Once the safety margin with respect to the eigenvalues has been acknowledge, this allows the designer of the error-based PD-control to account for the software processing delay, the signal sampling delay, the actuators delay and some slack time for unforeseen events, making sure that the system is still stable.

To sum up, this section has shown that enough time delay safety margin can be obtained. This directly depends on the $K_p - K_d$ combination and, it has been showcased that this safety margin maximizes when K_p is close to the left boundary of the stable region.

10

CONCLUSIONS AND RECOMMENDATIONS

This chapter serves to conclude the project summarizing all the results, relating them to the original problem statement and thesis objectives, and providing several recommendations and alternative research lines for any student interested in continuing to study this topic.

10.1. CONCLUSIONS

The main goals of this thesis can be summarized in three main points. First, we aimed at investigating dynamic behaviour of the EMS levitation system without controller. Second, we focused on investigating the implementation of an error-based PD-control in the levitation system. Third, we attempt to studying the vehicle-structure interaction through the EMS system after the control implementation.

The EMS levitation system has been confirmed to be unstable by nature, meeting Earnshaw's theorem, and the vehicle dynamics have been understood as a trade off between electromagnetic force and gravitational forces. Such a trade off is governed by the initial value problem for levitation air gap magnitude and rate of variation of the gap.

The P-control has proven not sufficient to stabilize the system, although it provides already a certain level of response trying to counteract the loss of attractive force for positions far from the track. Oppositely, for the PD-control a stable region defined for different values of the control gain parameters can be obtained. This system has proven to be stable for a significant range of initial conditions air gap and air gap variation rate.

Besides, the existence of a subcritical Hopf bifurcation has been confirmed for a critical proportional gain parameter K_p value laying on top of a boundary of the stability region and a given fixed K_d value. In this sense, it has been confirmed the direct relation between the value of the proportional gain parameter K_p and the convergence rate of the system response to the equilibrium point. Whilst a direct relation between the value of the derivative gain parameter K_d and the error variation amplitude around the design equilibrium value was derived as well. In this manner, a trade off has been defined, setting the basis for a tuning optimization of the parameters.

The implementation of an on/off switch on the electromagnetic force has proven to improve the system and avoid unrealistic negative electrical current. This turns out to increase the range of initial conditions, i.e. perturbations, in air gap and air gap variation rate, for which the system can be stabilized. Such a range has been proven to meet the main tolerances in the system state variables. For a more complex control strategy, the implementation of this switch can be avoided by tunning the control gains accordingly.

The overall vehicle-track system has been proven to stabilize by means of the error-based closed-loop PD-control system. While the on/off switch on the electromagnetic force improves the system response by avoiding the appearance of unrealistic negative electrical currents and enlarges the stable region in the phase portrait space. A stable region with respect to the control gain parameters has been derived using the eigenvalues of the linearized system.

Moreover, the inclusion of the beam motion yields a little more restrictive stable region with respect to K_d, considering that there is an additional boundary at the bottom side of the stability region. This stable region is extended progressively with respect to K_p , the higher the value of K_d becomes. In this case, the existence of a subcritical Hopf bifurcation has also been confirmed for this model, for which the secondary stability pattern has a little larger amplitude, making it more critical. The effect of the control gains parameter set up on the system has been analysed, confirming the same trade off observed in previous studies.

Finally, the safety margin for a certain amount of time delay on the control system response has been derived, providing a range of delay magnitude to be accounted when choosing a certain model of measuring device, processor, etc.

10.2. RECOMMENDATIONS

For further studies, it would be highly advised to implement certain optimization algorithms to tune the control parameters, such that the most efficient control system response is derived, avoiding the need of secondary mechanisms such as the on/off switch on the electromagnetic force.

The two degrees of freedom system is a simplification and accounting for the actual continuous system is important, making special emphasise in the vehicle-structure interaction. In this sense, this project proposed the modelling of the track-beam as an Euler Bernoulli beam, for simplification and following the assumptions listed in chapter 3. However, considering that recent design updates propose shorter sections and that important shear strains, like the ovalization of the tube, can be relevant in the track structural behaviour. For this reason, future investigations could shift the modelling of the track infrastructure to the Timoshenko beam theory.

Besides, for simplification a track span section is modelled as a simply supported beam. Nevertheless, this is not fully correct. The track-beam can be modelled in a more correct way by considering a continuous beam. One of the simplest starting points is the consideration of an infinite continuous beam laying on a continuous homogeneous viscoelastic support, accounting for a homogeneous bed. The vehicle can then be added using either a moving load or an equivalent spring dashpot oscillator system accounting for the electromagnetic levitation force between the two bodies.

For such a longitudinal beam analysis, if a continuous beam is introduced, there are more chances to account for the role of intermediate supports. Along these lines, the periodicity of the supports could be introduced. This can be addressed by considering an infinite beam defined on a periodically inhomogeneous support, accounting for the periodicity of the supports. As before, the vehicle can then be added using either a moving load or an equivalent spring dashpot oscillator system accounting for the electromagnetic levitation force between the two bodies.

Moreover, irregularities present on the track can be added to the levitation gap δ model as a time and longitudinal coordinate dependent function $p(x,t)$, so as to account for the unrealistic assumption of a perfectly smooth track. For an advanced modeling, this term could be represented by a Power Spectral Density function (PSD) accounting for the random nature of such irregularities. Other simplified and less realistic options are using a time dependent term with sinusoidal shape $p(t) = A_p \sin(2\pi V_m / w_L t)$ at the specific cross-section cut being studied.

If there is interest in studying the cross-sectional study further, the horizontal guidance system could be added, so as to understand the interaction between the vertical levitation system and the horizontal one. Such a horizontal guidance distance is only activated when facing bendings, track switches and track irregularities. For this reason, the mechanics of the system must be defined in a significantly different way, as gravitational forces do not play a role, but centrifugal/centripetal pair of forces and lateral pulse forces.

BIBLIOGRAPHY

[1] A. Schafer and D. G. Victor, "The future of mobility of the world population," *Transportation Research Part A - Policy and Practice,* vol. 34, p. 171, 2000.

[2] P. Vallance and J. Norman, "The Future of Mobility: A time of unprecedented change in the transport system," Governmetn Office for Science; Foresight, UK, January 2019.

[3] H. Ritchie, "Our World in Data - Climate change and flying> what share of global CO2 emissions come from aviation?," University of Oxford, 22nd October 2020. [Online]. Available: https://ourworldindata.org/co2-emissions-from-aviation. [Accessed 13th April 2022].

[4] B. Dodson, "Beyond the hype of Hyperloop: An analysis of Elon Musk's proposed transit system," 22nd August 2013. [Online]. Available: https://newatlas.com/hyperloop-musk-analysis/28672/. [Accessed 1st March 2022].

[5] S. Earnshaw, "On the nature of molecular forces which regulate the constitution of the Luminiferous Ether.," in *Transcription of the Cambridge Philosophical Society*, Cambridge, M. A. of St. John's Colledge, 1842, p. 97.

[6] X. Chen, W. Ma and S. Luo, "Study on stability and bifurcation of electromagnet-track beam coupling system for EMS maglev vehicle," *Nonlinear Dynamics,* vol. 101, pp. 2181-2193, 2020.

[7] X. Chen, W. Ma, S. Luo and R. Zou, "A vehicle-track beam matching index on EMS Maglev transportation system," *Arch. Appl. Mech.,* 2019.

[8] H. S. Han, B. H. Yim, N. J. Leec, Y. C. Hur and S. S. Kim, "Effect of the guideway's vibrational characteristics on the dynamics of a Maglev vehicle," *Vehicle System Dynamics*, vol. 47, no. 3, pp. 309-324, 2009.

[9] J. Hu, W. Ma, X. Chen and S. Luo, "Levitation Stability and Hopf Bifurcation of EMS Maglev Trains," *Mathematical Problems in Engineering,* 2020.

[10] J. H. Li, J. Li and D. F. Zhou, "Self-excited vibration problems of Maglev vehicle-bridge interaction system," *J. Cent. South Univ.,* vol. 21, no. 11, pp. 4184-4192, 2014.

[11] X. Li, D. Wang, D. Liu, L. Xin and X. Zhang, "Dynamic analysis of the interactions between a low-to-medium speed Maglev train and a bridge: field test results of two typical bridges," *Proceedings of the Institution of Mechanical Engineers, Part F: Journal of Rail and Rapid Transit,* vol. 36, pp. 2039-2059, 2018.

[12] X. H. Shi, L. H. She and W. S. Chang, "The bifurcation analysis of the EMS maglev vehicle-coupled-guideway system," *Acta Mechanica Sinica,* vol. 36, pp. 634-640, 2004.

[13] R. P. Talikdar and S. Talukdar, "Dynamic Analysis of High-Speed MAGLEV Vehicle-Guideway," *Urban Rail Transport*, vol. 2, no. 2, pp. 71-84, 2016.

[14] J. Xu, C. Chen, D. Gao, S. Luo and Q. Qian, "Nonlinear dynamic analysis on Maglev train system with flexible guideway and double time-delay feedback control," *Journal of Vibroengineering,* vol. 19, no. 8, pp. 6346-6362, 2017.

[15] J. D. Yau, "Vibration Control of Maglev vehicles travelling over a flexible guideway," *Journal of Sound and Vibration,* vol. 321, pp. 184-200, 2009.

[16] M. Zhang, S. Luo and C. Gao, "Research on the mechanism of a newly developed levitation frame with mid-set air spring," *Vehicle System Dynamics* , vol. 56, no. 12, pp. 1797-1816, 2018.

[17] T. E. Alberts, G. Oleszczuk and A. M. Hanasoge, "Stable levitation control of magnetically suspended vehicles with structural flexibility," in *American Control Conference*, 2008.

[18] A. M. G. Jacob and N. M. V. Monteiro, "A new concept of superelevation in magnetic levitation - prodynamic," *Transportation Systems and Technology,* vol. 4, no. 4, pp. 77-111, 2018.

[19] "Maglev Trains - McGill," 2007. [Online]. Available: https://www.cs.mcgill.ca/~rwest/wikispeedia/wpcd/wp/m/Maglev_train.htm. [Accessed 28th February 2022].

[20] Z. Liu, Z. L. Li and X. Li, Maglev Trains: Key Underlying Technologies, Berlin: Springer, 2015.

[21] "Technology Development - Hardt Hyperloop," 2020. [Online]. Available: https://hardt.global/technology-development/. [Accessed 2nd March 2022].

[22] Cassandra, "How does Hyperloop work? Everything you need to know about magnetic levitation - alphr," 16th November 2020. [Online]. Available: https://www.alphr.com/technology/1006815/how-hyperloop-works-launch-magnetic-levitation/. [Accessed 2nd March 2022].

[23] "XP-2 Test Vehicle - Virgin Hyperloop," 2022. [Online]. Available: https://virginhyperloop.com/pegasus?a=tech. [Accessed 2nd March 2022].

[24] J. L. He, D. M. Rote and H. T. Coffey, "Study of Japanese electrodynamic-suspension Maglev systems," *Technical Report,* 1994.

[25] "Magnetic Levitation - UCSB Physics," [Online]. Available: https://web.physics.ucsb.edu/~lecturedemonstrations/Composer/Pages/68.78.html. [Accessed 2nd March 2022].

[26] S. Yadav, S. Verma and S. Nagar, "Optimized PID Controller for Magnetic Levitation System," *International Federation of Automatic Control,* vol. 49, no. 1, pp. 778-782, 2016.

[27] R. Goodall, "Dynamics and control requirements for EMS Maglev suspensions," in *Proc. Int. Conf. Maglev,* Shanghai, Octrober 2004.

[28] E. Kong, J.-S. Song, B.-B. Kang and S. Na, "Dynamic reponse and robust control of coupled Maglev vehicle and guideway system," *Journal of Sound and Vibrations,* vol. 330, pp. 6237-6253, 2011.

[29] H.-S. Han and D.-S. Kim, Magnetic Levitation: Maglev Technology and Applications, Dordrecht: Springer, 2016.

[30] K. Wang, S. Luo and W. Ma, "Dynamic characteristics analysis for a new-type maglev vehicle," *Adv. Mech. Eng.,* vol. 9, no. 12, pp. 1-10, 2017.

[31] A. V. Metrikine, Dynamics, Slender Structures and an Introduction to Continuum Mechanics, Delft University of Technology: Lecture notes CT4145, 2020.

[32] E. M. J. Vicca, "Instability of a high-speed vehicle moving through a tunnel embedded in a viscco-elastic half-plane," Delft University of Technology , 2019.

[33] S. H. Strogatz, Nonlinear Dynamics and Chaos with Applications to Physiscs, Biology, Chemistry and Engineering, Boulder, CO: Westview Press, 2015.

[34] P. Wolf and e. al., "P, I, D, PI, PD, and PID Control," University of Michigan, December 2021.

[35] O.-o. c. system, "X-Engineer," [Online]. Available: https://x-engineer.org/on-off-control-system/. [Accessed 7th April 2022].

[36] A. Urquizo. [Online]. Available: https://en.wikipedia.org/wiki/PID_controller#/media/File:PID_en.svg. [Accessed 7th April 2022].

[37] K. Cui and X. Qin, "Virtual reality research of the dynamic characteristics of the soft soil under metro vibration loads based on BP neural networks," *Neural Computing and Applications,* pp. 1-10, 2017.

[38] F. Orban, "Damping of materials and members in structures," in *5th International Workshop on Multi-Rate Processes and Hysteresis*, Vancouver, 2011.

[39] D. Scott and J. Free, "Maglev: How they're getting trains off the ground?," *Popular Science,* p. 135, 1973.

ANNEX A: ELECTROMAGNETISM

The phenomenon of magnetic levitation is developed through magnetic fields between magnetic objects. Such magnetic fields are generated by the movement of electric charges. Let q be a moving charge at a velocity $\vec{v}$ that produces a magnetic field $\vec{B}$, as shown below (Fig. A.1) [29]. Then, this magnetic field is defined as:

$$\vec{\mathbf{B}} = \frac{\mu_0}{4\pi} \frac{q\vec{v} \times (\vec{r}/r)}{r^2} \tag{10.1}$$

From eq. 10.1, the magnitude of the field is given by

$$B = \frac{\mu_0}{4\pi} \frac{|q| v \sin\phi}{r^2} \tag{10.2}$$

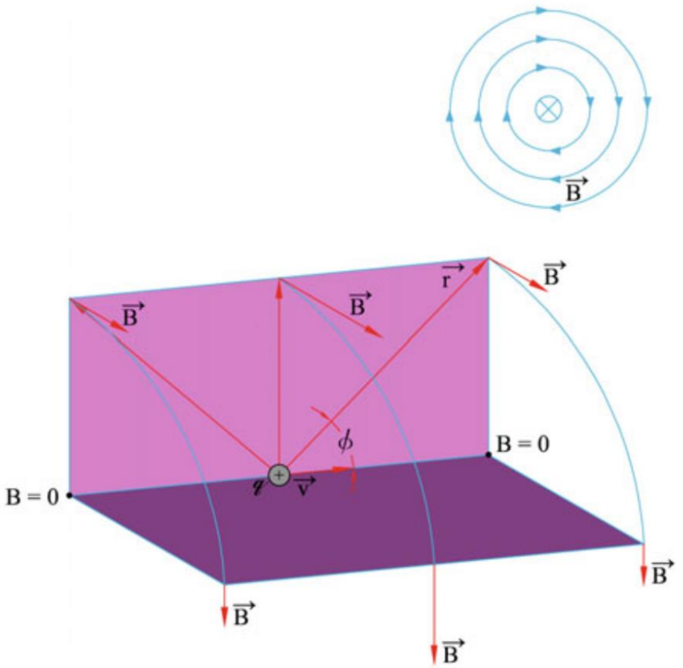

Figure A.1 Magnetic field produced by a moving electric charge [29]

This principle is the basis of permanent magnets and solenoids to produce magnetic fields. Such magnetic fields are generally represented by field lines with no beginning or end, forming closed loops. The field is spatial, as shown in Fig. A.2. The field lines come from the North pole (N) and enter the South pole (S). The lines are continuous and do not cross each other [29].

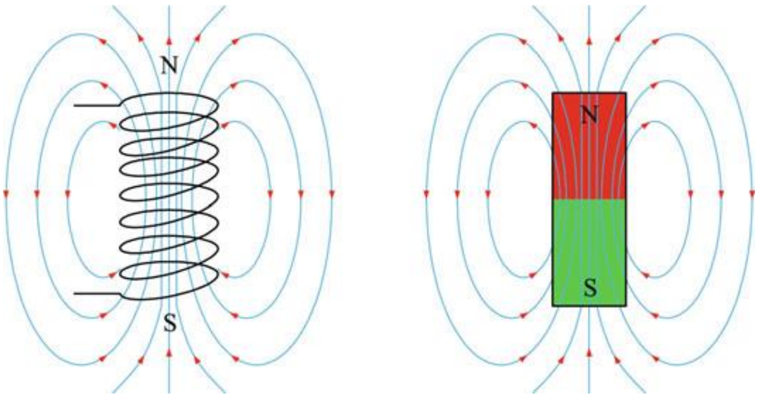

Figure A.2 Magnetic fields in solenoid (left) and permanent magnet (right) [29]

An attractive force is generated between two magnetized objects when the field lines go from one to another (Fig. A.3. a). Whereas if the same poles are facing each other, the field lines are pressured, resulting in a repulsive force between them (Fig. A.3. b) [29].

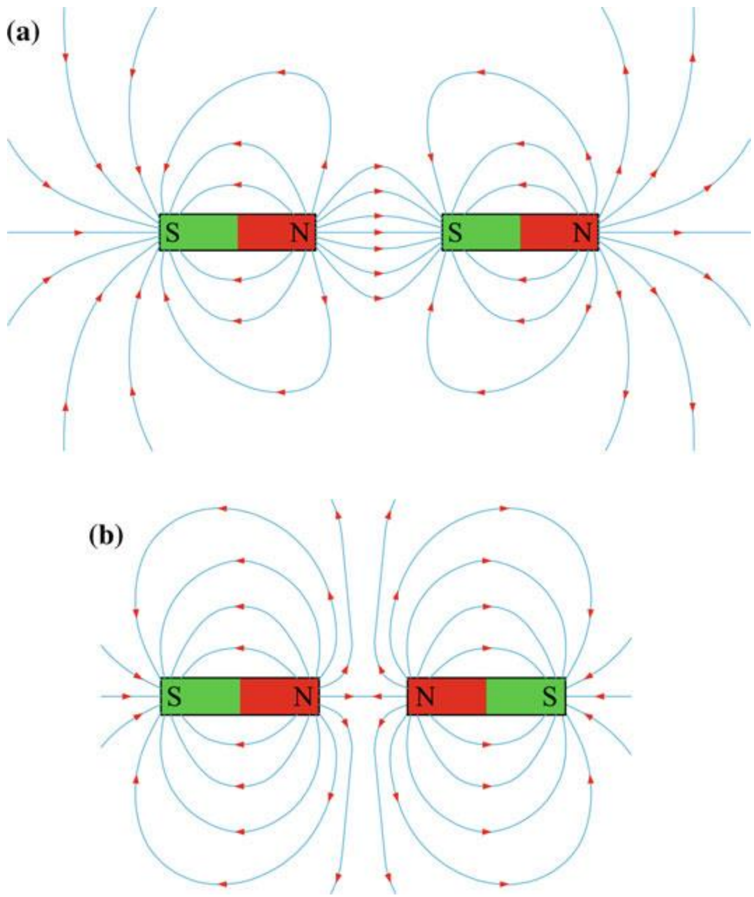

Figure A.3 Representation attraction (a) and repulsion (b) forces [29]

Although the permanent magnets and solenoids are the ones responsible for generating the magnetic field, some materials can be magnetized by an external magnetic field. This leads to the so-called magnetic substance. The most common types of these materials are iron, nickel, cobalt and most of their alloys. Ferromagnetic materials have the strongest capacity for magnetism. Whereas, diamagnetic materials do not respond to an applied magnetic field [29]. This phenomenon will take part in our system for the magnetization of the rail leading to a magnetic track.

A flux ϕ is a series of field lines. The value of the flux corresponds to the number of field lines. The more lines the stronger the magnetic field and the larger the flux. Consequently, the flux value is also seen as a measure of the magnetic field's strength. Its unit is the weber [Wb]. 1 Wb corresponds to 10^8 field lines. Then, the flux density B is defined as the flux per unit area normal to a magnetic field. Its unit is the tesla [T] [29]. B can be defined as follows

$$B = \frac{\phi}{A} \, [Wb / m^2] \tag{10.3}$$

If electrons flow through a conductor, a magnetic field is produced around it. This field is called an electromagnetic field, and the properties of the field are the same as the properties of a permanent magnet. The direction of the electromagnetic field is perpendicular to the wire and moves in the direction the fingers of your right hand would curl if you wrapped them around the wire with your thumb in the direction of the current, as shown in the following illustration (Fig A.4) [29].

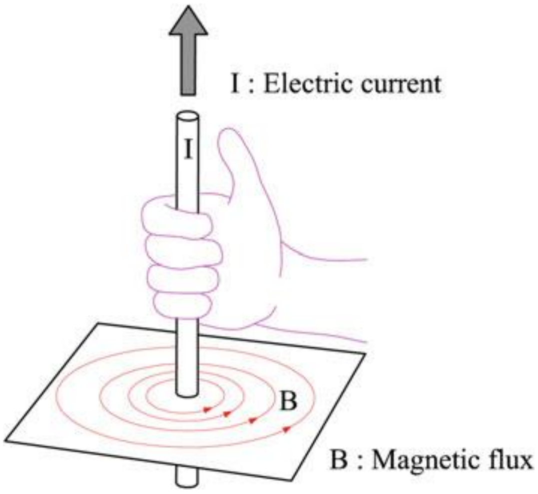

Figure A.4 Magnetic field formed around a conductor carrying current [29]

Magnetic permeability μ represents the relative ease of establishing a magnetic field in a given material. The permeability of free space is called μ_0, and its value is $\mu_0 = 4\pi \cdot 10^{-7}\ [H/m]$. Relative permeability of any material $\mu_r = \mu / \mu_0$ compared to μ_0 is a convenient way to compare its magnetization. For steels, the relative permeabilities range from 2000 to 6000 or higher. Thus, if an iron core is wound by coils carrying currents, almost all of the flux produced by the coils goes through the iron core, not air, which has a smaller permeability than that of iron [29].

Reluctance is a magnetic resistance in materials, which is the counterpart of electrical resistance. Let l be the length and A the area of the flux path [29]. Then reluctance $\Re$ is defined as

$$\Re = \frac{l}{\mu A} \tag{10.4}$$

Then, analogously to the voltage or electromotive force, the magnetomotive force is the cause of the magnetic flux in a magnetic circuit. Therefore, it can be defined as the effective current flow applied to the core. This can be mathematically described by eq. 10.5 as a function of the electrical current I and the number of coils turns N and graphically illustrated by the magnetic circuit below (Fig. A.5) [29].

$$F_m = NI\ [A \cdot\ N^o\ turns] \tag{10.5}$$

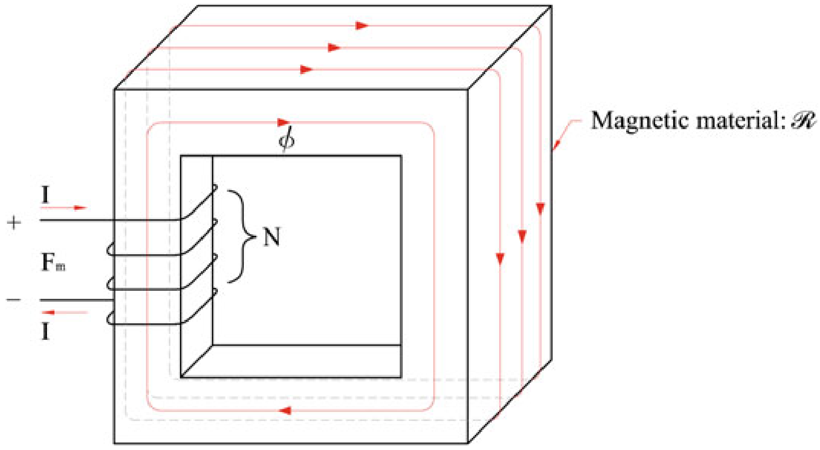

Figure A.5 Simple magnetic circuit [29]

Then, all the magnetic fields produced by the current will remain inside the core because the core's permeability is higher than air and the flux of the magnetic circuit is defined as [29]

$$\phi = \frac{F_m}{\Re} \tag{10.6}$$

An electromagnet is defined as a type of magnet in which the magnetic field is produced by an electric current. Generally, it consists of a large number of closely spaced turns of wire that create the magnetic field. The wire turns are often wound around a magnetic core made from ferromagnetic materials. The magnetic core concentrates the magnetic flux and makes a more powerful magnet. The main advantage of an electromagnet over a permanent magnet is that the magnetic field can be quickly changed by controlling the amount of electric current in the winding. The direction of a magnetic field is dependent on the direction of the electric current [29].

The degree to which a magnetic field by a current can magnetize a material is called magnetizing force H, and it is defined as the magnetomotive force F_m per unit length of material [29]. That is

$$H = \frac{F_m}{l} = \frac{NI}{l} \; [A \cdot \; n^o \, turns \, / \, m] \tag{10.7}$$

H is not related to a material's property. The magnetic flux B induced in the material depends upon the nature of the material [29], and the relationship between H and B is defined by

$$B = \mu H \tag{10.8}$$

Note that the flux in the materials is related linearly to the applied magnetomotive force in the unsaturated region, and approaches a constant value regardless of the magnetomotive force in the saturated region. Due to this behaviour, the operational region of EMS systems should be located in the unsaturated region [29].

Applying an alternating current to the windings on the core instead of a direct current with a frequency, the flux in the core traces out a path *abcdeb* in Fig. A.6. This is because the amount of flux present in the core depends not only on the amount of current applied to the winding of the core but also on the previous history of the flux in the core. This dependence on the preceding flux history and the resulting failure to trace flux paths is called hysteresis. The path *bcdeb* traced out in Fig. A.6 as the applied current changes are called a hysteresis loop. If the frequency of an alternating current is changed, the path is also changed with a different residual flux. This property may lower the control performance at higher frequencies in a levitation system with electromagnets [29].

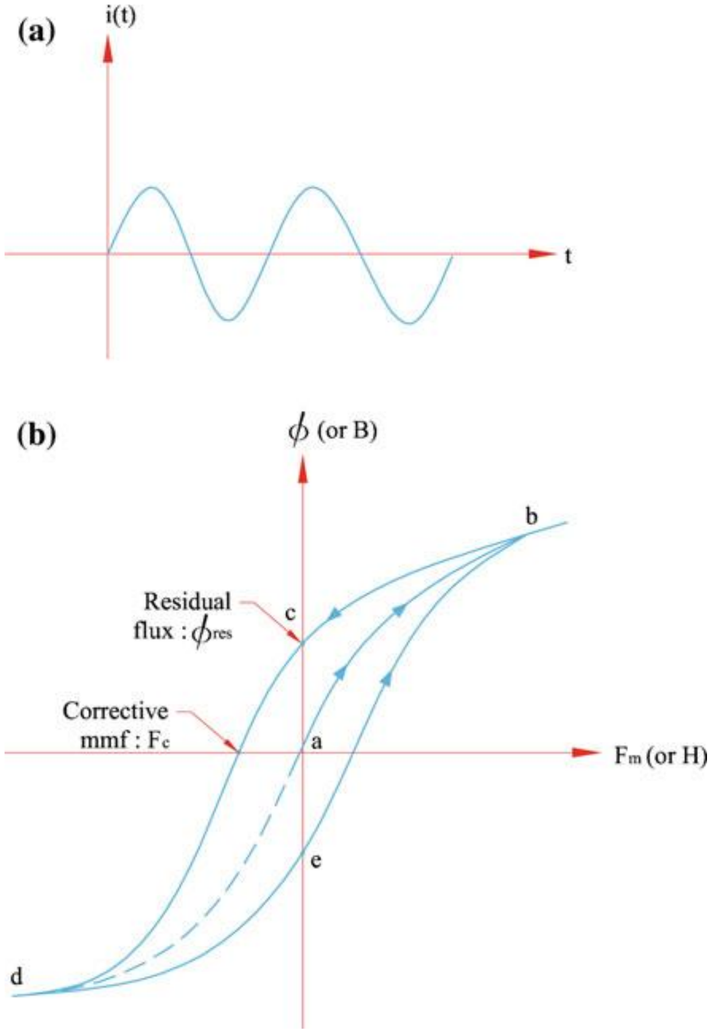

Figure A.6 The hysteresis loop traced out by the flux in a core when the alternating current is applied to it: a) alternating current, and b) hysteresis loop [29]

When a conductor is exposed to a time-varying magnetic field, a voltage is induced across it, as shown in the figure below (Fig. A.7). This can be mathematically described using Faraday's law of induction. Electric generators and motors as well as magnetic levitation systems are based on this electromagnetic induction. The polarity of induced voltage depends on the direction of relative motion [29]. Expressed in the form of an equation for induced voltage e_{ind}

$$e_{ind} = -N\frac{d\phi}{dt} \tag{10.9}$$

Where the minus sign in eq. 2.9 is an expression of Lenz's law [29].

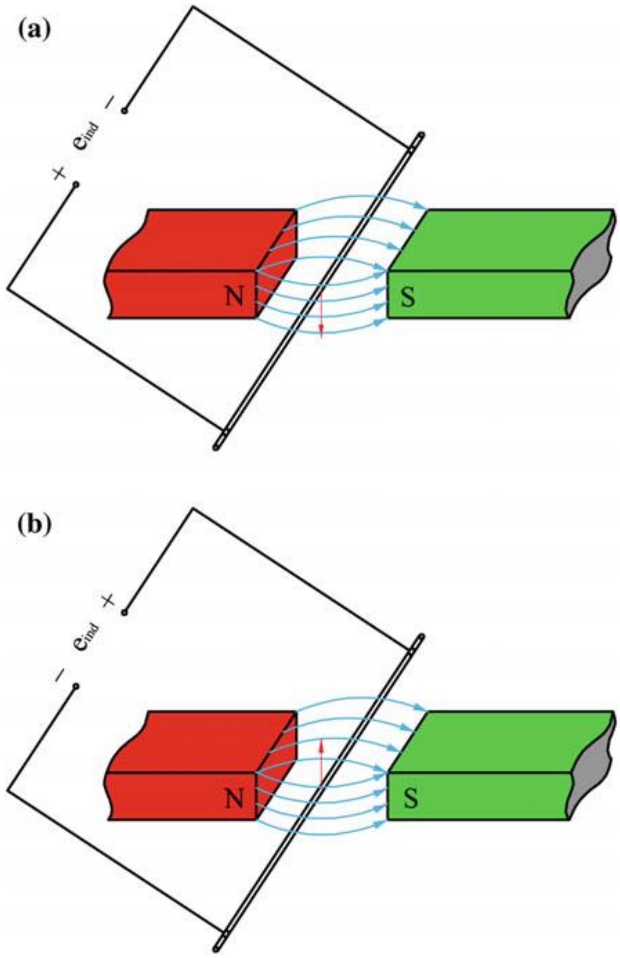

Figure A.7 Electromagnetic induction [29]

If a conductor has electrical resistance, an electrical current flows in the conductor. This current is called induced current i_{ind}. This is represented in the following figure (Fig. A.8) [29].

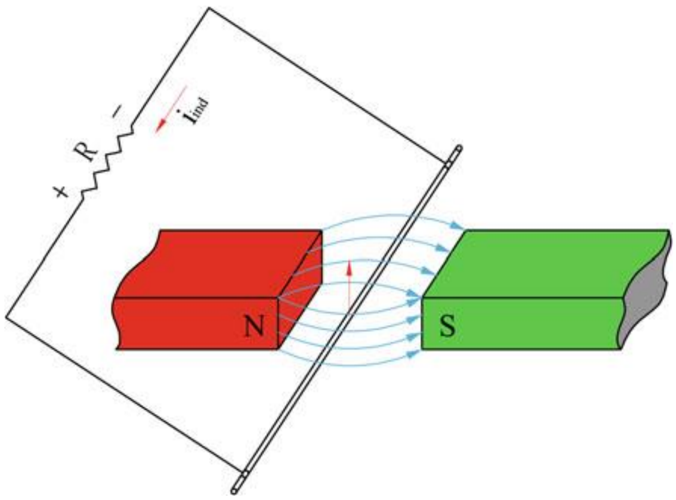

Figure A.8 Induced current [29]

If the directions of the flux lines from magnets and conductors are the same, the flux density increases. In contrast, if the directions are opposite, the flux density decreases. The resulting forces are exerted towards a weak magnetic pressure region from a stronger pressure region, as illustrated below (Fig. A.9). This is the operating principle of electric motors [29].

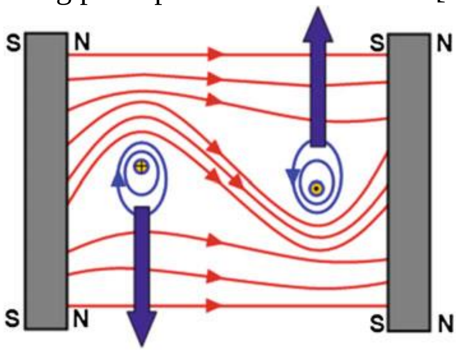

Figure A.9 Forces on current-carrying conductors in magnetic field [29]

In electromagnetism and electronics, inductance is the property of a conductor by which a change in current flowing through it induces a voltage or electromotive force in both the conductor itself (i.e. self-inductance) and any nearby conductors (i.e. mutual inductance). A changing electric current through a circuit that contains inductance induces a proportional voltage that opposes the change in current, as illustrated below (Fig. A.10). It is customary to use the symbol L for inductance. The unit for inductance is the henry $[H]$. The relationship among the parameters for a coil with inductance L is defined as [29]

$$V = IR - L\frac{dI}{dt} \tag{10.10}$$

where

$$L = \frac{N^2 \mu A}{l}$$

Eq. 10.10 indicates that inductance opposes the applied voltage. This property to oppose building up currents influences the control performance of levitation systems with electromagnets [29]. This is the theoretical derivation of the core part of the equation of motion relating the electrical variables to the mechanical variables governing the EMS system defined for this project. This relation is effectively derived using Kirchhoff’s total voltage law.

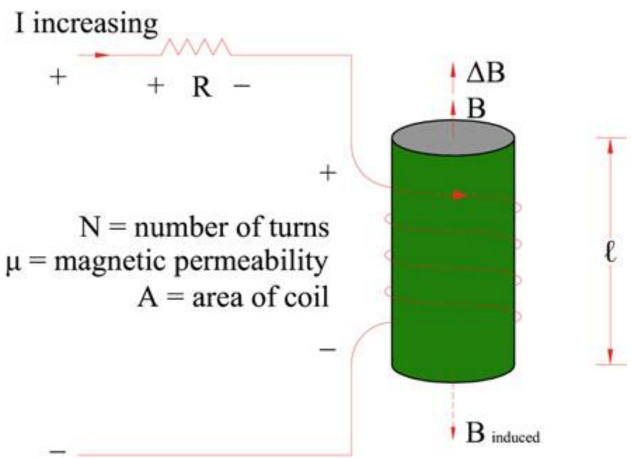

Figure A.10 Coil's reaction to increasing current [29]

ANNEX B:
STRUCTURAL DYNAMICS REVIEW

B.1. SINGLE DEGREE OF FREEDOM

Let us take a simple Single Degree Of Freedom (SDOF) mass-spring-dashpot system like the one represented below (Fig. B.1), where M is the lumped mass, k_0 is the spring stiffness, c_0 is the damping coefficient, $F(t)$ is a random time-dependent force acting on the lumped mass, and $y(t)$ is the DOF representing the vertical motion of the lumped mass.

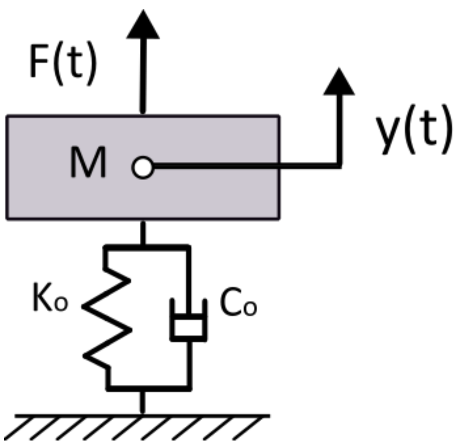

Figure B.1 SDOF mass-spring-dashpot system with F(t) random time-dependent external load

The equation of motion for such a system can be then obtained using the Newton's second law, expressing the equilibrium of forces acting on the lumped mass. For $\mathbf{y}(t) = \mathbf{y}$ notation, the equation is expressed as

$$\mathbf{F}(t) + \mathbf{F}_{spring}(t) + \mathbf{F}_{dashpot}(t) = M\,\ddot{\mathbf{y}} \tag{11.1}$$

Where $\mathbf{F}_{spring}(t)$ is the force exerted by the spring such that $\mathbf{F}_{spring}(t) = -k_0\mathbf{y}$ and $\mathbf{F}_{dashpot}(t)$ is the viscous resistance associated to the dashpot such that $\mathbf{F}_{dashpot}(t) = -c_0\dot{\mathbf{y}}$.

Keep in mind that all terms in eq. 11.1 are vectors. Substituting the aforementioned force definitions in eq. 11.1 and projecting the result onto the y-axis, the following expression is obtained

$$M\,\ddot{y} + c_0\dot{y} + k_0 y = F(t) \to \ddot{y} + 2\xi\omega_n\dot{y} + \omega_n{}^2 y = \frac{F(t)}{M} \tag{11.2}$$

Where ξ is a measure for the viscous damping in the system such that $\xi = (1/2\omega_n)(c_0/M)$, and ω_n is the natural frequency of the undamped system such that $\omega_n = \sqrt{k_0/M}$.

For which non-zero initial conditions can be defined as

$$y(0) = y_0\,;\ \dot{y}(0) = v_0 \tag{11.3}$$

At this point, two main cases can be differentiated: free vibrations and forced vibrations. The only main difference is the right-hand side term of the equality presented in eq. 11.2.

B.1.1. Free Vibrations

This is the case in which the external force $F(t)$ is absent. Then eq 11.2 reduces to a homogeneous differential equation

$$\ddot{y} + 2\xi\omega_n\dot{y} + \omega_n{}^2 y = 0 \tag{11.4}$$

This equation governs small free vibrations of the mass-spring-dashpot system [31]. The general solution of this second-order differential equation can be written as

$$y(t) = \sum_{n=1}^{2} Y_n \exp(s_n t) \tag{11.5}$$

Then, if eq. 11.5 is substituted in eq. 11.4 the following expression representing the characteristic equation of the system is obtained

$$s_n{}^2 + 2\xi\omega_n s_n + \omega_n{}^2 = 0 \tag{11.6}$$

Where s_n are the characteristic exponents, also called eigenvalues of the system, which can be easily obtained by solving the second-order polynomial characteristic equation eq. 11.6.

$$s_{1,2} = -\xi\omega_n \pm \omega_n\sqrt{\xi^2 - 1} \tag{11.7}$$

Thereby, the general solution for a single degree of freedom mass-spring-dashpot can be described.

$$y(t) = Y_1 \exp(s_1 t) + Y_2 \exp(s_2 t) = \exp(-\xi\omega_n t)[Y_1 \exp(\omega_n\sqrt{\xi^2 - 1}\ t) + Y_2 \exp(\omega_n\sqrt{\xi^2 - 1}\ t)] \tag{11.8}$$

Where Y_1 and Y_2 are arbitrary constants [31].

Four different solutions/behaviours can be distinguished depending on the value of the damping coefficient ξ:

1) $\xi = 0$ → Undamped vibrations:

The characteristics exponents, in this case, are defined as $s_{1,2} = \pm i\omega_n = \pm i\sqrt{k_0 / M}$. Hence, the general solution is expressed as

$$y(t) = Y_1 \exp(i\omega_n\, t) + Y_2 \exp(-i\omega_n\, t) \tag{11.9}$$

Then, Euler's formula can be used to express the exponential function as a trigonometric relation, which yields eq. 11.10, where A and B are unknown real-valued constants.

$$\begin{aligned} y(t) &= Y_1 (\cos(\omega_n t) + i\sin(\omega_n t)) + Y_2 (\cos(\omega_n t) - i\sin(\omega_n t)) = \\ &= (Y_1 + Y_2)\cos(\omega_n t) + i(Y_1 - Y_2)\sin(\omega_n t) = A\cos(\omega_n t) + B\sin(\omega_n t) \end{aligned} \tag{11.10}$$

A and B can be found by substituting eq. 11.10 into the initial conditions eq. 11.3.

$$A = y_0\, ;\; B\omega_n = v_0 \tag{11.11}$$

Thereby, the equation of motion of the undamped lumped mass M within the mass-spring- dashpot system from its equilibrium point is expressed as

$$y(t) = y_0 \cos(\omega_n t) + \frac{v_0}{\omega_n}\sin(\omega_n t) \tag{11.12}$$

For a better comprehension of the results plotted in the figure below (Fig. B.2), eq. 11.12 can be equivalently written as

$$y(t) = A_0 \cos(\omega_1 t - \varphi_0) \tag{11.13}$$

Where the amplitude A_0 and the phase angle φ_0 read

$$A_0 = \sqrt{{y_0}^2 + (\frac{v_0}{\omega_n})^2}\ ;\ \varphi_0 = \arctan(\frac{v_0}{\omega_n y_0}) \tag{11.14}$$

By plotting the displacement-time curve in accordance with eq. 2.24 (Fig. 2.16), one can see that vibrations of the mass-spring system are perfectly sinusoidal and last forever. In reality there almost always exist some damping (energy loss) in vibration systems. This damping causes the oscillatory motion induced by the initial disturbance to be reduced to zero over time [31].

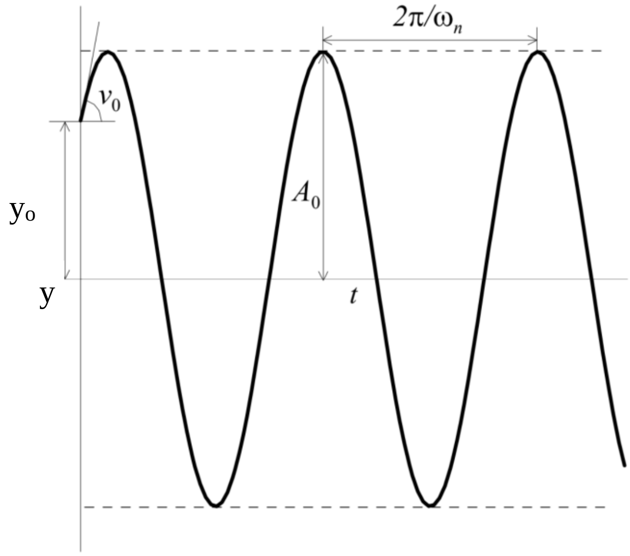

Figure B.2 Free Vibrations of the mass-spring system $\xi = 0$ *[31]*

2) $\xi \leq -1 \vee \xi > 1$ → Super-critically damped vibrations:

In this case, both characteristic exponents are real-valued. Hence, the general solution is expressed as

$$y(t) = A\exp[(-\omega_n\xi - \omega_n\sqrt{\xi^2 - 1})t] + B\exp[(-\omega_n\xi + \omega_n\sqrt{\xi^2 - 1})t] \tag{11.15}$$

Where coefficients A and B can be determined by imposing initial conditions. In this case, let's consider the particular case $y(0) = y_0;\ \dot{y}(0) = 0$ and substituting these into eq. 11.15 yields

$$A = -\frac{y_0(-\xi\omega_n - \omega_n\sqrt{\xi^2 - 1})}{2\omega_n\sqrt{\xi^2 - 1}};\ B = \frac{y_0(-\xi\omega_n + \omega_n\sqrt{\xi^2 - 1})}{2\omega_n\sqrt{\xi^2 - 1}} \tag{11.16}$$

Thereby, the equation of motion of the super-critically damped lumped mass M within the mass-spring-dashpot system from its equilibrium point is expressed as

$$y(t) = \frac{y_0}{2\omega_n\sqrt{\xi^2-1}}\{(-\omega_n\xi + \omega_n\sqrt{\xi^2-1})\exp[(-\omega_n\xi - \omega_n\sqrt{\xi^2-1})t] + \\ +(-\omega_n\xi - \omega_n\sqrt{\xi^2-1})\exp[(-\omega_n\xi + \omega_n\sqrt{\xi^2-1})t]\} \tag{11.17}$$

In connection with this solution, it should be noted that both s_1 and s_2 are negative, s_2 having a bigger absolute value. Thus, the displacement y of the mass has the same sign as y_0 and approaches zero as a limit when time tends to infinity. The displacement-time diagram plotted in accordance with eq. 11.17 is shown below (Fig. B.3), where we see that the motion is not a vibration at all, but an aperiodic motion in which the suspended mass, after its initial displacement, gradually creeps back toward the equilibrium position but takes theoretically infinite time to get there [31].

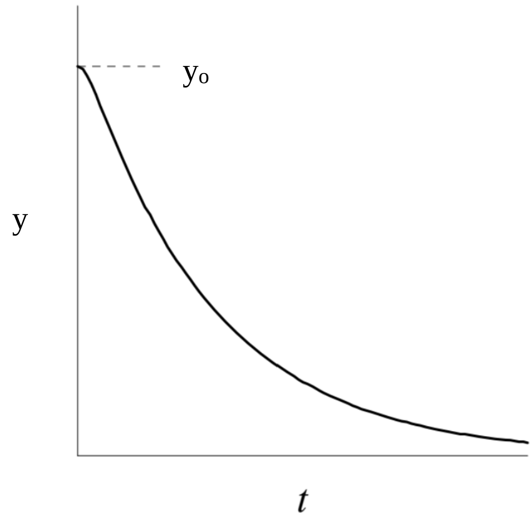

Figure B.3 Aperiodic free motion of mass-spring-dashpot system $\xi \le -1 \vee \xi > 1$ [31]

3) $-1 < \xi < 1 \wedge \xi \neq 0$ → Sub-critically damped vibrations:

In this case, both characteristic exponents are complex-valued. Aiming at clearly showcase the physical significance, a change of the eigenvalues structure introducing real positive values $\omega_1 = \omega_n\sqrt{1-\xi^2}$ is helpful. Then the characteristic exponents read

$$s_{1,2} = -\xi\omega_n \pm i\omega_1 \tag{11.18}$$

Hence, the general solution is expressed as

$$y(t) = \exp(-\xi\omega_n t)[A\cos(\omega_1 t) + B\sin(\omega_1 t)] \tag{11.19}$$

As performed in previous cases, the eq. 11.19 must be substituted in the initial conditions, in this case general initial conditions eq. 11.3, so as to obtain the expressions for arbitrary constants A and B.

$$A = y_0\ ;\ B = \frac{v_0}{\omega_1} + \frac{\xi\omega_n y_0}{\omega_1} \tag{11.20}$$

Thereby, the equation of motion of the sub-critically damped lumped mass M within the mass-spring-dashpot system from its equilibrium point is expressed as

$$y(t) = \exp(-\xi\omega_n t)[y_0 \cos(\omega_1 t) + (\frac{v_0}{\omega_1} + \frac{\xi\omega_n y_0}{\omega_1})\sin(\omega_1 t)] \tag{11.21}$$

For a better comprehension of the results plotted in the figure below (Fig. B.4), eq. 11.21 can be equivalently written as

$$y(t) = A_0 \exp(-\xi\omega_n t)\cos(\omega_1 t - \varphi_0) \tag{11.22}$$

Where the amplitude A_0 and the phase angle φ_0 read

$$A_0 = \sqrt{{y_0}^2 + (\frac{v_0}{\omega_1} + \frac{\xi\omega_n y_0}{\omega_1})^2}\ ;\ \varphi_0 = \arctan(\frac{v_0 + \xi\omega_n y_0}{\omega_1 y_0}) \tag{11.23}$$

By plotting the displacement-time curve in accordance with eq. 11.22 (Fig. B3), one can see that this motion is vibratory in nature and represents damped free vibrations. The main effect of damping on free vibrations is that it dissipates energy from the system leading to a decay of the amplitude of vibrations [31].

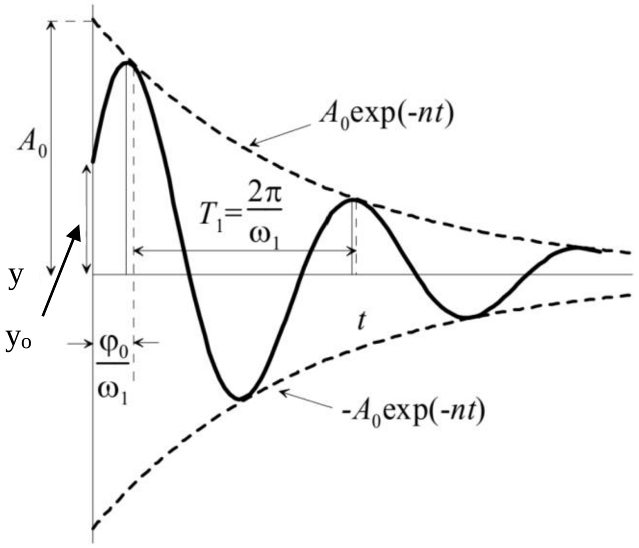

Figure B.4 Free vibrations of mass-spring-dashpot system $-1 < \xi < 1 \wedge \xi \neq 0$ *[31]*

In this manner, Fig. B.4 shows that each time that $\cos(\omega_1 t - \varphi_0)$ becomes equal to ± 1, the time-displacement curve is tangent to one of the envelopes $\pm A_0 \exp(-\xi\omega_n t)$ at the ordinates $t = \varphi_0 / \omega_1$, $t = (\varphi_0 + \pi)/\omega_1$, $t = (\varphi_0 + 2\pi)/\omega_1 \dots$. This quantity is called the amplitude of vibration. It is seen that, owing to damping, the amplitude gradually diminishes with time and that the rate of decay depends on the damping factor ratio ξ. The time $T_1 = 2\pi / \omega_1$

required to complete one cycle of the motion is called the period of vibration and its reciprocal $f_1 = \omega_1 / 2\pi$ is called frequency of vibration [31].

4) $\xi = 1$ → Critically damped system:

This is a special case of aperiodic motion for which the value of the damping coefficient corresponds to the so called critical damping, which is defined as

$$c_0 = 2\xi\omega_n m = 2\sqrt{km} \tag{11.24}$$

Along these lines, the characteristic exponents of the system are equal $s_{1,2} = -\omega_n$, i.e. there is one eigenvalue with multiplicity 2. This yields the following general solution

$$y(t) = A\exp(-\omega_n t) + Bt\exp(-\omega_n t) \tag{11.25}$$

B.1.2. Forced Vibrations

This is the case in which the external force $F(t)$ is present. Then, the equation of motion of the system is described by the second order inhomogeneous differential equation eq 11.2. Thereby, one should address this problem by breaking the solution into two pieces: a homogeneous solution and a particular solution. The homogeneous solution $y_h(t)$ is exactly the same as the aforementioned general solution for the free vibrations motion. Whereas the particular solution $y_p(t)$ carries with it a bit more complexity.

In case the shape of the function of time $F(t)$ is well known, as in the case of a harmonic force, generally, it can be obtained choosing a solution defined with a generic function with unknown parameters with the same shape as the load, i.e. with equal time signature than the load. Then, one can compute the unknown coefficients substituting the generic solution function selected into the equation of motion of the system. Lastly, the final solution to the problem is obtained by summing both parts as

$$y(t) = y_h(t) + y_p(t) \tag{11.26}$$

As an example, consider the dynamic response of the mass-spring-dashpot system to a harmonic sinusoidal force given by $F(t) = F_0\cos(\omega t)$. Then the equation of motion of the system considering the same notation used in the section above reads

$$\ddot{y} + 2\xi\omega_n\dot{y} + \omega_n y = f_0\cos(\omega t) \tag{11.27}$$

Where $f_0 = F_0 / M$.

The harmonic solution (i.e. general solution) to eq. 11.27 is given by eq. 11.19. Whereas, the particular solution to eq. 11.27 is found as

$$y_p = Y_c \cos(\omega t) + Y_s \sin(\omega t) \tag{11.28}$$

Where Y_c and Y_s are unknown constants which can be found by substituting eq. 2.39 into eq. 11.27. yielding

$$(-\omega^2 Y_c + 2\xi\omega_n Y_s + \omega_n{}^2 Y_c - f_0)\cos(\omega t) + (-\omega^2 Y_s - 2\xi\omega_n Y_c + \omega_n{}^2 Y_s)\sin(\omega t) = 0 \tag{11.29}$$

This equation can be satisfied for all values of t only if the expressions in parenthesis vanish. Thus, for calculating Y_c and Y_s, one has to solve the following system of linear algebraic equations [31]

$$\begin{cases} -\omega^2 Y_c + 2\xi\omega Y_s + \omega_n{}^2 Y_c = f_0 \\ -\omega^2 Y_s - 2\xi\omega Y_c + \omega_n{}^2 Y_s = 0 \end{cases} \tag{11.30}$$

From which it is obtained

$$\begin{cases} Y_c = f_0 \dfrac{(\omega_n{}^2 - \omega^2)}{(\omega_n{}^2 - \omega^2)^2 + 4\xi^2\omega_n{}^2\omega^2} \\ Y_s = f_0 \dfrac{2\xi\omega_n\omega}{(\omega_n{}^2 - \omega^2)^2 + 4\xi^2\omega_n{}^2\omega^2} \end{cases} \tag{11.31}$$

The last step, is to introduce the initial conditions in the overall solution so as to find the initial value problem.

However, the approach on this particular solution changes if the load function shape is not well known or it is wanted to be kept generic, as in the case of forced vibrations under a general disturbing force. Let's now consider the following equation of motion and initial conditions

$$\begin{aligned} &\ddot{y} + 2\xi\omega_n\dot{y} + \omega_n{}^2 y = f(t) \\ &y(0) = y_0\,;\ \dot{y}(0) = v_0 \end{aligned} \tag{11.32}$$

Assuming that the external force per unit mass $f(t)$ is an arbitrary function of time. For any instant of time one elementary impulse $f(t')dt'$ can be considered. In accordance with Newton's second law, this one impulse imparts to each unit of mass an instantaneous increase in velocity $d\dot{x} = f(t')dt'$. Treating the increment of velocity as if it was an initial velocity at instant t' and using eq. 11.21, it can be concluded that the corresponding displacement of the mass-spring-dashpot system at any later time will be [31]

$$y(t) = \exp(-\xi\omega_n(t-t'))\frac{f(t')dt'}{\omega_1}\sin(\omega_1(t-t')) \tag{11.33}$$

Note that this expression holds both for sub- and super-critically dumped vibrations, but only the nature of ω_1 changes.

Since each impulse $f(t')dt'$ between $t'=0$ and $t'=t$ has a like effect, as a result of the continuous action of the external force, the following displacement of the mass is obtained [31]

$$y(t) = \frac{1}{\omega_1}\int_0^t f(t')\exp(-\xi\omega_n(t-t'))\sin(\omega_1(t-t'))dt' \tag{11.34}$$

The complete solution to the initial value problem eq. 11.32, eq. 11.21 and 11.34 need to be added up. Bear in mind that eq. 2.32 represents the system response to the initial conditions [31]

$$\begin{aligned} y(t) &= \exp(-\xi\omega_n t)[y_0\cos(\omega_1 t) + (\frac{v_0}{\omega_1} + \frac{\xi\omega_n y_0}{\omega_1})\sin(\omega_1 t)] + \\ &+ \frac{1}{\omega_1}\int_0^t f(t')\exp(-\xi\omega_n(t-t'))\sin(\omega_1(t-t'))dt' \end{aligned} \tag{11.35}$$

An important remark is the concept of steady state response. Which is defined as a stationary situation that remains after the transient motion has died out over time [32].

$$y_{steady}(t) = \lim_{t\to\infty} y(t) \tag{11.36}$$

In case the system is dynamically unstable, the vibrations doe not decay, but grow exponentially, which means that the steady state response is never reached [32].

B.1.3. SDOF Stability with respect to Damping

On a side note, aiming at understanding a bit more the role of damping in the system's stability, certain definitions about the stability of the system can be listed. For a simple SDOF system as the one presented in this section, the stability of the system is directly related with damping.

In a dynamical system, one can define instability as the phenomenon that takes place when small initial perturbation grows in time. In this case, the system does not return to its equilibrium position. This phenomena cannot happen for the critically damped vibration and the undamped vibrations case (i.e. $\xi = 0 \wedge \xi = 1$), since they are always stable. However, when $\xi \neq 0 \wedge \xi \neq 1$ instability may occur [32].

On the one hand, if the system presents sub-critically damped vibrations, the term directly determining the stability of the system for both general solution forms eq. 11.19 and eq. 11.22 is the term $\exp(-\xi\omega_n t)$. Whereas the rest of the equation describes the sinusoidal vibration without any grow or decay. Remind that, for this specific case, both characteristic exponents have a positive real part. In this manner one can argue that: if $0 < \xi < 1$, the exponent remains negative, leading to an exponential decay which describes stability, i.e. fading of small perturbation induced vibrations over time; if $-1 < \xi < 0$, the exponent becomes positive, leading to an exponential growth which describes instability, i.e. small perturbation induced vibrations grow over time.

On the other hand, if the system presents super-critically damped vibrations, the relation is directly derived, considering the aperiodic motion nature. If $\xi > 1$, the system is stable as negative exponentials governs the general solution expression. If $\xi \le -1$, the system is unstable as positive exponentials governs the general solution expression.

Superposing the aforementioned main points, it is concluded that the SDOF system is unstable for negative damping coefficient values $\xi < 0$.This means that, when the system is negatively damped, the characteristic exponents have negative real part.

B.2. MULTIPLE DEGREE OF FREEDOM

In this thesis several models present a higher level of complexity, entailing a discretization into more than one single degree of freedom. In these cases, the principles discussed above for SDOF systems also applies. However, the equation of motion of the system is defined in matrix form.

$$[\mathbf{M}]\{\ddot{y}\}+[\mathbf{C}]\{\dot{y}\}+[\mathbf{K}]\{y\}=\{f\} \tag{11.37}$$

Where $[\mathbf{M}]$, $[\mathbf{C}]$ and $[\mathbf{K}]$ are $N \times N$ squared matrices accounting for mass, viscous damping and stiffness, respectively. Where N is the number of degrees of freedom of the system. Through this matrices, the coupling between several degrees of freedom is defined. Several different coupling situations can be observed depending on the nature of the system. If a spring or a spring-dashpot connects two lumped masses, the coupling between the degrees of freedom associated to such lumped masses is then manifested in the stiffness matrix and, if applicable, the damping matrix. However, for other type of connections between two lumped masses, the coupling between the degrees of freedom associated to such lumped masses may appear in the mass matrix, yielding an inertial coupling. Even in some cases, several different degrees of freedom might be decoupled.

If there is no damping, the solution of the system can be assumed to have the form below [29]

$$\{x\}=\{X\}\exp(is_n t) \tag{11.38}$$

Substituting this general solution in the undamped system equation of motion yields

$$\{X\}\exp(is_n t)([\mathbf{M}]\{s_n\}^2+[\mathbf{K}])=0 \tag{11.39}$$

The system has a non-trivial solution if the determinant of its coefficient matrix vanishes [31]. This defines the eigenvalue problem. The solution to this problem should yield N eigenvalues and when the eigenvalues are substituted back into the original set of equations, the values of $\{x\}$ that correspond to each eigenvalue are eigenvectors. These eigenvectors represent the mode shapes of the systems [29]. This means that it is the shape that the system takes when excited to the eigenfrequency associated to the eigenvector. This is important in order to understand the interaction between the degrees of freedom.

B.3. SIMPLY SUPPORTED EULER-BERNOULLI BEAM MODAL VIBRATION

As already mentioned in chapter 1, one of the objectives of this thesis is to analyse and understand the dynamics, the coupling and the stability vehicle-track infrastructure. Along these lines, as most of the sources presented in the literature review (chapter 2.1.5) pointed out, the flexibility of the guideway has a significant impact on the levitation stability ([30], [16]).

In this project, focus has been put on the tubular infrastructure of the Hyperloop design. This is one of the main differences from Maglev applications. Indeed one of the innovations of this thesis is the focus of the structural behaviour of this feature and its effect on the system stability.

Along these lines, one span of track is modeled as a simply supported, evenly elastic with equal cross-section Euler-Bernoulli beam, which yields the following equation

$$EI\frac{\partial^4 w(x,t)}{\partial x^4}+c\frac{\partial^5 w(x,t)}{\partial x^4\partial t}+\rho A\frac{\partial^2 w(x,t)}{\partial t^2}=f(x,t) \tag{11.40}$$

Where $w(x,t)$ is the transverse deflection as a function of the longitudinal axis of the beam x and time t, E is the Young's modulus, I is the second moment of inertia of the beam cross-section, c is the structural element damping, ρ is the mass density of the beam material, A is the cross-sectional area of the beam, and $f(x,t)$ is the external vertical loading on the beam.

Simply supported boundary conditions for a beam of length L supported at each end can be described as

$$\begin{aligned} x=0:\ w(x,t)=\frac{\partial^2 w(x,t)}{\partial x^2}=0 \\ x=L:\ w(x,t)=\frac{\partial^2 w(x,t)}{\partial x^2}=0 \end{aligned} \tag{11.41}$$

B.4. LAPLACE TRANSFORM

The Laplace transform is an integral transform which serves to transform signals and functions from the time domain to the frequency domain. This tool is particularly useful in order to solve linear ordinary differential equations, since in the frequency domain, these become simply algebraic equations. The Laplace transform of a function $G(t)$ is defined as

$$\Im_t[G(t)]=g(s)=\int_0^{+\infty} G(t)\exp(-st)dt \tag{11.42}$$

Where $G(t)$ is a function of the real variable t and s is the complex variable, i.e. $s=\sigma+i\omega$. $G(t)$ is called the original function and $g(s)$ is called the image function [31].

The operations, which are valid for the Laplace transform are shown in Table B.1.

Table B.1 Operations for Laplace transform [31]

	Original Function $G(t)$	Image Function $g(s)$
Definition	$G(t)$	$\int_0^\infty G(t)\exp(-st)\,dt$
Inversion Formula	$\frac{1}{2\pi i}\int_{\sigma-i\infty}^{\sigma+i\infty} g(s)\exp(st)\,dt$	$g(s)$
Linearity Property	$AG_1(t)+BG_2(t)$	$Ag_1(s)+Bg_2(s)$
Differentiation	$G'(t)$ $G''(t)$ $G^{(n)}(t)$	$sg(s)-G(0)$ $s^2g(s)-sG(0)-G'(0)$ $s^ng(s)-s^{n-1}G(0)-...G^{(n-1)}(0)$
Integration	$\int_0^\infty G(\tau)\,d\tau$	$\frac{1}{s}g(s)$
Convolution Theorem	$\int_0^t G_1(t-\tau)G_2(\tau)\,d\tau$	$g_1(s)g_2(s)$
Translation	$G(t-b)H(t-b),\ b>0$	$\exp(-bs)g(s)$

This method will prove to be very useful to compute the poles of our linearized system around the fixed points, given that the equations of motion are all linear ordinary differential equations. Besides, it makes the implementation of a control within the system easier to analyse and formulate in the frequency domain in case a study of the transfer functions, the frequency bandwidth of stabilization or a phase delay analysis wants to be performed.

Below, a table of Laplace transforms is presented (Table B.2), for the formulation of general functions of the real variable t and the complex variable s.

Table B.2 Table of Laplace transforms [31]

$g(s)$	$G(t)$
$1/s$	1
$1/s^2$	t
$1/s^n$	$t^{n-1}/(n-1)!$

$g(s)$	$G(t)$
$1/\sqrt{s}$	$1/\sqrt{\pi t}$
$s^{-(n+1/2)},\ n=1,2,3,\ldots$	$2^n t^{n-1/2}/\left((2n-1)!\sqrt{\pi}\right)$
$1/(s+a)$	$\exp(-at)$
$1/(s+a)^2$	$t\exp(-at)$
$1/(s+a)^n$	$t^{n-1}\exp(-at)/(n-1)!$
$\dfrac{1}{(s+a)(s+b)}\ (a\neq b)$	$\dfrac{\exp(-at)-\exp(-bt)}{b-a}$
$\dfrac{s}{(s+a)(s+b)}\ (a\neq b)$	$\dfrac{a\exp(-at)-b\exp(-bt)}{a-b}$
$\dfrac{1}{s^2+a^2}$	$\dfrac{1}{a}\sin(at)$
$s/(s^2+a^2)$	$\cos(at)$
$1/(s^2-a^2)$	$\sinh(at)/a$
$\dfrac{s}{s^2-a^2}$	$\cosh(at)$
$\dfrac{1}{s(s^2+a^2)}$	$\dfrac{1}{a^2}(1-\cos(at))$
$\dfrac{1}{s^2(s^2+a^2)}$	$\dfrac{1}{a^3}(at-\sin(at))$
$\dfrac{1}{(s^2+a^2)^2}$	$\dfrac{1}{2a^3}(\sin(at)-at\cos(at))$
$\dfrac{s}{(s^2+a^2)^2}$	$\dfrac{t}{2a}\sin(at)$
$\dfrac{s^2}{(s^2+a^2)^2}$	$\dfrac{1}{2a}(\sin(at)+at\cos(at))$
$\dfrac{s^2-a^2}{(s^2+a^2)^2}$	$t\cos(at)$
$\dfrac{s}{(s^2+a^2)(s^2+b^2)}\ (a^2\neq b^2)$	$\dfrac{\cos(at)-\cos(bt)}{b^2-a^2}$
$\dfrac{1}{(s^2+a^2)+b^2}$	$\dfrac{1}{b}\exp(-at)\sin(bt)$
$\dfrac{s+a}{(s^2+a^2)+b^2}$	$\exp(-at)\cos(bt)$

ANNEX C:
STABILITY

C.1. ONE-DIMENSIONAL FLOW BIFURCATIONS

The most basic bifurcation type is the saddle-node bifurcation, which is the basic mechanism by which fixed points are created and destroyed. As a parameter is varied, two fixed points move toward each other, collide and mutually annihilate. The prototypical example of a saddle-node bifurcation is given by the first-order system

$$\dot{x} = r + x^2 \tag{12.1}$$

Where r is a parameter, which may be positive, negative or zero. When r is negative, there are two fixed points, one stable and one unstable (Fig. C.1. a). As r approaches zero from below, the parabola moves up and the two fixed points move towards each other. When $r = 0$, the fixed points coalesce into a half-stable fixed point at $x^* = 0$ (Fig. C.1. b). This type of fixed point is extremely delicate, as it vanishes as soon as $r > 0$ and, afterwards, there are no fixed points at all (Fig. C.1. c). In this case, bifurcation occurs at $r = 0$ [33].

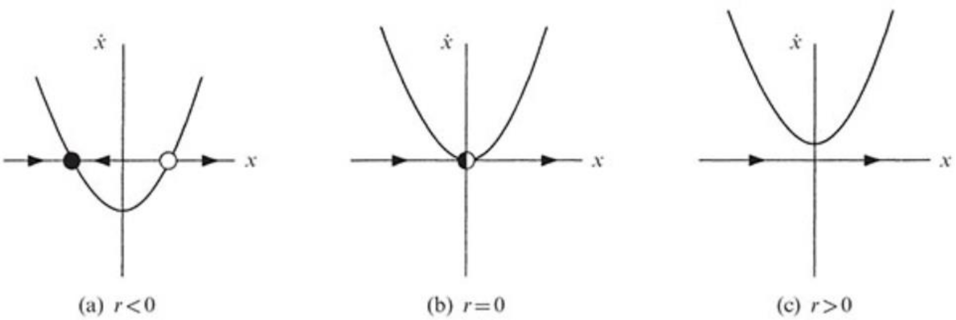

Figure C.1 Saddle-node bifurcation example

Therefore, if one represents the saddle-node bifurcation as a continuous stack of vector fields a picture of the generation of the bifurcation can be illustrated (Fig. C.2), which then can be represented in continuous lines accounting for stability and instability (Fig. C.3).

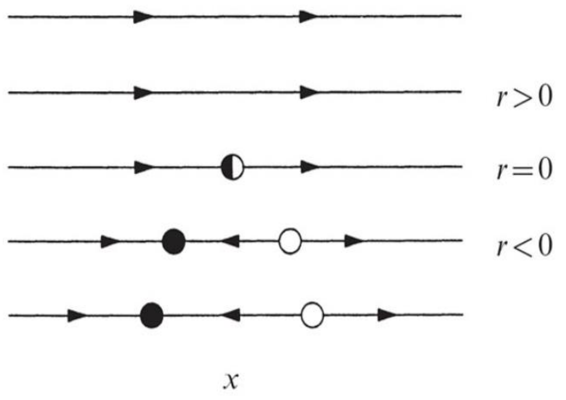

Figure C.0.2 Vector field stack [33]

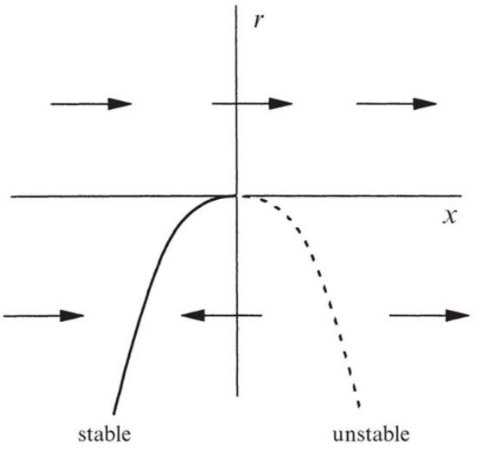

Figure C.0.3 Saddle-node bifurcation [33]

This example is the so called normal form of the saddle-node bifurcation as the dynamics typically look like eq. 12.1, so it is kind of the prototypical example of this pattern [33].

There are certain cases where fixed points must exist for all values of a parameter and can never be destroyed. Such a fixed point may change its stability as the parameter is varied. The transcritical bifurcation is the standard mechanism for such changes in stability (Fig. C.4). The normal form for a transcritical bifurcation is [33]

$$\dot{x} = rx - x^2 \tag{12.2}$$

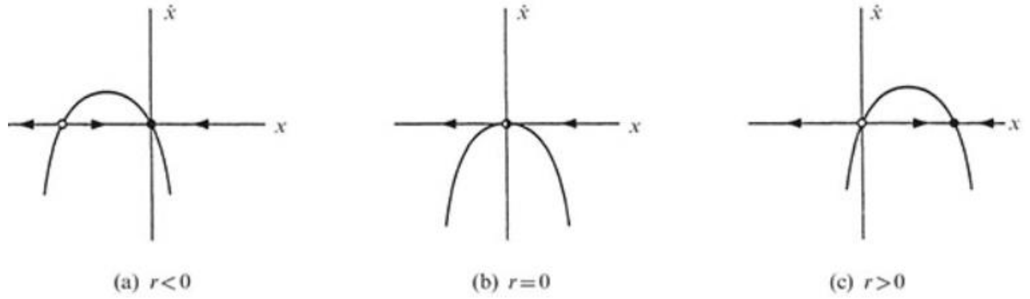

Figure C.4 Transcritical bifurcation example

Another kind of bifurcation is the so called pitchfork bifurcation, which is common for physical problems that have symmetry. Such a bifurcation can be supercritical or subcritical. The supercritical pitchfork bifurcation normal form is

$$\dot{x} = rx - x^3 \tag{12.3}$$

When r < 0, the origin is the only fixed point, and it is stable. When r = 0, the origin is still stable, but much more weakly so, since the linearization vanishes. Now solutions no longer decay exponentially fast, but instead the decay is a much slower algebraic function of time (Fig. C.5).This lethargic decay is called critical slowing down in the physics literature. Finally, when r > 0, the origin has become unstable. Two new stable fixed points appear on either side of the origin, symmetrically located at $x^* = \pm\sqrt{r}$ (Fig. C.5 and C.6) [33].

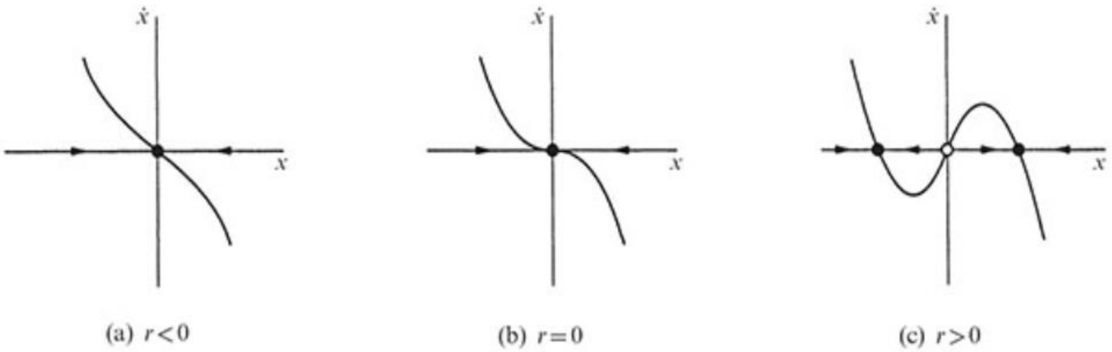

Figure C.5 Supercritical pitchfork bifurcation vector field [33]

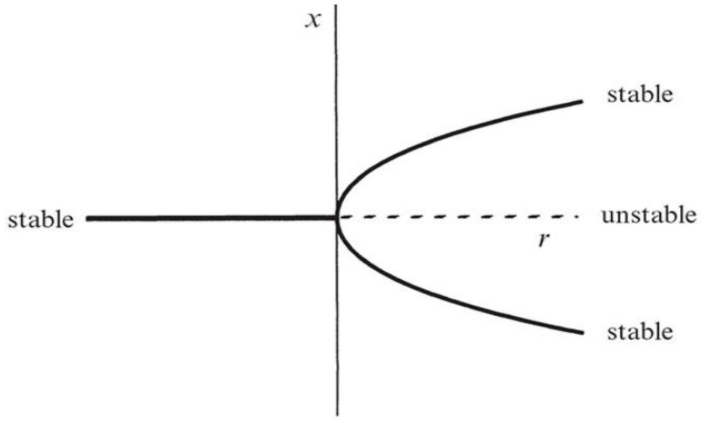

Figure C.6 Supercritical pitchfork bifurcation [33]

Whilst for the supercritical case, the cubic term is stabilizing, for the subcritical case, the cubic term is destabilizing. Which translates in the opposite pattern (Fig. C.7).

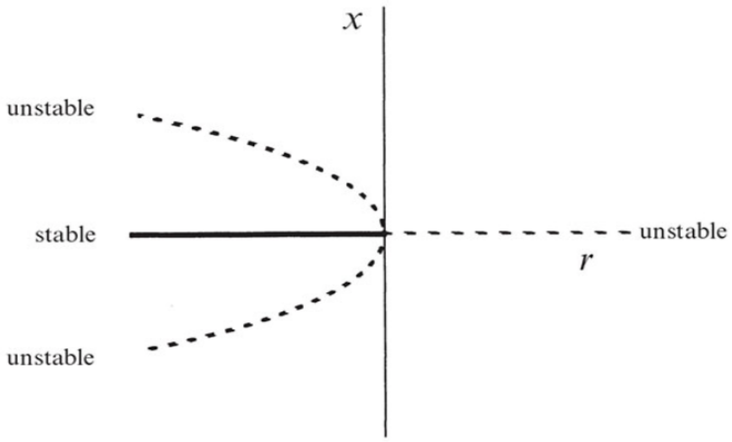

Figure C.7 Subcritical pitchfork bifurcation [33]